Doctoral Dissertation
Doctoral Program in Management, Production and Design (33rd Cycle)

Advanced Methods for the Mechanical and Topographical Characterization of Technological Surfaces

Giacomo Maculotti
* * * * * *

Supervisor
Prof. Maurizio Galetto

Doctoral Examination Committee:
Prof. Andreas Archenti, KTH Royal Institute of Technology
Prof. Martì Casadesus, Universitat de Girona
Prof. Dominik Matt, Libera Università di Bolzano
Prof. Massimo Pacella, Referee, Università del Salento
Prof. Guido Tosello, Referee, Technical University of Denmark

Politecnico di Torino
January 31, 2021

I hereby declare that, the contents and organisation of this dissertation constitute my own original work and does not compromise in any way the rights of third parties, including those relating to the security of personal data.

…….....

Giacomo Maculotti

Turin, January 31, 2021

Summary

Manufacturing is currently facing the challenging development of novel processes, e.g., additive manufacturing, and advanced materials, e.g., innovative composites and coatings, to cope with the more stringent customer demands for enhanced performances and customization and more sustainable use of resources. This requires flexible and fast quality inspections that rely on thorough, accurate, and precise characterization methods to cope with big data and interconnected cyber-physical systems within Industry 4.0.

Amongst several product properties, the characterization of technological surfaces is core to control the manufacturing process and engineer the product. In fact, it has long since it has been demonstrated processing conditions and process parameters induce a typical surface texture, i.e., the *manufacturing signature*. Therefore, characterizing the surface topography is essential to understand and qualify manufacturing processes and support process optimization and quality control. As the dependence of technological surface topographies on processing conditions has long been proved, also the fact that topographies can control a wide range of functional properties is well established. Consequently, the industry has targeted surface topographies' design to engineer products' functionality and increase their quality and performance. Thus, in the last decades, the increasing demand for enhanced performances pulled fundamental research in several fields, e.g., electronics, energy, IT, optics, tribology, to enable surface functionalization by surface technology.

The characterization is core to ensure the achievement of the modification goal and enable quality control. A complex set of characterization techniques must be adopted to achieve thorough characterization, considering complex interactions between surface topography and properties.

However, this set of complex characterization requires a continuous investigation and development to cope with new manufacturing challenges, such

as miniaturization, nanotechnologies, innovative processes, and materials. It is core to have precise and accurate characterization methods, to provide process engineers to exploit them with confidence and enable reliable and robust statistical process control of geometrical and technological properties of surfaces. Thus, a rigorous metrological framework is necessary to guarantee the measurements' traceability to enable their implementation for quality controls, results' comparability, and adoption for design specification within a sound and rigorous framework to enable total quality management. Therefore, this work aims to develop advancements for surface topographical and mechanical characterization by instrumented indentation test, as far as the methodological and metrological aspects are concerned, and apply them to interesting practical case studies.

Provided the massive attention received surface topography characterization in the last decades, this thesis will tackle two very specific aspects within this field. They are: (i) Assessing the effect of augmentation of conventional measurement techniques' informativeness on topography characterization to provide SMEs with tools to improve old-fashioned characterization methods' informativeness and increase their competitiveness in Industry 4.0; (ii) Evaluating measurement uncertainty of wear volume measurement methods based on topographical measurement, which is essential to enable comparability of results and improve the development of innovative material designed for wear reduction.

Instrumented indentation test is one of the most flexible mechanical characterization methods, enabling thorough multiscale characterization. It is widely exploited in industry and academia, in several sectors spanning from technological to life science. This notwithstanding and quite surprisingly, little research has been conducted on its metrological performances. Additionally, related standard shows some shortcomings in prescribing calibration procedures, thus hindering traceability and the exploitation of this technique to specify product requirement and statistical process control. Accordingly, this thesis tackles two main aspects pertaining to the metrological assessment: (i) Reducing measurement uncertainty, and (ii) Improving calibration procedure for testing machines. These two are strictly intertwined and aim to establish traceability for this technique and highlight potential impact factors in the calibration and characterization operations.

Acknowledgment

The first, I would like to thank my supervisor, Professor Maurizio Galetto, and Dr. Gianfranco Genta who guided me during these three years supporting my development both as a young researcher and as a young man, encouraging ideas and giving me the chance of learning and exploring so many different topics, meeting field experts and visiting different realities.

Also, I am thankful to Professor. Richard Leach, Professor Nicola Senin and Dr. Xiaobing Feng, from University of Nottingham, who hosted me for one year, giving me the opportunity of an exciting academic and life experience, making me feel at home.

I am thankful to Professor Giulio Barbato and Professor Raffaello Levi and Professor Don Lucca for their support by encouraging and insightful discussions; Dr. Massimo Lorusso for the fruitful collaboration and for giving me access to the facilities of the Istituto Italiano di Tecnologia and to and Dr. Roberto Cagliero for the interesting discussion had on his Ph.D. work, which I exploited to develop some of the results that will be presented.

I am grateful to the referees of this dissertation for their thorough review and insightful suggestion and comments.

I would like to thank my colleagues with whom I shared ideas, perspectives and this path long three years-time; the nice and friendly working environment help me through it.

Last, I need to thank my parents, my sister, my family and my friends who supported and bear me in this time.

Ai miei nonni, che ci saranno sempre.

Contents

List of Tables

List of Figures

Chapter 1

Introduction

Manufacturing is currently facing the challenging development of novel processes, e.g., additive manufacturing [1], and advanced materials, e.g., innovative composites [2] and coatings [3], to cope with the more stringent customer demands for enhanced performances, customization, and more sustainable use of resources. This requires flexible and fast quality inspections that rely on thorough, accurate, and precise characterization methods, to cope with big data and interconnected cyber-physical systems within the framework of Industry 4.0 [4–6].

Amongst several product properties, the characterization of technological surfaces is core to control the manufacturing process and engineer the product [7]. The *surface topography*, or simply surface, of an object is its geometrical feature that interacts with the surrounding environment [8]. The *technological surfaces* are a particular subset of surface topographies, including the surface topography of components manufactured by technological processes [9]. From a geometrical perspective, the topography includes both the form, i.e., the underlying shape, as the cylindrical geometry of a cylinder liner, and the texture, i.e., the residual geometrical features that remains once the form has been removed [8].

It has long since it has been demonstrated that the surface topography of a component is determined by the processing condition and the process parameters [10,11]. Therefore, the surface topography is intertwined with the manufacturing process and bears a typical signature, the *manufacturing signature*, i.e., a systematic pattern unique and distinctive of the process [12,13]. Typical examples of manufacturing signatures are shown in Figure 1 and Figure 2, where the dependence on the manufacturing process is clear: the honing and milling produce a “fuller” surface with some plateaus, depending on the shape of the cutting tool, turned surfaces are periodic and more “empty”, whilst EDM surfaces are characterized by very “empty” and stochastics profiles [14].

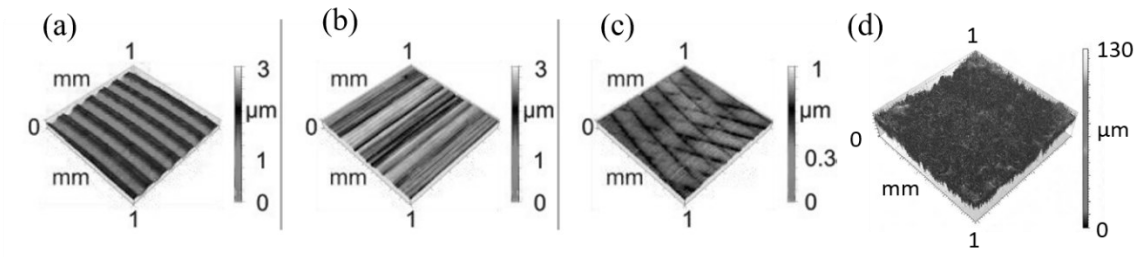

Figure 1 Example of manufacturing signature for (a) milling, (b) milling and grinding, (c) milling and honing (adapted from [15]) and (d) EDM (adapted from [16]).

Thus, research in both academia and industry has largely focused on investigating the main influencing process parameters: Figure 2 shows an example of the impact of process parameters, for a given process, on the topography. Some examples of manufacturing signature analysis, limited to two of the most widely adopted manufacturing processes, i.e., machining and injection molding, are provided in the following for reference.

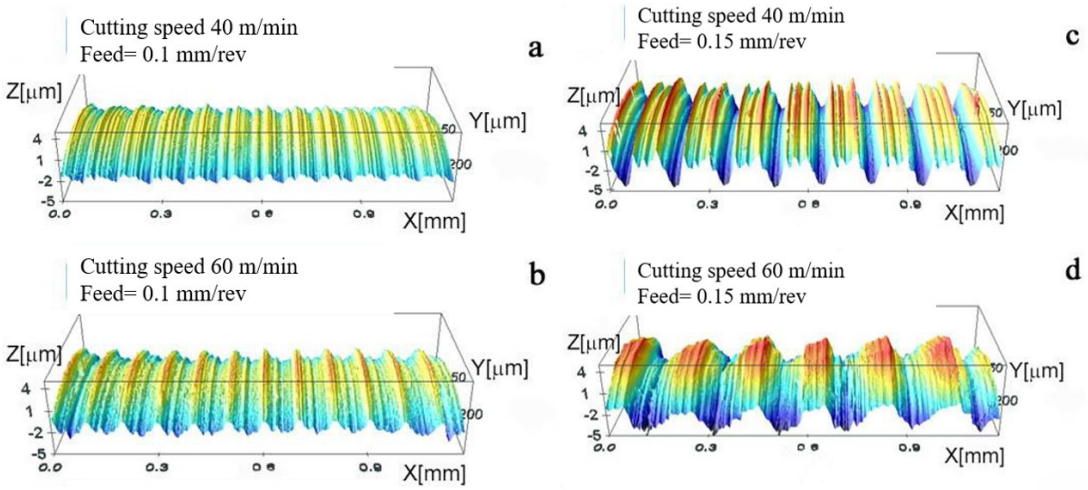

Figure 2 Effect of dry turning process parameters (cutting speed and feed rate) on the surface topography of a CoCrMo shaft (adapted from [17]).

Although a mature technology, machining still represents a significant share of manufacturing processes and is widely adopted for finishing, thus generating a significant market worldwide. Today, challenges are mostly associated with dry machining, aimed to reduce cooling agents' use and cutting fluids for sustainability [18], and processing innovative composite material [19]. Innovative processes are conceived to cope with customer demand for enhanced performances and, in some cases, with certain attention towards reusability and recyclability, within the framework of circularity and TPLM [2,20]. Consequently, the identification of the main influence factors to surface topography characteristics is still of interest. Chen et al. reviewed them for multi-axis ball-end milling [21], summarising the relevance of cutting parameters (feed rate, cutting speed, depth of cut, work inclination angle) and of boundary

conditions (the state of the raw material, of the lubricant, etc.). Gavalda Diaz et al. [19] reviewed critical machining conditions for Ceramic Matrix Composites, an innovative family of materials, appealing for their high-temperature and structural properties that find application in automotive, aerospace, and nuclear industries. Cheng et al. [22] analyzed the effect of cutting parameters in ultra-precision raster milling as Bordin et al. [17] investigated the effects of cutting speed and feed rate in dry turning.

Injection molding is a relevant manufacturing process that, given its capability to accurately produce large volumes of plastic components, with various components size and material composition and, hence, of different properties, finds application in automotive, aerospace, optical sectors [23]. The great flexibility, both in terms of design dimension and shape and material composition, of injection molding makes it extremely appealing to cope with the customization and modularity demand that will characterize manufacturing in the forthcoming future, within the paradigm of Industry 4.0 [4]. Martinez-Mateo et al. [24] investigated the effect of the mold surface integrity on the final component's quality. Rytka et al. [25] and Kuo et al. [26], respectively, addressed their attention to the effect of flow condition and holding phase parameters of injection molding and injection compression molding on surface topography and features repeatability for micro-structured surfaces.

These few examples, far from being exhaustive, prove that measuring and characterizing the surface topography is core for understanding and qualifying manufacturing processes. Therefore, they may also support the process optimization and ultimately enable identifying deviations from the in-control state. This concept has been variously deployed in literature.

Carbon Fibre Reinforced Plastic (CFRP) are composites materials that, thanks to their high specific strength, modulus, and fatigue resistance, find application in high-end automotive, aerospace, and military sectors. The fiber reinforcement makes them hard to machine without the generation of several defects, e.g., delamination, tearing, burr. Chen et al. [27] proposed optimizing the milling process for CFRP based on the benefits of component surface finish and tool durability when using a staggered polycrystalline diamond (PCD) cutter rather than a straight PCD cutter. Similarly, the need to control the topography depending on the type of cutting tool led Zhang and Liu to develop a prediction model of surface texture for finish turning [28].

As far as injection molding optimization is concerned, Martinez-Mateo et al. [24] and Bergstrom et al. [29] were able to determine the best set of processing parameters to achieve an adequate trade-off between the surface integrity of the manufactured component and the durability of the mold, respectively for glass-fiber reinforced PTB and PC. Similarly, Loaldi et al. [30] optimized the compression and holding phase pressure and duration to achieve the best surface topography accuracy and minimize the component's warpage for injection compression molding.

From a more general perspective, the analysis of surface topography has been exploited for statistical process control and tolerance verification. Polini et al. [31] exploited the manufacturing signature analysis to develop more robust and information-rich methods for geometrical tolerancing of components and assemblies; Colosimo et al. [32] investigated the presence of systematic errors in roundness profile through machine learning technique, i.e., principal component analysis (PCA) [33,34]. Pacella and Semeraro proved the adequacy of neural networks [35] to detect unnatural behavior in manufacturing processes for statistical process control [36,37] and employed them for geometrical tolerancing verification and control of profile roundness [38]. Further, the dependence of surface topography on processing parameters was exploited to design control strategies for quality control and statistical process control. As the pioneering work of Eppinger et al. [13] pointed out, the manufacturing signature first requires to be identified, then characterized on a set of dimensions (typically by synthetic indicators) and last analyzed and classified to establish whether the process is in control or not.

Once an out-of-control state can be detected, the next step entails inferring which process variable has drifted from the optimality condition by relating the process parameters to a particular manufacturing signature. A practical example can be found in Henke et al. [39], who developed a model to infer the manufacturing process given the geometrical error for machining internal cylindrical features. Others focused on the design specification based on the relationship between signature and process; Qi et al. [40] drawn correlation of surface texture parameters depending on the manufacturing process to help the designers define the product specification. Some exploited artificial intelligence to achieve this aim. Colosimo et al. employed PCA to study the effect of process parameters on 3D profiles geometrical verification and tolerancing [41]. Pacella et al. exploited multilinear algebra techniques to model and to enable statistical process control of turned surface topographies [42] and subsequently analyze and optimize the related manufacturing process [43]. Similarly, gaussian process regression (GPR) has been exploited to model [44] and monitor the quality of turning operation on the resulting surface topography [45]. Also, machine vision techniques have been exploited for tolerance verification of freeform topographies [46,47] and feature recognition [48].

As the dependence of technological surface topographies on processing conditions has long been proved, also the fact that topographies can control a wide range of functional properties is well established [49,50]. These, according to Bruzzone et al. [7], can be summarised according to the classification shown in Table 1.

Table 1 Main Functional properties of technological surfaces (adapted from [7]).

	Physical phenomenon	Functional property
Physical	Surface energy	Capillarity; wetting; adhesion
	Optical	Reflectivity; light absorption; diffraction
	Thermal	
Biological	Adsorption	
Technological	Mechanical	Fatigue; hardness
	Hydrodynamical	
	Tribological	Friction; wear; stiction

Consequently, the industry has targeted surface topographies' design to engineer products' functionality and increase their quality and performances. In fact, most relevant physical phenomena, which involve the exchange of energy and information, take place on the surfaces. Thus, in the last decades, the increasing demand for enhanced performances to enable surface functionalization pulled fundamental research in several fields, e.g., electronics, energy, IT, optics, tribology. The application of surface technology can achieve functionalization by modifying, structuring, i.e., optimizing the process parameters to obtain the functionalization, or depositing coatings [51]. When addressing surface modification, technological surfaces may result in being *structured* or *engineered*. According to Evans [50], the former have a deterministic pattern, and the latter are manufactured by a process optimized to generate a variation in the topography to guarantee a certain functionality; these definitions restrict the focus on surface textures.

Moreover, as components' dimension reduces (due to miniaturization and nanotechnologies development, this has been gaining increasing importance in the marketplace since the start of the millennium [52]), different surface phenomena can be exploited to achieve the same results in terms of functionalization. Conversely, at a given dimensional scale, the same result can be obtained by acting on different properties, e.g., the adhesion depends on both roughness and wettability; moreover, a given surface technology can modify a set of functional properties.

Surface technology provides an almost infinite range of opportunities exploiting a wide range of technologies. According to Bruzzone et al. [7], these can be grouped into four main categories:

- Adding material strategies, which either chemically or physically selectively deposit a coating on the substrate;
- Removing material strategies, which achieve a texturing by subtraction either by high temperature, e.g., laser, EDM, EBT, IBT, or chemical etching, with or without masking, or mechanical machining;

- Material moving strategies, in which plastic deformations are promoted either mechanically, e.g., by shot-blasting, embossing, or chemically, via molecular migration or UV contraction;
- Self-forming strategies, in which during the application matching components promote, either chemically, via localized diffusion, or mechanically, the creation of wear-resistant regions.

Literature is rich of surface technology application. For example, Davoudinejad et al. [53] developed an additive manufacturing photopolymerization process to structure at the micro-scale the topography of parts, to engineer the wettability, corrosion resistance, self-cleansing, and antibacterial surfaces or improve grip. The latter has interesting potential applications for components handling by robots, within human-machine interaction environment [54], and wall-climbing robots. Digital microfluidics applications, i.e., the control of fluid micro-flow based on the trigger coming from a physical signal, are extremely appealing for the biological and biomedical field to control drug release in the organism. To these aims, for examples, surfaces have been engineered to control and restrain the flow based on electrostatic fields [55,56], or at a larger scale, Bataille et al. [57] engineered the surface of a pump plunger providing a suitably high roughness, by optimizing the grinding process, to guarantee sealing abilities.

Regi et al. [58] optimized injection molding to engineer micro-structured surfaces for controlling optical properties with a high degree of repeatability. They patterned surfaces for electronic and information technology applications, e.g., enabling data storage and exchange based on computer vision through a patterning invisible to the naked eye.

As far as technological properties are concerned, Goeke et al. showed the impact of the appropriate selection of the finishing process on reducing the friction coefficient, which has a non-negligible effect on wear and energy dissipation [15]. In this sense, the automotive sector is incredibly receptive. It is well known that cylinder liners have to be plateau-honed textured [59–61] to improve cylinder lubrication, avoid wear and gripping, improve combustion efficiency and extend components life. Moreover, Etsion et al. [62–64] showed that a significant reduction in fuel consumption could be achieved by laser texturing piston pin and piston rings, collaterally reducing pollutant emissions. As far as coatings technology is concerned, Bewilogua et al. [51] conducted a review, though limited to the automotive sector, showing how effective and flexible the use of coatings can be, whose applications are summarised in Figure 3.

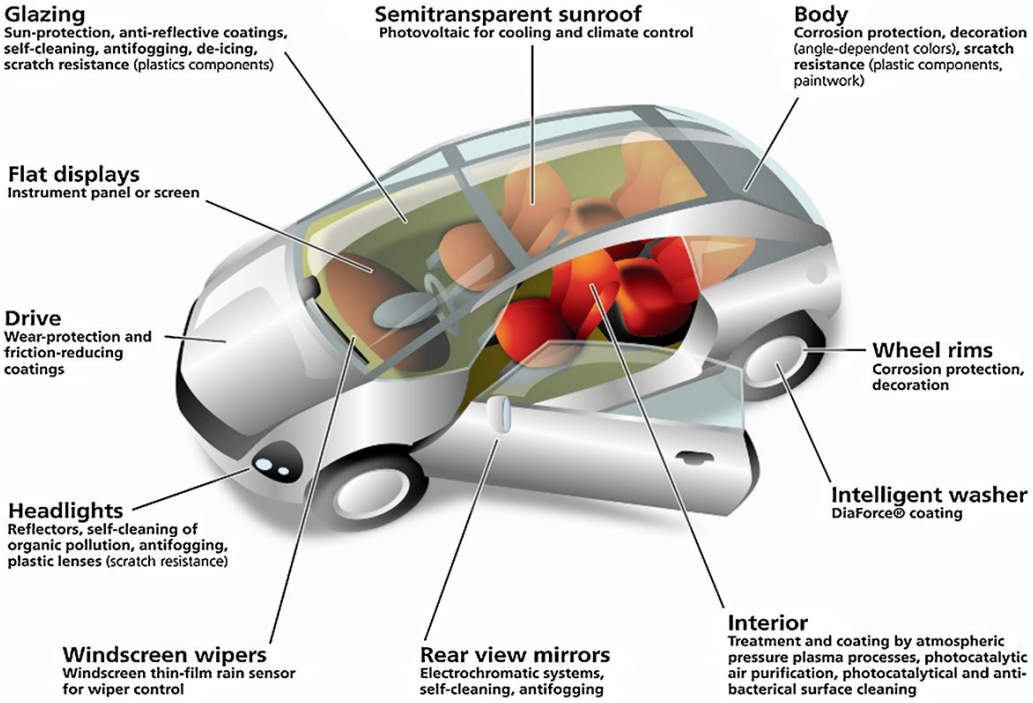

Figure 3 Examples of coating application in automotive sector (adapted from [51]).

1.1 A case study: Selective Laser Melting[1]

Additive manufacturing (AM) indicates a wide range of manufacturing technologies that, unlike traditional ones, rather than subtracting material, achieve final part geometry by adding it, usually layer-by-layer. This building strategy enables greater complexity and freedom in designing components allowing product optimization to the extent that would have been otherwise not feasible. The beginning of AM history can be set in 1985 when the first patent was released in USA. It was initially conceived to reduce prototypes' manufacturing time with the eventual target of overall time to market decrement. Since the late 1980s, Rapid Prototyping was introduced in the market and became strategic for US automotive OEMs to cope with increasing Japanese firms' competitiveness. In the 1990s, several AM techniques applications were developed to stand by traditional manufacturing processes such as casting and metal forming. In particular, AM was exploited to manufacture cores and patterns for investment casting (Rapid Casting) and die inserts for metal forming (Rapid Tooling). The new millennium's eve brought for AM the capability of processing final materials, which enabled this manufacturing process to be adopted in production lines for actual components and not only for prototypes. AM builds parts starting from a CAD model and manufacturing them by adding material layer-by-layer. Each of them is

[1] Part of this literature review was also previously published in: Galetto M., Genta G., Maculotti G., Verna E. (2020) Defect Probability Estimation for Hardness-Optimised Parts by Selective Laser Melting, *International Journal of Precision Engineering and Manufacturing*, 21(9):1739-1753.

a cross-section of the CAD model orthogonal to the building direction. Provided the general process of AM [65], this manufacturing process enables the production of innovative, complex, quasi-free form geometries without the need for tools, with limited waste material, and with time and cost only dependent on dimensions and not on geometric complexity of the component [1,66,67]. Consequently, as long as production volumes are limited and the part design benefits from high customization, AM processes are an effective alternative to traditional processes. Provided those caveats, they are increasingly replacing traditional processes and wedging their role in actual production from the mere prototyping stage with non-negligible savings [1,68,69]. Therefore, according to Gelter et al. [70], today is considered one of the pillars of Industry 4.0.

However, to allow for an actual introduction in production lines, process qualification and characterization are necessary to achieve control and eventually to define pipelines for total quality management of AM production chains.

One of the most widespread metal AM process is selective laser melting (SLM) or direct metal laser sintering (DMLS). In this process, a high-density object is built up layer by layer through the consolidation of metal powder particles with a focused laser beam, with certain laser power and diameter, that selectively raster scans, at a certain scanning speed and with a certain hatching distance, the surface of the powder bed, according to the geometry of the cross-section of the component [66,71–75]. Metal powders, also reactive materials like titanium and aluminium, e.g., Ti6Al4V or AlSi10Mg alloys, are melted without a binder's aid, as in the case for indirect laser sintering [76–80]. Researchers have recently shown an increasing interest in this process's potential, to build in one step full dense metallic parts with complex geometries used as final parts or functional prototypes [81,82]. Indeed, by choosing the proper input conditions, SLM components can achieve equivalent or very similar mechanical properties to those of parts produced by traditional manufacturing techniques [1,66]. However, despite the versatility of the materials and shapes that can be achieved, SLM features some criticalities requiring careful control of the process and the process variables used, which must be optimized to prevent defects from being generated. Defects may be classified into the following categories: residual stresses, porosity; cracking and delamination; balling; geometric defects and dimensional accuracy; surface defects, and microstructural inhomogeneity and impurities [83]. Geometrical defects depend on several complex phenomena related to melting and solidification phases, which, if uncontrolled, result in warpage, shrinkage, curling, and the so-called super elevated edges [84–87]. In particular, the latter, which consist of ridges of solidified material at the edges of the successive layer, may be critical as it deteriorates the surface topography and the overall dimensional accuracy, also by worsening the staircase effect and interacting, with the risk of damages, with the recoating system. SLM components surface topography depends on several factors, amongst whom we can quote a few: the staircase effect, powder particle size, orientation with respect to the growth direction, and other features that may happen to be generated during the process, e.g., super elevated edges and melt balls

The characterization of topographies of components by SLM has been addressed to control and understand defect generation.

Thompson et al. [88] initiated to draw an atlas of surface features for SLM. He noted that weld tracks typically dominate SLM topography. These results from the fusion and subsequent solidification of a melt pool and impart a strong texture directionality indicative of the laser (or electron) beam path. At smaller scales, weld tracks are covered by chevron-shaped ripples, i.e., weld ripples, indicating the beam scanning direction, and may feature smaller-scale thermal cracks and areas of local oxidization. Throughout weld tracks, high aspect-ratio singularities are observable, typically consisting of deep recesses or sphere-like protrusions. Recesses may result from incomplete seams between weld tracks, or within the track itself, or at smaller scales open micro-porosity [89–91]. Sphere-like protrusions are formed either from un-melted or partially melted powder particles (appearing alone or in clusters) or balling and spatter particles, i.e., molten material ejected from the melt pool during beam traversal, that impact the nearby surface during solidification. Moreover, the re-melting, which involves the current layer and those underneath, results in multiple, larger-scale, wave-like components that affect the top surface's final appearance. Figure 4 shows the main features of the SLM manufacturing signature.

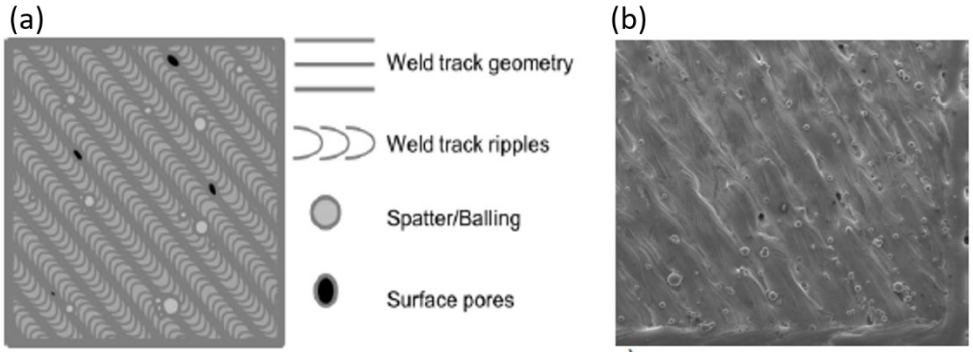

Figure 4 (a) Schematic diagram displaying the top view of features found on a typical SLM top surface. (b) SEM color map of the corresponding surface. Adapted from [88]

Literature [66,92–94] provides an overview of the most relevant influencing factors and a systematic study, using ANOVA, DoE, and RSM, of their effect on material characterization, both from mechanical and topographical perspectives. Amongst those, process variables represent a subset the component manufacturer can act on to control and optimize the process. According to Gibson et al. [65], notwithstanding their effects are intertwined, process variables can be divided into four categories: (1) laser-related variables (e.g., laser power, spot size), (2) scan-related variables (scan speed, scan spacing or hatching distance, and scan pattern), (3) powder-related variables (e.g., particle shape, size, and distribution, powder).

Consequently, extensive research has been carried out to infer the relationship between process variables and surface properties and defects. Krishnan et al. [95] found that among the process variables, hatch spacing had the most significant effect on the part mechanical properties, being capable of controlling the surface

finish and the surface hardness, hence the wear and tribological behavior of the component. In another study, Yan et al. [96] investigated the effect of volume fraction on the compressive strength and hardness of the DMLS-fabricated lattice structures. They also achieved near fully dense struts of AlSi10Mg lattice structures due to the overlap of melt pools. Ghasri-Khouzani et al. [97] tried to distinguish the microstructure and mechanical properties of different AM part planes.

Amongst the several process parameters, the laser power, P, the hatching distance, h_d, and the scan speed, v, are three of the most studied, as they can be easily modified by the end-user. Due to its working principle, SLM can be compared for issues (warping, thermal gradient, residual stresses) to casting, even though with quite the opposite microstructure, due to re-melting, and definitively without casting design constraints [98]. The laser source must generate a laser with a power sufficient to melt the layer and part of the layer underneath to guarantee adequate adhesion: the greater the laser power, the larger the re-melt zone. Because of the cyclic melting of layers, a fine microstructure results, which sometimes requires devoted heat treatments to be performed. Moreover, since the laser power controls the severity of the temperature gradient, it has a significant effect on the surface properties. Indeed, thermal gradient and resulting shrinkage may generate residual stresses leading to an increase in the probability of warping and cracks onset, which, though, can be relieved by slight oversizing the part [99,100] and devoted scanning strategies. The laser locally melts the cross-section with a pattern, i.e., scanning strategy, aimed at minimizing the thermal gradient and the residual stresses in the component, e.g., by means of the offset island strategy [101,102]; laser scans at a certain speed, v, which is critical to be appropriately set as it determines the amount of energy introduced during melting, hence influencing material properties and structure. Indeed, as Childs et al. (2005) noted [103], excessively high speed may hinder melting to occur or may yield to balling, whereas low speed entails high energy adsorption, E_A. Furthermore, complex interactions between P, v, and scanning strategy increase the complexity of the setup of this parameter [103]. Laser scans lines according to the scanning strategy to fill the cross-section. The distance between the center of two adjacent lines is the hatching distance or scan spacing, h_d, which is, therefore, a measure of the overlap of lines. In particular, multiple overlapping lines entails several passes of the laser on the same point, thus enabling higher v to be adopted [103,104]. Moreover, if the distance between two adjacent scan lines is larger than the laserbeam's diameter, the metal powders do not bind together well. Consequently, high hatch density entails greater energy adsorption and yields higher mechanical strength [105], hardness, and generally improved tribological behavior, thus decreasing defects generation probability.

Adhesion between layers is core to be achieved to avoid delamination and high part density and hardness. In particular, devoted scanning strategies have been developed to improve the layers' bonding, e.g., the alternate xy and the rotated hatch pattern [101,106]. Furthermore, layer thickness t has been demonstrated to affect adhesion, depending on energy absorption [101].

Therefore, these four process parameters, i.e., P, v, h_d and t, are strictly related to the degree of consolidation of the powder particles and surface topography properties. Hence, they may increase the probability of defect generation. Consequently, they are often adopted in literature as reference parameters for the setup of ANOVA, DoE, and RSM analysis of influencing factors on material properties [107].

1.2 Characterization technologies

Therefore, provided the complex interaction standing amongst the functional properties, the engineering technologies, and the application, the design of an application that exploits surface functionalization is definitively nontrivial. Thus, it requires thorough knowledge of the system, as summarised in Figure 5.

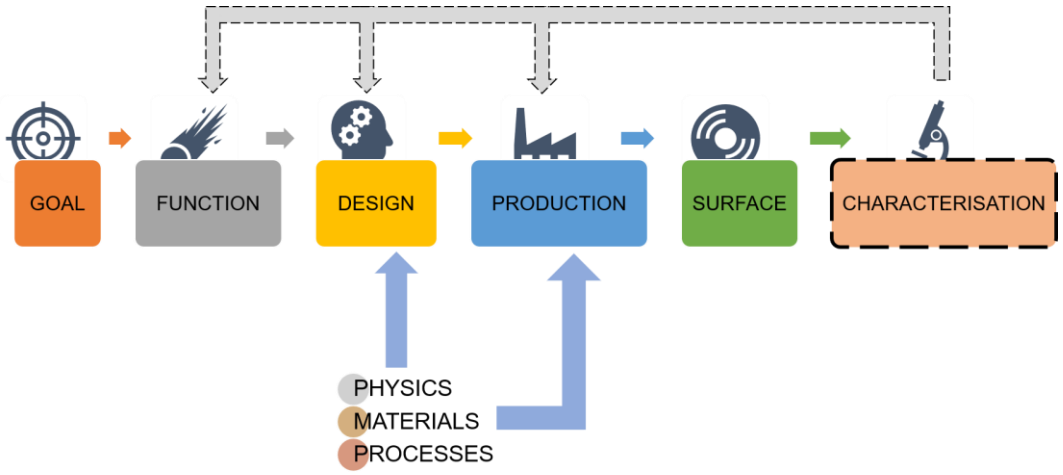

Figure 5 Workflow of a surface-based application (adapted from [7]).

Moreover, a core step to ensure the achievement of the goal and enable quality control is the characterization. It requires identifying the measurand in terms of properties that influence the functionality, the measurement scale, and, consequently, the most appropriate measurement method. Several properties may concur in defining certain functionality, which may also depend on the regions towards the bulk of the material [108], as outlined in Table 2.

Table 2 Surface regions and their functionality (adapted from [108]).

Depth regime	Depth	Examples of functionality
Upper Monolayer	~0.1 nm	Heterogeneous catalysis; surface tension; selective adsorption; chemical bonding
Thin Film	~0.1 nm – 100 nm	Emulsion; friction control; anti-reflective coatings; interference filters; corrosion protection; stiction; thermal conductivity
Near Surface	~0.1 μm – 10 μm	Semiconductor devices; surface hardening; membranes; photographic films; aerosols; grain structure
Thick Film	>10 μm	Anti-corrosion layers; surface cladding; painting

Provided the previous discussion, several characterization methods and properties are of interest. Lonardo et al. [108] and De Chiffre et al. [109] offered a thorough review of the several available characterization technologies. Rutherford Backscattering Spectrometry (RBS) achieves atomic composition and crystalline structure qualified through the elastic backscatter of colliding high energy ions; thus, RBS can detect impurities in composition and subsurface damages. Electrical properties can be probed by a broad set of scanning probe systems, e.g., scanning capacitance microscopes, scanning surface potential microscopes, and scanning spreading resistance microscopes. Electrical characterization allows detecting defects as they introduce changes in local atomic bonds, affecting the electrical properties. Chemical compositions can be effectively addressed by scanning electron microscopes (SEM), transmission electron microscopes (TEM), scanning tunnelling microscopes (STM), and energy-dispersive x-ray (EDX) systems. Surfaces' mechanical properties, e.g., hardness, elasticity, creep, residual stresses, can be effectively characterized through conventional tests, e.g., tribological tests, conventional hardness tests, and unconventional and non-destructive tests, e.g., nanoindentation. Last, undoubtfully, for a structured surface, the measurement of surface texture is necessary [7,108,109]. Provided the multi-objective nature of the characterization, multi-sensors characterization is necessary to describe the properties thoroughly. Therefore, multi-sensor data fusion is often resorted to augment the informativeness of individual characterization techniques [110–112].

1.3 Scope of this work

The former literature review, by some non-exhaustive examples, aimed to show the relevance of technological surface characterization for quality control of manufacturing processes. As mentioned, the characterization of technological surfaces entails several multi-objective methods. This set of complex characterization requires a continuous investigation and development to be capable of coping with new challenges of manufacturing, such as miniaturization, nanotechnologies, innovative processes, and materials. It is core to have precise and accurate characterization methods, to provide process engineers to exploit them with confidence and enable reliable and robust statistical process control of geometrical and technological properties of surfaces. Thus, a rigorous metrological framework is necessary to guarantee the measurements' traceability to enable their implementation for quality controls ultimately. In fact, without traceability and measurement uncertainty specification of the characterized value, it is impossible to ensure results comparability and design specification, tolerances and inspection strategies, and statistical process control, i.e., define control limits, within a sound and rigorous framework to enable total quality management. Furthermore, the evaluation of uncertainty allows identifying the most impacting influence factors and, thus, indicate the most effective actions to improve characterization techniques. Therefore, this work aims to develop advancements for surface topographical and mechanical characterization as far as the methodological and metrological aspects are concerned and apply them to interesting practical case studies. Figure 6 depicts the workflow of the research conducted, which is briefly outlined in the following.

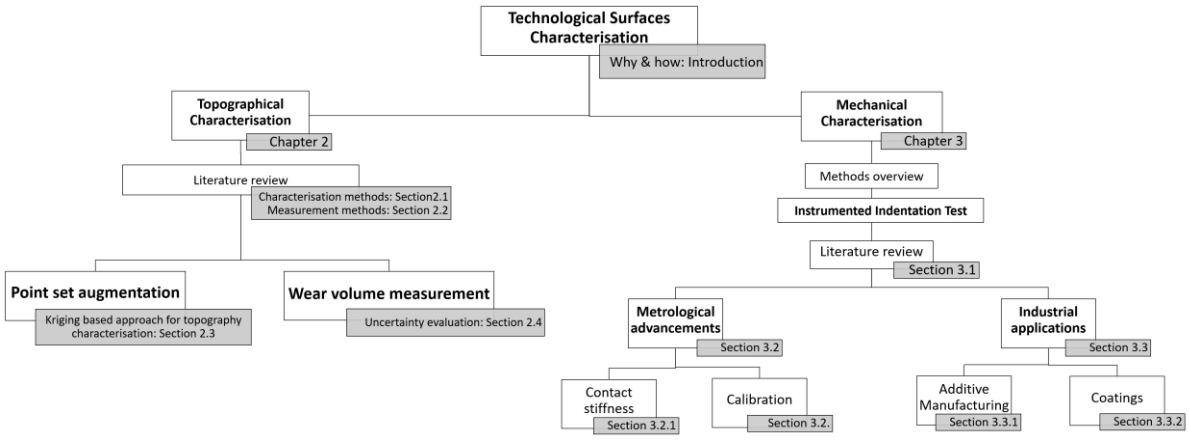

Figure 6 Workflow of the research conducted during the PhD.

Given the mentioned relevance, topographical characterization was largely investigated and exploited in both academy and industry; Section 2 will review the relevant literature limited to some characterization aspects. Provided the massive attention received by this topic in the last decades, this thesis will tackle very specific aspects within this field. In particular, it will focus on two main challenges, which will be succinctly motivated in the following:

- Assessing the effect of augmentation of conventional measurement techniques' informativeness on topography characterization,
- Evaluating measurement uncertainty of wear volume measurement methods based on topographical measurement.

Topography geometrical analysis has been performed since the beginning of the last century, and measurement techniques developed according to the industry requirements [113]. Nowadays, information-rich measurements are necessary to cope with manufactured products' complexity and enable characterization within interconnected cyber-physical systems [114,115]. However, surface topography measuring instruments can be expensive and require specific knowledge for their operation, which hinders their diffusion in Small and Medium Enterprises (SMEs). SMEs represent 10% of current European enterprises, in the technological and manufacturing sector, with an employment of about 7% (figures slightly higher for Italy) [116]. However, these often rely upon conventional measurement techniques, which, though, are less informative and, hence, might limit SMEs' competitiveness within the current industrial framework. Consequently, it is of interest to investigate enabling technologies to increase conventional measurement methods', e.g., contact probes, informativeness to make them compatible with more innovative and expensive ones. Although literature proposes methods to achieve the aim, see for example Senin et al. [110], the effect on surface topography characterization of these methods is unreported. Accordingly, this work investigates the effect of point set augmentation on the estimation of surface topography parameters to prove the representativeness consistency and provide users with confidence in their adoption.

The other main research question, related to surface topography characterization, is associated with wear measurement. Friction is responsible for a significant amount of worldwide energy consumptions and liable for generating wear, which often results in component failures and replacements [7]. Thus, within Industry 4.0 and sustainable industry, innovative materials, as hard metals, ceramic, and metal matrix composites coatings, have been studied to reduce friction and wear of components. As a result, the assessment of the wear of material is still of primary concern. However, because of the great complexity of wear processes, several testing methods are available, some of whom, e.g., pin-on-disc, are highly conventional and intended to enable comparison and repeatability of results. These tests rely upon methods that exploit surface topography measurements. However, the metrological performances and uncertainty of these methods are unreported. This thesis tries to fill this literature void within a metrological framework by developing a framework to evaluate related measurement uncertainty. In fact, lacking this, comparing conventional test results has limited statistical significance, and the identification of a set of parameters, hereby including materials, to enable the calibration and performance comparison of testing equipment is hindered.

The second focus of this thesis is the mechanical characterization of technological surfaces. Amongst several available mechanical characterization

methods, instrumented indentation test is one of the most flexible, enabling thorough multiscale characterization. Consequently, it is largely exploited in industry and academia, in several sectors spanning from the technological to life sciences [117]. This notwithstanding and quite surprisingly, little research has been conducted on its metrological performances, and related standard shows some shortcomings in prescribing calibration procedures. This may hinder traceability and comparability of characterization results obtained by instrumented indentation testing. In turn, this limits the exploitation of this technique to specify product requirements and statistical process control. Accordingly, Section 3 will review the technique and tackle two main aspects pertaining to the metrological assessment:

- Reducing measurement uncertainty,
- Improving calibration procedure for testing machines.

These two are strictly intertwined and aim to establish traceability for this technique and highlight potential impact factors in the calibration and characterization operations. As it will be discussed, due to the current literature and the state-of-the-art, advancements that are proposed in the present work for mechanical characterization are, in the author's opinion, more substantial than the one achieved for topographical characterization.

This thesis is structured as follows: Chapter 2 deals with surface topography characterization, Chapter 3 with mechanical characterization. Each chapter reviews the related characterization state-of-the-art, and presents individual subsections addressing the research objectives. Each of these subsections includes first a specific literature review to highlight the addressed shortcomings and then propose a methodology to overcome them; experiments to test the methods are then introduced, and results discussed. Each subsection includes a summary, when relevant, to highlight the main obtained results. Chapter 4 concludes on the findings and the limits of the present work, outlining future research perspectives.

Chapter 2

Advanced Methods for Surface Topography Characterization

As discussed in the introduction, the surface is the interface at which physical interaction between the component and the surrounding environment occurs. Moreover, technological surface topographies feature signatures, i.e., a texture, which can be determinant in qualifying the manufacturing process. According to Leach [113], 10% of components failure can be ascribed to a topographical specification's poor realization. Thus, the topography's geometrical characterization is core to understand, control, and engineer product and processes.

Texture characterization has long been exploited by conventional means, i.e., contact stylus instruments (or profilometers), since the late '40s of the past century. It entails measuring profiles extracted from the surface, i.e., surface heights as a function of the lateral displacement $z(x)$. The characterization relies on evaluating synthetic indexes, e.g., R_a or R_q, describing the profile heights' main statistical properties. The profile-based characterization of texture has been standardized by ISO 4287-1 [118], first released in 1987, latest updated in 1998, and currently under review. No major breakthroughs have been made in this field until 2000, with the completion of the European project CALISURF, which set the ground for the calibration standard (ISO 5436) by identifying a set of four type artifacts.

However, conventional measurements based on profiles are not adequate when dealing with contemporary surface technology and topographically complex surfaces, e.g., additive manufacturing surfaces, engineered structured surfaces for optical, surface energy, and biomedical application. In fact, despite profiles can yield some information about a component's functionality cannot be thorough; additionally, the extraction of profiles is inherently less robust, representative, and statistically significant than an extended areal measurement, as depicted by Figure 7 [119].

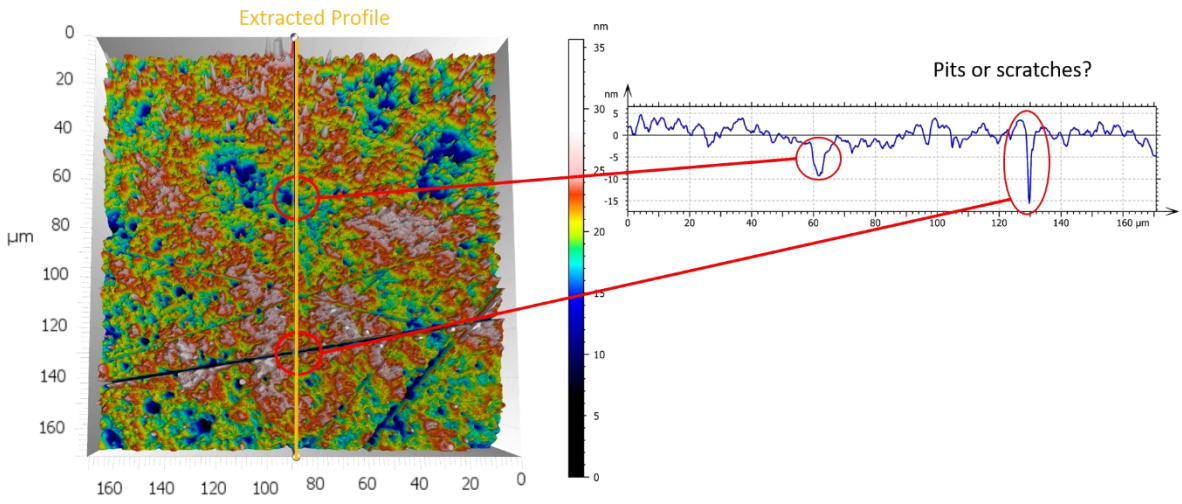

Figure 7 Representativeness of profile versus areal measurement.

The publication of the *Blue Book* [120] can be considered the first step towards areal surface texture measurement since it included the original set of fourteen parameters, the *Birmingham-14*, conceived to describe topographies. Later on, another European project, SURFSTAND, yielded the so-called *Green Book* [119], which is the basis of the development of the current standard framework of ISO 25178.

In the following, the main characterization and measurement methods and techniques will be reviewed before addressing some proposed developments for the characterization of surface topographies. In particular, as mentioned in the Introduction, two aims are pursued: assessing the effect of augmentation of conventional measurement techniques' informativeness on topography characterization and evaluating measurement uncertainty of wear volume measurement methods based on topographical measurement. Provided the long and extended research in this field, the objectives aim to incrementally contribute to the relevant literature within specific application areas concerning surface topography characterization.

2.1 Characterization standard

The current standard characterization framework is the ISO 25178 Geometrical Product Specification (GPS). The GPS model is defined in ISO 14638:2015 [121] and aims to define the geometrical properties of components. As far as the topography is concerned, the GPS model contains profile and areal surface texture. The series ISO 25178 is currently limited to the areal surface texture but will include the current profile characterization standards to provide the users a more general and uniform framework.

Areal surface texture characterization involves several steps. The topography can be thought of as the result of the superimposition of several structures at different length scales or different wavelengths. These include roughness at low scales, form at large scales, and waviness, i.e., a periodic structure typically at

large scales. The interaction between the surface and the measuring instruments further contribute to these topographical features. Consequently, preliminary filtering is required to isolate the scales that shall be the objective of the characterization. Filters are standardized; consequently, this operation is referred to as the application of *standard operators*. ISO 25178-2:2012 describes the sequence of standard operations and identifies two possible outcomes, i.e., two possible *scale-limited surfaces*: the S-F and the S-L surface. S-F surface results from applying an S-filter with a nesting index λs, i.e., a low-pass filter in the frequency domain with a cut-off wavelength λs, and of an F-operation, i.e., a least-square fitting to remove the known a-priori form of the surface. S-L surface results from the further application to the S-F surface of an L-filter, i.e., a high-pass filter in the frequency domain with a cut-off wavelength λc. Figure 8 summarises the sequence of filter operations and highlights the removed scales. ISO 25178-3:2012 defines standard nesting indexes and operators that can be applied depending on the instrument type.

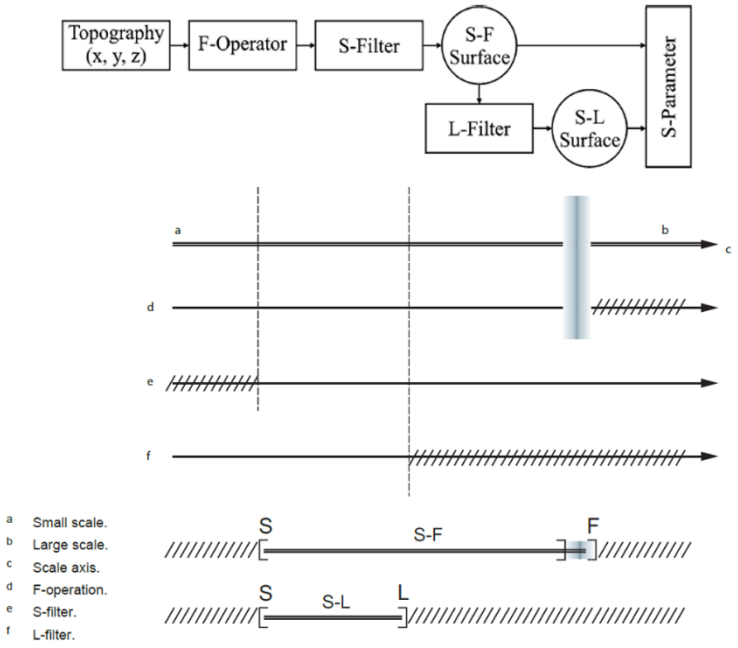

Figure 8 Sequence of standard operators to obtain scale-limited surfaces.

Due to this multi-scale structure, textures' characterization requires identifying the amplitude and the wavelength, or equivalently the frequency, of the main (periodic) scales are required. To this extent, the Fourier transform of *z(x,y)* allows computing the spectrum of the surface heights, i.e., the frequency-dependent amplitudes of *z(x,y)*, whose most typical representation makes use of the Power Spectrum Density (PSD). The analysis of amplitude peaks of the spectrum enables identifying the main harmonics, i.e., the periodic pattern's main frequency. Real surfaces typically show one of the main peaks at very low wavelengths: the amplitude of this peak estimates the random variation of *z(x,y)*

superimposed to the measurement noise, according to signal theory [8,122], which justify the application of the S-filter.

On the scale-limited surface, characterization can be carried out. It can either target the evaluation of surface texture parameters, which can describe the whole sampling area (these are the *areal field parameters*) or individual features (*feature parameters*), or the topographical feature characterization. Any of these is standardized in ISO 25178-2:2012 [123]

Areal field parameters

Field parameters aim to describe the whole sampling area, catering for different geometrical characteristics, e.g., height, slopes, complexity, anisotropy. The main parameters and the ones adopted in this work will be introduced and briefly discussed in the following.

- Height parameters
  - Arithmetic mean height, $S_a = \frac{1}{A}\iint_A \left|z_{(x,y)}\right| dx\, dy$
  - Root mean square height, $S_q = \sqrt{\frac{1}{A}\iint_A z^2_{(x,y)}\, dx\, dy}$
  - Skewness, $S_{sk} = \frac{1}{{S_q}^3}\frac{1}{A}\iint_A z^3_{(x,y)}\, dx\, dy$
  - Kurtosis, $S_{ku} = \frac{1}{{S_q}^4}\frac{1}{A}\iint_A z^4_{(x,y)}\, dx\, dy$
  - Maximum peak height, S_p
  - Maximum pit height, S_v
  - Maximum height, $S_z = S_p + |S_v|$.

S_a, S_q, S_{sk} and S_{ku} are the first four statistical moments of the empirical statistical distribution of surface heights $z(x,y)$; these are defined on the domain individuated by the sampling area A. However, statistical moments cannot suffice; thus, S_p, S_v and S_z describing the height range are introduced.

- Function and related parameters:
  - Areal material ratio function of the scale-limited surface, S_{mr}
  - Areal material ratio of the scale-limited surface, $S_{mr}(c)$
  - Inverse areal material ratio of the scale-limited surface, $S_{mc}(m_r)$

When describing the topography's statistical properties, it can be useful to rely upon the S_{mr}, also known as the Abbott-Firestone curve. It is the sample cumulative probability function of the measured heights within the evaluation area. This curve describes the material ratio $m_r = S_{mr}(c)$, i.e., the cumulative probability of finding a point of the topography whose height is at most $c = S_{mc}(m_r)$; Figure 9 depicts this relationship.

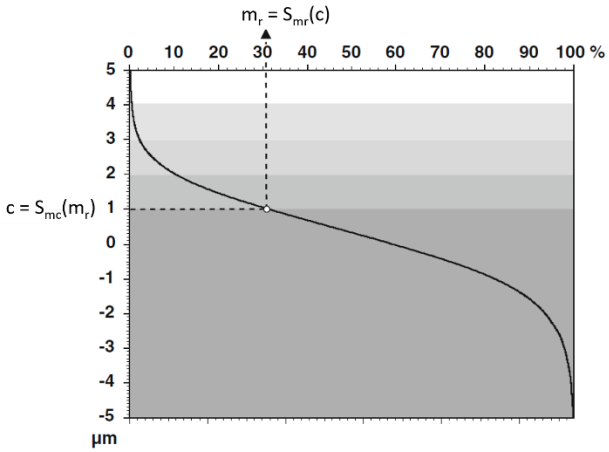

Figure 9 Areal material ratio curve and the relationship between $S_{mr}(c)$ and $S_{mc}(m_r)$ (adapted from [8]).

- Spatial parameters:
  - Autocorrelation function, $f_{ACT}(\tau_x, \tau_y) = \frac{\iint_A z_{(x,y)} z_{(x-\tau_x, y-\tau_y)}\, dx\, dy}{\iint_A z_{(x,y)} z_{(x,y)}\, dx\, dy}$
  - Autocorrelation length, $S_{al} = \min\{\sqrt{\tau_x{}^2 + \tau_y{}^2}\}, \tau_x, \tau_y \in R = \{(\tau_x, \tau_y) : f_{\mathrm{ACF}}(\tau_x, \tau_y) \leq s\}$
  - Texture aspect ratio, $S_{tr} = \frac{R_{min}}{R_{max}}$
  - Surface texture direction, S_{td}

where, $R_{min} = S_{al}$ and $R_{max} = \max\{\sqrt{\tau_x^2 + \tau_y^2}\}$. When measuring technological surfaces, textures can be structured and anisotropic. The quantification of these characteristics is core for components functionality assessment and process quality control. In fact, these geometrical characteristics can be either due to a product functionalization or to unwanted manufacturing signatures. Spatial parameters are the best-suited set of areal field parameters for this purpose. Being the f_{ACT} the autocovariance of $z(x,y)$ normalized by S_q^2, $f_{\mathrm{ACF}} \in [-1,1]$, it is maximized at the value 1 at the center of its domain, and it is apt to detect periodicities. S_{al} and S_{tr}, whose definitions exploit the f_{ACT}, are designed to characterize the isotropy of the surface synthetically. The former estimates the severity of the surface anisotropy, as it is the distance at which a portion of the surface is significantly different from the original location. The latter quantifies the significance of the anisotropy: provided that $S_{tr} \in [0,1]$, if $S_{tr} > s$, the surface can be considered isotropic. The threshold s is conventionally set to 0.2 [123]. In the case of anisotropy, the direction of the anisotropy, i.e., the main pattern, is orthogonal to the direction of S_{al} and quantified, as an angle, by the surface texture direction, S_{td}.

- Volume parameters:
  - Material volume, $V_m(m_r) = K \int_{0\%}^{m_r} S_{mc}(p) - S_{mc}(m_r)\, dp$
  - Void volume, $V_v(m_r) = K \int_{m_r}^{100\%} S_{mc}(m_r) - S_{mc}(p)\, dp$

K is a factor converting the relative volume into the most appropriate unit and is the surface topography horizontal development area. Given a specific section plane at height $h = S_{mc}(m_r)$, the V_m represents the volume of material enclosed below the surface and above this plane, whilst V_v the volume of missing material above the surface and below this plane, see Figure 10. Volume parameters are largely used for functional requirements, as a load-bearing surface for bearings or to characterize wear [124].

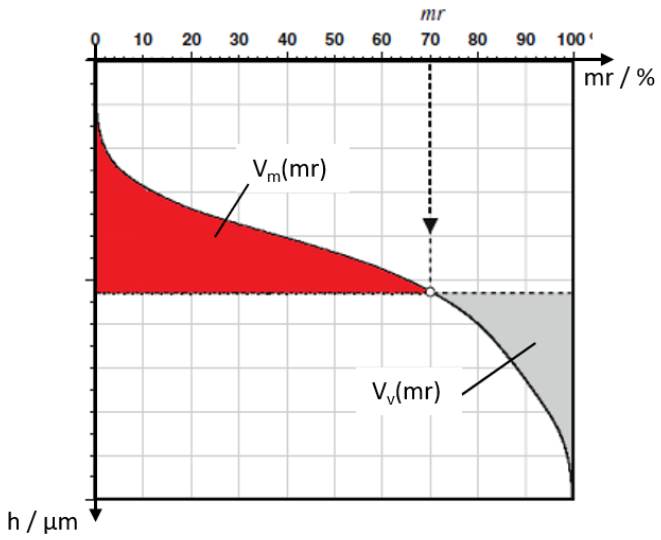

Figure 10 Void and Material volume parameters (adapted from [8]).

2.2 Main measurement techniques

Over the last four decades, several surface texture measurement techniques have been developed. In this section, a brief overview of the most industrially widespread technologies is provided. The focus will be limited to already standardized technologies. According to ISO 25178-6:2010 [125], the different measurement approaches can be classified into three main groups, as depicted in Figure 11:

- Line-profiling methods, which scan a profile, i.e., a 2D graph, of surfaces height, z, that can be mathematically represented as a function of the scanning direction, $z(x)$;
- Areal topography methods, which achieve a representation of the topography as 2.5D height function, $z(x,y)$, or by the juxtaposition along y of profiles $z(x)$; these methods are thoroughly reviewed by Leach [113];
- Area-integrating methods, which obtain the topography's characterization by measuring a representative area and then evaluating results dependent on area-integrated properties of the texture.

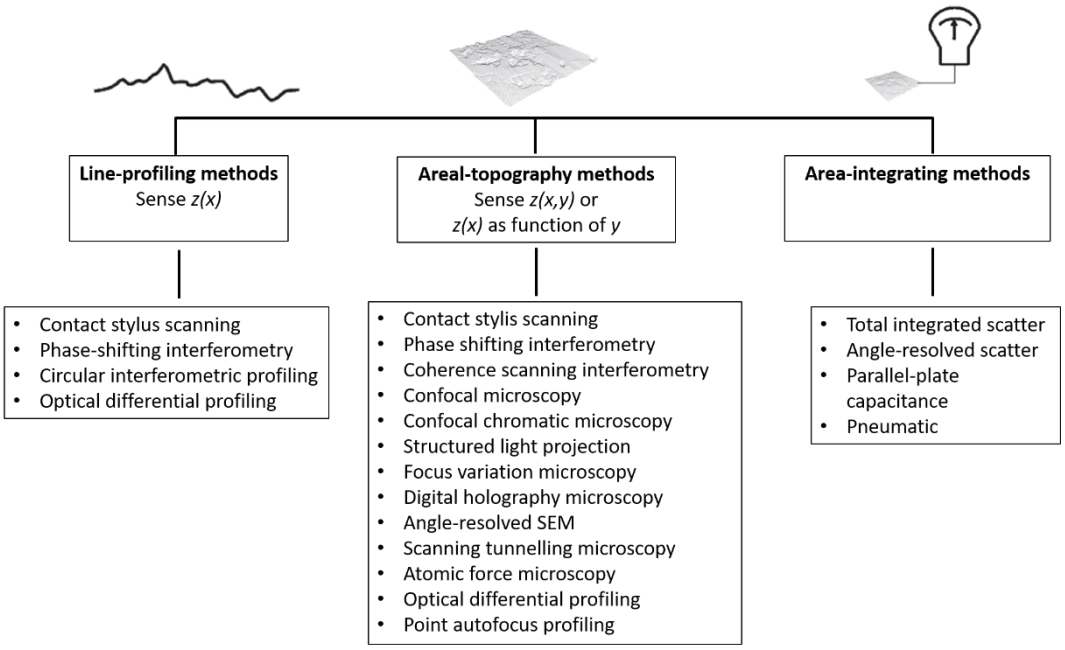

Figure 11 Standardized methods for areal surface texture measurement, according to ISO 25178-6:2010.

In addition to the more widespread and standardized approaches, which can achieve either a 2D or a 2.5D measurement of the topography, as the measurement instrument cannot measure what is beneath the surface but still provide a set of cartesian triplets, i.e., *(x,y,z(x,y))*, it is worth to point out the attention to techniques currently under development in academia based on X-ray Computed Tomography (XCT) which are capable of yielding true 3D topographical measurements [126,127]. These find application in the non-destructive qualification of topographies of hard to reach features, e.g., typical in additive manufacturing [128].

Contact stylus instruments

Contact stylus (CS) instruments are the first developed to measure topographies. These consist of a diamond tip, typically conispherical, mounted on a pickup, operated by a drive unit, and translating the tip across the surface at a constant speed. A transducer measures the lateral and vertical movement of the stylus. Figure 12 shows an example of a CS with its main elements. Areal measurement is achieved by raster scanning the surface, impractical and time-consuming in some applications.

Contact stylus instruments are robust and yield, as a measurement result, a mechanical surface, i.e., the surface resulting from the physical interaction between the probe and the actual surface. Therefore, they are largely used as primary instrumentations to characterize calibration samples, material measures and etalons for areal surface texture measurements [129] (application in which usability is not the primary concern), because it is simple to deconvolute the tip effect from the mechanical surface, correcting the error that may arise when

measuring valleys and peaks. Contact stylus is standardised in ISO 3274:1998 [130], ISO 25178-601:2010 [131], and best practices can be found in NPL Good Practice Guide 37 [132].

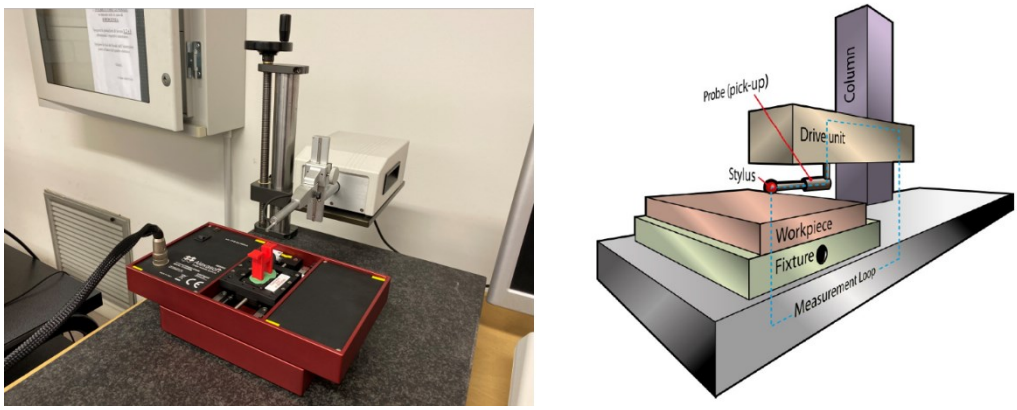

Figure 12 Contact Stylus instrument commercial system (MS RTP-80) and scheme with main components (adapted from [132]).

Surface topography measuring instruments based on interferometry

Coherence Scanning Interferometers (CSI) and Phase Shift Interferometers (PSI) are the two areal surface measuring instruments based on interferometry. CSIs have been more recently introduced in the market than PSI. They both are optical areal-topography microscopes that rely on interferometry to measure the surface topography. In these systems, the light is split by a splitting mirror in two paths, one impinging on a reference mirror and the second on the measurand surface. Their reflections are recombined and sensed by a camera (see Figure 13 for a schematic). Considering that destructive interferences decrease the intensity of the sensed signal, it is possible to deconvolute the interference fringes and reconstruct the path differences of the light from the reference mirror and the measurand surface, to measure the topographical difference of the latter with respect to the former. PSIs deconvolute fringes on the base of phase shift; CSIs additionally cater for intensity shift. This is achieved by additionally scanning on a vertical range, making CSI capable of dealing better with rougher and unpolished surfaces than PSI [133,134].

PSI and CSI are standardized, respectively, in ISO 25178-603 and -604:2013 [135,136], best practices can be found in NPL good practice guide 108 and 116 [137,138].

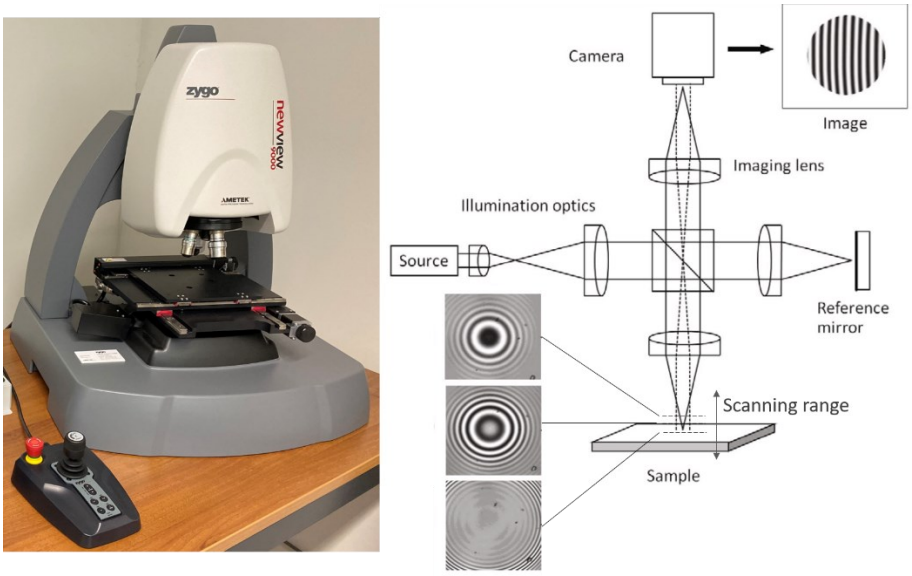

Figure 13 Coherence Scanning Interferometer commercial system (Zygo NewView9000) and working principle schematic (adapted from [134]).

Confocal surface topography measuring instruments

Imaging Confocal microscopes (ICM or CM) achieve surface topography measurement by producing optically sectioned images of the measurand surface. The working principle relies on illuminating the sample by a restricted, structured illumination pattern (through a pin-hole, set of pin-holes, slits, etc.) and observing the reflected light by a second identical pattern. This solution blocks the light from the region outside the focal plane and ultimately identifies points in focus [139]; see the schematic of the working principle in Figure 14. The addition of vertical scans allows achieving a topographical measurement. Confocal microscopes are standardized by ISO 25178-607:2019 [140].

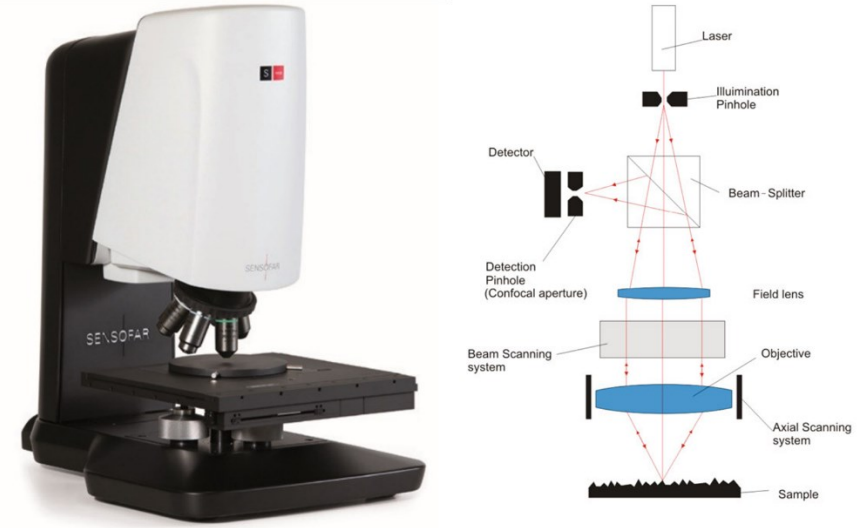

Figure 14 Confocal Microscope commercial system (Sensofar S-Neox 3D Profiler) and working principle schematic (adapted from [113]).

Focus variation instruments

Focus Variation (FV) microscopy is one of the most recent areal-topography optical methods to measure topographies. It relies upon searching for the best focus position of an objective with a limited depth of field (DOF) directed to the sample. Rays of white light pass through the objective to impinge the surface and are reflected back to a charge-coupled device (CCD) sensor, which generates images of the measured field of view (FOV). A drive unit onsets a relative vertical motion between the sample and the objective. Different images are measured at different positions of the scanned range [141]. Figure 15 shows the main components of a FV microscope.

The different images have, per each lateral position of the CCD sensor (i.e., pixels), a different contrast; the topography, i.e., the *z(x,y)*, is obtained seeking, per each pixel, the maximum contrast with respect to the neighboring pixels. Different approaches are available to locate the maximum contrast, and they may result in a lateral resolution smaller than the pixel size of the CCD sensor [141].

FV instruments are standardized in ISO 25178-606:2015 [142] and belong to the broader category of optical measuring systems. As the ones presented in the following, FVs achieve the measurement based on interactions between the optical system and the actual surface. This results in the measurement of the electromagnetic surface, which may not differ from the mechanical surface; however, because determining exact interaction, and hence the presence of systematic error with respect to the actual surface, is more difficult in this case, optical systems are not exploited for primary instrumentations [129].

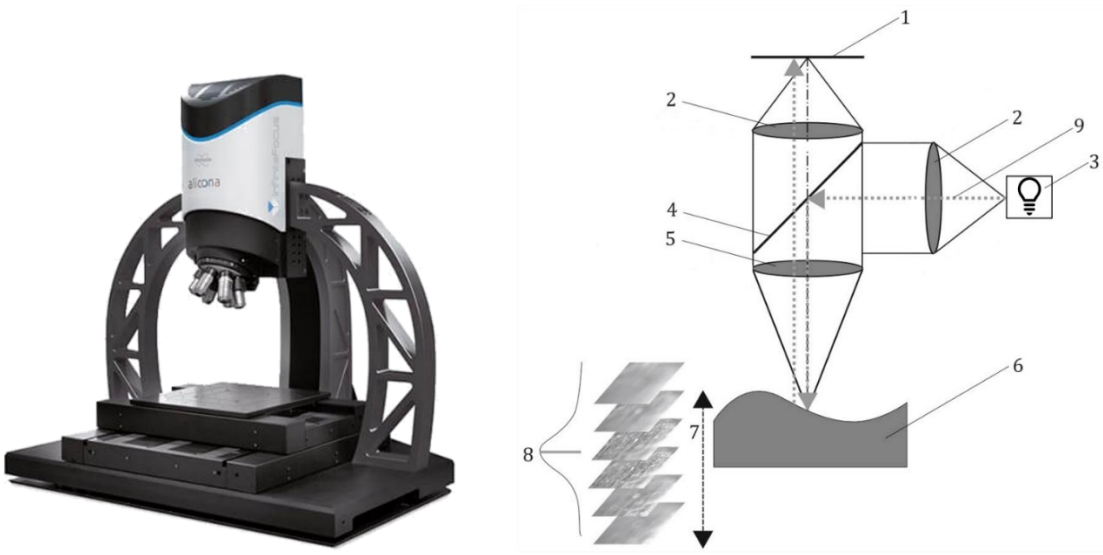

Figure 15 Focus Variation commercial system (Alicona Infinite Focus) and working principle schematic: 1) CCD sensor, 2) lenses, 3) white light source, 4) mirror, 5) objective lens, 6) sample, 7) vertical scan range, 8) contrast curve from a set of images at different positions, 9) light rays (adapted from [141]).

Point Autofocus Instruments

Point Autofocus Instrument (PAI) is a non-contact, optical areal topography measuring instrument consisting of a laser source, a microscope objective, an autofocus mechanism, and a precision moving stage. The laser beam is focused onto the surface so that the focal spot defines a height of a single point on the surface. Different strategies, e.g., beam-offset method, knife-edge method, astigmatic method, focus detection by critical total angle reflection [143], can achieve autofocus. The schematic working principle is shown in Figure 16.

PAIs are optical probes, typically equipped with five motion axes and obtain the surface topography measurement by raster scanning the surface; this can entail significant measurement time to complete the measurement. Thus, their main applications relate to measuring profiles and surfaces of hard to reach features as the flanks of gears [144] and cutting tools [145].

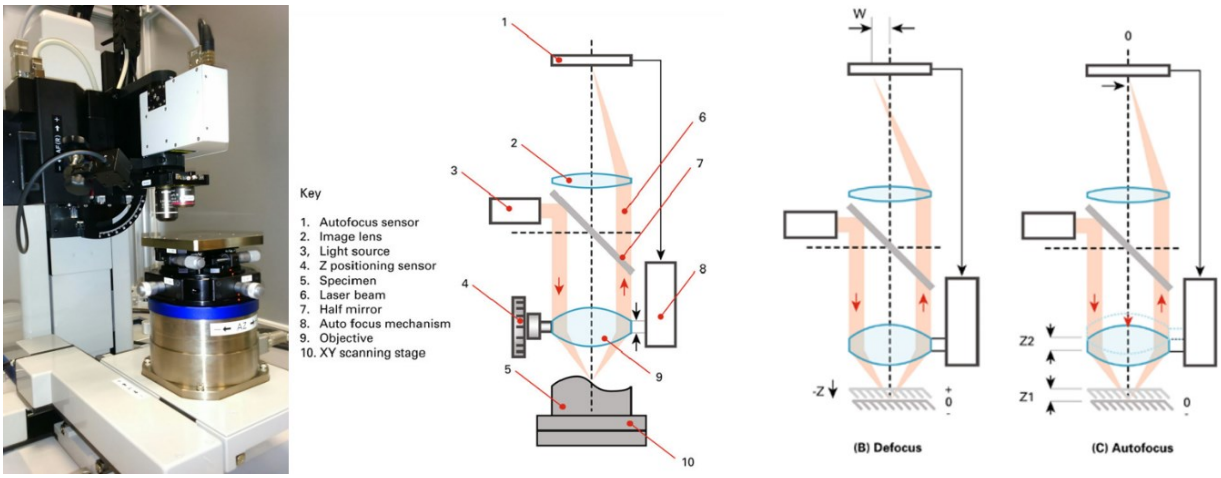

Figure 16 Point Autofocus Instrument commercial system (Mitaka-Kohki MLP-3SP) and working principle schematic (adapted from [143])

2.2.1 Metrological characteristics

When dealing with surface texture characterization for inspection, quality control, and process development, set-up and optimization, it is core to have confidence in the measurement accuracy and traceability, necessary to compare characterization results and performances of different instruments [129].

Traceability is obtained by calibrating the measurement axes and the instrument's spatial frequency response, exploiting material measures, i.e., calibrated artifacts. Primary instruments axes traceability is obtained by realizing axes directly traceable to the meter, i.e., based on interferometric scales. The traceability of frequency response and of software filtering and correction of systematic errors, e.g., contact stylus probe convolution, is more complex. Thus, there is not yet an adequate infrastructure for areal surface topography measuring instruments. The calibration of secondary instruments, i.e., industrial and

commercial instruments, is more complex as they cannot rely upon interferometric axes; their calibration is entirely based on the measurement of material measures, which must be calibrated by primary instruments [129].

Comparability of results requires the evaluation of measurement uncertainty, which, according to the International Vocabulary of Metrology (VIM) [146], is a (non-negative) *parameter, associated with the result of a measurement, that characterizes the dispersion of the values that could reasonably be attributed to the measurand*.

In surface texture characterization, uncertainty is rarely stated, probably because of the evaluation task's extreme complexity. Measurement uncertainty of surface texture characterization is due to several influence factors, the most relevant of which are summarised in Figure 17, which can be split into two main sources: instrument-based and characterization-based. The latter are particularly difficult to manage and assess. If the surface is not homogeneous, both in terms of topography and properties that interact with the instrument working principle, the specification area on which the measurement is carried out is highly impacting the result.

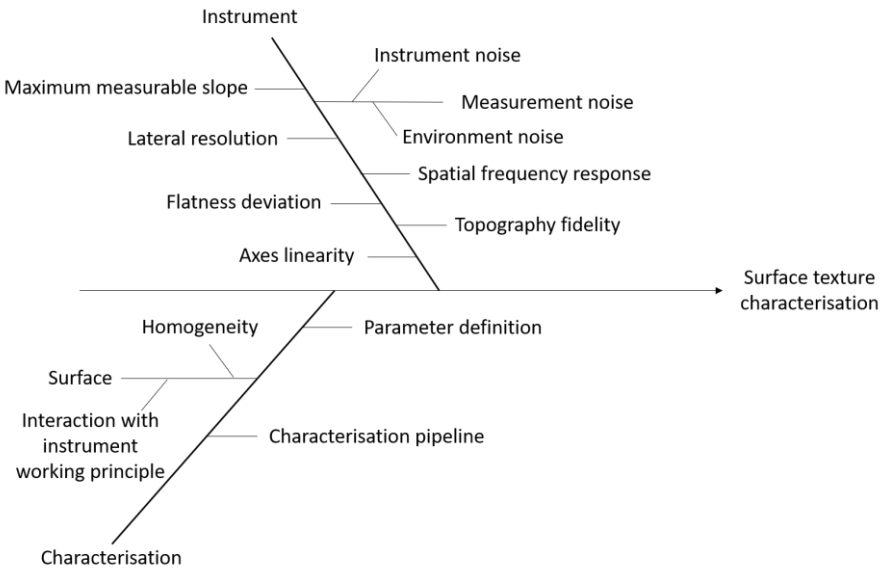

Figure 17 Main influence factors to surface texture characterization.

As far as instruments influence factors are concerned, only for the National Physics Laboratory primary areal surface topography measuring instrument, e.g., a contact stylus, a thorough uncertainty evaluation based on a Monte Carlo approach has been proposed [147]. Differently, for optical instruments, little and focused research on some selected part of the measurement apparatus has been carried out [148,149]. Even less is available, as far as parameter evaluation is concerned. A rigorous assessment for profile parameters is available in a NPL's report by Harris et al. [150], and Haitjema [151] attempted rigorous evaluation for few areal parameters, showing the practical difficulties of comprehensive analytical management.

Provided these practical limitations and still the need to enable metrological performances comparison amongst different measurement technologies, a simplified calibration routine was conceived in the community. The measurement uncertainty of an optical measuring instrument is influenced by several factors, such as environmental, mechanical and electrical noise, optical aberrations and mathematical algorithms. To assess each individual factor's contribution would be time-consuming, as formerly discussed, and often unnecessary for the end-user. Thus, an input-output model has been introduced to account for the influence factors based on these few synthetic indicators [113]. This calibration framework is based on the definition of the *metrological characteristics* (MCs), introduced by the ISO technical committee 213 working group 16. The MCs are defined, in the ISO 25178-600:2019 [152], as *characteristics of the measuring equipment, which may influence the result of measurement, may require calibration and have an immediate contribution to measurement uncertainty*. ISO 25178-600:2019 defines the MCs and the ISO 25178-6xx series provides their description and the nominal characteristics for the different surface topography measuring instruments. The MCs' calibration has to be carried out on material measures, and ISO/WD 25178-700 [153] specifies material measures and methods to perform this operation. *Material measures* are *measurement standards designated for the calibration of other measurements standards*. The set of material measures currently employed for calibrating MCs is defined in ISO 25178-70:2014 [153]; the calibration methods are further deployed per each measuring instrument type in the series ISO 28178-7xx, currently under development. Table 3 lists the MCs, specifying the main direction of the error they describe and the type of material measure to be used for calibration.

Table 3 Metrological characteristics.

Metrological characteristic	**Symbol**	**Main potential error direction**	**Type material measure**
Amplification coefficient	α_x, α_y, α_z,	x, y, z	ACG – Areal Cross Grid
Linearity deviation	l_x, l_y, l_z,	x, y, z	ACG – Areal Cross Grid
Flatness deviation	z_{FLT}	z	AFL – Areal Flat plane
Measurement noise	N_M	z	AFL – Areal Flat plane
Topographic spatial resolution	W_R	z	ASG – Areal Star-shape Grooves
x-y mapping deviation	$\Delta_x(x,y)$, $\Delta_x(x,y)$	x, y	ACG – Area Cross Grid
Topography fidelity	T_{FI}	x, y, z	AIR – Areal Irregular

Amplification coefficient and linearity deviation

The amplification coefficient α and the linearity deviation l are MCs that quantify the difference between an ideal response curve and the actual system response for the moving stage axes. The former is the *slope of the line obtained from the response function*, whilst the latter is the *maximum local difference between the line from which the amplification coefficient is derived and the response function* [152]; Figure 17 gives graphical representation to these definitions. The mapping deviations are a *gridded image of x- and y-deviation of actual coordinate positions on a surface from their nominal position*. They can be exploited to calculate α_x, α_y, l_x, and l_y [152]. According to these definitions, mapping deviations are only ultimately exploited to evaluate α and l. According to Giusca et al. [154], the mapping deviations are computed measuring the centers of the squared step features arranged in a grid, i.e., measuring a calibrated type ACG. The deviations from the measured (relative) location with respect to the calibrated values allow estimating α and l. Once evaluated, α describes a systematic error that requires an adjustment whilst l the random error, residual from this adjustment. The availability of a grid allows the evaluation of the in-plane repeatability. The reproducibility is computed by repeating the procedure at different positions of the vertical axis. Contribution to uncertainty also includes the calibration traceability, as described in Table 4. The evaluation α_z and l_z considers the step height measurements of the type ACG, rather than the ACG feature centres coordinates.

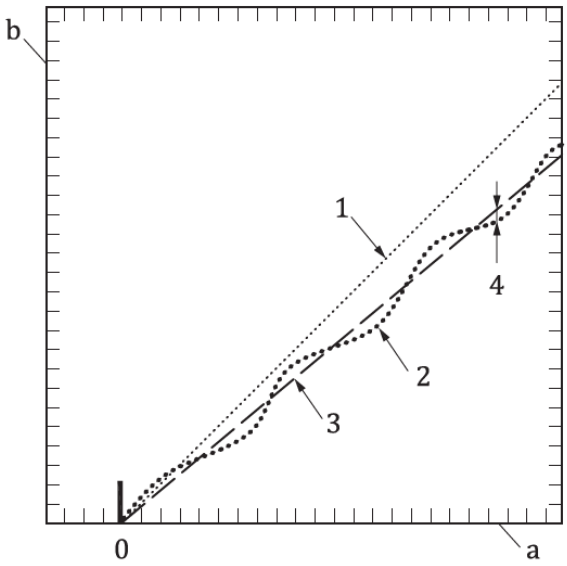

Key

a	actual input quantities
b	measured quantities
0	coordinate origin
1	ideal response curve
2	actual response curve of the instrument
3	line from which the amplification coefficient α (slope) is calculated
4	local linearity deviation (l)

Figure 18 Definition of amplification coefficient and linearity deviation [152].

Flatness deviation

The flatness deviation z_{FLT} is the *deviation of the measured topography of an ideally flat object from a plane* [152]. Thus, it describes the quality of the areal reference of an instrument. For optical instruments based on wide-field imaging, are mostly due to optical aberrations and for optical probes, e.g., PAIs, to lateral stage motion errors [155]. Giusca et al. [156] and Evans [157] proposed to compute it by assessing the *Sz* of averaged topographies measured in different locations of a type AFL.

Measurement noise

The measurement noise N_M is the *noise added to the output signal occurring during the normal use of the instrument*. Thus, it is a dynamic phenomenon including both the internal instrument noise and the environment noise. According to Giusca et al. [156], it can be calibrated computing the *Sq* subtracted or averaged replicated measurements of a type AFL. de Groot [158] offered interesting insights on the meaning and the specification of the N_M as a performance indicator along with the indication of data acquisition speed, to cater for the dynamic nature of this MC and the different bandwidth specification of the instruments, which are relevant to surface texture characterization, as noted by Leach and Haitjema [159].

Topographic spatial resolution

Topographic spatial resolution W_R *describes the ability of a surface topography measuring instrument to distinguish closely spaced surface features*. Although it describes an error on the *z-axis*, it is specified a distance in the *x-y* plane. The evaluation method of W_R is strictly dependent on the measuring principle and on the influence factors that can be considered for its definition. Therefore, several methods are available in the standard to cater for this requirement, and, as reviewed by de Groot [160], they can refer to:

- optical limits, as Sparrow or Rayleigh criterion, which consider as measurement constraints the optical lateral resolution properties of the system, dependent on, for example, the wavelength and the numerical aperture;
- sampling limits, as the lateral resolution R_l which consider as measurement constraint the sampling resolution of the CCD sensor, i.e., the pixel size (in a properly designed system, this should be far smaller that optical lateral resolution);
- spatial frequency response, as the lateral period limit D_{LIM}, based on the instrument transfer function, i.e., a *curve describing an instrument's height response as a function of the spatial frequency of the surface topography* [152].

As the adoption of D_{LIM} allows to cater for the capability of the instrument of measuring complex features [129] and for optical system is dependent on the Rayleigh criterion, it is largely adopted to calibrate the W_R. Leach et al. [161] outlined the calibration method and computed D_{LIM} exploiting the measurement of a type ASG.

Topography fidelity

The topography fidelity T_{FI} is the *closeness of agreement between a measured surface profile or measured topography and one whose uncertainties are insignificant by comparison*. According to the definition, it describes the trueness of the measurement system. It can be computed as the surface topography repeatability of a set of replicated measurements, e.g., the average of the S_q of the topographies computed as deviations from the measured and the average topography [135,136].

Contribution to measurement uncertainty

According to their definition, MCs have a direct contribution to the measurement uncertainty; and the resultant standard uncertainties are summarised in Table 4, and are combined as standard uncertainties of the axes as in Eq.(2.1).

Here is worth stressing that, because metrological characteristics are computed on average properties of the measured surface, i.e., exploiting surface topography parameters, these uncertainties represent the average of each measured element (pixel) uncertainty. Literature reports some attempts to describe the pixel-per-pixel variability, but these are extremely computationally heavy and hard to manage from an industrial point of view [162]. Though, some relevant effects were proven, as the correlation of noise by Venditti et al. [163], or yielded the development of virtual instruments model to numerically estimate uncertainty, as by Mohammed et al. [164] and Sims-Waterhouse et al. [165] for photogrammetry and by Su et al. [166] and Thomas et al. for CSI [167].

$$u(z) = \sqrt{u_{N_M}^2 + u_{z_{FLT}}^2 + u_{T_{FI}}^2 + u_z^2} \tag{2.1.1}$$

$$u(x) = \sqrt{u_{W_R}^2 + u_x^2} \tag{2.1.2}$$

$$u(y) = \sqrt{u_{W_R}^2 + u_y^2} \tag{2.1.3}$$

Table 4 Contribution to measurement uncertainties of the metrological characteristics.

Metrological characteristic	Distribution of the MC	Contribution to uncertainty
N_M	Normal	$u_{N_M} = N_M$
z_{FLT}	Uniform	$u_{z_{FLT}} = \frac{z_{FLT}}{\sqrt{12}}$
$l_{x,\,y,\,z}$	Normal	$u_{x,y,z} = \sqrt{\frac{l_{x,y,z}}{3}^2 + {u_{reproducibility}}_i^2 + {u_{repeatability}}_i^2 + {u_t}_i^2}$
W_R	Uniform	$u_{W_R} = \frac{W_R}{\sqrt{3}}$
T_{FI}	Normal	$u_{T_{FI}} = T_{FI}$

2.2.2 Performances comparison

When characterizing technological surfaces' topography to qualify products and processes for quality inspection aimed at defects identification, it is core to choose the most suitable instrument. This choice requires the knowledge of the instruments' metrological performances and identifying the specific features to be characterized, e.g., features' scale, features' properties that may interact with the measurement principle.

As far as metrological performances are concerned, the current literature suggests adopting the metrological characteristics. Examples of performance evaluation for different measurement technologies can be found in the literature. Giusca et al. [154,156] evaluated MCs for CS, CSI and CM instruments; as far as FV instruments are concerned, Giusca et al. [168] addressed N_M and Z_{FLT} and Alburayt et al. [169] the lateral scale characteristics; Maculotti et al. [155,170] applied the methods for PAIs, pointing out the relevance of the characterization pipeline in the calibration of MCs. Application of the evaluation of the W_R, based on the lateral period limit, can be found in Weckenmann et al. [171] for CSI and by Giusca and Leach [172] to PSI.

However, the interaction between the measurand and the instrument working principle is as much as relevant. They might result in significant limitations in the characterization and accurate measurement of topographical features.

As far as to contact and optical probes, it has already been noted their long measurement time.

CSIs have difficulties measuring too rough surfaces, even though some manufacturers today provide hardware and software approaches to overcome these limits. The working principle is inherently limited in measuring multi-materials on the same surface, possibly resulting in biased results. However, the correction does not represent a major criticality, as long as materials location and

optical properties are known [134]. Conversely, interferometry is particularly suitable in measuring semi-transparent films structure.

CM instruments may suffer from highly reflective or translucent materials. On the other hand, their measurements are not affected by several materials and layers (if they have adequate reflective and refractive properties, and the layer thickness is greater than the depth of focus).

FV instruments, requiring the identification of a contrast variation, cannot measure highly translucent or reflective samples and need the presence of nanoscale roughness (Ra = 15 nm at λc = 2 μm).

All these technologies allow getting 2.5D images, since surfaces' inner face cannot be imaged due to their working principle [113]. However, it may be useful to achieve its insights to reach a thorough understanding of surface topography. XCT has been demonstrated to be effective in obtaining actual 3D images of components surfaces and enabling non-destructive inspection to the inner part of the component [173].

Performance comparison is a relevant and challenging task for topography characterization and surface defects identification. Thus, literature has extensively addressed it. Most recent applications regard the measurement of complex topographies as the one resulting from additive manufacturing processes. In fact, AM surfaces topography is a challenging areal surface topography measurement. High slopes, variable aspect-ratios, an alternation between dark and overly bright regions (e.g., deep recesses and the tops of smoother regions of particles and weld tracks), as well as non-uniform optical properties as a result of local oxidization or micro-roughness effects, cause the main issues faced by optical measurement technologies [113]. XCT measurement is subject to an equally complex series of non-optical challenges that affect the spatial resolution of the measurement and to the procedure used to determine a surface from XCT data [173].

However, a significant part of the problem of assessing the measurement error associated with the different technologies is the lack of a traceable reference measurement. The only technology that can be relatively easily employed as a reference is the profile measurement via contact stylus for a complex topography. Unfortunately, how to reliably relocate profile data measured by a stylus onto areal topography data remains a challenge. Even in the case of a successful relocation, it only allows the comparison with the cross-section of the areal topography dataset. Consequently, Thompson et al. [174] proposed considering the interaction with a known set of features characterizing the AM surface, focusing mainly on SLM process manufacturing signature's distinctive features [88]. To compel with surface texture metrology requirements, they defined a benchmark internal to the measurement and a rigorous pipeline to analyze and compare resulting measurements [123]. The comparison was firstly carried out qualitatively by Senin et al. [175].

The attached particles measured by different technologies are shown in Figure 19. As it can be seen, the greatest differences occur in the region characterized by high local slope, which is in general critical for optical surface topography measuring instruments. Moreover, because these particles are very reflective, they

force FV to severely interpolate between better contrasted neighboring points, resulting in a plateau-like form [113,175].

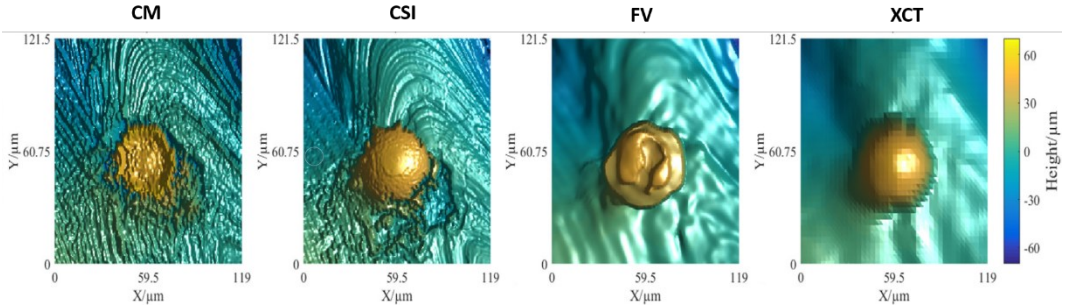

Figure 19 Surface topography measuring instrument performance comparison for a protruding attached particle (adapted from [175]).

Surface recesses measured by different technologies are shown in Figure 20. High slopes, lack of reflectivity, multiple reflections, and agglomerated particles at the ridges are the most severe criticality. These hinder CM and FV from obtaining high-fidelity measurements and leading CSI to return many non-measured points, whilst XCT low resolution hampers recognition of smaller scales recess.

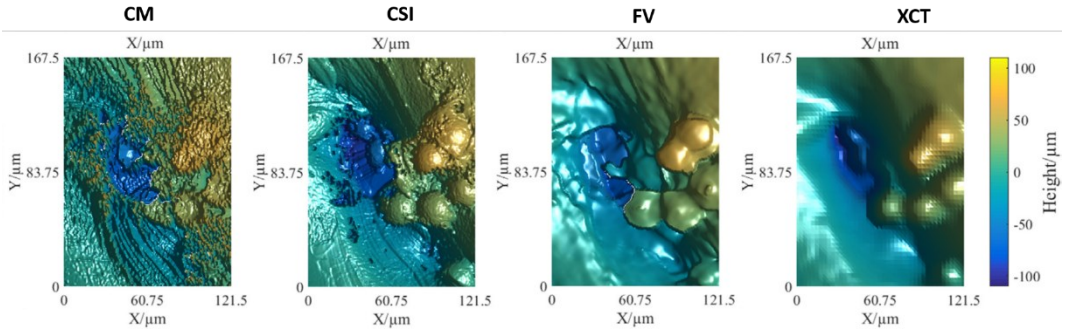

Figure 20 Surface topography measuring instrument performance comparison for a recess (adapted from [175]).

Weld tracks ripples measured by different technologies are shown in Figure 21. The measurements reflect different technologies' capability to cope with spatial frequencies. XCT loses most of the information due to its resolution; CM and CSI can measure low scale features, but CM is noisier than the latter; FV smooths out ripples at smaller scales.

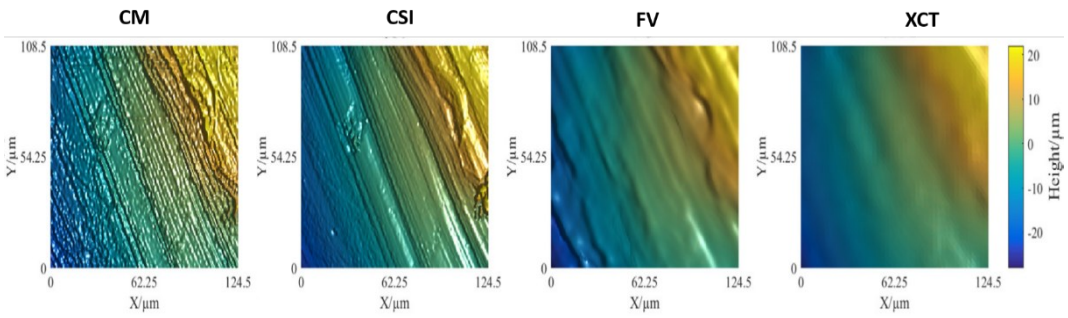

Figure 21 Surface topography measuring instrument performance comparison for weld ripples (adapted from [175]).

Those differences are reflected in the estimation of surface topography parameters. Therefore, quantitative evaluation based on parameters was addressed by Thompson et al. [174]. It was noted that there is little compatibility amongst different measurement technologies when statistical moments of the first, second, third, and fourth-order are evaluated over the considered field. In particular, XCT is characterized by a larger spread of results due to the lower lateral resolution. FV provides estimation systematically and severely different from the others, mostly for its working principle. Moreover, systems set up and characterization pipeline can significantly impact the results mentioned above [88,174].

2.3 Kriging-based approach for surface topography characterization[2]

The study of the manufacturing signature and the characterization of topographies modified by surface technologies is necessary to detect and infer errors. The measurement of surfaces requires dense sampling by appropriate technology [113]. In the last decades, new optical technologies have been developed to overcome the limitations of conventional inspection technologies based on contact probes, e.g., Coordinate Measuring Machines (CMM) and contact stylus instruments [176,177]. They may require extremely long times, and hence high costs, to achieve an adequate sampling density, limited in some cases by the physical dimension of the probe, to ensure that the measurement is statistically representative of the surface [177,178]. This is a base requirement to cope with the challenges of surface characterization in the modern manufacturing of Industry 4.0 [179], e.g., free form surfaces [180], additive manufacturing surfaces [181,182], born from the constant increase in the demand for flexibility and customization of products.

Conventional, i.e., contact, measurement methods would require an extremely long time, and hence high costs, to achieve an adequate and representative

[2] Part of this section was also previously published in: Maculotti G., Pistone G., Vicario G. (2021) Inference on errors in industrial parts: Kriging and variogram versus geometrical product specifications standard *Applied Stochastic Models in Business and Industry* in press

measurement. Small and Medium Enterprises would have to purchase expensive new equipment (typically optical instruments) or invest a consistent amount of time for quality assessments using the traditional ones to cope with technological challenges enforced by the current industrial framework.

The problem of point set augmentation is well known in literature and coped with on different complexity scales. In fact, when dealing with optical measurements of surface topography, sometimes measurement voids (or non-measured points) can be sourced by the complex interactions between the measurement system and the measurand. This may hinder proper characterization, i.e., estimation of surface topography parameters, and, in general, reduces the information content of the measure [183]. These are typically dealt with by interpolation strategies as smooth spline interpolation of filling with some particular value related to the neighboring points, e.g., the average, median [184]. A more complex situation relates to the case at hand, aimed at augmenting sparser measurement methods. This problem has often been addressed within the challenge of homogeneous multi-sensor data fusion for coordinate metrology [110,185]. In fact, when combining information coming from several sensors, depending on how the measurements are performed, often measurements are characterized by different data coverage. This affects the data fusion performance, which typically requires a registration step in the considered situation. Senin et al. [110] compared some methods available in the literature to augment the data coverage, i.e., linear interpolation, locally weighted scatterplot smoothing (LOESS or LOWESS) [186], and gaussian process regression (also known as Kriging) [187]. They showed that, at the cost of higher implementation complexity, LOESS and gaussian process regression metrologically performed best.

Kriging is a spatial interpolation method based on the correlation structure between the observations. Therefore, Kriging methods can accurately predict a surface response exploiting a limited set of spatial data and the reasonable assumptions that response values spatially close are much more alike than values that are more distant [110,187]. Consequently, this section's focus is limited to this method because of its capability of including spatial covariance in the prediction, which in the case of technological surfaces is often present and sourced by the manufacturing process itself [188].

This section investigates the effect on the estimation of surface texture parameters of the Kriging method applied to inspect surface texture by augmenting the characterization capabilities of cheaper measurement methods.

2.3.1 Kriging method for geometrical error detection

This subsection briefly reviews the literature that has addressed the development of statistical modeling based on Kriging methods to aid inspection designers to overcome these constraints and to enhance the informativeness of both the component geometry and the surface form measurement without increasing costs.

A first attempt at using Kriging modelling for the online design of inspection plans operated by CMMs was performed by Pedone et al. [189]. The approach proved to be useful in accurately estimating deviations from nominal dimensions and shape by probing only a few points, with benefits on the inspection process's economy. In that paper, the inspection plan as a sequential experiment to be designed online shown to be the best accuracy/cost trade-off, updating the Kriging models iteratively according to the new incoming data, and using the predictions from the updated model for selecting the next point to inspect. The methodology was applied to case studies for checking two form tolerances: straightness and roundness.

Subsequently, other practical situations have been addressed by Vicario et al. [190], who focused on flatness tolerance verification, and by Pistone and Vicario [191], who discussed wafer inspection strategies improvements.

Later on, Ruffa et al. [192] addressed a comparison between conventional and Kriging-based inspection strategies from the perspective of measurement uncertainty. Ascione et al. outlined adaptive inspection methods for coordinate measurement systems based on Kriging modeling [193].

The capability of Kriging models to detect geometrical and dimensional error was exploited by Kolios et al. [194] to develop predictive models for the reliability of cutting tools, by Song et al. [195] to detect a geometrical deviation in additive manufacturing processes for polymers and by Wang et al. [196] to provide corrective models to this building strategy.

Within statistical process control and geometrical tolerancing, Colosimo and Pacella contributed significantly to the field [188]. They first addressed the case of modeling topographies based on data collected on a regular inspection grid [45,197] by Spatial AutoRegressive models with eXogeneous variables (SARX). Then they generalized the analysis for non-uniform sampling strategies, adopting Gaussian Process Regressions [45] and Geodesic Gaussian Processes [198], which are relevant when the correlation structure is dependent on geodesic distances and not Euclidean ones. Moreover, they deployed these to improve and perform multi-sensor data fusion with the ultimate goal of carrying out dimensional and geometrical verification [199] and applied them to complex industrially relevant case studies, e.g., freeform surfaces [199]. Within this application filed, Wang et al. [200] and Wells et al. [201] exploited these very same ideas to develop an ad-hoc control chart to monitor surface topographical properties. The idea was then exploited to conceive a hybrid approach for topography classification by Dastoorian et al. [202], which currently is one of the most challenging issues [114,203].

Kriging models aroused interest also in assembling, where they were exploited to detect, and later correct, non-linear assembling errors for compliant [204] and composite materials [205].

The Kriging modeling is based, and hence, requires the detection, and consequently the modeling, of the correlation between observation. However, choosing the most suitable class of models for correlation amongst several available options is not trivial. Though mostly geo-statisticians, several

researchers favor using the variogram, or semi-variance diagram, in choosing the correlation function. This is very informative about spatial dependence, showing the averaged square difference in the response values between a pair of measurement points separated by a given distance. Moreover, the variogram is equivalent to the correlation function for stationary processes, which are the most frequently investigated [187].

This suggested further investigations on the relationship between variogram and correlation, which Pistone and Vicario addressed. First, they considered Gaussian vectors with constant variance. They showed how to parametrise the distribution as a variogram function and characterize all the Gaussian distribution with a given variogram [206]. Then, they discussed the constraints imposed on the set of parameters defining the variogram [207].

Recently, the effectiveness of using the variogram has been proved in other practical situations. Vicario et al. exploited variograms and kriging models to predict responses for computational fluid dynamic experiments to reduce computational time [208] and predict elongation and error in sheet metal forming [209].

Kriging and variograms were, thus, largely exploited for form and macro geometrical errors detection. Conversely, few applications, if any, can be found for surface texture characterization. One of the first works in this field was by Ruffa et al. [210], who noticed the sensitivity of the variogram of surface topography measurement by CMM to different manufacturing processes. Vicario and Pistone [211] took advantage of computer experiments and simulation to analyze the changes in the variogram due to stimuli of a noticeable trend in the model and to anisotropy. In fact, if the manufacturing process yields an anisotropic topography (as for many manufacturing signatures and in several applications of surface technology), the variogram is a function of both the distances between any pair of locations and the direction. Moreover, even in the most refined surface, and contrary to some common beliefs, the assumption of isotropy is disproved. Therefore, these features may be interpreted as technological signatures or probing system systematic errors.

2.3.2 Kriging method and variograms

As formerly stated, Kriging methods are a set of spatial interpolation based on the correlation structure between the observations. They rely on an optimality criterion that minimizes the mean squared prediction error (MPSE) of the linear combination of observations under unbiasedness constraints.

The ordinary Kriging model assumes that the observed values $Y(x)$ are the realization of a Gaussian random field $Z(\boldsymbol{x})$ plus an unknown constant term β:

$$Y(\boldsymbol{x}) = \beta + Z(\boldsymbol{x}) \qquad (2.2),$$

where *Z(**x**)* denotes the value of the spatial field in the point $\boldsymbol{x} = (\boldsymbol{x_1}, \dots, \boldsymbol{x_n})^{\boldsymbol{T}}$ of the design space $\chi_d \subset \mathbb{R}^d$. When analyzing topography, $d = 2$, and *Z(**x**)* is the height function, i.e., *z(x,y)*, obtained by measuring points of a surface with respect to a horizontal position. Moreover, the Gaussian random field is assumed to have zero mean and stationary covariance over the design space χ_d, i.e., $\mathbb{E}[Z(\boldsymbol{x})] = 0$ and $Cov\left[Z(\boldsymbol{x_i})Z(\boldsymbol{x_j})\right] = \sigma_Z^2 R(h; \theta)$, where σ_Z^2 is the process variance and *R* is the spatial correlation function depending only on the displacement vector $\boldsymbol{h}$ between any pair of points in χ_d and on a vector parameter $\boldsymbol{\theta}$. If the value of the auto-covariance function $\mathrm{C}(\mathrm{h})$ depends only on the length $\|\boldsymbol{h}\|$ of the vector $\boldsymbol{h}$, then the stochastic process is isotropic; opposite, the process is anisotropic.

Let now $\boldsymbol{Y}^{\mathrm{n}} = \left(\mathrm{Y}(\boldsymbol{x_1}), \dots, \mathrm{Y}(\boldsymbol{x_n})\right)^{\mathrm{T}}$ the vector of the observed values of the spatial field in the *n* sampled points $x_i, i = 1, \dots, n$ and $Y_0 = Y(\boldsymbol{x_0})$ the value in a new unsampled point $\boldsymbol{x_0}$. The most exploited prediction criterion is based on the minimization of the Mean Squared Prediction Error (MSPE), where the MSPE of $\widehat{\mathrm{Y}_0} = \widehat{\mathrm{Y}_0}(\mathrm{Y}^{\mathrm{n}})$ is:

$$\mathrm{MSPE}\left(\widehat{Y_0}, F\right) = \mathbb{E}_F\left[\left(\widehat{Y_0} - Y_0\right)^2\right] \qquad (2.3),$$

where *F* is the joint distribution of $(\mathrm{Y}_0, \mathrm{Y}^{\mathrm{n}})$. The predictor in Eq.(2.3) is unique, linear unbiased and the best one (BLUP) of $\mathrm{Y}(\boldsymbol{x}_0)$. If the joint distribution *F* of the observed values $\boldsymbol{Y}^{\mathrm{n}}$ and of the unobserved value Y_0 of the field is multivariate normal, the MSPE in Eq.(2.3) is equal to the conditional expectation of $Y(\mathbf{x_0})$ given $\boldsymbol{Y}^{n}$:

$$\hat{Y}_0 = \beta + \boldsymbol{r}_0^T \boldsymbol{R}^{-1}(\mathbf{Y^n} - \beta \mathbf{1}) \qquad (2.4),$$

with $\mathbf{1} = [1, \quad 1, \dots, \quad 1]^T$. The predictor in Eq.(2.4), i.e., the ordinary Kriging model, minimizes the MSPE in Eq.(2.3). Given of the interpolator property of Kriging, MSPE is zero at the sampled points and perfectly reflects the Kriging principle: it is large when $\boldsymbol{x_0}$ is far from the sampled points, small when it is close to them, thus expressing a measure of uncertainty of predictions and it can provide confidence intervals of the predictions. It follows that:

$$\mathrm{MSPE}\left(\widehat{Y_0}\right) = \sigma_Z^2 (1 - \boldsymbol{r}_0^T \boldsymbol{R}^{-1} \boldsymbol{r}_0 + \boldsymbol{c}_0^T (\mathbf{1}_T \boldsymbol{R}^{-1} \mathbf{1})^{-1} \boldsymbol{c}_0^T) \qquad (2.5),$$

with $\boldsymbol{c}_0^T = \mathbf{1} - \mathbf{1}_T \boldsymbol{R}^{-1} \boldsymbol{r}_0$. The expression of Eq.(2.5) takes into account that β parameter is replaced by its generalized least squares estimator $\hat{\beta}$. Moreover, the unknown parameter vector $\boldsymbol{\theta}$ in $R(\boldsymbol{h}; \boldsymbol{\theta})$ can be estimated by maximum likelihood. It has to be highlighted that Eq.(2.5) underestimates prediction variance as it does not account for the extra variability transmitted to $\boldsymbol{r}_0$, $\boldsymbol{R}$ and β by $\boldsymbol{\theta}$.

Concerning the correlation modeling in predicting the values of *Y* in unsampled points and in evaluating the MSPE in the predicted points, there are two approaches: the first one uses a spatial correlation function chosen within some parametric function families, driving this choice by some underlying phenomenon to model, choosing the parameter(s) in order to fit best the model

[212]; the second approach, proposed by Matheron [213] exploits the variogram, defined as:

$$\gamma(\mathbf{x}_i, \mathbf{x}_j) = \frac{1}{2}\mathbb{E}\left[\left(Z(\boldsymbol{x_i}) - Z(\boldsymbol{x_j})\right)^2\right] \quad (2.6).$$

The variogram may also be expressed in terms of the model covariance [206]:

$$\gamma(\boldsymbol{x_i}, \boldsymbol{x_j}) = Cov[Z(\boldsymbol{x_i})Z(\boldsymbol{x_i})] + Cov\left[Z(\boldsymbol{x_j})Z(\boldsymbol{x_j})\right] - 2Cov\left[Z(\boldsymbol{x_i})Z(\boldsymbol{x_j})\right] \quad (2.7).$$

The definition of the variogram and of $\boldsymbol{R}$, allows to highlight the dependence of the prediction on the variogram itself, by clarifying the terms in the right-hand side of Eq.(2.4):

$$\boldsymbol{R} = \begin{bmatrix} \mathbf{0} & \gamma(\boldsymbol{x_1}, \boldsymbol{x_2}) & \dots & \gamma(\boldsymbol{x_1}, \boldsymbol{x_n}) & \mathbf{1} \\ \gamma(\boldsymbol{x_2}, \boldsymbol{x_1}) & \mathbf{0} & \dots & \gamma(\boldsymbol{x_2}, \boldsymbol{x_n}) & \mathbf{1} \\ \gamma(\boldsymbol{x_n}, \boldsymbol{x_1}) & \gamma(\boldsymbol{x_n}, \boldsymbol{x_2}) & \dots & \mathbf{0} & \mathbf{1} \\ \mathbf{1} & \mathbf{1} & \dots & \mathbf{1} & \mathbf{0} \end{bmatrix} \quad (2.8.1)$$

$$\boldsymbol{r_0} = [\gamma(\boldsymbol{x_1}, \boldsymbol{x_0}) \quad \dots \quad \gamma(\boldsymbol{x_n}, \boldsymbol{x_0}) \quad \mathbf{1}]^{\boldsymbol{T}} \quad (2.8.2)$$

Achieving kriging estimate requires computing the empirical variogram between sampled points according to Eq.(2.6), exploiting Matheron's estimate; still, $\boldsymbol{r_0}$, i.e., the variogram between the unsampled location and the sampled points, still has to be determined. This can be achieved by interpolating the empirical variogram of Eq.(2.6).

Literature reports several interpolation models, but their choice is not trivial, and, in general, it is suggested to adopt a model linked to the physics of the system [187]. Given a certain mathematical model of the response function *Z(**x**)=f(**x**)*, only few closed-form solutions of the variogram are available, as their analytical determination is highly demanding. It is simple to demonstrate that a quadratic variogram characterizes a linear relationship; it is more complex to deal with different, non-linear functions [214].

Once the most suitable interpolation model for the empirical variogram has been chosen, the prediction in untried locations is straightforward, according to Eq.(2.4).

Within this framework, the Kriging approach can thus be seen as a method to augment the density of sparse, i.e., not densely sampled, measurement. The other way around, by evaluating the empirical variogram, an indication of the mathematical model *Z(**x**)=f(**x**)* can be obtained, enabling error detection or the deviation of a certain variable, e.g., a geometry, from the expected trend. Last, it is worth mentioning that the Kriging method was initially intended as a model, to be used in Geostatistics, of the physical randomness of the quantity of interest. Later a different interpretation of the same method has been devised to treat Computer Experiments, where the traditional notion of randomness is not applicable [215]. In such a case, for each given covariance, the method produces an interpolation of the given values even if the covariance lack any physical interpretation. Within this framework, the Kriging approach can thus be seen as a method to augment the density of sparse, that is, not densely sampled,

measurement (under the hypothesis that measurement noise is negligible with respect to the measured quantity [216]). The elicitation of a given covariance, together with the corresponding Gaussian distribution, corresponds then to the choice of a Bayes prior. Such a choice is made according to the qualitative type of the surface of interest.

2.3.3 Kriging-supported characterization of surface texture

Consequently, variogram and Kriging appear suitable for texture characterization, to detect anisotropies and predict surfaces to enrich sparse measurements.

Here, these tools are applied to augment characterization capabilities of cheaper measurement methods, e.g., CMM, CS. A comparison between a measured surface by means of a dense sampling method and a surface predicted by kriging is carried out, To test the capabilities of Kriging method to achieve these purposes. The comparison will rely upon the characterization of both surfaces according to ISO 25178-2:2012 to assess the accordance of surface texture parameters.

Materials and methods

Within the paradigm of Industry 4.0, the modern industry experiences a constant increase in the demand for flexibility and customization of products [217]. This has led to the development of innovative manufacturing strategies to satisfy the customers' requirements, for actual production processes. As discussed in Section 1.1, AM outstands other solutions for its capability to optimize the design of components and material and energy consumption [218]. Due to its flexibility and wide range of applications, we focus on the Fused Deposition Modelling (FDM), i.e., an additive process for polymeric material. The component is manufactured by fusing a wire of material deposited layer-by-layer raster scanning the layer cross-section of the part. Figure 22 represents a schematic view of the process and the manufactured specimen with a benchmark geometry.

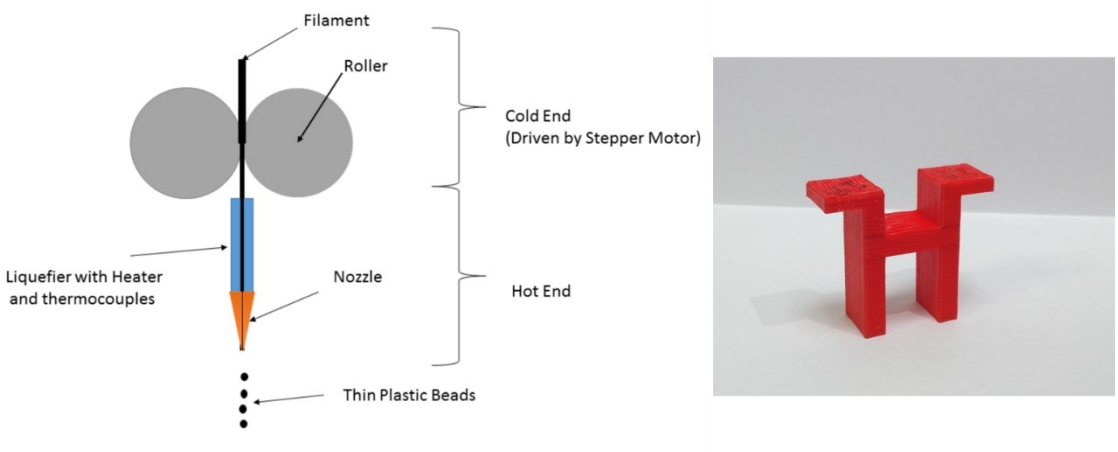

Figure 22 Scheme of a Fused Deposition Modelling process.

The specimen's top surface topography has been measured by a Coherence Scanning Interferometer (CSI), a Zygo NewView 9000 equipped with a 20× objective and a 0.5× digital zoom, shown in Figure 13, hosted in the Technological Surface Metrology Laboratory of Politecnico di Torino, Italy. Measurement of CSI will be the reference for the comparison, being the denser measurement methods; the sparse measurement is obtained simulating a CMM sampling.

The FDM features a characteristic manufacturing signature due to the raster scanning approach according to which the layers are built. The signature unfolds in a periodic pattern resembling the adjacent deposition of the molten wires of material. Prior knowledge of the manufacturing signature should be known to correctly reconstruct such pattern by setting up the simulated measurement with the CMM: a regular grid sampling with a pitch of one-third of the pattern's wavelength was chosen to respect Nyquist's theorem [122]. Here, to further test the robustness and the validity of the method proposed, this assumption is neglected, and a random sampling of the surface is performed to set-up the Kriging model. The approach here described, regardless of the sampling strategy, may be relevant in situations where, after a process optimization based on expensive characterization (e.g., optical surface topography instruments) yielded reference information about the surface, subsequent cheaper on-line quality controls are performed by probes. In this work, the CSI measurements are considered the reference to set-up the CMM measurements and qualify the effectiveness of the Kriging method in the prediction.

The characterization of the surfaces has been performed through the commercial software Mountains Map v7.4. As the characterization object is the surface texture, the waviness surface, i.e., the S-F surface, is considered. The standard operators' sequence involved an S-filter with a cut-off of 80 μm and an F-operator for leveling.

Results discussion

The surface measured by the CSI instrument allowed a dense sampling of the surface, with a lateral resolution of 3.56 µm, resulting in one million measured points. The measurement is shown in Figure 23. The manufacturing signature is clearly noticeable as a pattern along the *x*-axis; also, a deviation from planarity can be highlighted, even though to a minor extent.

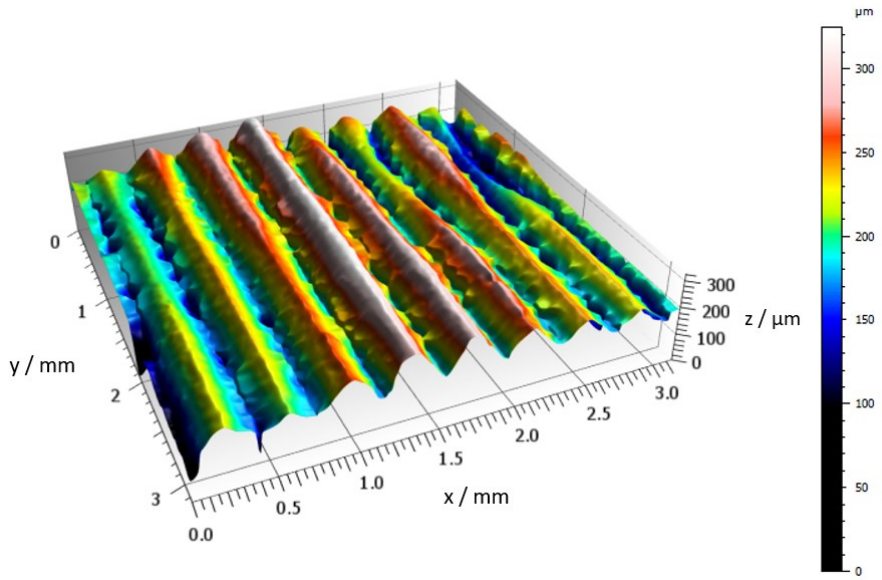

Figure 23 Surface topography measured by CSI.

Main parameters for the characterization of the surface texture according to ISO 25178-2:2012 are reported in Table 5; the PSD is shown in Figure 24.

Table 5 Surface texture parameters (ISO 25178-2:2012) for the CSI dataset.

Parameter	Value
S_a / µm	36.1
S_q / µm	45.5
S_z / µm	326
S_{al} / mm	0.149
S_{tr}	9.5%
S_{td}	178.0°

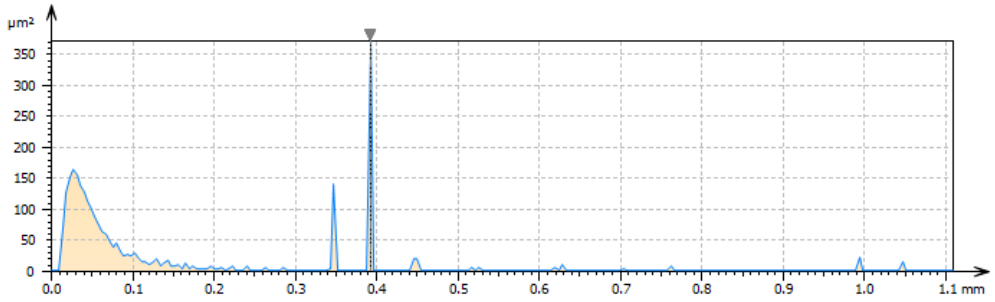

Figure 24 Power Spectrum Density of the surface topography measured by the CSI.

The anisotropy of the surface is correctly detected: the isotropy parameter S_{tr} is 9.5%, definitely less than the conventional threshold of 20%. The texture pattern direction, measured by the parameter S_{td}, is at 178° (or -2°) with respect to the *x*-axis. The principal harmonic exhibited by the PSD, i.e., the base wavelength, is at 0.39 mm. This wavelength is coherent with the surface topography in Figure 23, indicating the manufacturing signature and its entity. A second relevant harmonic is in the proximity of zero at 0.027 mm: this is the noise content of the surface, due to measurement noise and local random variability of the surface.

A set of 4,000 points was randomly selected from the large initial set of points (1e+6 points) measured using the CSI, to perform the planned comparison between the two approaches, i.e., Kriging with variogram methodology and the conventional protocol. The small number of points (the 0.4% of the measured ones) is due to contain computational times and make the comparison more persuasive. Before modeling the surface, the empirical variogram was computed. Figure 25 represents the variogram cloud and the (omnidirectional) variogram, based on the Euclidean distance and according to Matheron's estimator.

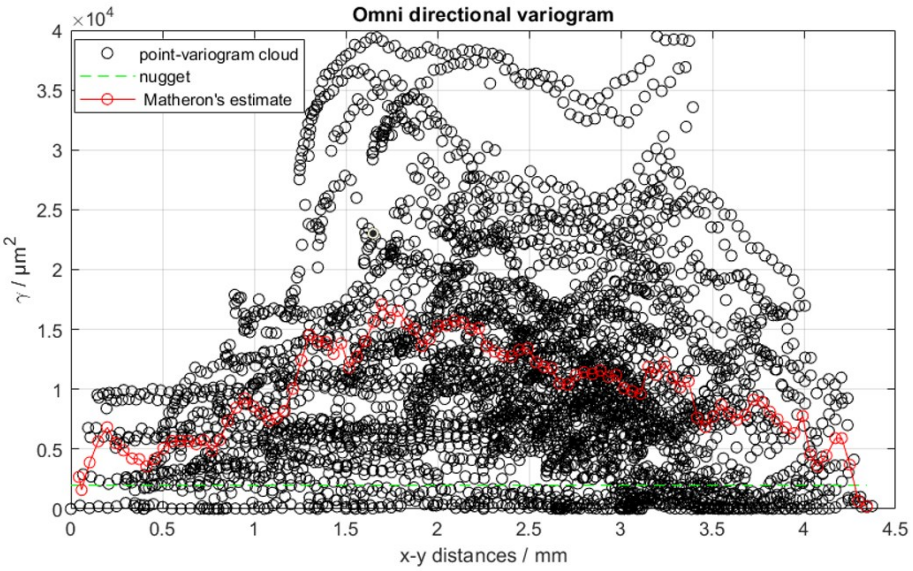

Figure 25 Omni-directional variogram cloud (in black) and estimated variogram (in red).

The variogram exhibits a structured correlation; the sampled points' behavior significantly and systematically differs from that of a set of points measured on a planar surface, without any trend. In particular, two deviations from planarity can be appreciated: a periodic pattern superimposed to a polynomial trend, at least of second order. This behavior suggests the presence of a sinusoidal texture and of a systematic deviation from planarity that can be generally described by a polynomial of at least first order (recall that a quadratic variogram characterizes a linear relationship between responses). The variograms along the *x*- and *y*-axis have been evaluated to investigate the possible presence of anisotropy. A severe anisotropy was detected as a waviness along the *x*-axis, as Figure 26(a) highlights;

whereas, Figure 26(b) does not detect departure from the surface's planarity because the empirical variogram does not give evidence of a correlation.

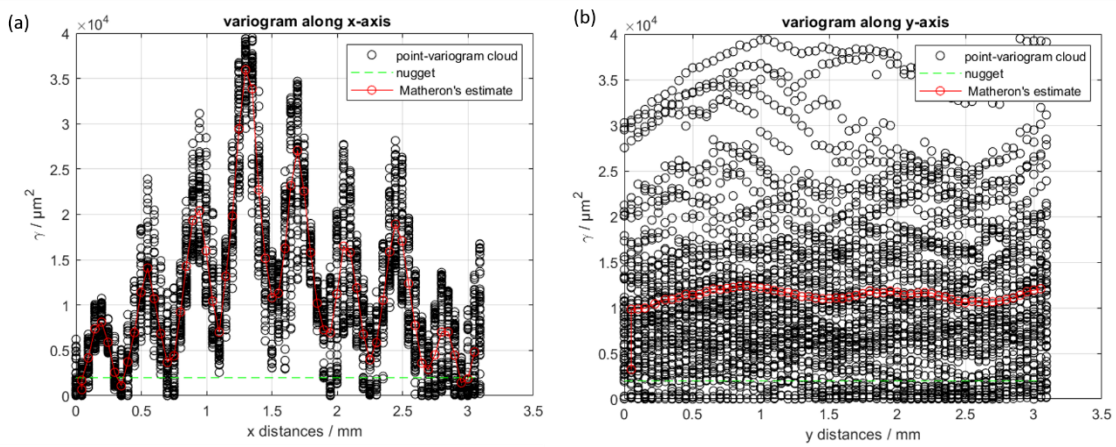

Figure 26 Variogram clouds along the (a) *x*-axis and (b) *y*-axis. In red the correspondent empirical variograms.

The measured surface height was predicted on 62,500 points (the 6.25% of the measured points dataset), relying on these findings. The code was written in MATLAB 2019b and exploited the DACE toolbox. It should be noted that computational constraints limited the size of the Kriging prediction set. However, it is not so small when compared with the starting data set (4,000 points), resulting in about 6.4% the percentage of predictor points to predicted ones.

A spline was chosen as the necessary spatial correlation function fitting model [187].

The prediction of the surface topography obtained with Kriging is represented in Figure 27. The manufacturing signature due to waviness can still be appreciated along the *x*-axis direction, despite the low sampling density. The interpolated surface has been characterized, exploiting the same set of surface texture parameters formerly defined, to provide a quantitative comparison. The procedure, i.e., sampling and related Kriging estimation, has been repeated 1,000 times to provide statistical meaningfulness to the evaluated parameters: average and standard deviation of the estimated parameters are reported in Table 6, and by the PDS, shown in Figure 28.

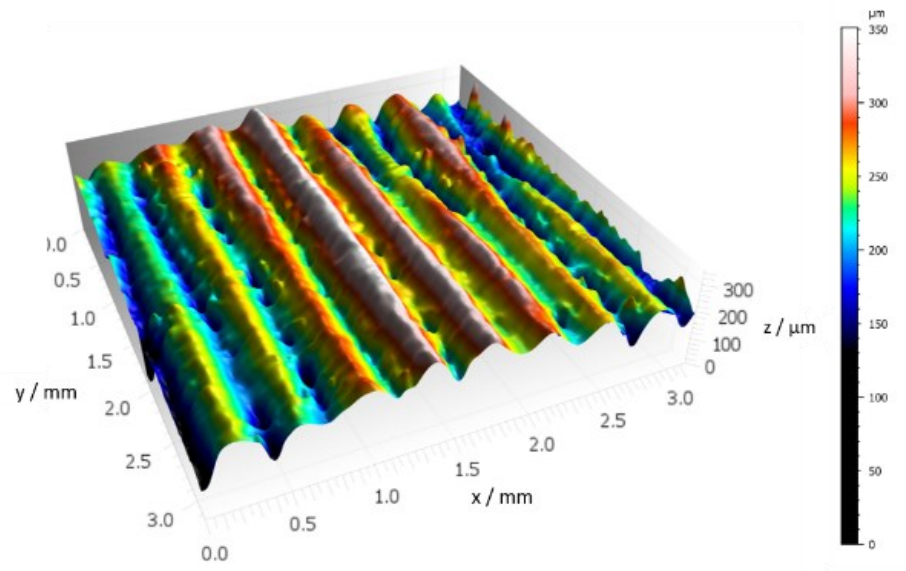

Figure 27 Surface topography obtained through the application of Kriging.

Table 6 Surface texture parameters (ISO 25178-2:2012) of Kriging-interpolated surface.

Parameter	Average value	Standard deviation
S_a / µm	35.6	0.3
S_q / µm	45.0	0.4
S_z / µm	322.1	35.9
S_{al} / mm	0.1655	0.0034
S_{tr}	10.4%	0.5%
S_{td}	178.7°	1.2°

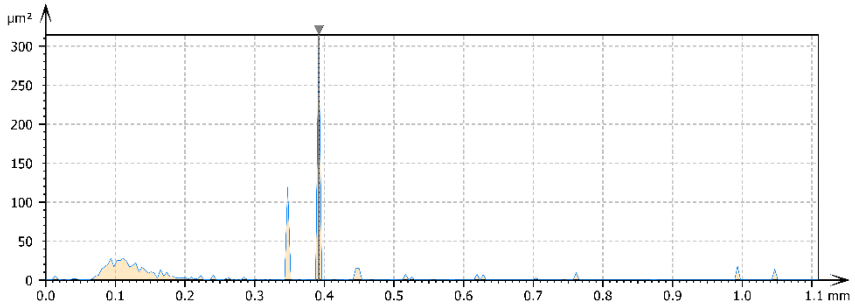

Figure 28 Power Spectrum Density of the Kriging-interpolated surface.

Comparing the results in Table 5, based on 10^6 measured points with the CSI, with the results in Table 6, computed on the predictions based on 0.4% of the mentioned measured points, it can be stated that the surface is still correctly characterized as anisotropic with the parameter S_{tr} significantly smaller than 20%. The texture pattern is directed at 178.7° (i.e., -1.3°) with respect to the *x*-axis. The main harmonic representing the base wavelength is evaluated correctly at 0.39 mm.

The interpolation is not affected by systematic errors, as the residuals' NPP showed a hyper-normality. Although leading to the rejection of the null

hypothesis of normality, it is not considered critical in this situation [219]. In fact, It can be mainly ascribed to spikes, isolated deviation from the regular pattern, and predicted values at the edge of the investigated field. The correctness of the trend interpolation can also be seen in terms of wavelength. Figure 29 shows the residuals' PSD, which is characterized by only one harmonic at 0.021 mm, not significantly far from the noise content of the original dataset, i.e., 0.027 mm.

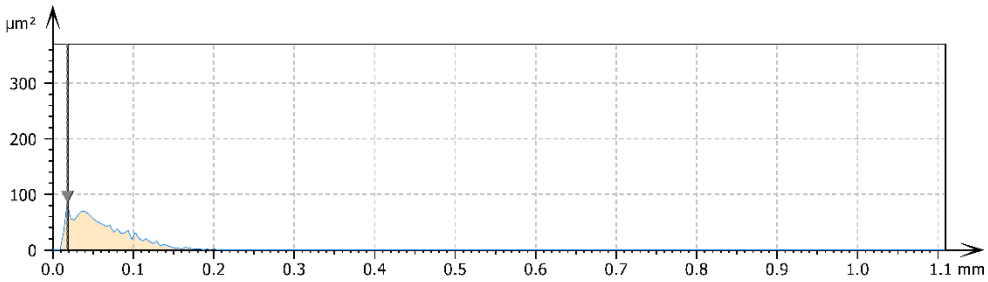

Figure 29 Power Spectrum Density of the residuals of the Kriging interpolation.

Due to the interpolation inherent in the Kriging, very low scale variation can only be partially captured. In fact, the PSD of the interpolated surface shows a peak at 0.1 mm (see Figure 28). This harmonic is near to the upper bound of the noise frequency of the CSI measured surface (0.027 mm), and shows that the procedure based on the Kriging acted as a high-pass filter. Despite these differences, the surface parameters evaluated on the Kriging-interpolated surface, with a 2-sigma confidence interval, are not significantly different from those computed on the dense measurement (comparing results in Table 5 and Table 6).

Section summary

The issue addressed in this section is the surface texture measurement and verification based on sparse and cheap measurements. The ordinary Kriging model, which proved to be effective in predicting geometrical errors in manufacturing, and the variograms for modeling a possible correlation between the sampled points of the measured surface, according to geostatistical practices for very noisy data, were exploited to enable this characterization.

A comparison between a conventional dense measurement approach and the Kriging method was based both on theoretical insights about using the variogram in case of random sampling and on a case-study based on real measurements where random sampling and Kriging predictions are used.

The Kriging methodology proved useful in predicting textured surface patterns, even if it was based on sparse economic measurements. The result of Kriging interpolation, once characterized according to the standard procedure, yielded information coherent with denser and more expensive measurement approaches. The current challenges of Industry 4.0 for surface texture characterization, herein including freeform surfaces and additive surface, require an extremely long time, and hence high costs, to achieve an adequate and representative measurement by traditional devices. The SMEs would have to

purchase extremely expensive new equipment (typically optical instruments) or to invest a consistent amount of time for quality assessments using the traditional one to cope with technological challenges enforced by the current industrial framework. Thus, the empirical variogram's adoption for detecting correlation structure and Kriging prediction can be considered adequate tools to achieve informativeness from a sparse and cheap set of measurements statistically.

Moreover, these findings can be considered an encouraging preliminary step to guide further developments in detecting anomalies, obtaining definitive practical advantages for SMEs.

Future work shall address the application of these tools for process control. A typical scenario may be applying the Kriging method for in-line process control with contact probes based on control limits set based on reference surface topography measurements performed by optical devices.

The software implementing the Kriging prediction can be straightforwardly incorporated into the CMM computer control, and it can run in real-time. It is possible to predict the surface texture over a tight grid, also providing a quantification of the uncertainty based on the MSPE, being the automation of the Kriging predictions relatively inexpensive.

2.4 Uncertainty-based comparison of conventional and surface topography-based methods for wear volume evaluation in pin-on-disc tribological test

Wear is a general term that indicates the natural and unavoidable surface damage occurring at the operating surfaces of mechanical bodies interacting under relative motion. Wear induces a loss of material from at least one of the bodies in contact.

A variety of wear processes may arise depending on the nature and the geometry of the materials in contact and the type of interaction, e.g., sliding wear, rolling wear, fretting, erosion, lubricated or dry wear, corrosive wear, impact wear, [220], even though they results from the combination of fundamental wear mechanisms. A commonly accepted classification distinguishes between adhesion, abrasion, tribo-chemical reaction and surface fatigue [221].

Wear is experienced by all mechanical components in machines and is one of the primary reasons for engineering systems malfunctions, reduced operational efficiency and components replacement, together with corrosion and fatigue failure. Moreover, the grand majority of machines lose their durability and reliability due to wear [222].

Wear is ultimately the effect of friction, which makes it responsible for both energetic and economic losses. Huge efforts have been made to broaden the understanding of tribological problems because the costs related to friction and wear are significant [221]. However, wear and friction impact go far beyond a mere cost reduction; in fact, definitive improvement in both energy efficiency and environmental footprint could be obtained. Moreover, the study of wear phenomena and the quantification of the amount of wear play a crucial role in applying the modern principles of Industry 4.0 and circular economy, potentially

to any industrial process. Therefore, wear control has become an urgent need for the advanced and reliable technology of the future. The precise evaluation of wear damage will likely become even more crucial in the next decades since it constitutes the basis to develop prediction models to be applied in the design stage of components and systems to support the design and process optimization.

Tribological phenomena are extremely complex. All mechanical, physical, chemical, and geometrical properties of the surface and the surrounding atmosphere affect the surface interactions and the system's tribological characteristics [223,224]. Therefore, the experimental practice often moves towards simplification, as identifying and quantifying each possible influence factor's effect is extremely demanding. Literature classifies six categories of tribo-tests (i.e., either friction or wear tests): Field Tests; Bench Tests; Subsystem Tests; Component Tests; Simplified Component Tests; Model Tests [220,223].

Testing results are further and further away from specific applications, going from the former to the latter. The complexity reduces, and the replicability and the ease of running the tests increase dramatically as some factors are suppressed [221]. Complex and expensive field and bench tests are necessary for tribological assessments of mechanical systems and are carried out over long periods and under conditions representative of actual working conditions; component tests help in-depth investigations of specific issues linked to applications. Model tests are the most widely used in laboratory studies and research on materials, where comparative analysis of results in standard conditions are relevant. Model tests are advantageous for scientific investigations because of the high reproducibility of test parameters and the results.

The test methods' variety expresses the need for researchers to devise an experimental procedure representative of the phenomenon, simple and not prone to arbitrary setup choices [225].

Amongst the model tests, pin-on-disc is a well-established and widespread wear test for research purposes. The test consists of applying, by means of a pin, a known force orthogonally to the surface of the tested material, which is rotated around an axis parallel to the force direction and at a certain radius R from the pin contact point, see Figure 30 for a test schematic. The sample is kept in rotation for a certain number of cycles; a wear track is generated, and wear can be assessed in terms of the track's volume.

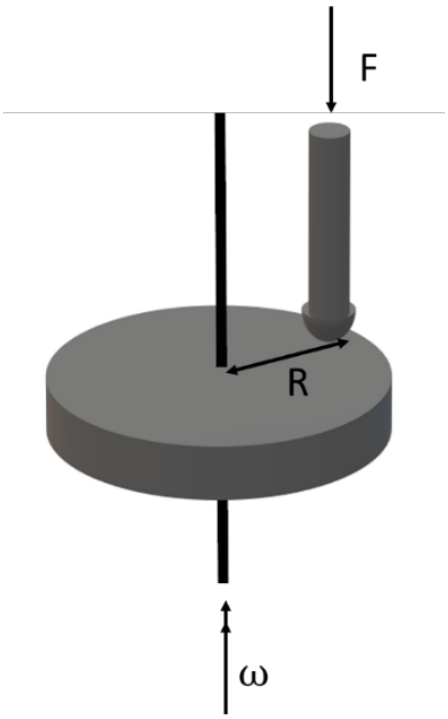

Figure 30 Scheme of pin-on-disc. *F* is the applied force, on a rotating disc at speed ω, at a distance *R* from the rotation axis.

A vast amount of experimental data from pin-on-disc tests have been made available in the scientific literature for the last fifty years. This method is still extensively used today in many leading research fields thanks to its flexibility, simple setup tests, and test parameters control.

Pin-on-disc tests are applied both at the environment and at high temperature to support the development for applications in aerospace [226,227], automotive, aeronautical sectors of new low-density and high strength alloys, e.g., Mg-Al-Si-Zn alloys [228], composite materials, e.g., Al-Metal Matrix Composites [229], and coating, e.g., cermet coatings as Ti[Nb,V]N [230], Mg-TiO_2/Al_2O_3 [231]. They also find applications in oil and gas industry to develop innovative materials capable of undergoing innovative processes, e.g., Manesmann process to avoid seams in tube junctions [232]. The exploration of tribological properties of innovative 2D-coatings, e.g., graphene and graphite-based coatings [233–237]. Literature shows a consistent adoption of this test also for the characterization and development of manufacturing processes, e.g., to analyze the wear of tools with innovative coatings [238–240], the wear behavior of components by additive manufacturing processes [241–245], the characterization of pioneering materials for additive manufacturing [246,247], and to support the development of cleaner processes as dry machining [248]. Also, pin-on-disc method is widely exploited to investigate lubricants and lubrication-related issues, e.g., the mutual influence of wear and the lubrication regimes for engineered surfaces [249–252] or the tribological properties of bio-lubricants for green industry [253–256].

Wear tests rely on the quantification of wear, i.e., the measurement of the damage brought by wear, in terms of volume. Two standard techniques to measure wear in pin-on-disc tests are available: precision weighting (gravimetric method) of samples and stylus-profilometry of the wear tracks cross-sections (volumetric method), as per ASTM G99-17 [257]. However, today's technology offers much more advanced and high-resolution, and information-rich inspection

techniques based on the measurement of surface topography. Nowadays, these methods are resorted to by increasing laboratories because their cost has become affordable [258,259,268,260–267]. Nonetheless, tribological standards have not incorporated them yet. Moreover, a rigorous metrological characterization is necessary to enable a performance comparison between standard and surface topography-based methods but is still lacking in the scientific literature.

This section aims at developing a computation of measurement uncertainty for surface-topography based methods to enable a performance comparison with respect to standardized approaches to quantify the wear in pin-on-disc test. The comparison will be carried out, considering cases of industrial interest.

2.4.1 Methods for wear quantification in pin-on-disc tribological test

In order to measure wear, it is first necessary to define it. Several definitions are available in literature as:

- DIN 50320 defined wear as *the progressive loss of material from the surface of a solid body due to mechanical action, i.e., the contact and relative motion against a solid, liquid or gaseous counter body* [269];
- According to ASTM G40, wear is *damage to a solid surface, generally involving progressive loss of material, due to relative motion between that surface and a contacting substance or substances* [270];
- The Organisation for Economic Co-operation and Development (OECD) research group on wear of engineering materials defined wear as the *progressive loss of substance from the operating surface of a body occurring as a result of relative motion at the surface* [271].

These definitions suggest that wear involves two key features: the contact between a solid surface and another substance with a relative motion [272] and damage by loss of material from the solid surfaces. However, from the viewpoint of design and quality, the surface damage is not necessarily limited to the loss of material from a surface. Other ways to cause surface damage is by the movement of material without loss of mass, i.e., plastic flow, or growth of deposited third layers [273]. Therefore, wear can be alternatively addressed as *a progressive change to a part that adversely affects its performance caused by relative motion with respect to another substance* [273]. The latter definition fits best the engineering use. It focuses on any surface modifications resulting from mechanical interactions, not necessarily the loss of material, implied in the former material-science-oriented definitions of wear. This last definition shifts the focus towards topography modification that may alter the proper functioning of the components.

This more inclusive definition of wear requires rigorously defining the measurand, which may impact the appropriateness of the choice of the measurement method. To this aim, it is worth to recall some terminology from the ASTM G40-17 [270] and consider the outcome of a pin-on-disc test to outline some practical aspects related to the measurand identification in wear measurements:

- *damage*, **n** = any effect on a solid body resulting from its exposure to these phenomena. This may include loss of material, surface deformation, or any other changes in microstructure, properties, or appearance.
- *galling*, **n** = a form of surface damage arising between sliding solids, distinguished by macroscopic, usually localized, roughening, and the creation of protrusions above the original surface; it is characterized by plastic flow and may involve material transfer.
- *wear*, **n** = alteration of a solid surface by progressive loss or progressive displacement of material due to relative motion between that surface and a contacting substance or substances

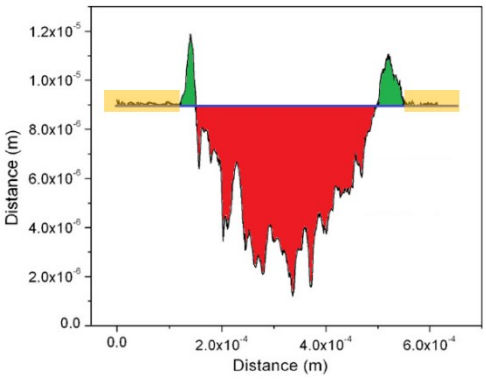

Figure 31 Typical pin-on-disc wear track profile. In red volume due to wear, in green volume due to galling. The blue line is the reference to distinguish wear and galling; it is computed fitting profile in the yellow zones.

Figure 31 shows the cross-section appearance of typical wear tracks on the disc of a pin-on-disc layout. It is straightforward to infer that the green part of the section, above the reference line, represents the volume by plastic flow or debris deposition, i.e., *galling*. On the other hand, the red region under the reference line is mainly material loss, i.e., *wear*. Moreover, it is impossible to exclude, a-priori, that the displaced or transferred material does not affect the track. From this discussion, Eq.(2.9) follows:

$$V_{damage} = V_{wear} + V_{galling} \qquad (2.9).$$

As anticipated, two standardized approaches are available to measure wear: the gravimetric and the volumetric approaches; they both achieve a characterization of wear in terms of volume of material loss [257]. The gravimetric approach relies upon a definition of wear by measuring the mass loss due to wear phenomenon and is frequently used to measure wear, because of the relative ease of performing a gravimetric measurement [273]. However, it is insensible to damages related to plastic effects and its result is altered by transferred material, which binds to the surface and cannot be removed by cleaning the surfaces. Moreover, the gravimetric method is sensitive enough only if the wear is relatively large with respect to the body's mass; thus, it is inappropriate for fretting or low-wear phenomenon analysis. Furthermore, to comply with the definition of wear, the knowledge of the measurand density is necessary, which limits the application of this method, with confidence, to homogeneous materials, as multi-phase and layered, e.g., coated, materials, may yield some substantial error in the estimation of wear [274,275].

The volumetric approach directly considers the volume of the surface damage as a measure of wear. The measurand is the amount of material that has undergone modifications during the interaction (removed or displaced). Although the measurement of a volume may be affected by transfer or debris accumulation, this method often allows distinguishing between the contribution coming from material displacement and material loss, and sometimes even between material loss and transfer phenomena. Additionally, it is unaffected by the inhomogeneity of materials and can provide an accurate indication of wear on different phases. Therefore, the volumetric method is more flexible, allowing to characterize only the wear, i.e., the removed material, e.g., when testing materials for brake pads or clutches, or the total damage, i.e., the overall effect of wear and galling. The latter scenario is preferable if the shape and tolerances of the profile are of paramount importance, e.g., in gears, couplings, in the study of alteration of lubrication regimes by wear effects.

Therefore, in the following, the gravimetric method will be disregarded.

Also, only the assessment of wear on the disc will be discussed.

Standardized volumetric methods

According to ISO 18535:2016 [276] and ASTM G99-17 [257] wear of the disc, resulting from a pin-on-disc test can be evaluated as:

$$V_{ISO} = \frac{2\pi}{N} R \sum_{j=1}^{N \geq 4} S_j \qquad (2.10.1),$$

where R is the radius of the wear track and S_j the area of the wear track cross-section profile at the j-th location, see Figure 32 for reference.

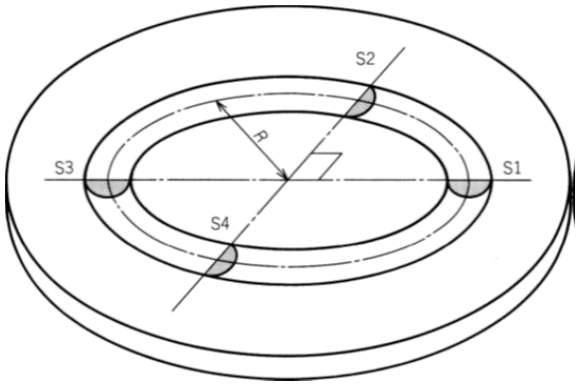

Figure 32 Scheme of volumetric wear measurement according to ISO 18535:2015.

The wear track radius can be chosen either as the nominal track radius, R_{nom}, or as the average radius of the extracted profiles, $\bar{R} = \frac{\sum_{j=1}^{N \geq 4} R_j}{N}$. The standard volumetric method requires to extract N profiles from the cross-section. Recalling that profiles are heights z as a function of the lateral displacement, i.e., lateral scanning along x-axis, $z(x)$ (as shown in Figure 33a), one way to compute the cross-section area, S_j, is the rectangle method, depicted in Figure 33b:

$$S_j = d_x \sum_{i=1}^{M} |z_i| \qquad (2.11),$$

where M is the number of sampled points in the profile and d_x is the lateral sampling step, i.e., the lateral resolution, along the x-axis.

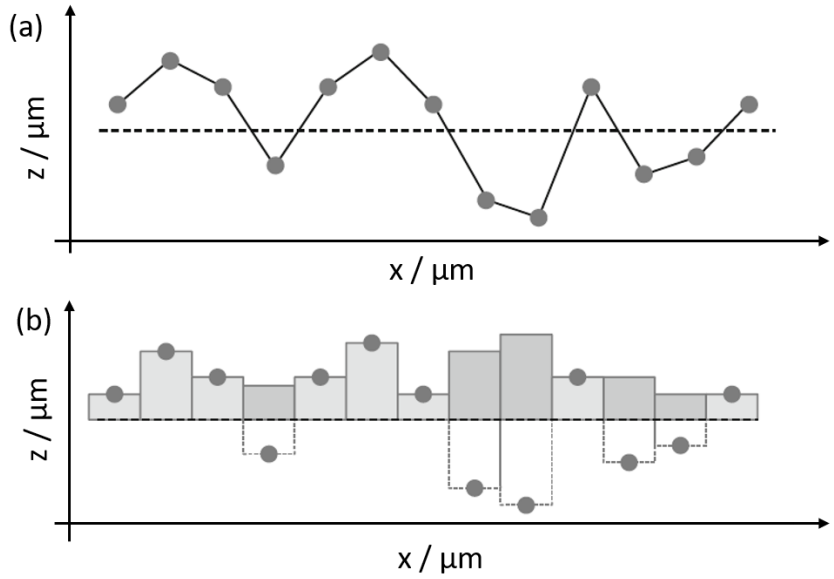

Figure 33 (a) profile heights z as function of lateral scanning step x. (b) rectangle method for area evaluation. (adapted from [176]).

Eq.(2.10.1) can also be rewritten to explicit the dependence on the average value:

$$V_{ISO} = \frac{2\pi}{N} R \sum_{j=1}^{N \geq 4} S_j = 2\pi R \bar{S} = \overline{V_{ISO}} \qquad (2.10.2),$$

which points out that standard volumetric methods evaluate the average wear volume of the track, by considering the average cross-section. This is inherent with the limited representativeness of the approach. When extracting few profiles, $N \geq 4$, if the track is highly irregular, regardless of whether it is circumferentially or along to the depth. In this regard, Colbert et al. [277] showed that, for reasonably regular tracks, a suggested threshold to reduce approximation errors is $N = 8$.

An alternative to this method, hereby proposed, consists of considering averages of the volumes that would result when considering N cross-sections, rather than the mean volume evaluated from the average cross-section, as:

$$\overline{V_{prof,alt}} = \frac{2\pi}{N} \sum_{j=1}^{N \geq 4} R_j S_j \qquad (2.12.1).$$

All equations thus far introduced are general and refer to the evaluation of the V_{damage}. It is necessary to evaluate a reference line with respect to which compute the heights and, most importantly, separate contributions for the computations to distinguish between volumes due to wear and galling. Typically, the reference line is computed by linearly least-square fitting the profile heights outside a specific region of interest of the profile, e.g., the yellow regions in Figure 31.

Even though standards are conceived for applying the volumetric methods through contact profilometers, e.g., CS instruments, literature reports implementations of standard volumetric methods based on areal-topography methods e.g., CSI, CM. After the areal surface topography measurement, these measurement approaches extract, through software, profiles on which computations required by Eq.(2.10) and (2.12) are carried out.

Volumetric methods based on surface topography measurements

The adoption of areal-topography measurement methods to extract profiles generates a significant data loss and yields no significant practical advantages, in terms of representativeness [278]. More in general, as pointed out in the former subsection, volumetric methods based on profiles yield the mean wear volume evaluation due to the inherently limited representativeness.

Therefore, recently, literature reports the introduction and adoption of wear volume characterization methods that exploit in full the measured topography.

Two approaches can be distinguished: a numerical one that still relies upon profile extraction and the second based on surface texture parameters.

In both cases some preliminary operations are necessary. The first, standard operators to get the S-F surface must be applied; then the wear track identification should be carried out to extract a region of interest (ROI). The track identification can either be done manually or exploiting segmentation methods [275]. The extraction of the ROI is necessary to exclude the effect of roughness and topographical features that are not due to tribological test from following computations. Even if extremely computationally demanding, an effective mean consists of measuring the tested surface both before and after the test and evaluating the worn surface by subtraction of the two, provided a preliminary registration step [265,279–281].

Then topographical methods can be applied. The former is completely automatic and implemented in several commercial software for surface topography characterization. It requires extracting the complete series of N profiles $z(x)$ across the orthogonal direction of profile scanning, i.e., the y-axis, and computing the (total) damage volume as:

$$V_{aut} = d_y \sum_{j=2}^{N-1} S_j + \frac{d_y}{2}(S_1 + S_N) \qquad (2.13),$$

where d_y is the sampling distance along the y-axis [282–284]. The evaluation of a reference surface height, again by plane-lest square fitting the topography outside the ROI allows distinguishing between wear and galling contribution to the damage.

The second approach is based on volume areal field parameters [124,176,285] and allows computing total damage as:

$$V_{VP} = V_m(m_r) + V_v(m_r) \qquad (2.14).$$

Here, the relevance of appropriately choosing the reference height, i.e., m_r, is even clearer. the Abbott-Firestone curve is an effective tool to identify m_r, as it

can be chosen as the flex of the material ratio curve. For a nominally flat plane with Gaussian distributed heights, i.e., without a structured texture, this point would correspond to the average height. The introduction of a topographical feature, as a wear track, modify the average height and the shape of the material ratio curve. Because points on hills and dales correspond to the two opposite tails of this curve, and the track has a height range significantly greater from the original surface S_z, these tails are separated by a plateau that contains one flex. i.e., the threshold to distinguish hills and dales. Therefore, the following relationship between Eq.(2.9) and Eq.(2.14) can be written as:

$$\begin{cases} V_{galling} = V_m(m_r) \\ V_{wear} = V_v(m_r) \end{cases} \quad (2.15).$$

2.4.2 Uncertainty evaluation of volumetric wear measurements

It is necessary to have available the evaluation of their measurement uncertainty, to enable performance comparison of the different volumetric wear measurement methods. The Guide to the expression of uncertainty in measurement (GUM) [286] establishes methods for computing the measurement uncertainty. In the case a known mathematical model can be explicitly written between the measurand (dependent) quantity *y* and the independent quantity $\boldsymbol{x}$ can be written as:

$$Y = f(\boldsymbol{X}) = f(\boldsymbol{X}), y \in \mathbb{R}^1, \boldsymbol{X} \in \mathbb{R}^{n,1} \quad (2.16).$$

If this model is linearisable, the variance of the dependent quantity $u^2(Y)$ can be computed according to:

$$u^2(Y) = \boldsymbol{c}^T \boldsymbol{VCV} \boldsymbol{c} = \sum_{a=1}^{n} \sum_{b=1}^{n} c_a c_b VCV_{ab} \quad (2.17),$$

where $\boldsymbol{c} \in \mathbb{R}^{n,1}$ is the vector of sensitivity coefficients, i.e., the partial derivatives, so that $c_a = \frac{\partial f}{\partial x_a}$ and $\boldsymbol{VCV} \in \mathbb{R}^n$ is the variance-covariance matrix of the independent quantities so that $VCV_{ab} = Cov(X_a, X_b)$. Eq.(2.17) is the law of uncertainty propagation, which is a particular case of the law of variance propagation. In the case of uncorrelated independent quantities, Eq.(2.17) can be rewritten as:

$$u^2(Y) = \sum_{a=1}^{n} \left(\frac{\partial f}{\partial x_a}\right)^2 u^2(X_a) = \sum_{a=1}^{n} u_a^2(y) \quad (2.18),$$

where $u^2(X_a)$ is the variance of the *a*-th influence factor and can be either statistically, i.e., being a type A contribution, or non-statistically, i.e., being a type B contribution, evaluated.

Under the non-trivial, but reasonable in most of practical cases, assumption that *Y* distributes normally, i.e., $Y \sim N(\mathbb{E}[Y], \mathbb{V}ar[Y])$, its (expanded) uncertainty *U(y)* is:

$$U(Y) = k \cdot u(y) \quad (2.19.1)$$

$$k = T_{\nu,P}^{-1} \quad (2.19.2)$$

$$\nu = \left\lfloor \frac{u^4(y)}{\sum \frac{u_a^4(y)}{\nu_a}} \right\rfloor \qquad (2.19.3),$$

where k is the coverage factor computed as the quantile of a t-Student distribution with ν degrees of freedom at a specific confidence interval P. Degrees of freedom are computed according to the Welch-Satterthwaite formula in Eq.(2.19.3) as a function of the degrees of freedom with whom each contribution is estimated.

In the following results will be provided in terms of variances for the sake of compactness.

Standardized method

Colbert et al. [277] developed the computation for the wear volume measurements according to the standard. However, in that paper, metrological characteristics of measuring instruments were not considered. According to the current standard framework of ISO 25178, they are supposed to support and simplify measurement uncertainty propagation. In this section, his computation will be revised to be compliant with the ISO 25178-600:2019, with the hypothesis of uncorrelated independent variables.

Recombining Eq.(2.10.1) and (2.12), it follows:

$$\overline{V_{ISO}} = \frac{2\pi}{N} d_x R \sum_{j=1}^{N\geq 4} \sum_{i=1}^{M} |z_{ji}| \qquad (2.20),$$

that highlights the measured independent quantities, which are summarised with their variability contribution, i.e., their measurement uncertainties evaluated according to Eq.(2.1) to cater for metrological characteristics, inTable 7.

Table 7 Influence factor to standardized wear volume evaluation.

Influence factor	Measured quantity	Standard uncertainty
S_j	d_x	$u(d)$
	z_{ij}	$u(z)$
R	R	$u(R)$

The variance due to the pixel size d, according to Giusca and Leach [172], can be associated with a triangular distribution having half-range d, so that $u^2(d) = \frac{d^2}{6}$ More convenient management of uncertainty propagation exploits, though, Eq.(2.10).

The first, the variance $u^2(S_j)$ can be evaluated according to Eq.(2.18) and to its definition in Eq.(2.11):

$$\boldsymbol{X} = \begin{bmatrix} d_x \\ \sum_{i}^{M} |z_i| \end{bmatrix} \qquad (2.21.1)$$

$$\boldsymbol{c} = \begin{bmatrix} \sum_{i}^{M} |z_i| \\ d_x \end{bmatrix} \tag{2.21.2}$$

$$\boldsymbol{VCV} = \begin{bmatrix} u^2(d) & 0 \\ 0 & u^2(\sum_{i}^{M} |z_i|) \end{bmatrix}, u^2\left(\sum_{i}^{M} |z_i|\right) = Mu^2(z) \tag{2.21.3}$$

$$u^2(S_j) = \left(\sum_{i}^{M} |z_i|\right)^2 u^2(d) + (d_x)^2 u^2\left(\sum_{i}^{M} |z_i|\right) = \left(\frac{S_j}{d_x}\right)^2 u^2(d) + {d_x}^2 M u^2(z) \tag{2.21.4},$$

from which the variance of the average cross-section follows:

$$\bar{S} = \frac{\sum_{j=1}^{N\geq 4} S_j}{N} \tag{2.22.1}$$

$$u^2(\bar{S}) = \frac{\sum_{j=1}^{N\geq 4} u^2(S_j)}{N^2} = \frac{\mathbb{E}[u^2(S_j)]}{N} \tag{2.22.2},$$

which is different from the variance of the sample mean, despite the definition of $\bar{S}$, because $u^2(S_j)$ depends on S_j (as shown in Eq.(2.21.4)).

Then the contribution *u(R)* due to the track radius *R* is assessed. It depends on the choice of *R* between R_{nom} and $\bar{R}$. In the first case, u(R_{nom}) can be estimated according to the P.U.Ma. method as two units of the least significant digit of the mean value, 2·*LSD*, and associating to this half range a uniform distribution [286], so that its equivalent variance results:

$$u^2(R_{nom}) = \frac{2 \cdot LSD}{3} \tag{2.23}.$$

In the second case, the law of variance propagation is required, proceeding from the definition of $\bar{R} = \frac{\sum_{j}^{N\geq 4} R_j}{N}$. As shown in Figure 32, typically, profiles are extracted in pairs along a radial direction $\vec{r}$. In this case, on each measured pair, an external diameter D_{ext} and an internal diameter D_{in} can be identified, so that:

$$R_j = \frac{1}{2}\left(\frac{D_{ext,j} + D_{in,j}}{2}\right) \tag{2.24}.$$

Therefore, it is necessary to express the coordinate change from cartesian coordinates *O(x,y)* to polar coordinates *O(r, θ)*:

$$\begin{cases} r = x\cos\vartheta + y\sin\vartheta \\ \vartheta = \tan^{-1}\left(\frac{y}{x}\right) \end{cases} \quad (2.25.1)$$

$$x = r\cos\vartheta \quad (2.25.2)$$

$$y = r\sin\vartheta \quad (2.25.3).$$

Because diameters are extracted along $\vec{r}$, the variance of the length *r*, due to the change of coordinates must be computed following the law of uncertainty propagation:

$$\boldsymbol{X} = \begin{bmatrix} x \\ y \\ \vartheta \end{bmatrix} \quad (2.26.1)$$

$$\boldsymbol{c} = \begin{bmatrix} \cos\vartheta \\ \sin\vartheta \\ -x\sin\vartheta + y\cos\vartheta \end{bmatrix} = \begin{bmatrix} \cos\vartheta \\ \sin\vartheta \\ -r\cos\vartheta\sin\vartheta + r\sin\vartheta\cos\vartheta \end{bmatrix} = \begin{bmatrix} \cos\vartheta \\ \sin\vartheta \\ 0 \end{bmatrix} \quad (2.26.2)$$

$$\boldsymbol{VCV} = \begin{bmatrix} u^2(x) & 0 & 0 \\ 0 & u^2(y) & 0 \\ 0 & 0 & u^2(\vartheta) \end{bmatrix} \quad (2.26.3)$$

$$u^2(r) = u^2(x)\cos\vartheta^2 + u^2(y)\sin\vartheta^2 \quad (2.26.4).$$

Eq.(2.26.4) shows that the uncertainty of the length *r* along the direction ϑ depends only on ϑ; therefore, because D_{ext} and D_{in} are measured in the same direction, $u^2(D_{ext}) = u^2(D_{in}) = u^2(D)$. It is hence possible to evaluate the variance of R_j, following the definition in Eq.(2.24):

$$\boldsymbol{X} = \begin{bmatrix} D_{ext} \\ D_{in} \end{bmatrix} \quad (2.27.1)$$

$$\boldsymbol{c} = \begin{bmatrix} 1/4 \\ 1/4 \end{bmatrix} \quad (2.27.2)$$

$$\boldsymbol{VCV} = \begin{bmatrix} u^2(D_{ext}) & 0 \\ 0 & u^2(D_{in}) \end{bmatrix} = \begin{bmatrix} u^2(D) & 0 \\ 0 & u^2(D) \end{bmatrix} \quad (2.27.3)$$

$$u^2(R_j) = \frac{2}{16}(u^2(x)\cos\vartheta^2 + u^2(y)\sin\vartheta^2) = \frac{1}{8}(u^2(x)\cos\vartheta^2 + u^2(y)\sin\vartheta^2) \quad (2.27.4),$$

from which the evaluation of the variance of the average radius is computed as:

$$\bar{R} = \frac{\sum_{j=1}^{N\geq 4} R_j}{N} \quad (2.28.1)$$

$$u^2(\bar{R}) = \frac{\sum_{j=1}^{N\geq 4} u^2(R_j)}{N^2} = \frac{\mathbb{E}[u^2(R_j)]}{N} \quad (2.28.2),$$

which is different from the variance of a sample mean, because $u^2(R_j)$ depends on the extraction direction ϑ.

Finally, the variance of the standardized volumetric method for mean wear volume measurement can be computed exploiting its definition in Eq.(2.10.2) and

the contribution from the area of the average cross-section, Eq.(2.22), and from the track radius, for which two alternatives are possible:

$$\boldsymbol{X} = \begin{bmatrix} R \\ \bar{S} \end{bmatrix} \tag{2.29.1}$$

$$\boldsymbol{c} = \begin{bmatrix} 2\pi\bar{S} \\ 2\pi R \end{bmatrix} \tag{2.29.2}$$

$$\boldsymbol{VCV} = \begin{bmatrix} u^2(R) & 0 \\ 0 & u^2(\bar{S}) \end{bmatrix} \tag{2.29.3}$$

$$u^2(\overline{V_{ISO}}) = 4\pi^2\left(\bar{S}^2 u^2(R) + R^2 u^2(\bar{S})\right) \tag{2.29.4}.$$

The latter can be re-written expliciting the two choices of *R*:

$$u^2\left(\overline{V_{ISO,R_{nom}}}\right) = 4\pi^2\left(\bar{S}^2 u^2(R_{nom}) + {R_{nom}}^2 \frac{\mathbb{E}\left[u^2(S_j)\right]}{N}\right) \tag{2.30}$$

$$u^2\left(\overline{V_{ISO,\bar{R}}}\right) = \frac{4\pi^2}{N}\left(\bar{S}^2\mathbb{E}\left[u^2(R_j)\right] + \bar{R}^2\mathbb{E}\left[u^2(S_j)\right]\right) \tag{2.31}.$$

Alternative method based on profile extraction

As discussed in Section 2.4.1, a possible alternative to the computation of the mean wear volume evaluated from the average cross-section, consists in considering averages of the volumes that would result when considering *N* cross-sections, i.e., $\overline{V_{prof,alt}}$ as per Eq.(2.12.1), that, to simplify computations, can be rewritten as:

$$\overline{V_{prof,alt}} = \frac{2\pi}{N}\sum_{j}^{N\geq 4} R_j S_j = 2\pi\overline{RS} \tag{2.12.2}$$

The evaluation of the variance of the mean volume evaluated in this case exploits previous computations, being the influence factors R_j and S_j. It first estimates $u^2\left(R_j S_j\right)$:

$$\boldsymbol{X} = \begin{bmatrix} R_j \\ S_j \end{bmatrix} \tag{2.32.1}$$

$$\boldsymbol{c} = \begin{bmatrix} S_j \\ R_j \end{bmatrix} \tag{2.32.2}$$

$$\boldsymbol{VCV} = \begin{bmatrix} u^2\left(R_j\right) & 0 \\ 0 & u^2\left(S_j\right) \end{bmatrix} \tag{2.32.3}$$

$$u^2\left(R_j S_j\right) = {S_j}^2 u^2\left(R_j\right) + {R_j}^2 u^2\left(S_j\right) \tag{2.32.4},$$

from which $u^2(\overline{RS})$ can be written as:

$$u^2(\overline{RS}) = \frac{\sum_{j=1}^{N\geq 4} u^2(R_j S_j)}{N^2} = \frac{\mathbb{E}\left[u^2(R_j S_j)\right]}{N} \quad (2.33),$$

that allows to write the wanted result:

$$u^2\left(\overline{V_{prof,alt}}\right) = 4\pi^2 u^2(\overline{RS}) = 4\pi^2 \frac{\mathbb{E}\left[u^2(R_j S_j)\right]}{N} \quad (2.34).$$

Automatic surface topography-based method

Although literature recently reports several applications of this method, to the author's best knowledge, methods for estimating measurement uncertainty are not available.

The definition in Eq.(2.13) highlights the influence factors, which are summarised in Table 8:

Table 8 Influence factor to automatic wear volume evaluation based on surface topography.

Influence factor	Measured quantity	Standard uncertainty
S_j	d_x	*u(d)*
	z_{ij}	*u(z)*
$\boldsymbol{d_y}$	d_y	*u(d)*

Thus, the variance computation can be carried out as follows, according to the law of uncertainty propagation and relying on the evaluation of $u^2(S_j)$ in Eq.(2.21.4):

$$\boldsymbol{X} = \begin{bmatrix} S_1 \\ S_N \\ S_j \\ d_y \end{bmatrix} \quad (2.35.1)$$

$$\boldsymbol{c} = \begin{bmatrix} {d_y}/{2} \\ {d_y}/{2} \\ d_y \\ \sum_{j=2}^{N-1} S_j + \frac{S_1 + S_N}{2} \end{bmatrix} \quad (2.35.2)$$

$$\boldsymbol{VCV} = \begin{bmatrix} u^2(S_1) & 0 & 0 & 0 \\ 0 & u^2(S_2) & 0 & 0 \\ 0 & 0 & u^2(S_j) & 0 \\ 0 & 0 & 0 & u^2(d) \end{bmatrix} \quad (2.35.3)$$

$$u^2(V_{aut}) =$$

$$\frac{d_y^2}{4}\left(u^2(S_1)+u^2(S_N)\right)+d_y^2\sum_{j=2}^{N-1}u^2(S_j)\ +\left(\sum_{j=2}^{N-1}S_j+\frac{S_1+S_N}{2}\right)^2 u^2(d) \quad (2.35.4).$$

It is necessary to express the mean volume's uncertainty, to enable a comparison with standardized methods based on the extraction of a few profiles, which leads to the evaluation of a mean wear volume. The comparison is enabled by considering the variance of the sample mean, provided that the sample includes *N-1* extracted profiles:

$$u^2(\overline{V_{aut}}) = \frac{u^2(V_{aut})}{N-1} \quad (2.36).$$

Volume areal field-based method

Measurement uncertainty for volume areal field parameters are unreported in the literature to the author's best knowledge. It is first necessary to pass from the continuous definition, as in Section 2.1, to the discrete, to enable this evaluation:

$$V_m(m_r) = K\int_{0\%}^{mr} S_{mc}(p) - S_{mc}(mr)\,dp \approx K\sum_{j=1}^{B}\Delta z_j m_{r\,j} \quad (2.37.1).$$

$$V_v(m_r) = K\int_{mr}^{100\%} S_{mc}(mr) - S_{mc}(p)\,dp \approx K\left(100\%(z_{max}-h) - \sum_{j=B+1}^{N_{bin}}\Delta z_j m_{r\,j}\right) \quad (2.37.2)$$

$$K = n_x n_y d^2 \quad (2.37.3)$$

with $h = S_{mc}(m_r)$, n_x and n_y respectively the number of measured pixels along the *x*- and *y*-axis, *d* the pixel dimension, with the hypothesis that $d_x = d_y = d$. It is necessary to approximate the material ratio curve by a histogram, to pass to the discrete domain. The histogram has N_{bin} bins, so that *h* belongs to the *B-th* bin; the *j-th* bin is wide Δz_j and is associated with a material ratio of $m_{r\,j}$.

Under the assumption that the material ratio curve is computed exactly, i.e., the histogram is built exactly, $m_{r\,j}$ does not contribute to measurement uncertainty and the only influence factors are the height and the pixel width as summarised in Table 9.

Table 9 Influence factor to wear volume evaluation based on volume areal field parameters.

Influence factor	Measured quantity	Standard uncertainty
Δz_j	z_i-z_j	$\sqrt{2}\cdot u(z)$
h	h	$u(z)$
K	d	$u(d)$

The first, the variance of *K* can be computed as:

$$\boldsymbol{X} = [d] \tag{2.38.1}$$

$$\boldsymbol{c} = \left[2dn_x n_y\right] \tag{2.38.2}$$

$$\boldsymbol{VCV} = [u^2(d)] \tag{2.38.3}$$

$$u^2(K) = 4 \cdot \left(n_x n_y\right)^2 \cdot d^2 \cdot u^2(d) = 4Kn_x n_y u^2(d) \tag{2.38.4}.$$

Then, the variance of V_m, i.e., the $V_{gallling}$, is computed:

$$\boldsymbol{X} = \begin{bmatrix} K \\ \Delta z_j \end{bmatrix} \tag{2.39.1}$$

$$\boldsymbol{c} = \begin{bmatrix} \sum_{j=1}^{B} \Delta z_j m_{r_j} \\ K m_{r_j} \end{bmatrix} \tag{2.39.2}$$

$$\boldsymbol{VCV} = \begin{bmatrix} u^2(K) & 0 \\ 0 & 2u^2(z) \end{bmatrix} \tag{2.39.3}$$

$$u^2\left(V_m(m_r)\right) = \left(\sum_{j=1}^{B} \Delta z_j m_{r_j}\right)^2 u^2(K) + 2K^2 \sum_{j=1}^{B} m_{r_j}^2 \, u^2(z) \tag{2.39.4}.$$

Similarly, the variance of V_v, i.e., the V_{wear}, results from:

$$\boldsymbol{X} = \begin{bmatrix} K \\ z_{max} - h \\ \Delta z_j \end{bmatrix} \tag{2.40.1}$$

$$\boldsymbol{c} = \begin{bmatrix} \left((z_{max} - h) - \sum_{j=B+1}^{N_{bin}} \Delta z_j m_{r_j}\right) \\ K \\ -K m_{r_j} \end{bmatrix} \tag{2.40.2}$$

$$\boldsymbol{VCV} = \begin{bmatrix} u^2(K) & 0 & 0 \\ 0 & 2u^2(z) & 0 \\ 0 & 0 & 2u^2(z) \end{bmatrix} \tag{2.40.3}$$

$$u^2\left(V_v(m_r)\right) = \left((z_{max} - h) - \sum_{j=B+1}^{N_{bin}} \Delta z_j m_{r_j}\right)^2 u^2(K) + 2K^2 \left(1 + \sum_{j=B+1}^{N_{bin}} m_{r_j}^2\right) u^2(z) \tag{2.40.4}.$$

Last, if the total damage is of interest, and consequently its variance, the last two results can be combined so that it results:

$$u^2(V_{VP}) = u^2\left(V_m(m_r)\right) + u^2\left(V_v(m_r)\right) \tag{2.41.1}$$

$$u^2(V_{VP}) = \left[\left(\sum_{j=1}^{B}\Delta z_j m_{r_j}\right)^2 + \left((z_{max}-h) - \sum_{j=B+1}^{N_{bin}}\Delta z_j m_{r_j}\right)^2\right]u^2(K) + 2K^2\left[1+\sum_{j=1}^{N_{bin}} m_{r_j}^2\right]u^2(z) \quad (2.41.2)$$

$$u^2(V_{VP}) = \left[\left(\frac{V_m(m_r)}{K}\right)^2 + \left(\frac{V_v(m_r)}{K}\right)^2\right]u^2(K) + 2K^2\left[1+\sum_{j=1}^{N_{bin}} m_{r_j}^2\right]u^2(z) \quad (2.41.3)$$

Variances of mean volumes can be computed as follows, to perform a comparison with standard methods:

$$u^2\left(\overline{V_{galling}}\right) = \frac{u^2\left(V_m(m_r)\right)}{n_x n_y} \quad (2.42.1)$$

$$u^2\left(\overline{V_{wear}}\right) = \frac{u^2\left(V_v(m_r)\right)}{n_x n_y} \quad (2.42.1)$$

$$u^2\left(\overline{V_{damage}}\right) = \frac{u^2(V_{VP})}{n_x n_y} \quad (2.42.1)$$

2.4.3 Materials and Methods

The theoretical framework, formerly developed, is then applied to a case study to assess the available methods' performances to estimate wear volumes in a pin-on-disc tribological test. Tribological tests were performed using an Anton Paar TRB pin-on-disc tribometer. An aluminium sample and a PTFE sample were tested against a 100Cr6 6 mm diameter steel ball to generate wear tracks with different features and shape in similar testing conditions. One test was performed with a duration of 40 m run on each sample under 5 N load, and linear speed of 0.05 m/s. The wear track radius was kept the same to ensure that the observed tribological phenomena are fully comparable, R_{nom} = 5 mm. Figure 34 shows the tribometer used to run the test, the schematic of the pin-on-disc layout and the appearance of the surface damage on the two samples at the end of the tests. The two material were chosen to provide different wear situations as Aluminium is known to generate debris, attached particles, and is characterized by a highly irregular track, whilst PTFE features a regular track, with limited galling.

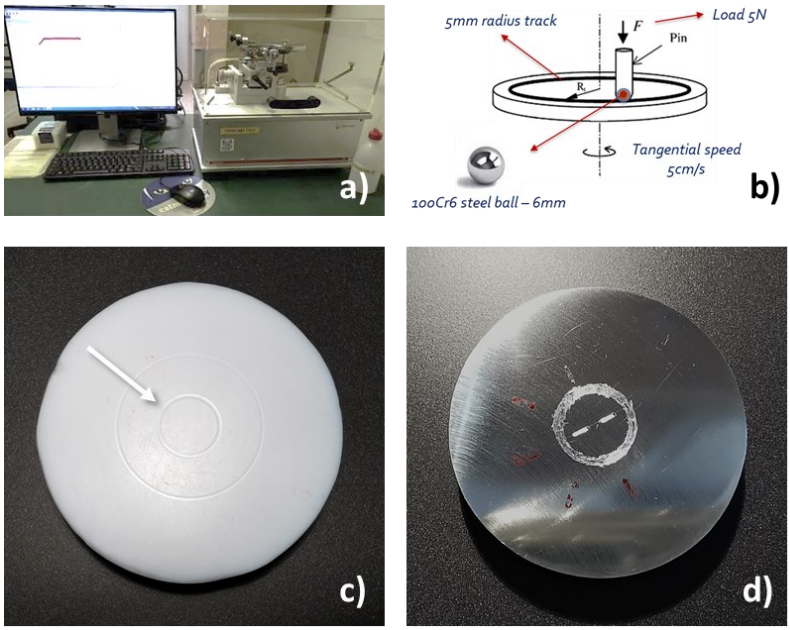

Figure 34 (a) Anton Paar TRB pin-on-disc tribometer at DIMEAS Laboratory; (b) pin-on-disc testing layout; (c) wear track on the aluminium sample; (d) wear track appearance on the PTFE sample.

Both samples were grinded and polished before the test in order to improve the surface finish. Table 10 summarises the main topographical and mechanical properties of the samples and ball material.

Table 10 Mechanical and topographical properties of tested samples. For the samples, λs is 1 μm and F-operator is a 2nd order polynomial, to eliminate shape introduced by manual polishing; for the ball, λs is 2.5 μm and the F-operator a least-square fitted sphere. Vickers scales were chosen to test the same scale of the worn material during the pin-on-disc test; ball hardness specified by the manufacturer.

Material	S_a / μm	S_q / μm	**Hardness**
100Cr6 (ball)	0.13	0.22	60 HRC
Aluminium	0.31	0.40	76.89 HV 0.2
PTFE	0.34	0.48	2.95 HV 0.025

At the end of the test, the samples were accurately cleaned with acetone to remove wear debris and wear tracks were analyzed to calculate the volume of the surface damage.

Wear, galling and total damage volumes are measured exploiting the formerly introduced methods and considering, for the methods based on profile measurements, four and eight profiles (to test the consistency of these results with the literature [277]). Moreover, profile measurements were considered both directly measured by a CS, an MS RTP-80, and extracted by a surface topography measurement performed by a CSI, a Zygo NewView 9000. This instrument was also employed to enable the application of methods based on surface topography. In the latter case, to consider the possible effect of the lateral resolution, two different measurement objectives were used: a Michelson 5.5×, with numerical

aperture 0.15 and pixel size d of 1.56 µm and a Mirau 20× with digital zoom at 0.5× with a numerical aperture of 0.4 and d of 0.87 µm. In both cases, the stitching of several field-of-views was necessary. In real practice, the lower magnification would be chosen to limit the measurement time (about 15' and 30' respectively). The experimental setup and the volume measurement methods are summarised in Table 11 and Table 12.

Table 11 Measurement setup for the comparison of wear volume measurement method based on profile.

Profile-based method	**Standard**				**Alternative**	
R measurement	R_{nom}		$\bar{R}$		-	
Number of profiles (N)	4	8	4	8	4	8
Instrument setup	CS, CSI 5.5×, CSI 20×					

Table 12 Measurement setup for the comparison of wear volume measurement method based on surface topography.

Surface topography-based method	**Automatic**	**Volume parameters**
Instrument setup	CSI 5.5×, CSI 20×	

Both instruments are hosted in the Technological Surface Metrology Laboratory of Politecnico di Torino, Italy. The contributions to measurement uncertainty of their metrological characteristics are summarised in Table 13 and estimated as type B contribution from the literature [154,156,171]. They are combined according to Eq.(2.1), yielding results in Table 14.

Table 13 Contribution to measurement uncertainties of metrological characteristics of considered instruments.

	CS	**CSI**
$\boldsymbol{u_{NF}}$ / nm	35	1
$\boldsymbol{u_x}$ / nm	400	100
$\boldsymbol{u_y}$ / nm	400	100
$\boldsymbol{u_z}$ / nm	5	10
$\boldsymbol{u_{WR}}$ / nm	3608	902 (5.5×)
		600 (20×)

Table 14 Measurement uncertainty along the measuring axes of the considered instruments.

	CS	**CSI**	
		5.5×	20×
$\boldsymbol{u(x)}$ / nm	3630	908	608
$\boldsymbol{u(y)}$ / nm	3630	908	608
$\boldsymbol{u(z)}$ / nm	35	10	10

Systematic differences amongst the methods in terms of their capability to estimate the average volume will be assessed by performing a hypothesis t-test at a confidence level of 95% on the difference of the estimated average volumes. Qualitatively same results can be obtained by comparing the uncertainty bars: a systematic difference can be highlighted if they do not overlap. The surface topography-based methods are considered the benchmark to compare results: although they are nonstandard methods, the measuring methods' greater representativeness provide the necessary confidence to support this choice. For the topography-based methods' application, ROIs were extracted manually as the measured region hindered automatic identification methods because of computational limits.

2.4.4 Results discussion

Figure 35 shows the surface topographies of the two inspected samples. As intended, PTFE is characterized by a smooth and regular wear track, whilst aluminium's depth is highly irregular and additionally shows attached particles inside the track and severe galling at the edges. The black lines represent the profile extraction direction from the CSI. Figure 36 shows examples of measured profiles on both samples.

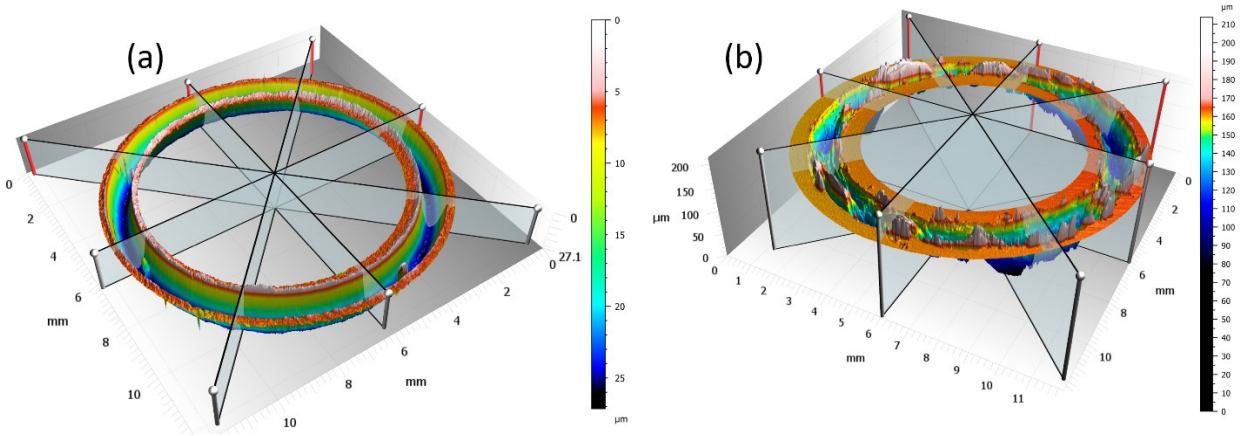

Figure 35 Wear tracks of (a) PTFE and (b) Aluminium.

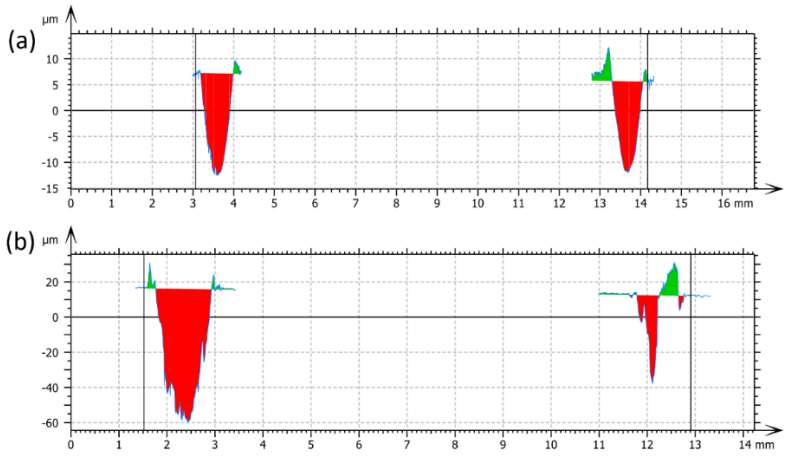

Figure 36 Examples of measured profiles of (a) PTFE and (b) Aluminium. In red wear, in green galling volume contributions.

The comparison of the performances of the method for total damage is reported in Figure 37 and Figure 38, which respectively shows the results for PTFE and Aluminium. Error bars represent expanded uncertainty at a confidence level of 95% and 30 degrees of freedom, i.e., $k = 2$.

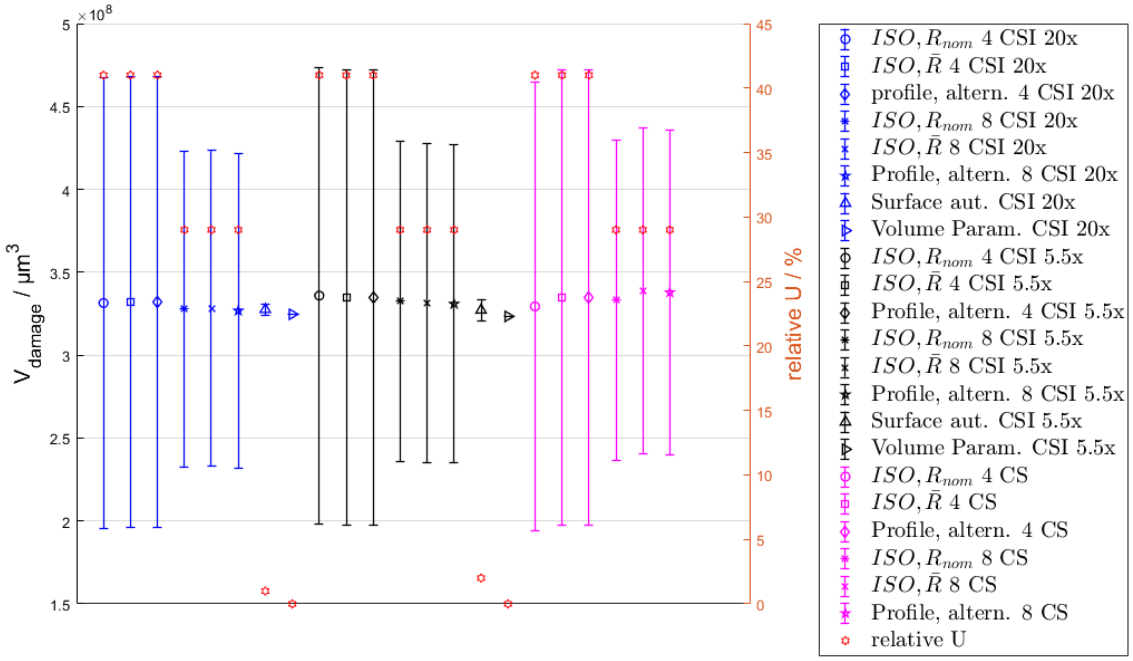

Figure 37 Volume of damage for PTFE sample.

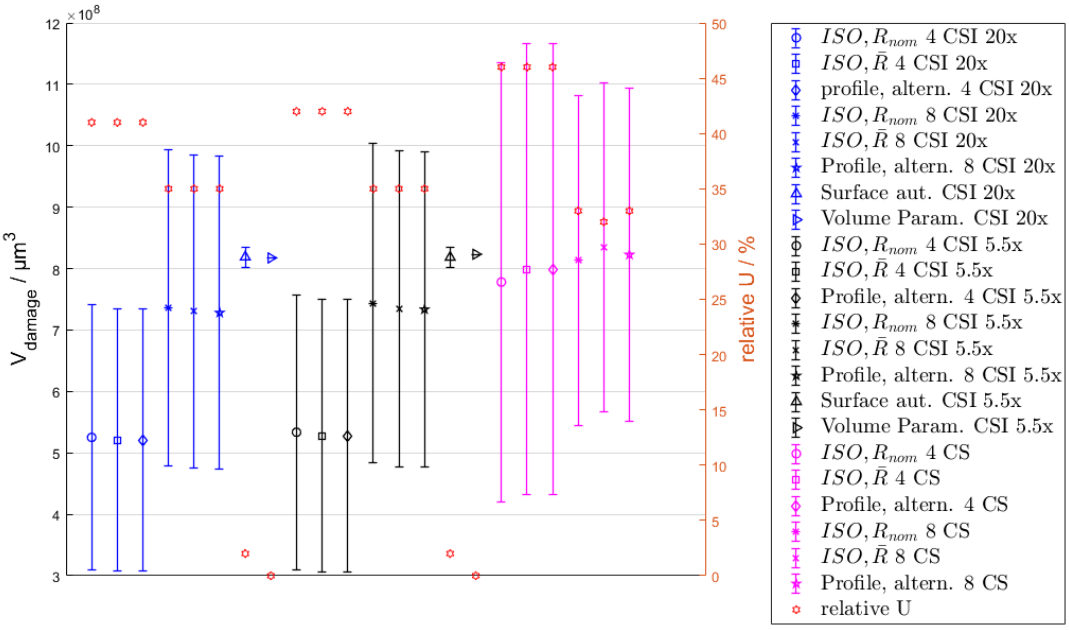

Figure 38 Volume of damage for Aluminium sample

Total damage volume shows that for regular tracks, i.e., in the case of PTFE, no significant differences in accuracy performances are present (differences of the average values are within 5%). Profile methods for increasing profiles, consistently with the average volume computation and literature [277], improve their precision. Surface topography-based methods are inherently the best for precision (expanded uncertainty smaller than 1%). Considering the aluminium, which is characterized by a highly irregular track, the adoption of profilometric methods based on extracted profiles, e.g., the standard method applied on CSI measurements, with few profiles show poor accuracy (in some cases with differences between average values up to 60%). It improves by increasing the number of sampled profiles (again following [277]). The actual measurement of profiles, i.e., by a CS, significantly improves the accuracy; however, this is an effect that can be ascribed to the worst lateral resolution, which tends to overestimate areas, see a graphical depiction in Figure 39.

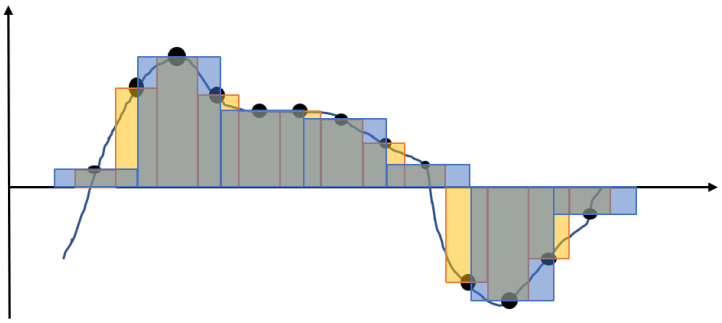

Figure 39 Effect of lateral sampling resolution on the estimation of area. Coarser resolution (blue) overestimates areas.

Insights on the performances can be obtained by analyzing the wear and galling volumes. Wear volume measurement results are shown in Figure 40 and Figure 41, and galling volumes in Figure 42 and Figure 43. For a regular wear track, in which wear is the dominant phenomenon (V_{wear} is the 95% of V_{damage}), accuracy amongst the methods is still acceptable (differences are within 5%). However, profiles methods tend to overestimate the wear slightly and significantly and systematically underestimate the contribution due to galling. This effect is due to the lower representativeness of the profile methods, limiting its capability to measure a small and localized phenomenon, as is galling in PTFE case. Conversely, a severe underestimation of wear volume results for an irregular track in which galling is not negligible (V_{wear} is the 88% of V_{damage}). In this situation, methods based on profile extraction from topographical measurement can result in differences up to 10%, partially compensated when a CS instrument is used, due to the resolution effect. This affects the estimation of galling volume.

Annex A report detailed results for relative accuracies between the methods and t-test.

The lateral resolution also affects the uncertainty, with larger uncertainties associated with coarser measurement methods.

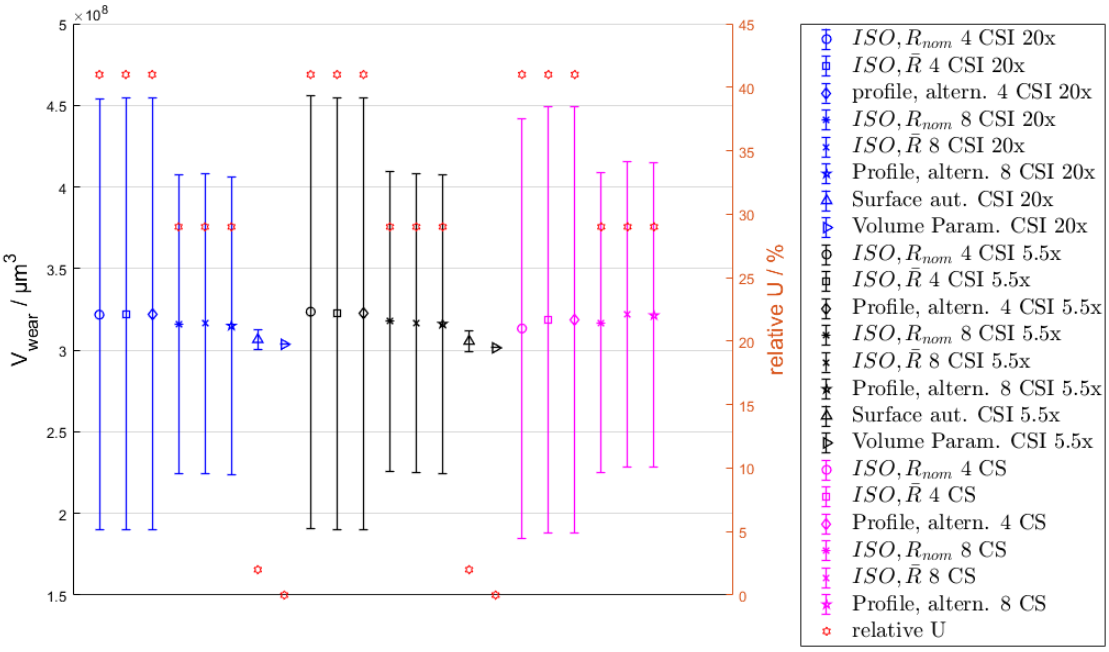

Figure 40 Volume of wear for PTFE sample.

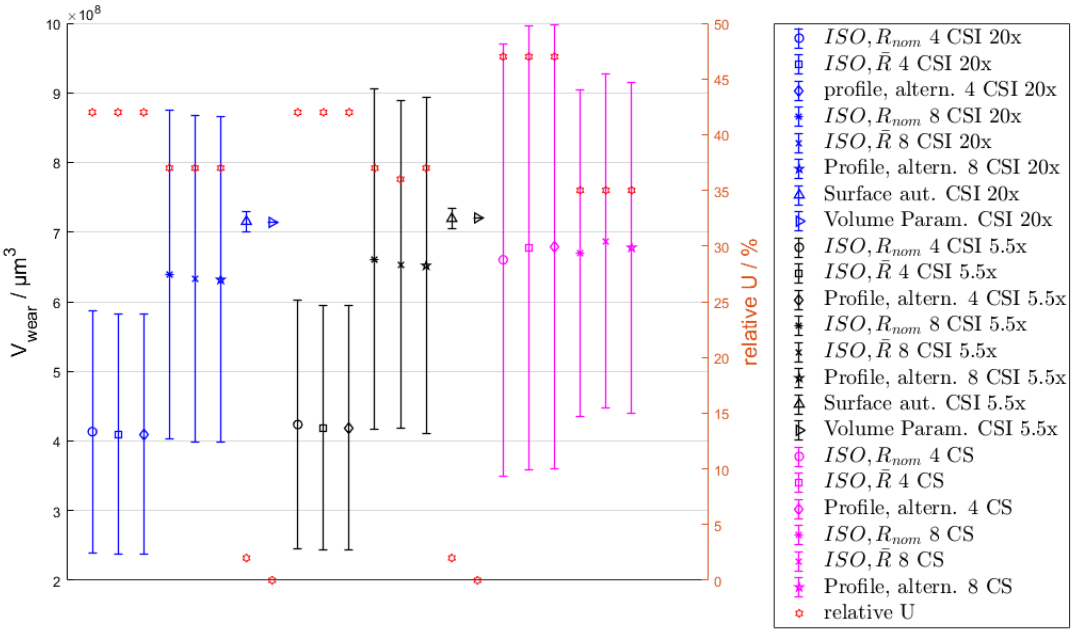

Figure 41 Volume of wear for Aluminium sample.

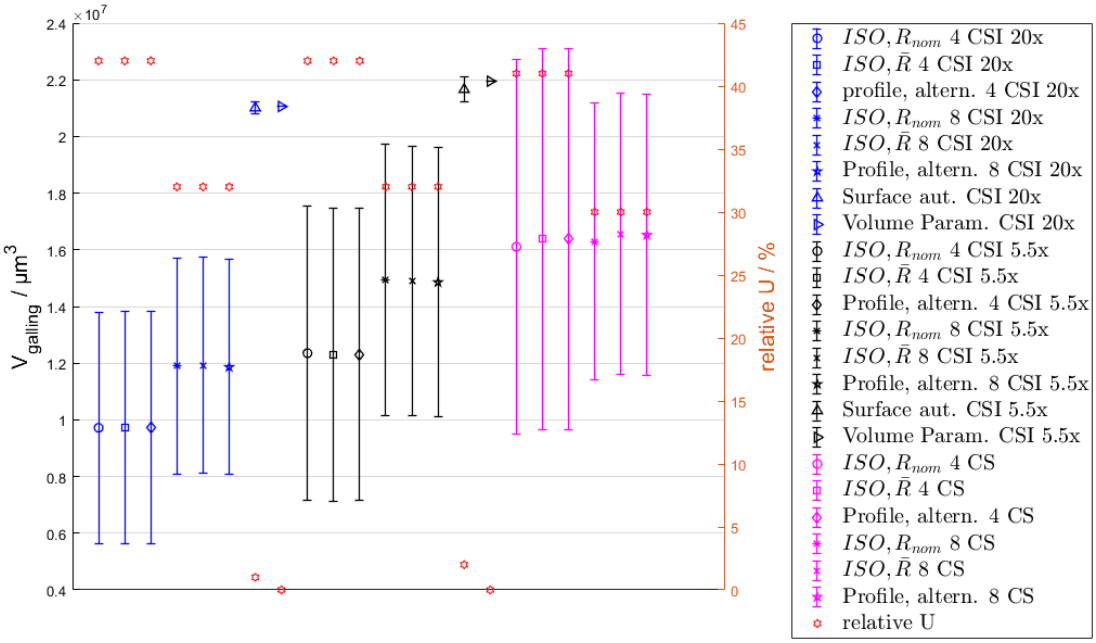

Figure 42 Volume of galling for PTFE sample.

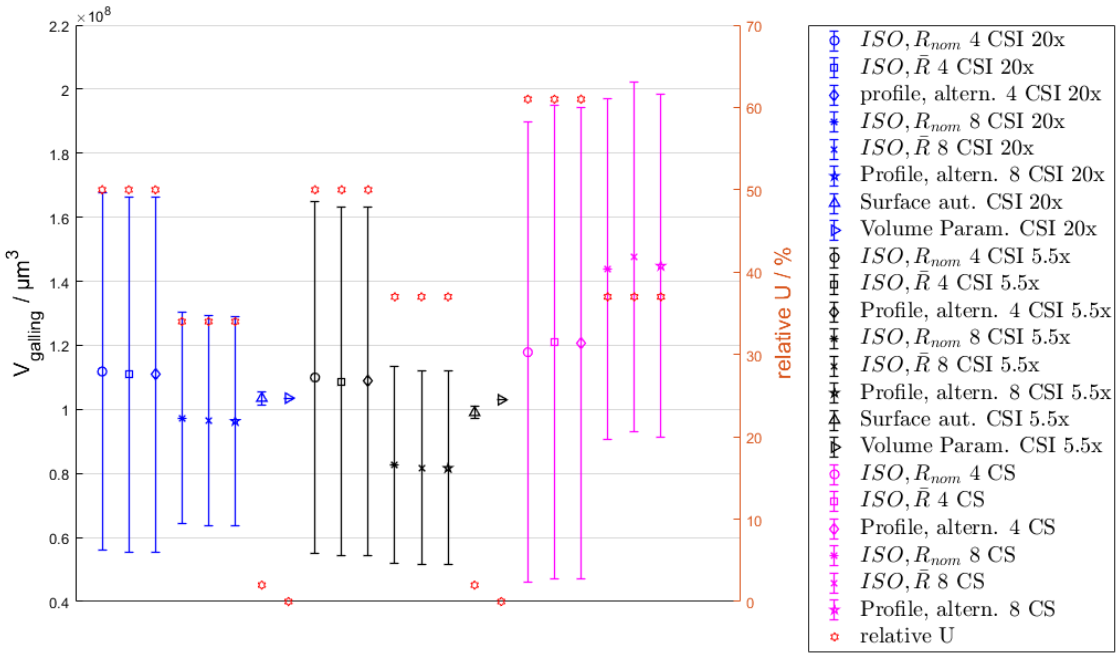

Figure 43 Volume of galling for Aluminium sample.

2.4.5 Section summary

This section dealt with the challenge of measuring wear phenomenon in the pin-on-disc tribological test. The standards propose methods based on the measurement or the extraction of profiles; in literature, methods based on surface topography measurements are available. However, their performances are unreported in terms of measurement uncertainties, which hinders a proper comparison of the methods. In this section, measurement uncertainties evaluation based on the current standardized framework of metrological characteristics of surface topography measuring instruments was developed. The theoretical framework was then exploited to compare performances of available methods and instruments to measure wear volumes.

Surface topography-based methods provide a thorough description of the phenomenon and are the most precise. Profile methods are affected by two phenomena. On the one hand, the lateral resolution of the measuring instrument introduces systematic differences in the accuracy. Additionally, in the case of a CS, it provides a systematic relative overestimation of the measured volume. On the other hand, the sampling associated with the measurement, or the extraction, of few profiles generates representativeness criticalities limiting the capability of dealing with irregular tracks and localized galling phenomena. Therefore, also in terms of accuracy and robustness, surface topography-based methods were demonstrated to perform better. The relative high uncertainty, i.e., the low precision, that characterizes standard methods questions their suitability in the case of very low volumes, which nowadays are more and more common, e.g.,

innovative hard coatings, composites with ceramic reinforcements, lubricated wear.

Future works will exploit these results to improve understanding of the pin-on-disc's main influence parameters, to support the development of calibration standards and procedure, and to establish traceability of the method.

Chapter 3

Advanced methods for surface mechanical characterization

As diffusely discussed in the introduction, surface technologies aim at engineering surfaces to optimize and enhance the performances of components. This is achieved by modifying the surface to induce a change of a set of material properties. Amongst the several properties that can be modified, technological properties are particularly interesting and relevant as they ultimately control the performances of functional components in mechanical assemblies. Within technological properties, mechanical properties are of the utmost importance. They include the elasto-plastic behavior, fully described by the stress-strain curve (hence by the Young's modulus E, the Poisson's coefficient ν, the yield stress Y, and the ultimate tensile stress UTS), the creep and relaxation behavior, the fatigue behavior, hardness, etc.

The assessment of mechanical properties for the bulk material is necessary to design components. However, when considering surface interactions, they are equally relevant because they influence several phenomena as tribological performances, e.g., wear, and crack's onset and propagation. Thus, it is core to control and measure them. However, conventional tests, e.g., tensile test for evaluating the stress-strain curve, creep test, conventional hardness test, i.e., Brinell, Rockwell, Vickers tests, cannot be exploited to characterize surface properties. In fact, they operate on larger scales, i.e., millimeters or more. Moreover, conventional tests require ad-hoc shaped specimens, e.g., dog-bone samples for the tensile test. This requirement limits their application on and representativeness of final components for challenging applications, as free-form components [287], biomedical implants, or newborn bone tissues on implants [288–290]. These limitations hamper their application to characterize surface phenomena, thin- and nano-films, and nanostructures, these being of the utmost relevance in contemporary manufacturing. Therefore, industry and academia have developed alternative methods to cope with these challenges.

Sonic resonance method, also known as frequency resonance method, has been developed since the 1960s to couple resonance frequencies of materials of known geometry and density to elastic properties, i.e., E, G and ν [291,292]. Today, it is exploited to characterize these properties by a non-destructive procedure and has been further developed to cope with damping properties.

Recently, nano-tensile and nano-compression tests have been developed to scale the conventional test at nanoscales. However, the former are mostly conceived for tensile properties of free-standing thin films, and their major criticality is the alignment and grip of samples to guarantee uniaxial loading [52]. The latter exploits the fabrication and subsequent testing of micro- and nano-pillars of materials or directly nanotubes and reinforcement fiber, e.g., carbon nanotubes; these are typically carried out in SEM and focused ion beam (FIB) systems to couple to the mechanical test the microstructural investigation [52,293].

A large set of complex characterizations, ranging from mechanical to microstructural, can be achieved by depth-sensing indentation techniques, also known as nanoindentation or with their standardized name Instrumented Indentation Test (IIT) [117]. Given its great flexibility, it will be the focus of this chapter and will be introduced more diffusely and discussed thoroughly in the following section.

Coatings characterization nowadays see the diffused employment of scratch test and nano tribological test that can be performed both by nanoindentation platforms or AFM. Scratch test aims to provide quantitative outputs to the outcome of traditional tests, such as peeling or scrape adhesion test. Scratch test was conceived in the late 1980s [294] and, amongst the other results, quantifies the critical load at which the coating fails, also identifying the type of failure. Additionally, it can provide information about viscoelastic properties of the coating, fracture toughness characterization, and estimates of friction coefficients [295,296].

However, mechanical characterization alone may not suffice; in fact, mechanical properties depend on the microstructure. Therefore, often, surface mechanical characterizations are complemented by microstructural and chemical composition characterization. Typically, SEM, TEM, EDX are employed; in the most recent years, an innovative technique has been proposed to allow faster, cheaper, and non-destructive characterization of microstructure. This is the Spatially Resolved Acoustic Resonance (SRAS), which relies on the elastic wave generated by the surface of a tested specimen undergoing an acoustic excitation. SRAS can resolve the microstructure distinguishing between different phases and grain size and orientations [297–299].

3.1 Instrumented Indentation Test[3]

Hardness measurements can be considered semi- or non-destructive tests, allows the final component characterization. Therefore, the lack of ad-hoc shaped specimen need, along with ease and low cost of testing, enabled these characterization procedures to find application in several industrial fields. Hardness is defined as a material's capability to resist indentation up to the onset of permanent deformation or cracking, respectively, for plastic or fragile materials. A loading and unloading cycle is performed on the sample by means of an indenter at a certain maximum load; when the load has been completely removed, a residual indentation will be present, and its surface can be related to the material hardness, which can be computed as the ratio between the maximum test load and the residual indentation area.

Brinell first introduced hardness test in 1900. Later, alternatives, such as Rockwell (1922), Vickers (1935), Knoop (1939), and Martens (2000) hardness were developed, featuring different indenter shapes and procedures to characterize the material at low loads, down to micro-scale [300,301]. Hardness measurements find technological and metallurgical application because, in addition to tribological properties, they enable the estimation of the relationship between measured quantities and material characteristics, such as yield strength, elastic modulus, creep, and resilience [300].

Since the late 1980s, miniaturization and surface technologies became prominent in industry and academia, the need for characterizing smaller, i.e., nano, scale arose. However, conventional hardness scales based on optical methods to determine residual indentation area proved to be either non-effective due to limited lateral resolution or overly time consuming [117]. This promoted the development of so-called depth-sensing indentation. Amongst them, Instrumented Indentation Test (IIT) can be found. IIT was early developed in the mid-'70s in the former Soviet Union [117,302], even though, because of contingencies, it was not until the late '80s and early '90s, thanks to the works of Doerner and Nix [303] and Oliver and Pharr [304], it was capable to arose actual interest in the research and industrial community.

IIT is one of the most appealing mechanical characterization techniques. It consists of a semi-destructive test, which requires limited sample preparation and can be performed on the final product. It allows to achieve a thorough multiscale mechanical characterization, i.e., ranging from grain to bulk properties, in terms of Young's modulus, hardness, creep, relaxation, and stress-strain behavior [117]. Nowadays, nano-indentation is exploited to optimize manufacturing processes by characterizing related products. It finds applications in characterizing

[3] Part of this section was also previously published in: Maculotti G, Genta G, Lorusso M, Pavese M, Ugues D, Galetto M (2019) Instrumented Indentation Test: Contact Stiffness Evaluation in the Nano-range *Nanomanufacturing and Metrology*, 2:16-25 and in Galetto M, Genta G, Maculotti G (2020) Single-step calibration method for nano indentation testing machines *CIRP Annals*, 69:429-432.

microstructures by quantitatively distinguishing different phases [305] and precipitates [306], and estimating the characteristic dimension of the microstructure for both mono-[307,308] and poly-crystalline materials [309]. IIT is applied to multi-layer materials to assess the effective thickness and mechanical properties, decoupling the coating and substrates' contribution [310,311]. It is capable of estimating residual stresses [312], characterizing micro- and nano-structures, e.g., MEMS and NEMS [313], also in terms of fracture toughness [314]. Moreover, with proper modifications, it is capable of estimating the stress-strain curve [315], identifying microstructural change under the load application [316], and characterizing damping properties, i.e., dynamic elastic modulus, of materials [317,318].

Considering the broad characterization capabilities and its limited destructiveness, IIT seems suitable for online quality controls and rapid set-up of manufacturing processes and was standardized by the ISO 14577, latest updated in 2015. The standard covers four parts: testing procedure [319], calibration of testing machines [320], calibration of reference blocks [321], and coating testing [322]. The latter is the latest update results and is the outcome of the European project INDICOAT [323]. Moreover, the ISO published in 2008 a technical report, ISO 29381:2008 [324], to outline methods that can be adopted for estimating true stress-strain curves from instrumented indentation testing.

The base technique will be presented in the following, first highlighting main influence factors and criticalities, and then outlying main research perspectives and challenges for applications.

3.1.1 Measurement method

IIT consists of performing an indentation on a sample by applying a loading-holding-unloading cycle. The applied force, *F*, and the related displacement of the indenter in the material, *h*, are measured during the cycle. The material's characterization is then achieved by analyzing the indentation curve (IC), i.e., the *F(h)* curve, see Figure 44.

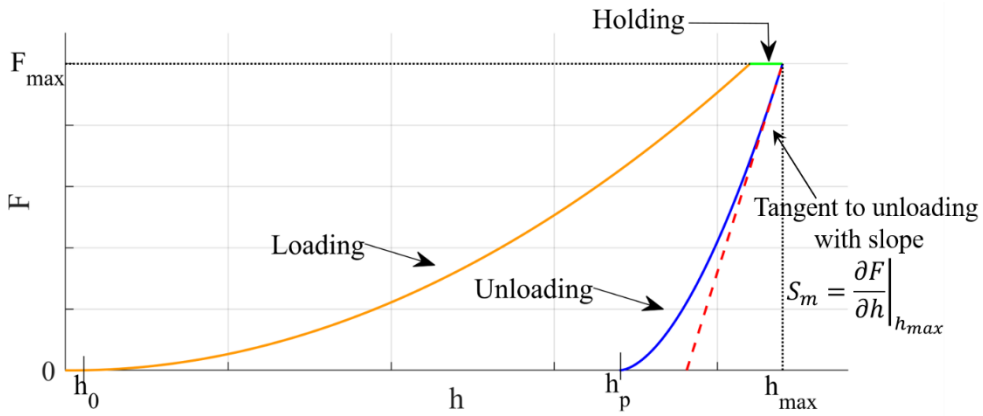

Figure 44 Example of IC: loading from first contact h_0, holding at maximum load F_{max} for creep compensation, unloading from maximum penetration h_{max} and the residual indentation depth h_p.

The measurement of h during the whole test allows resolving hardness, for whom IIT was originally conceived, and other mechanical properties at nano-scales, where optical resolution hampers the application of traditional methods [117,304]. The synchronous measurement of F, and resulting h, is usually obtained by a high-accuracy three-plate capacitive transducer [117,304]; see, as reference, the typical scheme of an indentation platform in Figure 45.

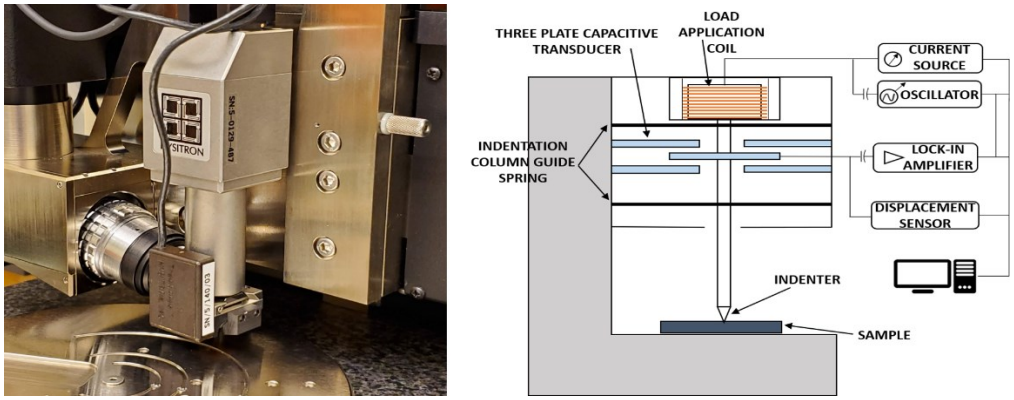

Figure 45 A commercial indentation platform (Hysitron TriboScope) detail of the indentation head and scheme.

Depending on the electronic circuit input, the cycle can be performed in force or displacement control. With reference to Figure 46 and a force-controlled cycle, the two fixed (drive) plates (violet and blue) are the electrodes driven by two AC voltage signals with the same amplitude and a phase shift of 180°. This design makes zero the electric field potential at the mid (floating) plate (red), which is connected to springs (green), for a mechanical guide, and to the output electrode. Force is applied electrostatically by a DC voltage bias at the lower plate. The three-plate design generates a linear electric field voltage. Because the input impedance is significantly larger than the output's, the floating electrode electric potential is the same as the electric field at its location. Thus, by continuously recording the input voltages, e.g., both the AC and the DC, at the drive plates and the resulting output voltage at the floating plate, its resulting displacement can be retrieved by the known, by design, electric field. This design aims to provide high sensitivity, a large dynamic range, a linear output signal, and small sensitivity to vibration by means of a low mass of the transducer mid-plate.

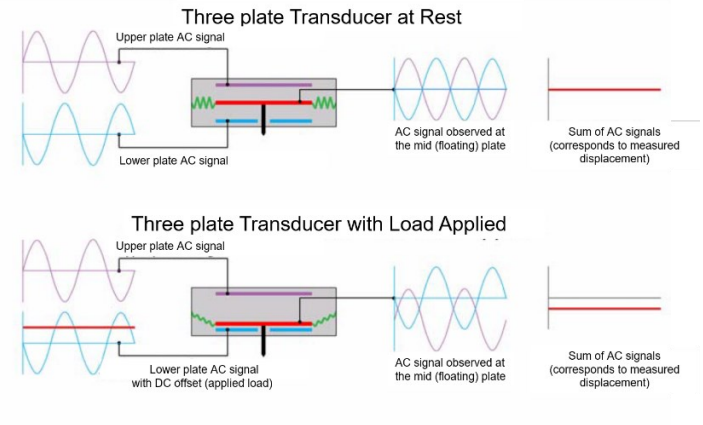

Figure 46 Three-plate transduce actuation diagram. Courtesy of Hysitron Inc.

IIT is classified, according to ISO 14577-1:2014 [319] based on the force range and indentation depth as summarized in Table 15:

Table 15 IIT range classification.

IIT range	**Specification**
Macro range	$2\ \text{N} \leq F \leq 30\ \text{N}$
Micro range	$F < 2\ \text{N}$, $h > 0.2\ \mu\text{m}$
Nano range	$h \leq 0.2\ \mu\text{m}$

Amongst the several possible characterization outputs, the indentation hardness, H_{IT}, and the indentation modulus, E_{IT}, i.e., an estimate of the Young modulus E of the material, are the most commonly reported. They are defined in Eq.(3.1) [319]:

$$H_{IT} = \frac{F_{max}}{A_p(h_{c,max})} \tag{3.1.1}$$

$$E_{IT} = \frac{1-\nu_s^2}{\frac{2\sqrt{A_p(h_{c,max})}}{S\sqrt{\pi}} - \frac{1-\nu_i^2}{E_i}} \tag{3.1.2},$$

where, ν_i and ν_s respectively are the Poisson's modulus of the indenter and tested material, E_i is the indenter Young's modulus, S is the contact stiffness, i.e., the sample stiffness, and A_p is the projection, on the sample surface, of contact area between the indenter and the specimen.

S can be computed by modeling the indenter-sample system as a couple of ideal springs representing the testing machine and the sample, respectively, with a compliance C_f and $1/S$ [117,325]. The system's total compliance,

$$C_{tot} = C_f + \frac{1}{S} \tag{3.2.1}$$

$$S_m = \frac{1}{C_{tot}} = \frac{\partial F}{\partial h}\Big|_{h_{max}} \tag{3.2.1}$$

is obtained as the reciprocal of the measured total stiffness, S_m, which is the slope of the tangent to the unloading curve at its onset (see Figure 44), and can be evaluated according to standard methods [319].

The measurement of h during the whole test allows expressing A_p as a function of the corrected displacement h_c. Literature requires to correct h, as per Eq.(3.3), to account for the zero error (h_0) and the elastic deformations respectively of the indentation testing machine ($C_f F$) and of the sample surface ($\varepsilon\left(C_{tot} - C_f\right)F$, where ε is a shape factor depending on the indenter type, e.g., for Berkovich indenter, it is 0.75) [319,325].

$$h_c = h - h_0 - \left[C_f + \varepsilon\left(C_{tot} - C_f\right)\right]F \tag{3.3}$$

The functional form of A_p depends on indenter geometry. In the most typical case of a modified Berkovich indenter, i.e., a tetrahedron with a dihedral angle of 130.56° (see Figure 47), or a Vickers indenter, square-base straight pyramid with the same dihedral angle, it is $A_p(h_c) = 24.5h_c^2$ [319]. Berkovich indenters are preferred for nanoindentation because having only three faces better determines the vertex and reduces the tip offset; Vickers indenters are equally employed for micro- and macro-range.

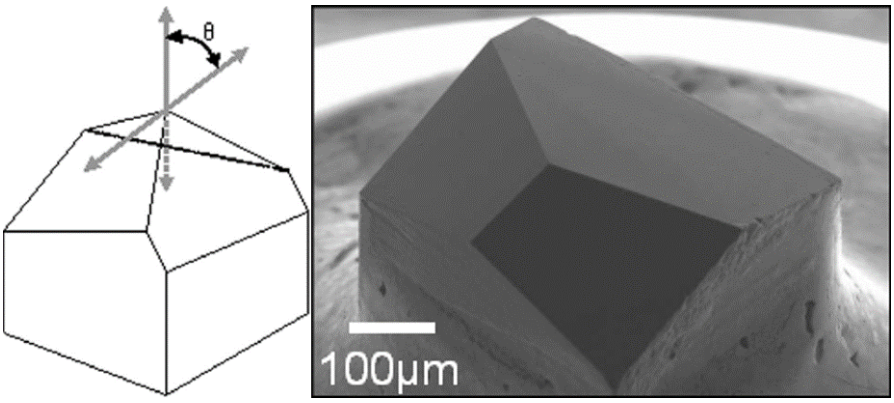

Figure 47 Left: Berkovich indenter geometry (θ is half tip dihedral angle). Right: image of Berkovich indenter obtained with a Scanning Electron Microscope (SEM)

However, due to wear and deviation from ideal geometry, e.g., tip blunting and offset, a more general form can be written as in Eq.(3.4) [320,326,327]:

$$A_p(h_c) = \sum_{n=0}^{8} a_{2^{1-n}}(h_c)^{2^{1-n}} \tag{3.4}.$$

Furthermore, A_p is related to the reduced Young's modulus, E_r, according to the following equation [319]:

$$A_p(h_{c,max}) = \frac{\pi S^2}{4E_r^2} = \frac{\pi}{4E_r^2\left(C_{tot} - C_f\right)^2} \quad (3.5.1)$$

$$1/E_r = \frac{1-\nu_s^2}{E_s} + \frac{1-\nu_i^2}{E_i} \quad (3.5.2).$$

Further mechanical characterization, according to the standard, can be obtained. The indentation creep, C_{IT}, estimates the material creep by considering the indentation depth change during the holding phase relative to the initial depth, as in Eq.(3.6.1). If a displacement-controlled cycle is performed instead, the force variation during the hold phase measures the indentation relaxation R_{IT}, i.e., estimates the material relaxation behavior, as in Eq.(3.6.2):

$$C_{IT} = \frac{h_2 - h_1}{h_1} \times 100 \quad (3.6.1)$$

$$R_{IT} = \frac{F_2 - F_1}{F_1} \times 100 \quad (3.6.2).$$

3.1.2 Main influence factors

This section will address an overview of the most critical factors that may influence an instrumented indentation test's results.

Test piece topography

Because IIT ultimately relies upon identifying the projected contact surface, it is core to guarantee contact condition as much as possible resembling theoretical requirements, i.e., surface orthogonal to the loading direction.

Therefore, samples according to the standard must be flat or should guarantee this condition in the indentation neighborhood. When performing nanoindentations, the surface roughness may introduce deviations from this condition. The standard requires, to guarantee adequate precision, accuracy and avoid biased results, to achieve maximum indentation depth in excess of twenty times of R_a. Thus, samples are required to be lapped and polished. However, sometimes this may not suffice; therefore, literature proposes several models to cater for surface roughness and correct measurement results accordingly [328–331]. The standard does not include or recommend their adoption as they seem to lack in generality and robustness, as they are mostly based on profile roughness parameters, e.g., R_a.

Edge effects

The indentation procedure generates plastic phenomena in the material within a region in the indenter application's neighborhood. The plastic flow of the material coupled with the physical constraint set by the indenter's presence itself generates deformations at the edge of the indentation. Empirically, the material can tend to pile up or sink in at the edges, resulting in severe discrepancies from the theoretical shape of the indentation, see Figure 48. Cheng and Cheng [332] and Oliver and Pharr [327] demonstrated, respectively for Vickers and Berkovich indenters and for spherical indenters, that these phenomena depend on the strain-hardening capability of the tested materials; so that low strain-hardening materials tend to pile up against the indenter, whilst high strain-hardening materials behave oppositely.

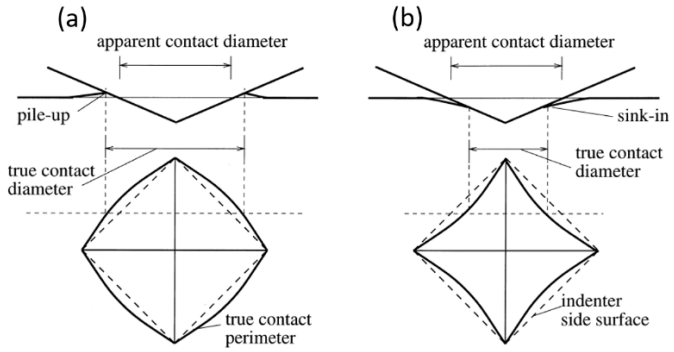

Figure 48 (a) pile-up and (b) sink-in effect on indenter shape (adapted from [333]).

Literature [327,332–334] reports different methods, although not included in the standard, which shall be catered for when the material under test is known to promote severe edge effect. Thus, reference blocks are out of materials, such as fused silica, tungsten, sapphire, which are not affected by these phenomena, to avoid edge effect altogether.

Moreover, in everyday practice, the literature also suggests characterizing properties independent from the absolute value of the corrected contact depth that may be affected by edge effects. The adoption of the F/S^2 ratio is reported by Oliver and Pharr [327]. Thanks to its independence from the evaluation of the indenter area function, as is shown in Eq.(3.7), obtained recombining Eq.(3.1) and Eq.(3.5):

$$\frac{F}{S^2} = \frac{4}{\pi}\frac{H_{IT}}{E_r^2} \qquad (3.7).$$

Indentation size effect

The plastic flow of material is due to both strain and strain gradient, as the material flow is constrained and hence dependent on length scales, i.e., the available geometric dimension [335]. Therefore, flow stress can be explained by

the motion of statistically stored dislocations, e.g., dislocation motion due to homogeneous strain, and geometrically necessary dislocations, i.e., dislocations created by strain gradient or curvature of crystalline lattice due to the length scales [335].

These phenomena are responsible for the so-called indentation size effect (ISE), i.e., the apparent dependence according to inverse proportionality, of the hardness on the penetration depth. Nix and Gao [307] proposed a model for the correction of this phenomenon, which relies on identifying a critical length scale below whom ISE occurs. Later, exploiting this framework, Hou and Jennet developed models to estimate the characteristic dimension of the microstructure for both mono-[307,308] and poly-crystalline materials [309].

Reference block materials are preferred to be amorphous, e.g., fused silica, to avoid ISE.

Evaluation of measured contact stiffness

The measured contact stiffness, S_m, is defined, see Eq.(3.2) as the slope of the tangent to the force-displacement unloading curve at the onset of the unloading. Its evaluation is critical because it resulted to be often one of the major sources of uncertainty for the mechanical characterization based on instrumented indentation test [325,336] at very low loads, see Figure 49. Moreover, it has a further indirect contribution from the calibration of the testing equipment, as it intervenes in evaluating the frame compliance, C_f, which is consequently another main contributor to measurement uncertainty [337] and is a parameter that has to be calibrated [320].

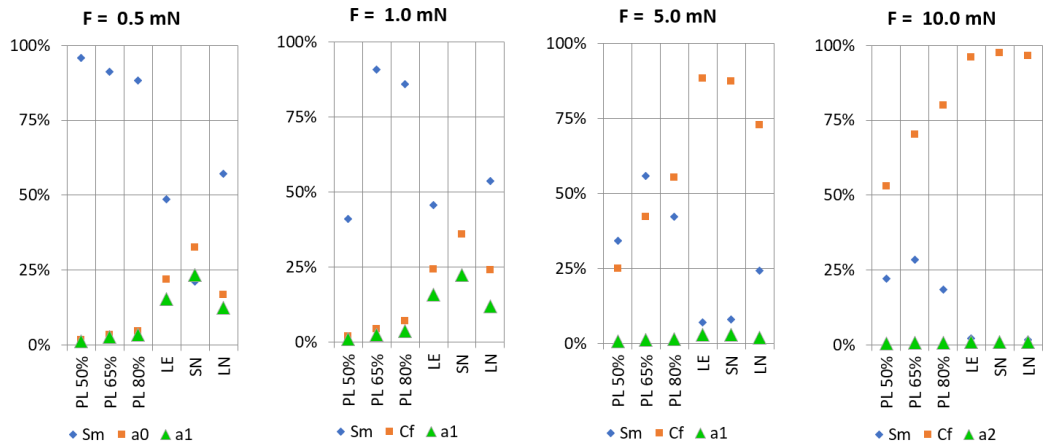

Figure 49 Relative contribution of main influence factor to the U(E_{IT}) at different loads: S_m dominates low load, C_f and estimation of indenter area shape function parameters higher loads (adapted from [336]).

To evaluate the S_m, literature and standards require the unloading curve to be fitted according to a pre-defined mathematical model, which has to be differentiated and computed in the point corresponding to the onset of unloading. Four models have been proposed, which are the linear extrapolation (LE) [303],

the power-law method (PL) [304,327], the sinus (SN) [325] and the logarithmic (LN) [336] model.

The models have been defined catering for different solutions of the Boussinesq's problem, e.g., solution of the stress-displacement field generated by a concentrated load, applied orthogonally to the surface of an elastic half-space, which models the indentation. In fact, indentation with punches of arbitrary geometry can be reduced to Boussinesq's problem [338].

LE has been defined by Doerner and Nix [303] considering that an indentation, at least in the neighborhood of unloading onset, can be well approximated by the Hertzian solution, i.e., flat punch geometry. This approximation implies that the contact area is constant and that a linear function can model the unloading curve.

However, Oliver and Pharr [304,327] observed that the unloading curve is far from being linear; therefore, according to general Sneddon's solution of Boussinesq's problem [338],

$$F = \beta h^m \tag{3.8.1},$$

they suggested adopting a non-linear fitting with a power-law (PL) relationship,

$$F = B\left(h - h_p\right)^m \tag{3.8.2},$$

where β and B are material parameters, h_p is the residual indentation depth (Figure 44), and m depends on indenter geometry (e.g., it is equal to two in the case of conical and pyramidal indenter). However, both LE and PL present shortcomings. In fact, the former tends to evaluate the secant rather than the derivative of the unloading curve, which results in underestimating the contact stiffness, despite being associated with small measurement uncertainty. On the other hand, the latter, due to the presence of the residual indentation depth parameter, whose evaluation is highly uncertain, provides results that are unsatisfactory from the measurement uncertainty perspective.

Therefore, improvements in LE methods have been recently defined to cater for experimental curvature [325,336]. They require the unloading curve to be non-linearly fitted according to sinus or logarithmic models,

$$F = F_{max} - \frac{1}{k_Y}\sin\left(k_X(h_{max} - h)\right) \tag{3.9.1}$$

$$F = F_{max} - \frac{1}{k_Y}\ln\left(k_X(h_{max} - h)\right) \tag{3.9.2}$$

where h_{max} is the maximum indentation depth (Figure 44), and k_X and k_Y are fitting parameters, which account for sample material and indenter geometry.

Indenter area function

The analytical dependence of the projected contact area on the penetration depth is the key of depth-sensing techniques, ultimately enabling to overcome limits set by lateral resolution of optical instruments necessary in conventional hardness measurements. Therefore, the determination of the indenter area function is of primary importance.

As formerly discussed and according to Oliver and Pharr [327], polynomial models, as in Eq.(3.4), that describe the deviation from ideal geometry of the indenter, can be used for different indenter geometries, depending on the considered terms. In fact, for Vickers of Berkovich indenters ideal case is represented by $n \in \{0\}$, i.e., $a_2 h_c^2$; for paraboloid of revolution the sole $n \in \{1\}$, i.e., $a_1 h_c$; whilst for spherical indenters, $n \in \{0,1\}$ should be used, with appropriate choices of the constant terms. For macro-range, negligible errors are introduced by considering the ideal indenter shape. When operating at micro- and nano-range, simple deviation from ideality can be effectively described for cone or pyramids by the use of the first three terms, $n \in \{0,1,2\}$, i.e., $a_2 h_c^2 + a_1 h_c + a_{1/2} h_c^{1/2}$, or by setting a further approximation to cater for possible small flat regions at the tip, i.e., $a_2 h_c^2 + a_1 h_c + a_0$ [339].

The complete model with nine terms is rarely adopted in literature for its difficult handling; the standard allows the adoption of a spline function, which provides best calibration performances but does not allow simple management of uncertainty evaluation [336].

For nanoindentations, the choice of the indenter area function model is definitively not trivial. However, the literature does not report the metrological performance assessment of the model choice on the characterization results to the writer's best knowledge.

Differently, Barbato et al. [336] showed that the calibration of indenter area function parameters is critical as the area function parameters are one of the main contributors to measurement uncertainty of the mechanical characterization, as summarised in Figure 49.

Indentation curve parameters

The appropriate choice of the indentation curve parameters, i.e., loading pro (linear, quadratic, etc.), duration of loading, holding, and unloading phase, is of the utmost relevance. In fact, these impact the stress flow and affect the mechanical characterization. The standard suggests adopting linear loading and unloading profiles in quasi-static conditions, and a typical indication is 60 s per phase.

The holding phase is critical as it has been added to compensate for creep phenomena. Too short holding may result in creep that can be highlighted in the IC by the presence of a characteristic nose at the onset of the unloading, which ultimately hinders the contact stiffness evaluation. The selection of holding time is

strictly dependent on the tested material, and some practical indications can be found in [340].

First contact point identification

To provide accurate and unbiased mechanical characterization, the evaluation of the first contact point, h_0, is fundamental. The identification is critical because it is the first contact point with a sensed contact stiffness that is, consequently, infinite, and with the possibility of elastic rebound and instability if the approach speed is too high. According to the standard, two methods are available: either by a quadratic linear least-square fitting of the first 10% of the loading curve or by identifying the first significant increase in the sensed contact stiffness. Alternatively, Barbato et al. [341] proposed a segmented regression, which proved to yield better reproducibility of the detection [342].

3.1.3 Non-standard characterizations

Although the instrumented indentation test has been developed for almost half a century, several improvements are currently being proposed and significantly extend IIT's characterization capabilities.

True stress-strain curve determination

Historically, since Brinell test introduction, hardness tests aimed to evaluate tensile properties through a non-destructive test [343]. The adoption of pyramidal indenters generates an auto-similar state of stress, i.e., a stress field constant and independent from the penetration depth. In fact, for ideal pyramidal indenters, according to Sneddon's solution of Boussinesq's problem [338], the loading force is quadratic with respect to the penetration depth, and the projected contact is also a quadratic function of h. Thus, constant stress results. This relationship does not hold anymore if a spherical indenter applies the load. This allows testing several stress states depending on the penetration depth. Literature has developed approaches that enable IIT to estimate true stress-strain curve. They need the availability of stress and strain representative models, which requires the prior knowledge of several parameters dependent on material, and a correct estimation of $A_p(h_c)$ [344], e.g., unbiased from edge effects. Provided those caveats, fitting (according to the material's constitutive equation) several IC curves obtained indenting at different maximum loads, yields the stress-strain curve [345–347]. However, true strain models' determination is complex and, currently, the object of research [348–350]. Other numerical methods are available based on inverse finite element analysis or neural networks, though with greater computation capability and different criticalities. A major issue related to inverse FEA is determining the relevant scales of the problem and may or may not require prior knowledge of some material parameters [351,352]. The last method is the most demanding, as it requires specific knowledge to train the network based on a

consistent amount of physical and computer experiments, i.e., FEM, to make the prediction robust to experimental error [324,353].

Dynamic indentation

Dynamic indentation, also known as Continuous Measurement of Contact stiffness (CMC) or Sinus Mode, allows the measurement of contact stiffness and hence mechanical properties during the whole test. It requires performing multiple indentation tests at the same location with an increasing maximum load and superimposing to the loading profile a sinusoidal oscillation at a relatively high frequency, e.g., 60 Hz. The approach, proposed by Oliver and Pharr [327], requires calibrating the indentation testing platform's dynamic properties and, once performed the test, decoupling by dynamic analysis the tested material's harmonic response from the platform's characteristic response. Dynamic indentation allows characterizing materials in the orthogonal direction with respect to the tested surface, thus avoiding sectioning the sample, to test the core of the material, which is relevant to distinguish residual stress affected zones after machining or different layers in multilayer coating [310,354–356]

High-speed indentation

Indentation platforms typically feature a motorized stage that allows performing grids of indentations that can be exploited to map the mechanical properties over the investigated area. Costantinides et al. [357] and Randall et al. [358] showed that it is possible, by deconvoluting the statistical distribution, to distinguish different phases and their interfaces through nanoindentation characterization.

However, performing indentation matrixes is time-consuming, and the industry requires high-throughput measurements. Therefore, high-speed nanoindentation systems are currently being developed [359–362]. These allow performing a complete indentation in about 1 s. The characterization's criticality is the correction of the dynamic phenomena, i.e., damping of the indentation head, the indenter's inertia, and dynamic contact between the indenter and the specimen. Although this characterization method provides extremely appealing capabilities, is broadly sponsored by platform manufacturers, and is used in academia and industry, it still requires a thorough metrological characterization and methods for its calibration to guarantee its traceability.

Electrical contact resistance method

Materials are known to undergo phase transformation under high stresses, e.g., in some machining process setups. Identifying the limit stress and the study of the phase change paths is of the utmost importance to optimize the manufacturing processes. For example, in the case of non-metallic materials, silicon proved to experience a phase change under the application of high pressures, tens of gigapascals, resulting in substantial modification of its

mechanical and electrical properties, result of great interest for electronic industry. Phase changes can be induced by nanoindentation. Moreover, literature [363–367] has shown that performing indentations on a conductive material by conductive diamond indenters can support these investigations. In fact, electrical current and voltage through the system can be measured by these conductive elements, in addition to force and indenter displacement. The electrical quantities analysis supports the identification of phase change in the materials, aiding the study of the conditions that trigger these changes.

More recently, the measurement of electrical quantities has been exploited to create redundancies in the measuring system to improve the contact area's estimation [368–370]. This latter solution is little investigated in literature and may also provide definitive advantages from the metrological perspective.

3.2 Metrology advancements for Instrumented Indentation Test

Instrumented indentation test offers a wide range of characterization capabilities, with few limitations and sample preparation requirements. Several equipment manufacturers are present worldwide, e.g., Anton-Paar (A), Hysitron (USA), MicroMaterials (UK), Brucker (D), and its market in the sole Europe is estimated to be around 13 M€.

However, in order to make this appealing technique exploitable for quality controls, traceability is necessary. Results must be provided to the users with confidence that they are repeatable and comparable between different platforms and plants.

The first step towards this is international inter-laboratory comparison. Since the introduction of the technique, two inter-laboratory comparisons were sponsored by the CIRP. The first between 1993 and 1997 [371] and the latter, after the publication of the ISO standard, between 2005 and 2009 [353]. This showed that despite the standard's introduction, which also defined calibration methods, significant differences in both accuracy and precision amongst the participants were shown in determining E_{IT} and H_{IT}. Results showed a reproducibility as high as 30% at low forces, i.e., 10 mN, and 15% at 1 mN on H_{IT} and of 15% on E_{IT}, with expanded uncertainties exceeding 30% at lower loads, in some cases.

Therefore, before addressing further developments, it is necessary to improve the standard technique's metrological performances.

This section will propose methods to support the development of IIT in this sense by investigating the main contributors to measurements uncertainty, i.e., the measured contact stiffness S_m, and the calibration of frame compliance C_f and of the parameters of the indenter area shape function.

3.2.1 Direct evaluation of contact stiffness[4]

The measured contact stiffness S_m is as the slope of the tangent to the force-displacement unloading curve at the onset of the unloading, as in Eq.(3.2), and according to Barbato et al. [336] is one of the main influence factors to the measurement uncertainty of the mechanical characterization from IIT.

As reported in the former section, the literature reports several methods to estimate S_m. However, when coming at a throughout comparison, methods are affected by bias (LE and SN) or high uncertainty (PL) or show little agreement with each other (LN is particularly critical) [336], as in Figure 50. These shortcomings add to the formerly mentioned limitations in representing the unloading curve, i.e., LE evaluates the secant and not the tangent to the unloading, and PL depends on the portion of the unloading curve.

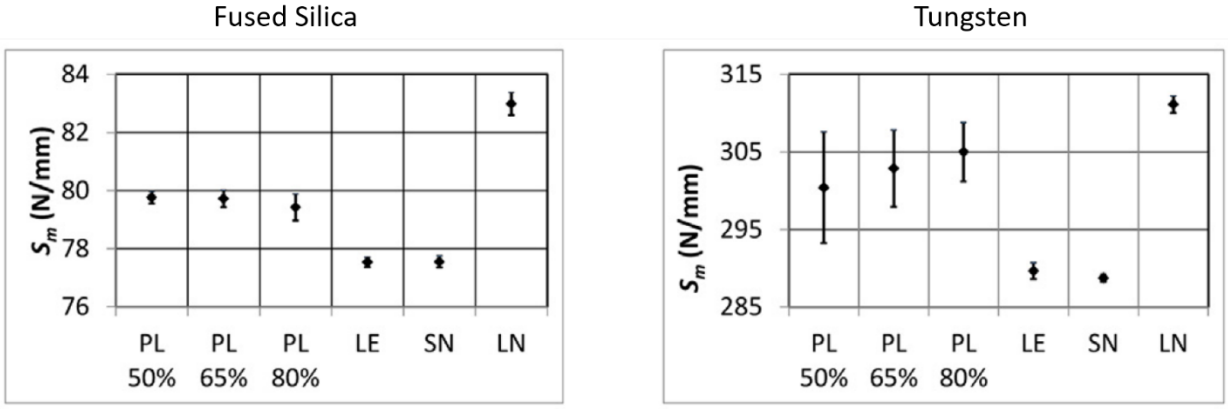

Figure 50 Performances of literature methods in estimating Sm of fused silica and tungsten at 10 mN (adapted from [336]). PL is evaluated on different length portion of the unloading curve.

Therefore, when the S_m evaluation models' compatibility is addressed, critical conditions are highlighted that prevent from concluding on an absolute preference of a model with respect to the others [336]. In fact, independently from the adopted mathematical model, the literature's procedures present an inherent criticality due to the parameter to be computed. S_m evaluation requires the interpolated model to be differentiated, considering its definition. However, even though regression minimizes the sum of squared residuals, it does not guarantee any derivative properties. Furthermore, literature [336] demonstrated that the fitting operation residuals are characterized by a trend that limits fitting adequacy. Thus, it is suggested to consider direct derivative evaluation to provide a metrological evaluation consistent with the parameter definition.

[4]Part of this section was also previously published in: Genta G, Maculotti G, Barbato G, Levi R, Galetto M (2018) Effect of contact stiffness and machine calibration in nano-indentation testing *Procedia CIRP*, 78:208-212 and in Maculotti G, Genta G, Lorusso M, Ugues D, Galetto M (2019) Instrumented Indentation Test: Contact Stiffness Evaluation in the Nano-range *Nanomanufacturing and Metrology*, 2:16-25.

Methodology

Consequently, the derivative of the unloading force-displacement curve, *F(h)*, should be evaluated at the start of unloading. However, this is not a trivial issue because of the derivative computation's sensitivity to spikes and the measurement noise of the signal to be differentiated. Literature has faced this issue and introduced several solutions that have been later developed to solve differential equations [372]. Algorithms are generally based on the requirement for smoothing local disturbances, which may be due to measurement noise. This is usually achieved by average weighting incremental differences evaluated on different interval width in the studied point neighborhood.

In this dissertation, the algorithm proposed by Fornberg [373] has been adopted. It computes the derivative of a signal, *f'*, as a function of the signal itself, *f*, as stated in Eq.(3.10) by means of weights calculation.

$$\left.\frac{d^M f}{d^M x}\right|_{x_0} \approx \sum_{\nu=0}^{N} \delta_{N,\nu}^{M} f_{(\alpha_\nu)} \tag{3.10.1}$$

$$\delta_{n,\nu}^{m} = \frac{(\alpha_n - x_0)\delta_{n-1,\nu}^{m} - \delta_{n-1,\nu}^{m-1}}{\alpha_n - \alpha_\nu} \tag{3.10.2}$$

The algorithm requires specifying the derivative order *M*, which in this case has been set to 1, and a precision order *N*, set to 20, in this case. *M* and *N* define the node vector α in which the function is computed. The algorithm computes the weights as a function of *m*, yielding from zero to *M*, and *n*, from *m* to *N*, and α_ν.

However, to reduce measurement uncertainty, a devoted procedure (named DM, derivative method) has been applied. First, to reduce spikes, i.e., outliers, and measurement noise, force and displacement signals have been filtered by a mobile-average filter. Second, to provide reasonable uncertainty, the derivative's trend was evaluated by applying Fornberg algorithm to the filtered signal in a suitably long interval. Finally, S_m has been evaluated by computing, at the onset of unloading, the fitting curve of the derivative trend obtained by non-linear regression with a power-law model, as in Eq.(3.11), with a proper change of reference system set in h_{max} to reduce uncertainty. This choice depends on the fact that, because h_{max} is defined at the intercept between a plateau (the hold phase of the indentation curve) and a power-law curve in a point with derivative different from zero (onset of unloading), it yields to a less uncertain evaluation with respect to h_p, which is instead at the intercept of the *x*-axis and a point with an almost null derivative of the unloading curve [325,336].

$$\frac{\partial F}{\partial h} = \beta m h^{m-1} = \beta m (h_{max} - H)^{m-1} \tag{3.11.1}$$

$$S_m = \frac{\partial F}{\partial h}\Big|_{h_{max}} = \beta m \tag{3.11.2}$$

This procedure is necessary to cope with the low number of available points in the neighborhood of the start of unloading and provide the evaluation with an uncertainty assessment. DM is applied to the unloading curve portion ranging from 98% to 20% of the maximum applied force in line with the standard application of PL [319,374].

Following the approach followed in literature for other models [336], the standard uncertainty of the estimation of S_m based on DM is obtained by propagating uncertainties according to GUM [286], see Eq.(2.18), on the model of Eq.(3.11), exploiting the parameters' estimate standard error of the regression as the standard deviation of the parameters $\beta$and m, and the noise floor of the displacement sensor as standard deviation of the displacement:

$$\boldsymbol{X} = \begin{bmatrix} \beta \\ m \\ h_{max} - h_{max} \end{bmatrix} \tag{3.11.3}$$

$$\boldsymbol{c} = \begin{bmatrix} m \\ \beta \\ \beta m(m-1) \end{bmatrix} \tag{3.11.4}$$

$$\boldsymbol{VCV} = \begin{bmatrix} SE^2(\beta) & 0 & 0 \\ 0 & SE^2(m) & 0 \\ 0 & 0 & u^2(h) \end{bmatrix} \tag{3.11.5}$$

$$u^2(S_m) = m^2 SE^2(\beta) + \beta^2 SE^2(m) + \big(\beta m(m-1)\big)^2 u^2(h) \tag{3.11.6}.$$

However, numerical evaluation of the derivative is severely affected by random measurement errors, making high measurement uncertainty expected.

Therefore, alternative approaches have been investigated to overcome this possible issue. They are based on the robustness of the secant evaluation of the *F(h)* unloading curve. These approaches can be exploited to evaluate the derivative trend to extrapolate the contact stiffness through linear regression, according to Sneddon [338], by considering secant, d_i, at different positions. In particular, two further methodologies have been considered.

The first (named S1, secant 1) evaluates the secant at different positions as the slope of the regression line of a portion, or window, of the unloading curve that yields from the start of unloading to an increasing distance from it, see Figure 51(a).

On the other hand, the second (named S2, secant 2) evaluates the regression line on portions, or window, of the unloading curve of the same width, expressed as a number of considered points, but centered on different locations, see Figure 51(b).

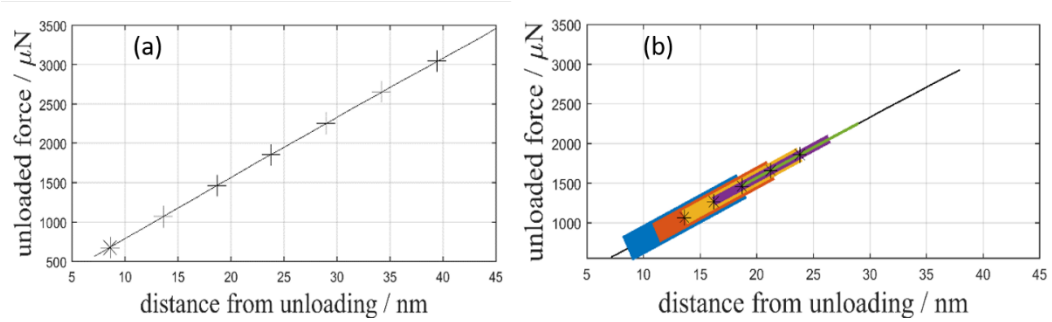

Figure 51 (a) Method S1 applied to unloading indentation curve: * start of windows, + end of windows at different distances from onset of unloading. (b) Method S2 applied to unloading indentation curve: * centre of windows, different colours highlight position of different windows. Reference system has been changed according to methodology proposed for SN and LN. Test performed on fused silica at 10 mN.

Once the secants have been computed, they must be fitted; however, uncertainty associated with secant evaluation at different positions has to be accounted for properly. In fact, the standard deviation of the slope of the regression line, $s(d_i)$, is related to the number of fitted points. Moreover, when considering secant evaluation near unloading onset, greater uncertainty has to be expected due to the noisier signal generated in this transient operating condition of the force-displacement transducers. Therefore, to introduce uncertainty effect in the extrapolation of the derivative trend, linear fitting is applied to a point cloud built as follow: at the different locations at which secants are computed, a set of one hundred points extracted from a normal distribution $N(d_i, s(d_i))$ are considered. The assumption of a normal distribution is supported by the preliminary application of a mobile-average filter to the measured force and displacement signals devoted to eliminating measurement noise and outliers and verifying the absence of significant systematic components affecting the measurements and hence slope.

For both S1 and S2 methods, to be consistent with linear derivative approximation, only the initial part of the unloading indentation curve is considered, by properly choosing the width and position of curve portion, i.e., centering windows from 2.5% to 15% with steps of 2.5%, which are exploited for secant evaluation. Considering the previous discussion about the requirement of a trade-off between accuracy and precision, for S2, a window width of 10% of unloading curve length was considered appropriate. Similarly, trial and error suggested adopting a symmetric window wide ten points per side to apply the mobile-average filter. Positions of the windows for secants evaluations are summarised in Table 16.

S1 and S2 ultimately estimate S_m as the intercept of the evaluated model and estimate its standard uncertainty from the standard error of the intercept estimated by the regression.

Table 16 Window width and center adopted for M2 and M3 expressed with respect to unloading curve length and from start of unloading, respectively.

S1			S2		
i	Window width	Window centre	*i*	Window width	Window centre
1	5%	2.5%			
2	10%	5%	1	10%	5%
3	15%	7.5%	2	10%	7.5%
4	20%	10%	3	10%	10%
5	25%	12.5%	4	10%	12.5%
6	30%	15%	5	10%	15%

Experimental setup

The three methodologies introduced in the previous subsection have been applied to nano-indentations performed on both a reference material, i.e., fused silica (Young's modulus of (73.3±0.6) GPa), and a high-alloyed bearing steel, i.e., Ferrium® C61 (Young's modulus of (205±2) GPa). Indentations were performed at two different load levels, 10 mN and 5 mN. The above mentioned Young's modulus values and the relevant uncertainties were obtained by resonance frequency method. Indentations were performed at the Istituto Italiano di Tecnologia (IIT) and at Oklahoma State University (OSU) with two different testing machines platforms manufactured by Hysitron, i.e., respectively the TriboScope and the Triboindenter TI 950, shown in Figure 45 and Figure 52. These indentation platforms mount a three-plate capacitive force-displacement transducer and are characterized by the metrological characteristics reported in Table 17.

Table 17 Metrological characteristics of a three-plate force-displacement transducer of Hysitron TriboScope and TI 950.

	TI 950	**TriboScope**
Maximum force / mN	10	10
Load resolution / nN	1	1
Load noise floor / nN	100	75
Maximum displacement / µm	5	5
Displacement resolution / nm	0.04	0.006
Displacement noise floor / nm	0.2	0.2

The adoption of two instruments to indent different calibrated specimen of the same standard material is aimed to test the generality of results. Indentation performed on reference material and steel were repeated ten times in order to cater

for reproducibility. Data were processed by authors' implementation in *MATLAB 2018b*.

Figure 52 The Hysitron TI 950 indentation testing platform exploited to perform the indentations.

Results discussion

Comparison of the methodologies that have been already presented in the literature, i.e., SN and LN, or accepted in reference standard, i.e., PL and LE, with the three introduced in this section will be presented in terms of both the measured contact stiffness S_m and indentation modulus E_{IT} evaluation. Moreover, expanded uncertainty, evaluated consistently with GUM [286], as introduced in Section 2.4.2, will be assessed with proper uncertainty propagation to provide results with a metrologically consistent framework.

Because frame compliance requires calibration, which entails evaluating contact stiffness, results will be provided in terms of measured contact stiffness, rather than contact stiffness, to avoid any indirect contribution from the testing equipment's calibration.

First of all, the adequateness of the mobile-average filter has to be investigated. Therefore, normality of the distribution of both force and displacement residuals was investigated by performing a Chi-squared test with a risk of error of first kind (conventionally set to 5%). The test cannot reject the null hypothesis of a normal distribution of the residuals, since both force and displacement residuals appear linear when considering their Normal Probability Plot (NPP), as Figure 53 shows.

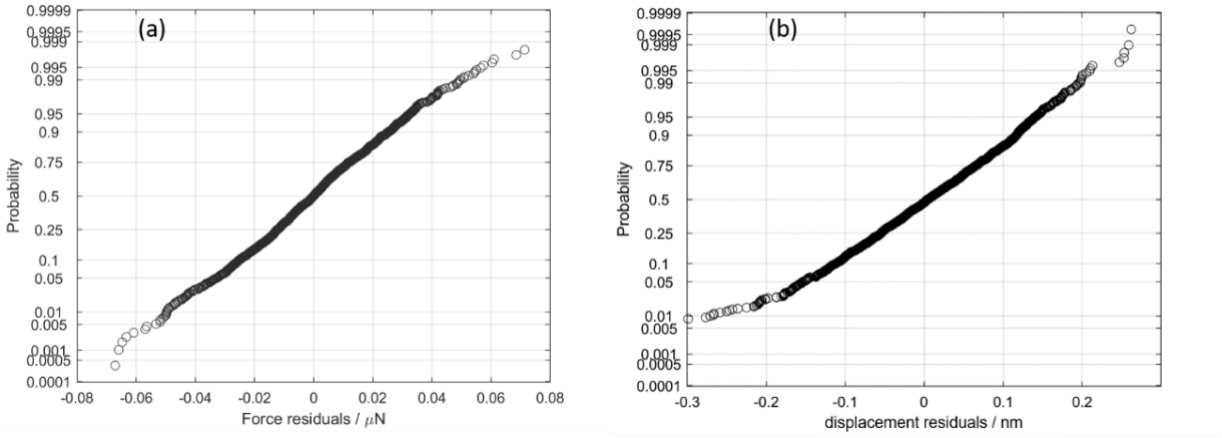

Figure 53 NPP of mobile average filter residuals of (a) force and (b) displacement. Sample indentation performed on fused silica.

Figure 54 and Figure 55 show the results of the application of the three proposed methodologies for the derivative's direct evaluation. Although Sneddon's solution of contact between a flat surface and a conical indenter [338] represents a reliable first approximation for elasto-plastic regime, the power-law regression (purple curve in Figure 54) has been applied to DM. This choice is due to the relevant curvature that can be highlighted in the derivative (blue curve in Figure 54), which hinders from adopting a linear model (orange curve in Figure 54). Fitting with a linear model could be a viable solution considering only the first portion of the curve, i.e., up to 80% F_{max}, to be consistent with Sneddon's theory. However, preliminary studies demonstrated high sensitivity of this approach to local disturbances in the derivative, which led to prefer a power-law model to provide suitable robustness. Furthermore, the adoption of such non-linear fitting is compliant with Oliver and Pharr [327]. In fact, they highlighted that the actual condition of elasto-plastic contact at the onset of unloading introduces deviation from Sneddon's theoretical quadratic dependence of force on displacement, which results in a trend of the curve that lies between the linear and the quadratic.

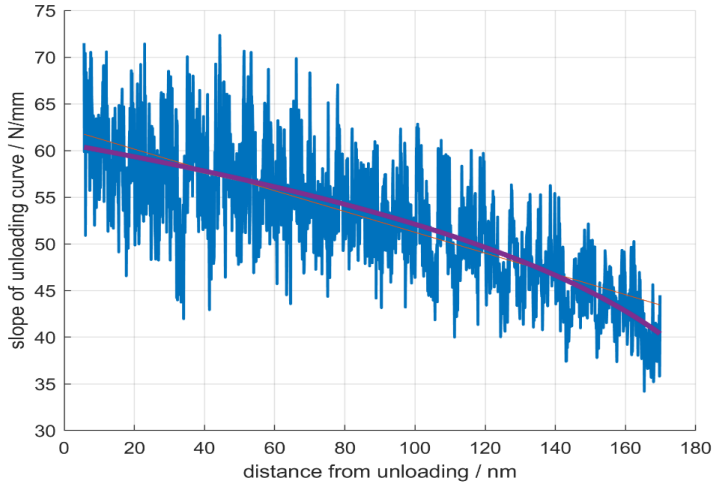

Figure 54 Results of the application of DM method to sample indentation on fused silica at 10 mN. Blue: slope of the unloading curve as a function of distance from onset of unloading. Orange: linear interpolation of the unloading curve slope, notice unsatisfactory fitting. Purple: power-law interpolation of the unloading curve slope.

On the other hand, differently from DM, the linear fitting has been adopted for S1 and S2. Because they consider a shorter portion of unloading, but high sensitivity to local fluctuation is shown, see Figure 55 (a) and Figure 55 (b) respectively, this often results in the inappropriateness of the power-law model.

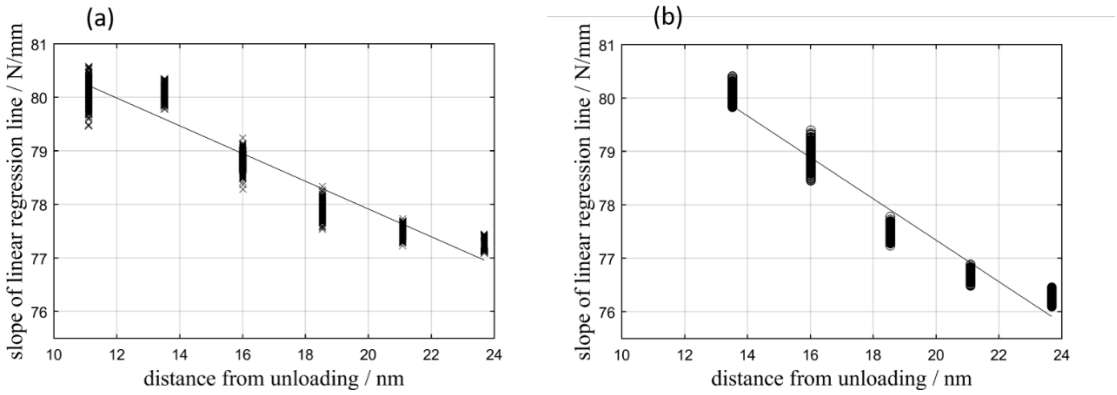

Figure 55 Constructed data set for the interpolation of secants computed with methods (a) S1 and (b) S2. Sample indentation on fused silica at 10 mN. Slope of the unloading curve as a function of distance from onset of unloading is shown.

In the following, results are presented in terms of measured contact stiffness and indentation modulus, respectively in Figure 56 and Figure 57. Error bars represent expanded uncertainty evaluated with a coverage factor $k = 2$.

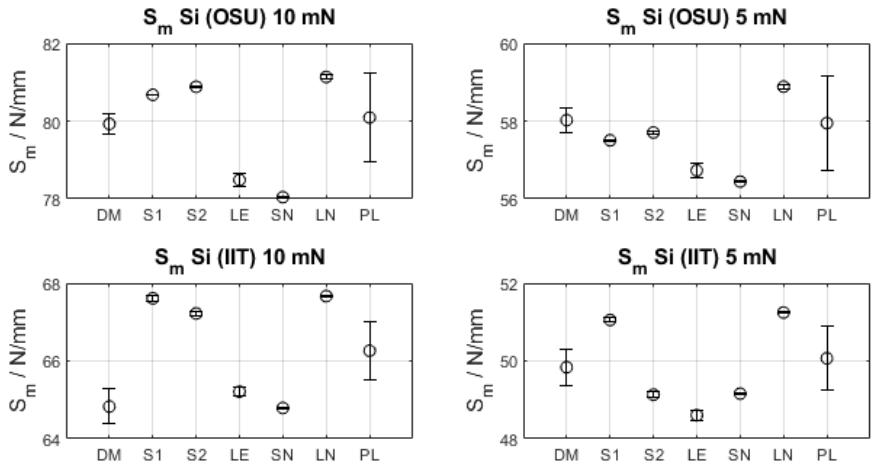

Figure 56 Measured contact stiffness of fused silica indented at 10 mN and 5 mN at the Oklahoma State University (OSU) and at the Istituto Italiano di Tecnologia (IIT).

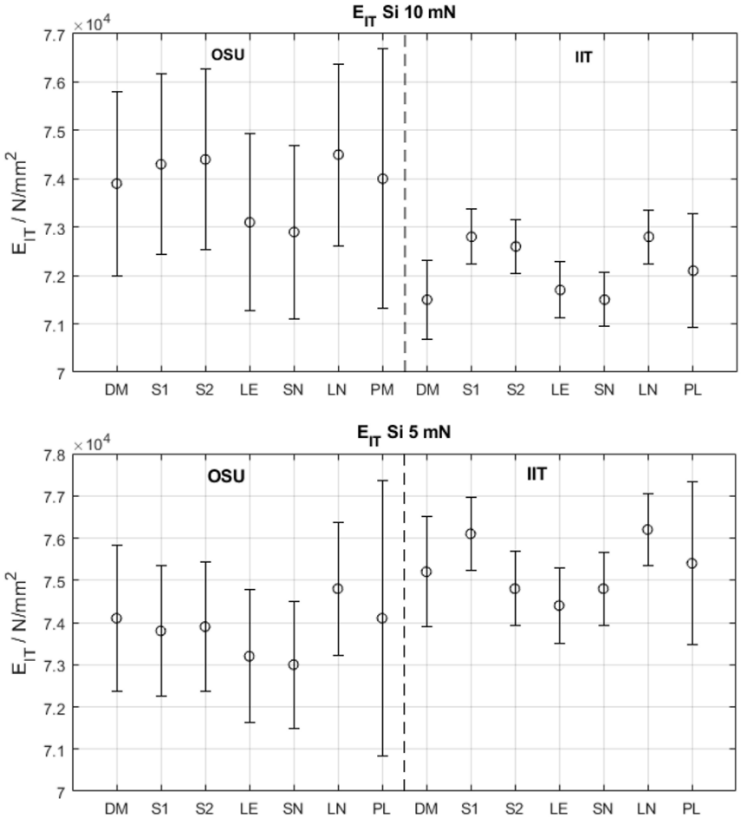

Figure 57 Indentation modulus of fused silica indented at 10 mN and 5 mN Oklahoma State University (OSU) and at the Istituto Italiano di Tecnologia (IIT).

As far as S_m is concerned, LE and SN provide a relative underestimation, consistent with their definition that evaluates the secant rather than the tangent to the unloading curve. On the other hand, S_m assessed by LN is systematically higher. PL provides S_m estimation with higher uncertainty, mostly due to h_p evaluation. This estimation lies between other literature methodologies, but it is weakly compatible with them.

As far as proposed methodologies are concerned, DM generally provides S_m estimation similar to PL method with lower measurement uncertainty if data are not affected by significant noise (the system at IIT is known to be affected by a greater environmental noise). These disturbances demonstrate to lead to evaluation systematically different, such as in the case of indentations of fused silica performed at the Istituto Italiano di Tecnologia at maximum load of 10 mN.

S1 and S2 results tend to be compatible with formerly proposed methods and are associated to limited measurement uncertainty. However, due to their definition, which caters for limited unloading curve portion, differently from DM, when significant noise is present, disturbances introduce component that is strongly smoothed by the method, thus never providing discordant values, as in DM. On the other hand, although S1 and S2 evaluations fluctuate within the largest uncertainty range provided by formerly defined methods, their definition makes them highly sensitive to the experimental curve's spikes and singularities. This induces fluctuation of the results, which hampers from concluding on their general behaviour and robustness.

Since results on reference material were consistent between different testing machines, a Ferrium® C61 was tested. Also in this case, methods provide S_m estimation, whose relative trend is in line with indentations performed on fused silica, see Figure 58. In particular, tests performed at 5 mN offer a further example of DM sensitivity to measurement noise (in fact, related results are not shown for scale issues).

However, DM, when adopted in best environmental conditions (as in the OSU tests) or on standard materials, e.g., fused silica, yields more consistent results and consequently seems the more promising method.

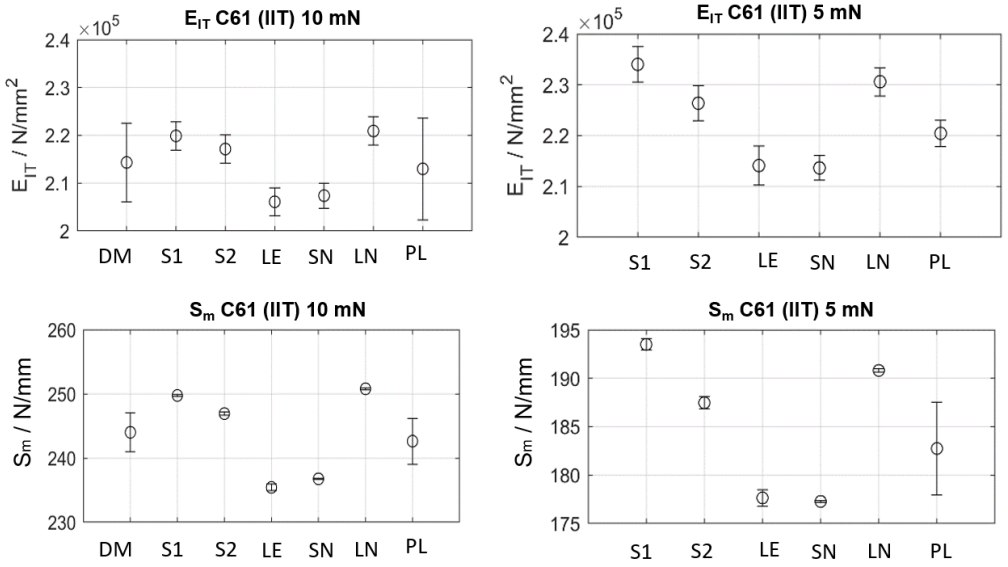

Figure 58 Indentation modulus and contact stiffness of Ferrium® C61 indented at 10 mN and 5 mN at the Istituto Italiano di Tecnologia.

Given the mathematical relationship between indentation modulus E_{IT} and contact stiffness S, see Eq.(3.1), estimation of E_{IT} allows similar observations to be drawn. However, due to uncertainty propagation, differences are less evident. Moreover, S is linked to S_m by the calibration of C_f. Therefore, to conclude the actual effect on E_{IT} of the evaluation methods for the measured contact stiffness, it is necessary to discuss the frame compliance calibration.

3.2.2 Calibration of indentation platforms

The accuracy and precision of material characterization is core to be achieved. Therefore, careful calibration of testing machines according to ISO 14577-2[320] is necessary to guarantee traceability and establish uncertainty contribution to final results. Barbato et al. [336] demonstrated that major contributors to measurement uncertainty of the indentation modulus, in the nano-range, are the C_f and the parameters of $A_p(h_c)$. The annex D of ISO 14577-2:2015 introduces five methods for their calibration. Methods no. 1, 3 and 5 allow calibrating $A_p(h_c)$ parameters by the indentation tip measurement through a metrological AFM and calibrating C_f subsequently. On the other hand, methods no. 2 and 4 rely upon iterative procedures outlined to achieve the calibration, by exploiting relationships that can be inferred from IC without requiring the AFM calibration of the $A_p(h_c)$. Adoption of metrological AFM yields to lower measurement uncertainty [326]. However, considering that the availability of such a Scanning Force Microscope (SFM) entails high cost and longer calibration time, which are critical for industrial users, often methods no. 2 and 4 are adopted. Thus, in the following, only the two methods of industrial interest will be presented and discussed.

Both methods no. 2 and 4 rely upon some common methodology based on the relationships amongst the parameters to be calibrated and general considerations about the indentation system.

First of all, it is necessary to recall the indentation system's modeling as a series of springs, with compliance C_f, and the sample, with stiffness S. The resulting stiffness is measured from raw data, according to its definition as in Eq.(3.2). Moreover, considering the definition of reduced modulus E_r and its relationship with $A_p(h_c)$, in Eq.(3.5), we can rewrite Eq.(3.5) as in Eq.(3.12). Plugging right-hand side of Eq.(3.12) in Eq.(3.2), the linear relationship of Eq.(3.13) between $1/S_m$ and $1/\sqrt{A_p(h_{c,max})}$ results, whose intercept is the C_f and from which Eq.(3.14) follows.

$$C_{tot} = \frac{1}{S_m} = C_f + \frac{1}{S} \tag{3.2}$$

$$\frac{1}{E_r} = \left(\frac{1-\nu_s^2}{E_s} + \frac{1-\nu_i^2}{E_i}\right)^{-1} = \frac{2\sqrt{A(h_{c,max})}}{S\sqrt{\pi}} \tag{3.12}$$

$$\frac{1}{S_m} = C_{tot} = C_f + \frac{\sqrt{\pi}}{2E_r\sqrt{A(h_{c,max})}} \tag{3.13}$$

$$A(h_{c,max}) = \frac{\pi}{4E_r^2(C_{tot} - C_f)^2} \tag{3.14}$$

Thus, an iterative procedure, whose workflow is shown in Figure 59, can be outlined to calibrate parameters and achieve convergence of the values obtained [375]. It requires I indentations, $I \geq 5$, to be performed over a load range representative for the instrument's application field [320]. The initialization of the problem is performed in step 2 and 3, assuming ideal conditions, i.e., infinitely stiff testing machine and ideal indenter geometry. The procedure follows the steps of Figure 59 holds fixed ε, dependent on the tip geometry, and E_r, which ultimately enables the calibration. The steps are iterated until convergence is achieved.

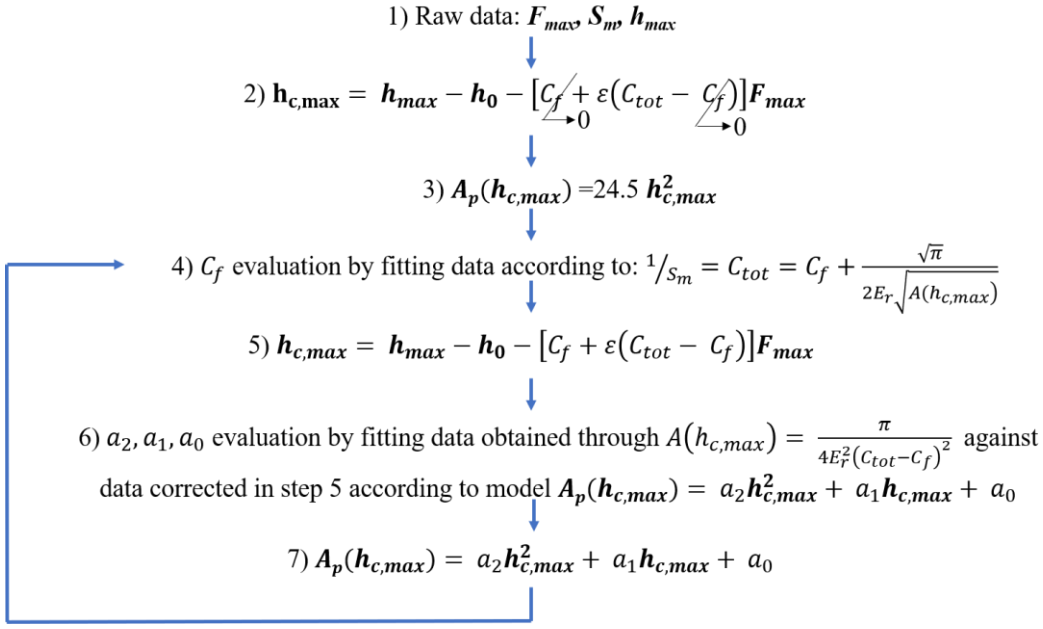

Figure 59 Workflow of standardized calibration iterative procedure. Particular case of indenter area shape function is shown.

In Figure 59, F_{max}, S_m, h_{max}, $h_{c,max}$, and $A(h_{c,max})$ are column vectors built, exploiting F_{max} as an example, as $F_{max} = \{F_{max,i,j}\}$, where i counts the load range levels at which J replicated indentations are performed, i ranges from 1 to I, j from 1 to J. Moreover, arrays are sorted so that $F_{max,w,\cdot} > F_{max,w+1,\cdot}$, with w ranging from 1 to I-1.

ISO 14577-2:2015 method no.2

Method no. 2 (M2) prescribes the calibration to be performed according to the workflow presented in Figure 59 by indenting a single sample. Fused silica or monocrystalline aluminium can be used, considering that to calibrate $A_p(h_c)$

parameters even at shallow depth a relatively elastic material is required. The problem initialization is performed by exploiting data from the indentations at the two higher loads, i.e., $i \in \{1,2\}$.

ISO 14577-2:2015 method no.4

Method no. 4 (M4) prescribes the calibration be performed according to the workflow presented in Figure 59 by indenting two samples of different materials. A stiffer material, e.g., tungsten (W), shall be considered to calibrate C_f, whilst an elastic material, e.g., fused silica (SiO_2) or monocrystalline aluminium (Al), enables the calibration of $A_p(h_c)$ parameters. Therefore, steps 1 to 4, and consequently 7, have to be performed considering data from tungsten indentations, whilst steps 5 and 6, which calibrate indenter area shape function parameters, require data from the elastic material. By coupling calibration and material, this method guarantees faster convergence [326] and allows the initialization to be performed considering all data, i.e., $i \in \{1, \ldots, I\}$.

3.2.2.1 Criticalities of iterative calibration procedures for indentation testing machines in the nano-range[5]

The wide adoption of the method no. 2 and 4 notwithstanding, ISO 14577-2:2015 does not suggest any good practice to perform such calibrations. Moreover, literature [326,376] and practices of research laboratories or testing machine manufacturers show quite various solutions, whose compliancy is not reported. Therefore, this section aims to compare C_f and parameters of $A_p(h_c)$ calibration results when method no. 2 and 4 of ISO 14577-2 are adopted. Additionally, it will investigate the effect of different load ranges to perform calibration to establish a route towards good practices in calibrating testing machine.

Experimental set-up

A Triboindenter TI 950 by Hysitron (shown in Figure 52), hosted in the facilities of the Istituto Italiano di Tecnologia and equipped with a modified diamond Berkovich indenter (Elastic modulus 1140 GPa and Poisson's modulus 0.07), was calibrated on reference samples. The samples' characteristics are summarised in Table 18, calibrated by the frequency resonance method.

[5] Part of this section was also previously published in: Galetto M, Maculotti G, Genta G, Barbato G, Levi R (2019) Instrumented Indentation Test in the Nano-range: Performances Comparison of Testing Machines Calibration Methods *Nanomanufacturing and Metrology*, 2:91-99 and in Maculotti G, Genta G, Galetto M (2020) Criticalities of iterative calibration procedures for indentation testing machines in the nano-range *Proceedings of the 20th International Conference and Exhibition of EUSPEN,* Geneva (CH) June.

Table 18 Calibrated material characteristics.

Material	**Calibration laboratory**	**E / GPa**	**ν / -**
SiO_2	NPL	73.3 ± 0.6	0.161 ± 0.003
W	NPL	413.0 ± 2.8	0.281 ± 0.003

According to the literature [320,326,376] the experimental plan, summarised in Table 19, was outlined to properly cater for different degrees of freedom, i.e., calibration method, contact stiffness evaluation method, material, load range, and replications per each load.

Table 19 Considered cases in the implemented experimental plan to assess performances of calibration methods.

Material	**M2** (Material)				**M4** (W (1-10) mN + Material)			
	PL		**DM**		**PL**		**DM**	
SiO_2 (1-10) mN	10r	DS	10r	DS	10r	DS	10r	DS
SiO_2 (3-10) mN	10r	DS	10r	DS	10r	DS	10r	DS

In particular, calibration method no. 2 (M2) and no. 4 (M4) from ISO 14577-2:2015 are applied, considering the evaluation of the contact stiffness by both the PL [304] and the formerly introduced DM [377] method.

The calibration methods are respectively applied on SiO_2 and on the couple of W and SiO_2, for two different load ranges, i.e., from 1 mN to 10 mN and from 3 mN to 10 mN. Load ranges are indicated in terms of the maximum force reached during the force-controlled indentation test. Tungsten is always tested on the 1 mN to 10 mN range to provide C_f calibration in the machine's whole operating range. On the other hand, provided the known greater signal to noise ratio at low loads, the reduced range from 3 mN to 10 mN has been introduced for SiO_2.

Moreover, provided from experience a suitably high number of points, i.e., 50 points, for calibration, two different load range sampling conditions are catered for: either five load levels evenly spaced in the range are considered, and at each load level 10 replicated measurements are performed (case "10r"), or tests at 50 evenly spaced points of the load range are performed, i.e., providing a denser sampling (case "DS"). For reference, tested load in the case *10r* has a pace of 2.25 mN, ranging from 1 mN to10 mN, and of 1.75 mN, for the range from 3 mN to10 mN.

According to manufacturer best practices, force-controlled tests feature a loading curve of 9 s, a hold phase of 2 s and an unloading phase of 5 s.

Results will be provided in terms of C_f and, considering an indentation performed with the same force-controlled cycle with a maximum force of 10 mN on SiO_2, of $A(h_{c,max})$, H_{IT} and E_{IT}.

Uncertainty estimation: a Monte Carlo approach

Calibration results must be compared in terms of mean value and measurement uncertainty to compare calibration methods performances. However, neither the calibration standard ISO 14577-2:2015 [320] nor reference literature propose methods to evaluate the calibrated parameters' measurement uncertainty.

According to JCGM 100 (GUM) [286], the uncertainty estimation requires the uncertainty contributions to be composed. However, the iterative algorithms, which enable the calibration to be performed, hamper the implementation of simply closed formulae, defined in JCGM 100 and discussed in Section 2.4.2. As a first step toward uncertainty estimation, to assess calibration methods performances within a metrological framework, it is proposed to estimate their uncertainty by a Monte Carlo method (MCM). According to JCGM 101 (Supplement 1 to GUM) [378], MCM is a parametric simulative method to estimate the uncertainty of the output by computing the model response at the sampled input values and assessing the resulting output dispersion, provided the probability distribution of the inputs of a model and performing a random sampling from them, i.e., a simulation. Better estimates are obtained by including include, amongst the inputs, the most relevant influencing factors of the output measurement uncertainty.

Here, the MCM will be applied to the standard calibration methods no. 2 and 4, from which a certain number of input parameters to be simulated can be distinguished. Figure 60 and Table 20 summarise the input parameter setup and highlight the considered influence factors

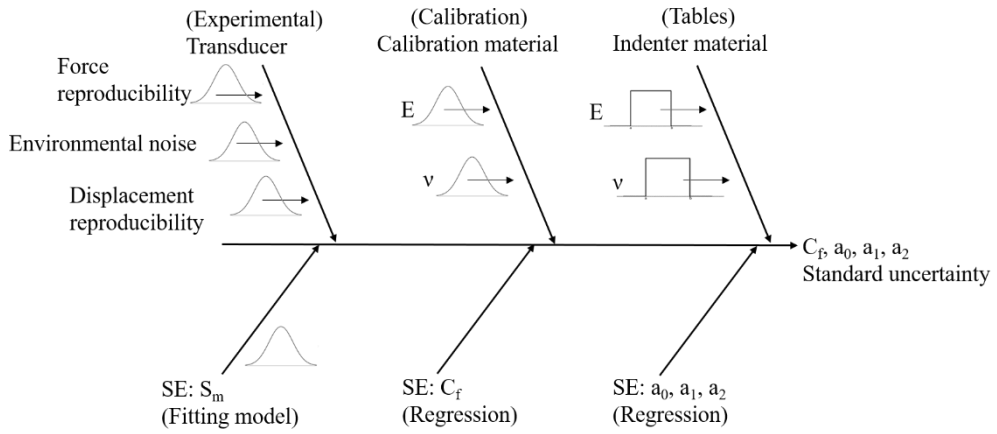

Figure 60 Ishikawa diagram for influencing factors of standard uncertainty of calibration methods results.

Table 20 Sources and distribution assumptions for the simulated input parameters of the MCM.

Parameter	Source	Distribution
E_s	Calibration certificate	$N(E_s, U(E_s)/2)$
ν_s	Calibration certificate	$N(\nu_s, U(\nu_s)/2)$
E_i	Tables	$Rect(E_i \pm 2 \cdot LSD)$
ν_i	Tables	$Rect(\nu_i \pm 2 \cdot LSD)$
F	Raw IC	N(F, u(F))
h	Raw IC	N(h, u(h))
S_m	Raw IC processed with devoted algorithm	$N(S_m, u(S_m))$

Considering that the force and displacement three-plate capacitive transducer is calibrated, and environmental noise can be considered white Gaussian noise, normal distributions are associated with *F* and *h*.

Calibration samples' mechanical properties, being calibrated at NPL and provided with expanded uncertainty (k=2), are assumed to distribute according to a normal distribution. On the other hand, the indenter, being made out of diamond, has a low impact on the characterization results [336]. Moreover, since its properties are not calibrated, they are assumed to distribute according to a rectangular distribution, with bounds at twice the least significant digit (LSD) of the mean value, according to the P.U.Ma. method [379].

S_m, being the result of regression and depending on *F* and *h*, is assumed to distribute normally. However, to consider the variability due to different curves, its standard uncertainty has been evaluated as the mixture's standard deviation. In fact, given a certain maximum force level, each of the experimental curves yields an estimate of S_m, $\widehat{S_m}$, by a regression together with an indication of the standard error of such an estimate $SE[S_m]$, such that $S_m \sim N(\widehat{S_m}, SE[S_m])$. Therefore, *J* curves, each of whom consisting of *B* points in the portion exploited for the regression, provide *J* estimates of both $\widehat{S_m}$ and $SE[S_m]$, representing a mixture [380] of within and between the curve variability. Consequently, it follows:

$$u^2(S_m) = s_W^2[S_m] + s_B^2[S_m] \tag{3.15.1}$$

$$s_B^2[S_m] = \mathbb{V}ar\left[\widehat{S_m}\right] \tag{3.15.2}$$

$$s_W^2[S_m] = \mathbb{E}\left[SE^2[S_m]\right] \tag{3.15.3}$$

Figure 60 includes the calibration procedure results, i.e., C_f, a_0, a_1, and a_2, amongst the influencing factors because of the iterative structure of the methods. Parameters of the distribution of *F*, *h* and S_m are obtained from the experimental data with replicated measurements, see Table 19. Per each load, either an equivalent standard deviation for all levels, if homoscedasticity cannot be rejected [380–383], or the experimental standard deviation of the data at each level was considered. This dispersion is then applied also to data without replicates. Because *s(F)* is smaller than the force noise floor, the noise floor is considered, rather than the experimental standard deviation.

Because calibration methods no. 2 and no. 4 rely upon regression to achieve the results, they yield to an estimated parameter, $\hat{x}$ (where $\hat{x}$ generally represents C_f, and a_i), and its regression's standard error, *SE(x)*. Thus, the standard uncertainty of the calibrated parameter, *u(x)*, must include the contribution of both the variability of x, which represents the variability between the K simulations, i.e., introduced by the variability of input parameters and of regression's standard error, i.e., due to data used within an individual simulation, i.e., J replicates at I different loads. Once more, a mixture of groups is considered, and its variance is computed according to Eq.(3.15). Where s_B^2 results directly from the MCM and s_W^2 requires the analysis of the regression performed in each iteration. These two contributions are combined as in Eq.(3.15.1), according to JCGM 100 [286].

Similarly, the evaluation of standard uncertainty of $A_p(h_{c,max})$, H_{IT} and E_{IT} is obtained by propagating the s_W^2 of the calibrated parameters according to the law of variance propagation [286], thanks to their definition through closed formulae, and applying Eq.(3.15.1) to these results and the s_B^2, also in this case directly obtained by the MCM.

Results discussion

Sixteen configurations are considered, referring to the experimental plan of Table 19. Results are discussed in terms of relative consistency amongst the methods, expanded uncertainty, method computational speed, and estimation correctness. Ten thousand Monte Carlo iterations were performed to rely on the estimate of the variable's statistical distributions. The Monte Carlo has been set up by performing the experimental plan of Table 19 on the Hysitron TI 950 hosted at the Istituto Italiano di Tecnologia. This platform allows neglecting the correction of h_0 [336]. Indenter area shape function with the known term was chosen, as in Figure 59.

In particular, the method speed is evaluated in terms of iteration to achieve convergence, impacting the calibration cost and computational effort. Consistently with Herrmann et al.'s results [326], M4 provides faster convergence with less than ten iterations for all the cases, whilst M2 requires, depending on the case, from a minimum of thirty to about one hundred iterations.

Calibration results of C_f are shown in Figure 61, where error bars represent uncertainty intervals evaluated exploiting an MCM with a coverage factor $k = 2$.

Method no. 2 generally has worse performances in both terms of accuracy and precision than method no. 4: mean estimate shows greater variability between different cases of the former with respect to the latter, and, in some cases, the distribution is not symmetrical. This suggests a lack of robustness of method no. 2 to measurement disturbances, which are more likely to happen when lower loads are included, i.e., (1-10) mN range, or when replicated measurements are not included, i.e., *DS* case. The decoupling of C_f and $A_p(h_c)$ parameters calibration in method no. 4 allows relieving those issues. Provided limitations of method no. 2, the adoption of several load points, i.e., load range sampling case, *DS*, does not provide any advantage in calibration accuracy but worsen the precision. Similarly,

a wider range coupled with a more robust calibration method, i.e., *[M4; (1-10) mN]*, provides more precise results than a narrower one. A wider range also guarantees an unbiased estimation of C_f, as shown in Figure 62.

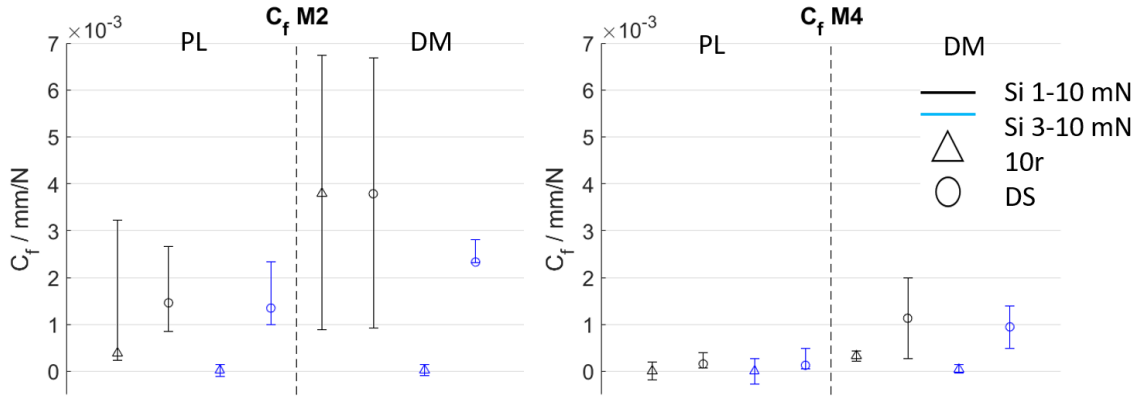

Figure 61 Performance comparison of calibration method for C_f.

Because the estimates of the indenter area shape function parameters are tightly intertwined and depend on the estimation of C_f, results are not shown. Moreover, because a theoretical reference is not available for the projected area evaluation, as the ideal indenter is inherently inappropriate, the effectiveness of the calibration of the indenter area shape function parameters is addressed indirectly by discussing the results of the mechanical characterization.

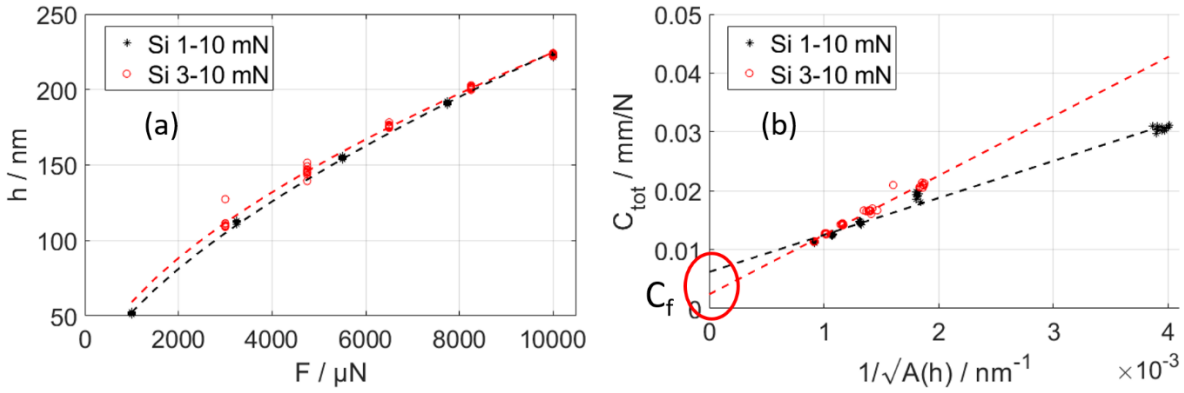

Figure 62 (a) *h(F)*, see Eq.(3.8): despite the consistency in *h* measurement at *F*=1 mN in data set (1 - 10) mN and the expected value from (3-10) mN, (b) different data spread biases the estimate of C_f, i.e., the intercept.

These calibration methods' behaviors depending on the investigated degrees of freedom affect the mechanical characterization. Figure 63 and Figure 64 show estimated E_{IT} and H_{IT} for the corresponding calibration for measurement on SiO_2 at 10 mN. Scaling the analysis from C_f to H_{IT} and E_{IT}, the difference in accuracy amongst considered cases becomes less significant. However, precision becomes critical and shows that results are sometimes not compliant with the calibrated value of H_{IT}, which can be explained considering that the calibration methods only

require information of E_r. Also, adopting DM yields more precise results than PL, consistently to the method definition, when noise content is limited.

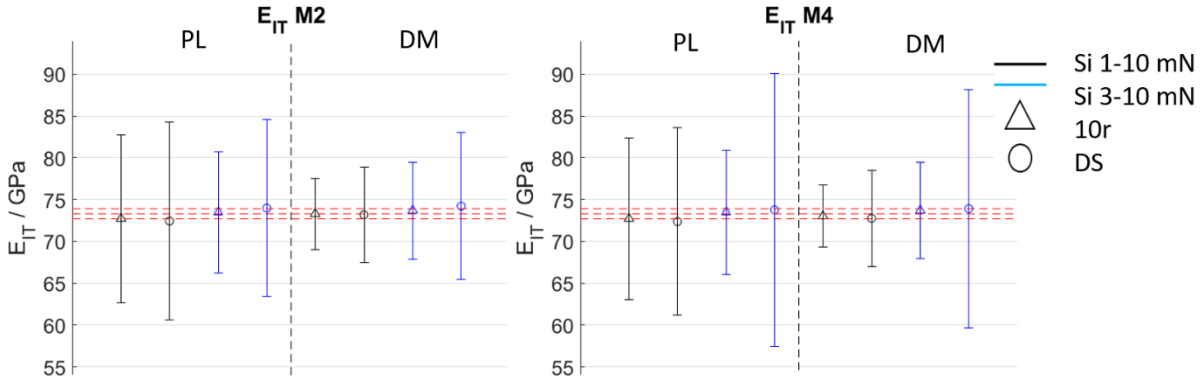

Figure 63 Calibration method effect on E_{IT}. Red lines are reference from calibration certificate.

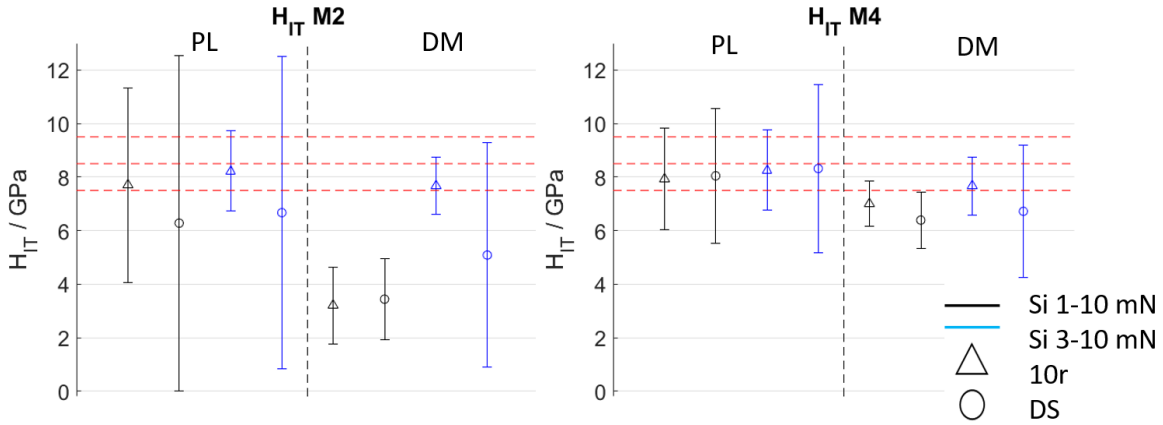

Figure 64 Calibration method effect on H_{IT}. Red lines are reference literature data, with an average of 8.5 GPa and uncertainty assigned according to PUMa method as 1 GPa.

The adoption of the MCM highlights severe asymmetries in the estimation of the calibrated parameters. This hinders applying statistical tools, e.g., ANOVA, to test the significance of the two contributions, i.e., within and between each MC iteration, to the estimated measurement uncertainty.

3.2.2.2 Single-step calibration method for nanoindentation testing machines[6]

Provided the industrial relevance of this characterization technique, traceability, accuracy, and precision are core to be achieved. ISO 14577-2:2015 establishes the testing machine's calibration procedure to guarantee them, and

[6] Part of this section was also previously published in: Galetto M, Genta G, Maculotti G (2020) Single-step calibration method for nano indentation testing machines *CIRP Annals*, 69:429-432.

ISO 14577-1:2015 lists uncertainty contributions to final characterization results. Barbato et al. [336] proved that C_f and the parameters of A_p are the major contributors to the measurement uncertainty of E_{IT}. These are calibrated through a procedure described in annex D of ISO 14577-2:2015 and formerly presented. This procedure is multi-step and iterative and relies on performing a set of J replicated indentations at I different maximum loads. It can be deployed in two methods, method no. 2 of the standard, which employs one calibrated material, and no. 4, which requires two materials.

The previous section showed that different choices, all compatible with standard recommendations, for I and J yield significant variability of calibration results' accuracy and precision. This variability makes the standard calibration methods potentially ineffective to establish traceability and ensure comparability amongst different platforms and laboratories.

Here it is proposed an improved calibration method based on a single-step procedure rather than an iterative method to improve both the implementation of the calibration and mechanical characterization results to overcome the criticalities of the standard cheaper calibrations approaches. Moreover, refinements on the evaluation of uncertainty will be addressed to enable a comparison of the hereby proposed calibration method and the standard approach.

Single-step method

This work proposes a single-step method to calibrate C_f and A_p parameters to cope with shortcomings of ISO 14577-2:2015. Rearranging equations from Eq.(3.1) to Eq.(3.5), considering the A_p function with the known term, the multivariate function $f=f(F_{max}, h_{max}, S_m)$ in Eq.(3.16) is obtained:

$$f = \begin{cases} \dfrac{\pi}{4E_r^2} = \left(\dfrac{1}{S_m} - C_f\right)^2 \left\{ a_2 \left[h_{max} - h_0 - \left[C_f + \varepsilon \left(\dfrac{1}{S_m} - C_f \right) \right] F_{max} \right]^2 + \right. \\ \left. + a_1 \left[h_{max} - h_0 - \left[C_f + \varepsilon \left(\dfrac{1}{S_m} - C_f \right) \right] F_{max} \right] + a_0 \right\} \\ H_{IT} = \dfrac{F_{max}}{a_2 \left[h_{max} - h_0 - \left[C_f + \varepsilon \left(\dfrac{1}{S_m} - C_f \right) \right] F_{max} \right]^2 + a_1 \left[h_{max} - h_0 - \left[C_f + \varepsilon \left(\dfrac{1}{S_m} - C_f \right) \right] F_{max} \right] + a_0} \end{cases} \quad (3.16),$$

which is a multivariate multivariable nonlinear model.

Once J indentations at I force levels have been performed, the calibration can be achieved by performing a regression having as predictors the measured F_{max}, h_{max} and S_m and as responses the calibrated E_r and H_{IT} of reference material. Because Eq.(3.16) is strongly nonlinear and parameters and predictors' variability is not negligible, as they are influencing factors to measurement uncertainty [320] (see Figure 60), a nonlinear Orthogonal Distance Regression (ODR) is necessary [384].

ORD is a regression technique that assumes that the dependent variable $\boldsymbol{Y} \in \mathbb{R}^{p,1}$ is a function, that must be at least smooth, of a set of independent variables $\boldsymbol{X} \in \mathbb{R}^{m,1}$ and of parameters $\boldsymbol{B} \in \mathbb{R}^{b,1}$:

$$\boldsymbol{Y} = f(\boldsymbol{X}, \boldsymbol{B}) \tag{3.17}$$

Through the *n* observations of the independent, $\boldsymbol{y}$, and dependent $\boldsymbol{x}$, variables ODR aims at estimating the parameters, $\boldsymbol{\beta}$, catering for the presence of errors in both sets of observations, respectively $\boldsymbol{Z}$ and $\boldsymbol{\Delta}$, which are typically assumed to be normally distributed. Therefore, the model in Eq.(3.17) can be rewritten as:

$$\boldsymbol{y} = f(\boldsymbol{x} + \boldsymbol{D}, \boldsymbol{\Delta}) - \boldsymbol{Z} \tag{3.18.1}$$

$$\boldsymbol{y}_i = f(\boldsymbol{x}_i + \boldsymbol{\delta}_i, \boldsymbol{\beta}) - \boldsymbol{\zeta}_i, i = 1, \dots, n \tag{3.18.2}$$

where the latter includes empirical observation of the errors. $\boldsymbol{\beta}$ is found by solving the minimization of the squared error determined by:

$$r_i^2 = \boldsymbol{\zeta}_i^T \boldsymbol{\zeta}_i + \boldsymbol{\delta}_i^T \boldsymbol{\delta}_i \tag{3.19}$$

under the constraint set by Eq.(3.18), i.e.:

$$\begin{cases} \min\limits_{\boldsymbol{\beta},\boldsymbol{\zeta},\boldsymbol{\delta}} \sum\limits_{i=1}^{n} r_i^2 = \boldsymbol{\zeta}_i^T \boldsymbol{\zeta}_i + \boldsymbol{\delta}_i^T \boldsymbol{\delta}_i \\ \boldsymbol{\zeta}_i = f(\boldsymbol{x}_i + \boldsymbol{\delta}_i, \boldsymbol{\beta}) - \boldsymbol{y}_i \end{cases} \tag{3.20}$$

which yields to the general nonlinear ODR:

$$\begin{cases} \min\limits_{\boldsymbol{\beta},\boldsymbol{\delta}} \sum\limits_{i=1}^{n} \left[\boldsymbol{\zeta}_i^T \boldsymbol{W} \boldsymbol{\zeta}_i + \boldsymbol{\delta}_i^T \boldsymbol{D} \boldsymbol{\delta}_i\right] \\ \boldsymbol{\zeta}_i = f(\boldsymbol{x}_i + \boldsymbol{\delta}_i, \boldsymbol{\beta}) - \boldsymbol{y}_i \end{cases} \tag{3.21}$$

where $\boldsymbol{W}$ and $\boldsymbol{D}$ introduce a general weighting scheme.

Reducing the problem dimensions to *p, m* = 1, simplifies Eq.(3.19) in $r_i^2 = \zeta_i^2 + \delta_i^2$, whom minimization leads to find the radius of the smallest circle centered in (x_i, y_i), tangent to $f(x_i, \boldsymbol{\beta})$, i.e., the minimum orthogonal distance between observed points and the response prediction curve; which explains the name of the regression technique, see Figure 65.

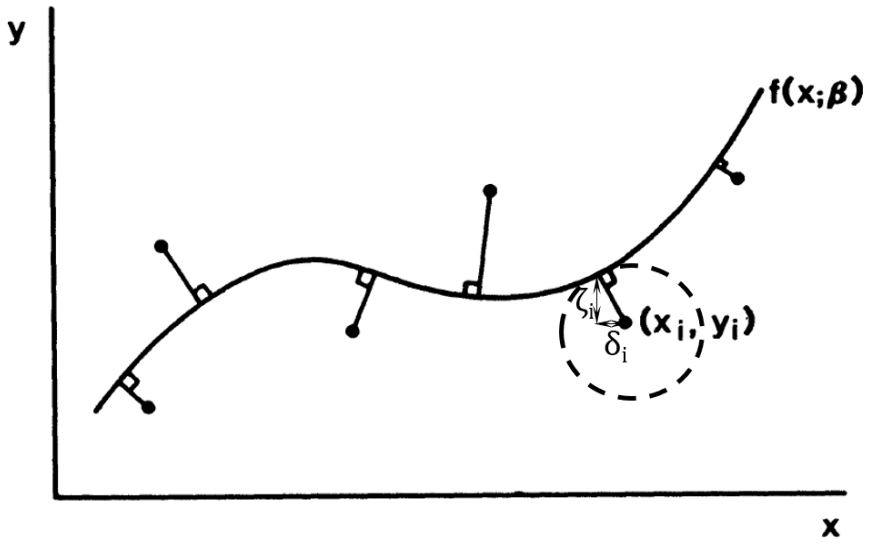

Figure 65 ODR. Error and minimum distance definition (adapted from [384]).

According to the ODR problem's solution, the regression will yield more accurate results than an OLS, at the cost of a worse precision in estimating the dependent variable. In fact, the ODR minimization does not target the sole error on the dependent variable.

The non-trivial hypotheses underlying the ODR have not been adequately investigated in previous approaches [320,326,376], for this reason, the standard assumes an Ordinary Least Square (OLS) to suffice for the regressions, thus neglecting predictors variability and affecting the estimate of parameters. Eqs. from 3.1 to 3.5 must be combined in the system reported in Eq.(3.16), to implement the ODR approach. Eq.(3.16), due to the current use of OLS, has never been proposed and investigated before in the scientific literature. This, with respect to the standard method, has twofold advantages. First, a mathematical and statistical formality to the calibration problem is provided, which avoids possible misinterpretation of the unclearly defined multi-step iterative algorithm and allows the adoption of a more appropriate statistical tool. Second, H_{IT} is introduced in the calibration pipeline: because calibrated parameters are exploited to characterize also hardness, conceptually, it is core to include it in the calibration procedure. The only trivial requirement for this approach is that calibration laboratories upstream in the traceability chain should also calibrate reference materials in terms of H_{IT} via an independent technique, e.g., by calibrating A_p by a metrological AFM.

Uncertainty evaluation: a Bootstrap-based approach

As discussed in the former Section 3.2.2.1, neither the standard nor reference literature proposes methods to evaluate measurement uncertainty. In that section, a Monte Carlo method was proposed [385,386].

However, it is necessary to point out that MCM, being parametric, requires performing non-trivial assumptions on the model input variables statistical

distributions. Accordingly, extensive experimental plans shall be implemented to estimate these distributions' parameters. Moreover, in the case at hand, experimental input quantities, i.e., F_{max}, h_{max}, S_m, are dependent on each other (see Eqs from 3.1 to 3.5). Though, to enable a simple management of the MCM, correlations amongst these inputs were neglected. However, this might introduce errors in the response statistical distribution estimation and, consequently, in the evaluation of the measurement uncertainty.

Here, a solution of these criticalities is addressed by exploiting a non-parametric method, i.e., Bootstrap, to estimate the measurement uncertainty.

The bootstrap approach was introduced by Efron [387] and can be regarded as a particular type of MCM. In fact, rather than performing computer experiments, i.e., simulations, on data sampled from statistical distributions a-priori determined, it resamples a pool of experimental data with replacement and re-entry. These *K* generated samples, i.e., the Bootstrap samples, are the input for the simulation and the estimate of a set of *K* model output(s).

Here a procedure based on the Bootstrap method is outlined to estimate the measurement uncertainty of the calibrated parameters.

The empirical data set consists of *J* measured replicated indentation curves at *I* different maximum loads, and each curve contains *B* points. Therefore, the inputs result in pairs of *F* and *h*, both in $\mathbb{R}^{B,J,I}$ The Bootstrap samples will be sets of resampled *I*:*J* curves, i.e., pairs of *F* and *h*, both in $\mathbb{R}^{B,J,I}$. Each of them, to cater for the input correlation, i.e., *F(h)*, at the *b-th*, $b \in \{1, \dots, B\}$, at the *i-th* load, will resample the *b-th* point of the IC from the sample of the *J* observations of this point $F(h) \in \mathbb{R}^{b,\cdot,i}$. In so doing, per each load, a maximum of J^B replicated curves may results. Considering that the bootstrap samples contain *J* replicated curve at each load, *K* is upper bounded by J^{B-1}.

Therefore, *K* calibrations can be performed. Both the standard multi-step iterative approach, see Figure 60, and the single-step method, see Eq.(3.16) requires in input the calibrated mechanical properties of the calibration samples. These are sampled from parametric distributions and hold constant per each *k-th* bootstrap iteration. Conceptually, this allows including the contribution due to the traceability in the calibration method.

The *K* sets of calibrated parameters are exploited to compute their standard uncertainties as the standard deviation of a group mixture, modeled with ANOVA, as per Table 21. The adoption of ANOVA modeling refines Eq.(3.15) by catering for the degrees of freedom of the estimates, as per

$$SS_{TC} = SS_W + SS_B \tag{3.22}$$

where *SS* is the sum of squares. ANOVA operates on variances of the parameter; therefore, the between iterations contribution is estimated from the variance of the mean estimate of the calibrated parameters, $\mathbb{V}ar[\hat{x}]$, i.e., variance of a sample mean, by multiplying it for the sample numerosity, *IJ*.

Table 21 ANOVA table for the estimate of the variance of regression results from a Bootstrap-based approach.

Factor	Degrees of freedom	Sum of Squares	Variance
Between	$K-1$	$s_B^2[x]\cdot(K-1)$	$\mathbb{V}ar[\hat{x}]\cdot IJ$
Within	$K\cdot(IJ-1)$	$s_W^2[x]\cdot K(IJ-1)$	$\mathbb{E}\left[SE^2[x]\right]$
Total	$KIJ-1$	SS_{TC}	$SS_{TC}/_{KIJ-1}$

These results can then be employed to propagate uncertainties according to GUM JCGM 100 and estimate mechanical characterization results' measurement uncertainties. To this extent, the raw measured inputs, i.e., F_{max}, h_{max} are considered to be influenced by reproducibility, accuracy, and resolution of the force-displacement transducer. The respective contributions are summarised in Table 22. The standard uncertainty of S_m, which accounts for its reproducibility, is determined according to Eq.(3.15) from measured data and associated with a normal distribution.

Table 22 Influence factor to input quantities of mechanical characterization following the calibration for measurement uncertainty of mechanical characterization.

Metrological characteristic	Input quantity F_{max}	Input quantity h_{max}	Input quantity S_m	Contribution type	Distribution
Accuracy	±1%	±0.5%	-	B	Uniform
Resolution	1 nN	0.04 nm	-	B	Uniform
Reproducibility	data	data	Data	A	Normal

The propagation of uncertainty contributions for mechanical characterization parameters, e.g., E_{IT}, H_{IT}, E_r, will ultimately consist of two main contributions: u_{repr} and u_{acc}. The former represents the reproducibility, which includes the influence of input parameters of Table 22 and the standard uncertainty of calibrated parameters, as per Equations from Eq.(3.1) to Eq.(3.5); the latter is due to the accuracy of the measured value and is computed as the RMSE of the estimated characteristic with respect to the calibrated value, when available, i.e., for H_{IT} (only for the single-step method) and E_r.

Experimental setup

Data were collected during the last CIRP international comparison on nanoindentation [353] according to the literature [320,326]: fifty (I = 5 and J = 10) indentations on W and SiO_2 calibrated reference materials at (0.1, 0.5, 1.0, 5.0, 10.0) mN; as shown in the previous section, the setup is chosen to optimize standard method accuracy and precision. Indentations were performed by a

Hysitron TriboScope, hosted in the facilities of the Oklahoma State University and equipped with a modified Berkovich indenter (E_i = 1140 GPa, ν_i = 0.07 and ε = 0.75), see Figure 45, was calibrated on calibrated samples, whose characteristics are summarised in Table 18. The testing equipment features a force-displacement transducer with the characteristics reported in Table 17. This platform allows neglecting the correction of h_0 [336].

The data were exploited to set up the Bootstrap method previously discussed. The calibrated mechanical properties of reference samples were sampled according to distributional hypotheses of Table 18 and Table 20. The calibrated value of H_{IT} is taken from literature sources, with an average value of 8.5 GPa for SiO_2 and 8 GPa for W, and is assumed according to P.U.Ma method to distribute according to a uniform distribution with an expanded uncertainty at 95% confidence level of 1 GPa.

The bootstrap samples were then employed to apply the hereby proposed single-step calibration methods and the calibration method no. 4 of the ISO 14577-2:2015, whose results will be considered the benchmark for the following comparison of the two calibration approaches. Method no. 4, according to the former section, should optimize the performances of the standard multi-step iterative calibration [375,386].

The software implementation is performed on *MATLAB 2019b* for the standard multi-step approach and on Python 3.3 for the single-step method, as a library for a nonlinear multivariate multivariable ODR is not available in *MATLAB*, whilst Python offers scipy.odr. Software are run on a Windows10, ×64 OS with an Intel Core i7-8750H and 16 GB of RAM. Parallel computing was employed on 32 threads to optimize runtime.

Results discussion

Results, as mean and expanded uncertainty, in terms of C_f and A_p parameters are shown in Figure 66. Good practices prescribe to validate the calibrated parameter by characterizing calibrated reference materials. E_{IT}, H_{IT} and F/S^2 (since it is independent of A_p [327]) of W and SiO_2, as these materials represent a wide range of mechanical properties, are shown from Figure 67 to Figure 69.

Uncertainty is computed with a coverage factor $k = 2$, because the bootstrap method showed that calibrated parameters have a distribution non significantly different from a normal distribution, thus supporting the ANOVA modeling. This will ultimately allow assessing the relevance of a simulative approach in estimating the uncertainty of calibrated parameters.

Multi-step iterative methods proposed in the standard requires 6.5’ to run, whilst single-step method 30’’.

Calibrated parameters estimated with the two approaches are compatible with each other, but the single-step method yields more precise results. ANOVA modeling showed, at a confidence level of 95%, that the variability between the iterations is significantly greater than the variability ascribed to random factors, i.e., the variability within the groups.

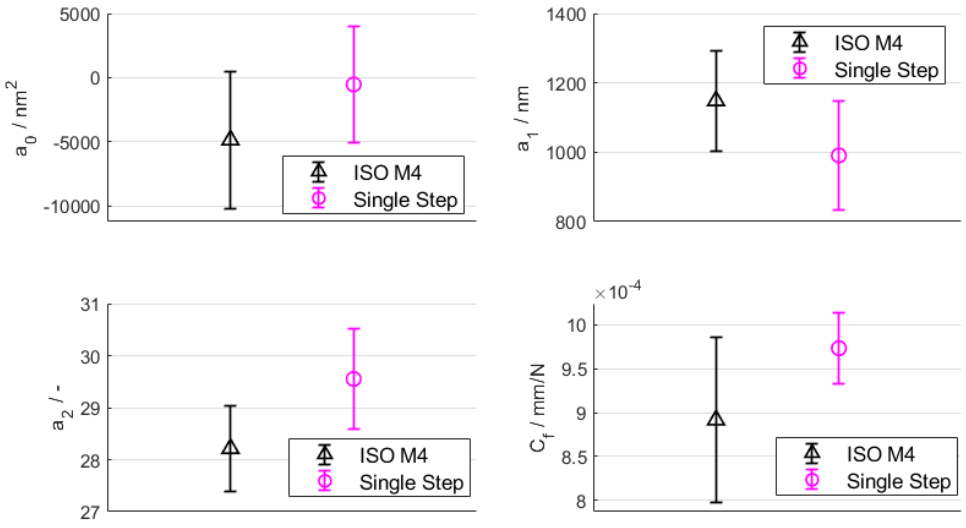

Figure 66 ISO and single-step method calibrated parameters comparison.

The mechanical characterization results for the four higher loads are shown (measurements at 0.1 mN were characterized by a too high noise and thus excluded from the analysis).

As far as indentation hardness is concerned, see Figure 67, the standard approach provides better performance. Accuracy is the most relevant contribution for both methods on both materials, as summarised in Table 23. In the case of tungsten, a possible indentation size effect can be noticed at lower loads.

Table 23 Relative contributions to measurement uncertainty of H_{IT} for the two proposed methods.

Force / mN	Material	ISO			Single step		
		u_{repr}^2%	u_{acc}^2%	U%	u_{repr}^2%	u_{acc}^2%	U%
10	SiO_2	15%	85%	17%	12%	88%	19%
5		19%	81%	17%	16%	84%	19%
1		42%	58%	21%	36%	64%	23%
0.5		63%	37%	26%	55%	45%	27%
10	W	3%	97%	28%	2%	98%	37%
5		5%	95%	27%	3%	97%	35%
1		27%	73%	26%	17%	83%	32%
0.5		50%	50%	29%	33%	67%	34%

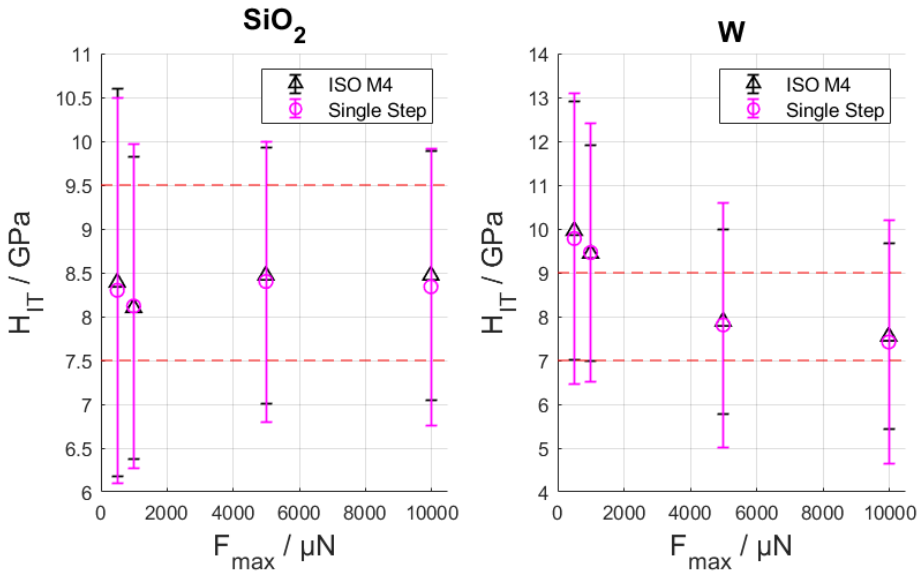

Figure 67 ISO and single-step method validation: H_{IT} of fused silica and tungsten.

Reduced modulus and indentation modulus characterizations show definitive advantages in adopting the single-step calibration method, as the results are more accurate and precise. As in the case of H_{IT}, tungsten shows the worst performances, that are connected to the measurement reproducibility. Consistently with the regression methods, the reproducibility contribution in the single-step method is relatively more relevant than the accuracy, as summarised in Table 24, for the E_r. This consistently propagates on the results of the expanded uncertainty for the E_{IT}, as shown in Table 24 and Figure 68.

Results on the F/S^2 ratio combine the previously discussed, as shown in Figure 69, and prove adequate choice of the calibration method for the frame compliance.

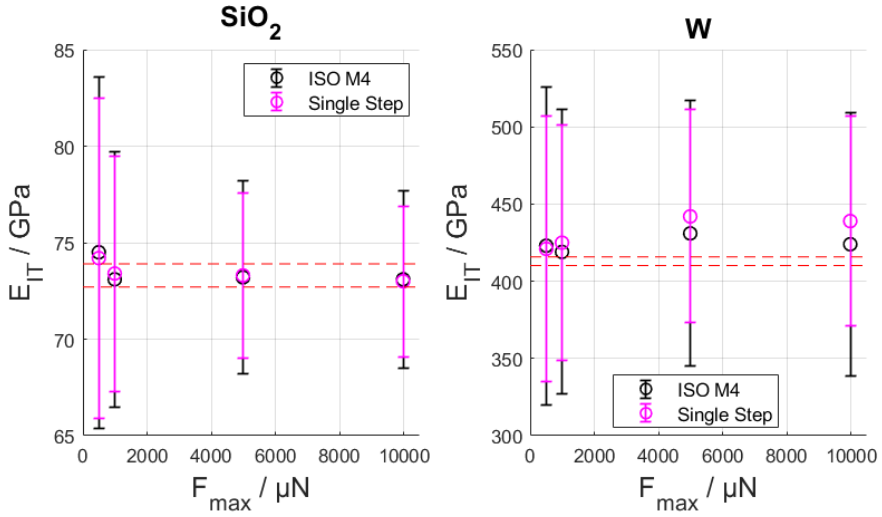

Figure 68 ISO and single-step method validation E_{IT} of fused silica and tungsten

Table 24 Relative contributions to measurement uncertainty of E_r for the two proposed methods. Also results of relative expanded uncertainty of E_{IT} are reported.

Force / mN	Material	ISO				Single-step			
		u_{repr}^2%	u_{acc}^2%	U%	$U(E_{IT})$%	u_{repr}^2%	u_{acc}^2%	U%	$U(E_{IT})$%
10	SiO_2	28%	72%	6%	6%	41%	59%	5%	5%
5		35%	65%	6%	7%	50%	50%	5%	6%
1		64%	36%	9%	9%	76%	24%	8%	8%
0.5		81%	19%	11%	12%	87%	13%	11%	11%
10	W	3%	97%	15%	20%	6%	94%	11%	15%
5		5%	95%	15%	20%	8%	92%	11%	16%
1		18%	82%	16%	22%	28%	72%	13%	18%
0.5		35%	65%	18%	25%	45%	55%	15%	20%

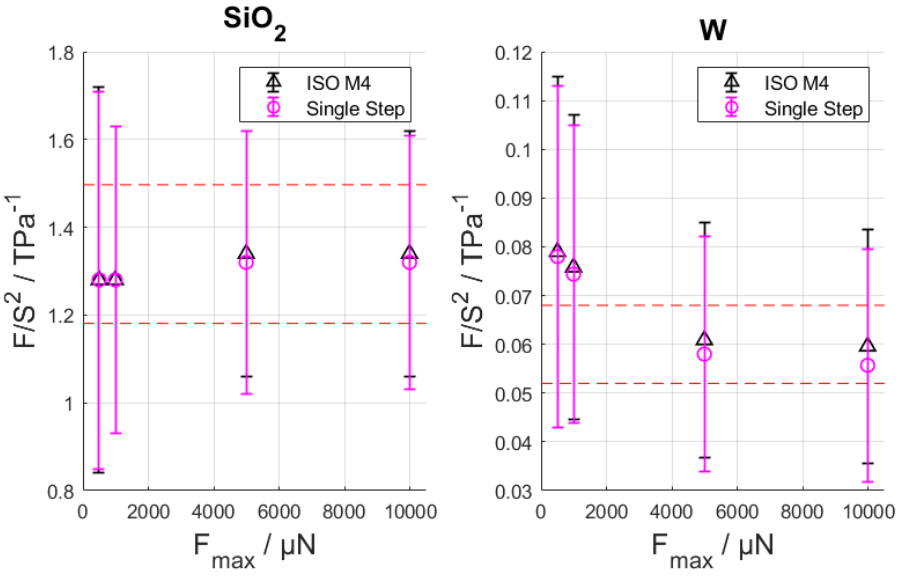

Figure 69 ISO and single step method validation: F/S^2 of fused silica and tungsten.

3.2.3 Section summary

This section addressed some of the critical influencing factors to measurement uncertainty of the mechanical characterization by instrumented indentation test, i.e., the contact stiffness and the calibration of the frame compliance and the indenter area shape function parameters.

A new approach for estimating the contact stiffness based on a direct numerical evaluation of the derivative of the unloading curve was proposed, and,

in addition of being more rigorously adherent to the definition of the measurand, it provided promising results for the reduction of the mechanical characterization precision.

Standard calibration approaches based on the multi-step iterative method were discussed, highlighting several shortcomings and a general lack of standard's prescriptiveness. A method based on a single-step approach was here defined, which has both conceptual and practical advantages. The former consist of providing rigorous mathematical formulation to the problem, catering for the variability of inputs by relying on an Orthogonal Distance Regression (ODR), and introducing the hardness as a calibration reference. The latter have been proved, through experimental comparison, to be a greater accuracy and precision with respect to the standard approach, not only for the calibrated values but also for the validation on reference materials. Even if this approach requires calibration laboratories upstream in the traceability chain to calibrate indentation hardness by an independent technique, the related costs are negligible compared to the procedural and metrological advantages.

These sets interesting perspectives for future works, which should aim at testing the performances of different calibration materials, e.g., to substitute tungsten, which seems liable of low reproducibility, comparing performances in the choice of the indenter area function model and then combine the effect to the newly proposed single-step calibration approach with the derivative method for the contact stiffness evaluation.

3.3 Relevance of surface mechanical characterization in Industry 4.0

This section aims at providing some application of methods for mechanical characterization of technological surfaces relevant to the Industry 4.0 framework, to support the development of new materials, processes, and quality inspections.

3.3.1 Additively manufactured components qualification by indentation tests

As discussed in the Induction of the present thesis, additive manufacturing is one of the pillars of Industry 4.0. It provides definitive advantages for customization, design flexibility, and optimization with relevant cost reduction and better materials usage.

However, as new additive processes are developed and new materials are being processed, they require the additive manufacturing process to be optimized to achieve desired part quality and design specification.

Conventional and non-conventional hardness tests are particularly suitable for inspecting surface mechanical properties because they achieve a thorough mechanical characterization non-destructively, thus making unnecessary the adoption of samples and the destructive mechanical characterization test.

Here, two applications on AlSi10Mg by Selective Laser Melting (SLM) are proposed discussing the possibilities offered by indentation tests in the product and process characterization.

Aluminium-Silicon alloys are extremely attractive cast aluminium alloys, thanks to their high fluidity, weldability, corrosion resistance, and low thermal expansion coefficient. Moreover, by introducing magnesium as an alloying element, the formation of precipitates of Mg_2Si is promoted, which strengthens the matrix and enables effective hardening to be achieved by heat treatments or rapid solidification techniques. Conversely, it limits the feasible designs [92,107,388–390]. Therefore, aluminium alloys are of great interest for automotive and aerospace industries due to their combination of high strengths, low densities, and thermal capacity [390], finding application in heat exchangers, heat sinks, turbine blades, carters, and cylinder blocks [391,392]. Moreover, near-eutectic composition, thanks to the small solidification range, eases laser processing [107]. Therefore, AlSi10Mg is an alloy that is particularly suitable and interesting for SLM processing, which, ultimately, enables freedom design for this high-performance material.

Amongst the available AM processes, SLM can, a high-density object is built up layer by layer by consolidating metal powder particles with a focused laser beam that selectively scans the surface of the powder bed [73,74,105,388,393,394]. Metal powders, also reactive materials like titanium and aluminium, e.g., Ti6Al4V or AlSi10Mg alloys, are melted without a binder's aid in the case for indirect laser sintering [395–401]. Recently, researchers have shown an increased interest in this process's potential that enables to build in one step full dense metallic parts with complex geometries that are used as final parts or functional prototypes. The part building process takes place inside an enclosed chamber filled with nitrogen gas to minimize oxidation and degradation of the powdered material, or inert gas, e.g., Argon or Helium, to avoid material to react with the environment. The powder in the build platform is maintained at an elevated temperature just below the powdered material's melting point or glass transition temperature. Infra-red heaters are typically exploited to this aim, which also reduces laser power needed to locally melt the powder and the heat exchange, which is a source of warping. As soon as a layer of powder is spread by a counter-rotating roller on the building platform, which must be ground and polished, a focused laser beam is directed onto the powder bed. The laser beam is moved using galvanometers so that it thermally fuses the material to form the slice cross-section. Surrounding powder remains loose and serves as a support for subsequent layers, thus eliminating the need for the secondary supports necessary for photopolymer vat processes. After completing a layer, the build platform is lowered by one-layer thickness, t, typically (20÷50) μm for metal, and a new layer of powder is laid, and the beam scans the subsequent cross-section. A schematic of the process system's main component is shown in Figure 70 [104].

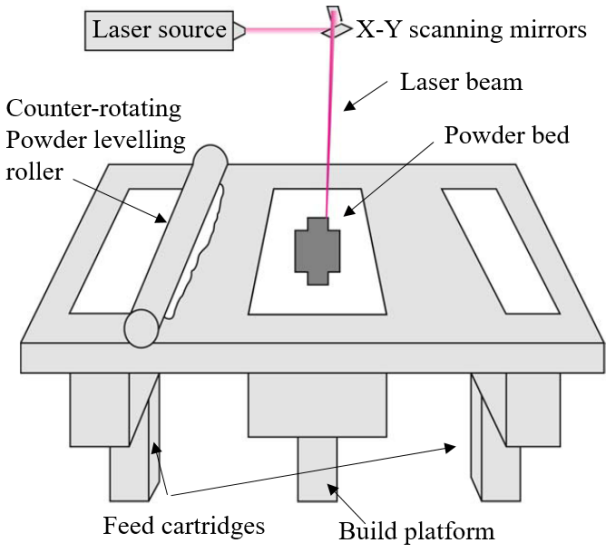

Figure 70 Schematic of SLM (adapted from [104]).

Different boundary conditions for heat exchange between the layer and the environment are met along the building direction during the build. The bottom region is in contact with the building platform, below it, and laser exposed areas, above it. The top region has exposed areas below. The region in between contacts exposed areas above and below itself [402–404]. These three regions can be respectively named the down-skin, the up-skin, and the core or in-skin [102,104–106,388,405], as shown in Figure 71. It is standard practice to set up different process parameters for each of these three regions, considering that the down-skin consists of two layers and the up-skin of three, to optimize the process [388,405]. Literature [102,105,107,388,406] has shown that this region-wise differentiated parameter set-up can relieve the effect of boundary conditions for heat exchange and achieve control of material properties. According to Fig. 3, up- and down-skin parameters are related to surface properties, whilst in-skin parameters to the core, bulk average properties of the component.

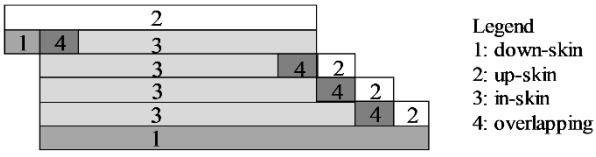

Figure 71 Up-skin, down-skin and core regions (adapted from [106]).

3.3.1.1 Hardness optimization for AlSi10Mg by Selective Laser Melting[7]

As formerly, reviewed, three main input parameters have been demonstrated to influence the part quality, and mechanical properties of the build (microstructure, hardness, adhesion between adjacent laser scans, and topography): the laser power P, the hatch distance h_d, and the scan speed v. Their interaction is well summarised by the energy adsorption E_A:

$$E_A = \frac{P}{h_d \cdot v}\left[\frac{J}{\mathrm{mm}^2}\right] \quad (3.23).$$

The layer thickness t is an additional source of possible defects. If P is not sufficient, it may promote delamination. Therefore, considering the three main input parameters here accounted for, the laser heat input is using the energy density function, ψ, which is described by:

$$\psi = \frac{P}{h_d \cdot v \cdot t}\left[\frac{J}{\mathrm{mm}^3}\right] \quad (3.24).$$

In general, the laser heat input is strictly related to the degree of consolidation of the powder particles. It may cause defects by creating turbulence in the melt pool that can form a keyhole-like defect in extreme conditions [101]. Consequently, it is often adopted in literature as a reference parameter for the setup of ANOVA, DoE, and RSM analysis of influencing factors on material properties [107]

Amongst the several mechanical properties, this section focuses on hardness. This measurement evaluates a characteristic that allows inferring other properties of the material, e.g., plasticity. However, as far as influence of process parameters is concerned, here is relevant to recall the works of Li Y. et al., Song et al., Lam et al., Li X. P. et al. and Ghasri-Khouzani et al. [390,407–410]. They demonstrated that due to the local melting and high cooling rate typical of the SLM process, which yields finer microstructure with respect to cast or wrought part, greater hardness, and higher strength result, further enhanced by the alloying elements and the interactions of dislocation for the AlSi10Mg. SLM introduces anisotropy in the material due to the layer-by-layer building strategy; however, it has been demonstrated that, at least at macro and micro scales, it does not introduces significant differences in the material mechanical behavior [390].

Methodology

Design of Experiment (DoE) is a practical statistical approach for optimizing the process when different input variables and their interactions affect selected responses [411]. Then, Response Surface Methodology (RSM) uses experimental

[7] Part of this section was also previously published in: Galetto M., Genta G., Maculotti G., Verna E. (2020) Defect Probability Estimation for Hardness-Optimised Parts by Selective Laser Melting, *International Journal of Precision Engineering and Manufacturing*, 21(9):1739-1753

designs to fit a model by the least-squares technique. In fact, RSM is a collection of mathematical and statistical techniques aimed for empirical exploration of the relationship between continuous response(s) and a set of input factors [412]. In the exploratory stages of model building, stepwise regression may identify the best subset of predictors. It is an automatic technique implemented in several statistical software such as *MINITAB*®, used in this analysis. Stepwise regression adds and removes predictors at each step, according to selected Alpha-to-Enter and Alpha–to-Remove values [412]. The ANOVA is used to estimate the statistical significance of parameters' effects with respect to the observed differences in response. The adequacy of the obtained model is demonstrated by using diagnostic checking tests such as the coefficients of determination and the residual plots, analyzed to verify the basic assumptions to perform the ANOVA. Finally, the response surface plots can be employed to study the surfaces and locate the optimum. For this reason, the RSM is usually used to assess results and efficiency of operations [101]

Experimental setup

In this case study, the EOS M 290 SLM machine is considered. This platform is a high productivity system of limited dimensions that enables to build components within a volume of (250×250×320) mm. It features a Yb-fibre laser with a nominal power of 400 W and a focus diameter of 100 μm, with a scanning control based on *f-θ* lenses with a focal length of 410 mm, that operates in an Argon shielded environment.

The output variable measured on the samples was Brinell hardness, and the input variables were laser power, scan speed, and hatching distance of the in-skin. Of course, controlling and changing the latter variables results in different quality outputs of the parts. The samples' geometry, shown in Figure 72, was designed to perform, in forthcoming analyses, surface roughness measurements and hardness tests.

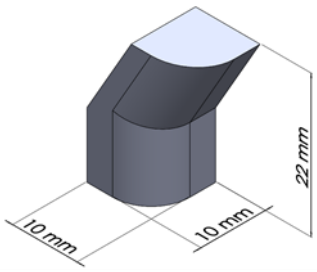

Figure 72 Samples geometry.

An experimental plan was designed to obtain optimal process parameters that result in the best values of hardness. Specifically, a 3^3 full factorial design was realized to investigate possible quadratic effects of input variables. The three input variables relevant to the in-skin, laser power (P), scan speed (v), and hatching distance (h_d), were kept at three levels (see Table 25). For each of the 27 parts, the

layer structure contour was exposed with the same value of speed (1000 mm/s) and laser power (355 W) of the up-skin. Additionally, a post-contour strategy was realized (with a speed of 900 mm/s and a power of 80 W). The choice of the levels of the process parameters set in the experimental plan allowed to get a wide range of energy density function, ψ, see Eq.(3.24). Specifically, ψ varied from 35.09 J/mm^{3}to 124.58 J/mm^3. The experiments were not randomized because the machine's high repeatability allowed building the samples in a single job by varying process parameters for each sample. This approach, as a first approximation, is the one adopted in the computer experiment field.

After the production, the 27 specimens for hardness measurements were milled and polished. The Brinell hardness test was then performed according to the industrial standard ISO 6506-1:2014 [413]. The test was carried out using a sphere with a diameter of 2.5 mm and applying a force of 62.5 kgf, thus evaluating Brinell hardness in the scale HBW 2.5/62.5 to provide a reference to powder supplier specification. Three measurements for each specimen were taken, and the average value was examined, to account for the variability of the measurement procedure.

Table 25 Process parameters values used in the planned experimentation.

Process Variable	Values
P / W	340 – 355 - 370
v / mm/s	900 – 1300 - 1700
h_d / mm	0.11 – 0.15 – 0.19

Results discussion

After collecting the data obtained from the Brinell hardness measurements on the 27 samples of the experimental plan, the statistical analysis was performed, using the RSM on the average of the three hardness measurements carried out on the samples.

This arrangement allowed identifying the appropriate empirical equation, i.e., a second-order polynomial multiple regression equation. The standard stepwise regression was adopted to obtain a model containing exclusively significant factors. Alpha-to-Enter and Alpha–to-Remove values were set to 10% to allow entering terms close to the significance level of 5%. The software *MINITAB*® 17.1 was used to perform the analysis. The RSM provided the ANOVA (see Table 26), the coefficients of the regression models with their relevant standard errors (see Table 26

Table 27), and the regression equation:

$$HB = \beta_0 + \beta_1 \cdot P + \beta_2 \cdot v + \beta_3 \cdot h_d + \beta_4 \cdot v^2 + \beta_5 \cdot v \cdot h_d \qquad (3.25).$$

The predicted response, the Brinell hardness *HB*, was therefore correlated to the set of regression coefficients (β): the intercept (β_0), linear (β_1, β_2, β_3),

interaction (β_5), and quadratic coefficient (β_4). In this analysis, Brinell hardness is evaluated in the scale HBW 2.5/62.5; however, for simplicity of notation, the corresponding measurement unit is only indicated by the symbol HB.

Table 26 ANOVA for hardness HB [HB].

Source	*df*	Sum of squares	*F*	*p*-value
P	1	81.64	3.93	6.1%
v	1	3950.62	190.29	<0.1%
h_d	1	529.93	25.53	<0.1%
v*·*v	1	458.40	22.08	<0.1%
$v \cdot h_d$	1	222.45	10.72	0.4%
Residual error	21	435.98		
Total	26	5679.02		

Table 27 Estimates of parameters of the regression model, see Eq. (3.24), and the relevant standard errors.

Variable	Parameter	Estimate of parameter	SE on estimate of parameter
constant	β_0 / HB	$-5.12 \cdot 10^{1}$	$3.57 \cdot 10^{1}$
P	β_1 / HB/W	$-1.42 \cdot 10^{-1}$	$7.16 \cdot 10^{-2}$
v	β_2 / HB/(mm/s)	$2.19 \cdot 10^{-1}$	$3.28 \cdot 10^{-2}$
h_d	β_3 / HB/mm	$4.85 \cdot 10^{2}$	$1.10 \cdot 10^{2}$
v*·*v	β_4 / HB/(mm/s)^2	$-5.46 \cdot 10^{-5}$	$1.16 \cdot 10^{-5}$
$v \cdot h_d$	β_5 / HB/(mm^2/s)	$-2.69 \cdot 10^{-1}$	$8.22 \cdot 10^{-2}$

By performing a qualitative analysis on the main effect of the process parameters and observing the main effect plot, shown in Figure 73, it can be concluded that all the three input variables have a main effect on hardness. In main effect plots, the higher the slope of the line that connects the process variables' levels, the greater the influence of each variable. The main effect on the hardness seems to be due to the scan speed *v*: a speed of 900 mm/s produces a hardness of about 90 HB; conversely, using a speed of 1700 mm/s the resulting hardness is about 120 HB. The second most impacting variable is the hatching distance h_d, while the laser power *P* seems to have a weaker effect than the other process variables on the hardness. It is worth noting that the trends are of direct proportionality for the scan speed and the hatching distance and of inverse proportionality for the laser power: lower laser power yields better, i.e., greater, hardness. On the contrary, diminishing the scanning speed and the hatching distance, worse hardness values are obtained. These results are confirmed by the analysis of variance, in Table 26, where it emerges that *v* and h_d are highly

significant, i.e., their *p*-values are less than 0.1%, and *P* is significant at a 6% significance level

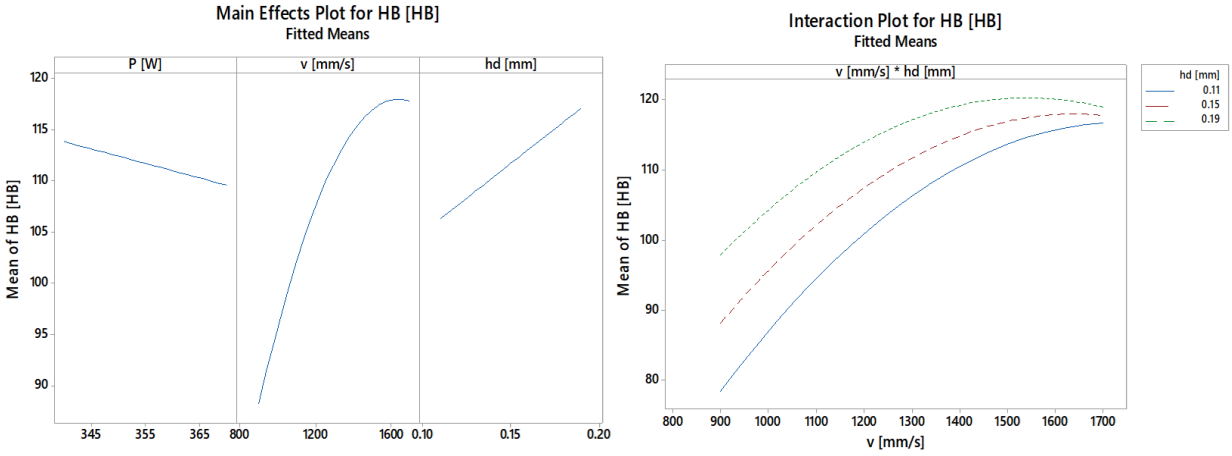

Figure 73 Main effects plot and interaction plot for hardness HB [HB].

With respect to the quadratic terms in Table 26, only the effect of the scan speed is found to be highly significant. The interactions between variables can be visualized with the interaction plot, shown in Figure 73. Parallel lines in interaction plots indicate no interaction. The greater the departure of the lines from the parallel state, the higher the degree of interaction. The graph shows that it is possible to obtain high *HB* using high values of scan speed and high hatching distance values and that there are strong interactions between these two parameters. The ANOVA confirms that result, by showing that the interaction between v and h_d is highly significant (p-value of 0.4%). Furthermore, the RSM provided the estimates of the regression model's parameters (see Eq. (3.25)) with the relevant standard errors reported in

Table 27. The analysis of residuals, i.e., the differences between the observed and the corresponding fitted values, is shown in Figure 74 and suggests that the model fits the data well. The normality of the residuals is confirmed graphically both by the normal probability plot (NPP), in which the points follow approximately a straight line, and by the histogram (see Figure 74). Furthermore, by performing the Anderson-Darling test, the null hypothesis that the residuals follow a normal distribution cannot be rejected with a p-value of 0.51 [414]. The plot of residuals versus fitted values shows a horizontal band around the residual line (value 0), and no recognizable patterns are found. However, the residuals-versus-order-plot reveals that non-random error, especially of time-related effects, may be present. The R^2 value, a measure of the model's goodness-of-fit, shows that the variation in the response explained by the model describing the relationship between the process parameters and the Brinell hardness is 92.3%. Even the predicted R^2 value is very high, reaching 85.9%, suggesting a great predictive capability of the model.

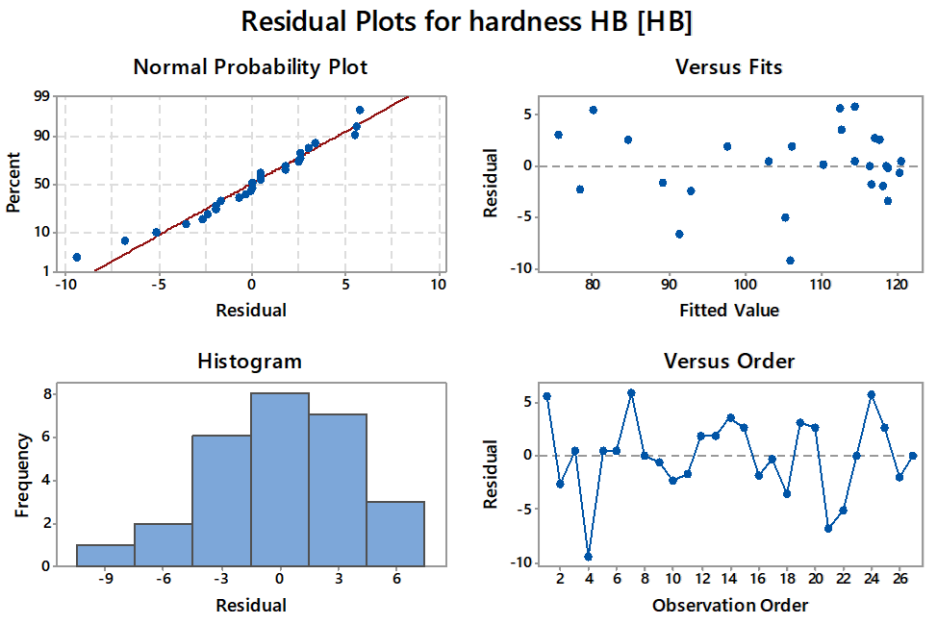

Figure 74 Residual plots for hardness HB [HB].

In Figure 75, surface plots showing how the fitted response relates to the three pairs of independent variables are reported. A surface plot displays the three-dimensional relationship with the independent variables on the *x*- and *y*-axis, and the response (*z*) variable represented by a smooth surface. The graphs are generated by calculating fitted responses using the independent variables while holding the third control variable constant at a certain specified value, i.e., the central value.

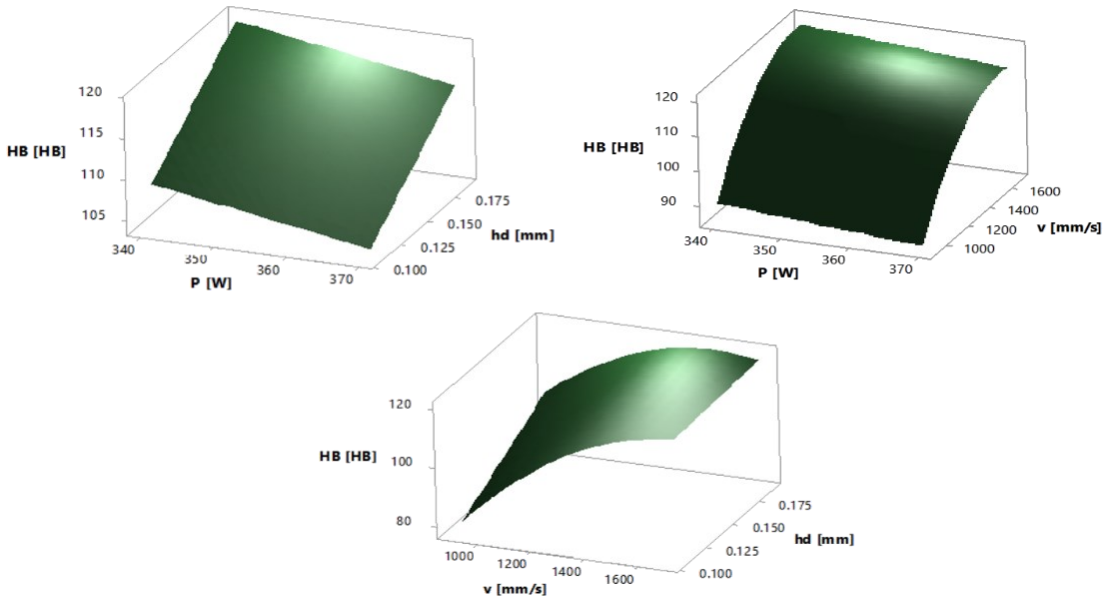

Figure 75 Surface plot of hardness HB [HB] versus: a) hatching distance h_d [mm] and laser power P [W] (scan speed v was set to 1300 mm/s); b) scan speed v [mm/s] and laser power P [W] (hatching distance h_d was set to 0.15 mm); c) versus hatching distance h_d [mm].

A response optimization was performed to find the values of laser power, scan speed, and hatching distance of the in-skin resulting in the best value of hardness. Specifically, the objective function was set to maximize the hardness. Parameters setups and the respective value of energy density ψ, are summarized in Table 28, together with the predicted value of hardness and the related 95% confidence interval.

Table 28 Process setup (maximum HB). Response optimization and predicted value.

Control factors				Response predicted value	
P / W	v / mm/s	h_d / mm	ψ / J/mm^3	Hardness / HB	95% confidence interval / HB
340	1538.4	0.19	38.78	122.45	(118.08;126.83)

The optimization plot for *HB* is reported in Figure 76. As far as P and h_d values are concerned, they are situated at the limits of the ranges selected for the planned experimentation. Specifically, P is located at the lower limit of the range and h_d at the upper limit. Regarding v, the value that leads to the optimal hardness is placed at about three-quarters of the interval. This parameter set corresponds to a low energy density value (38.78 J/mm^3).

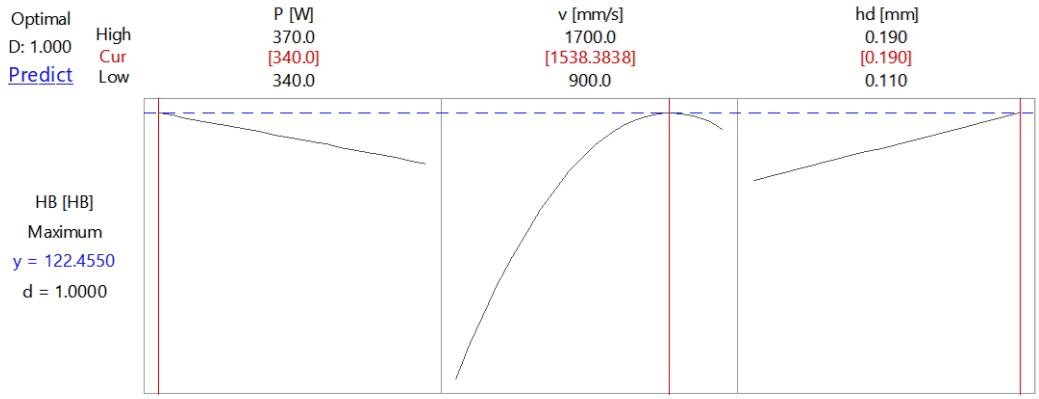

Figure 76 Optimization plot for hardness HB [HB].

From a physical point of view, the obtained values can be considered reasonable. In fact, when the energy density is too high, i.e., increasing laser power and decreasing scan speed, the melt pool volume increases, and its viscosity decreases, leading to irregularities and very deep penetration into the previously formed layers, and partial evaporation takes place [415]. Conversely, when the energy density is too low, a partial penetration of the melt pool to the underlying layers occurs, wetting is unsatisfactory, and droplets are formed [105,415]. The obtained process parameters setup, which lies in the process window defined by Kempen et al. [415], allows getting parts characterized by good mechanical properties, high hardness in this case.

Section summary

The purpose of the current study was to determine the effect of some process parameters on the macro-hardness of AlSi10Mg parts produced by SLM process with an EOS M 290 machine through statistically designed experiments. Selected process parameters were laser power, scan speed, and hatching distance of in-skin, i.e., the core, of the parts. A 3^3 full factorial design was realized in order to evaluate possible non-linear effects of process parameters. It was found that scan speed, hatching distance, their interaction, and the quadratic effect of scan speed have the most significant influence on the hardness. The response surface methodology (RSM) provided the mathematical model that correlates the process parameters with the hardness. By optimizing this response surface, it was obtained that hardness is maximized when the laser power is 340 W, the scan speed is 1538.4 mm/s, and the hatching distance is 0.19 mm. In addition to the optimal configuration of the parameters, the most significant contribution of this study has been to propose a methodology based on the design of experiment and response surface methodology, which allows:(i) the identification of process parameters and interactions which have a significant effect on the hardness; (ii) the definition of a correlation model between process parameters and hardness.

The obtained model, i.e., the response surface, has the great potential of enabling the monitoring and prediction of hardness according to the main process parameters. In fact, as reported by Galetto et al. [416], despite the large number of published studies focusing on the optimization of the AM process, no specific attention has been paid to the remarkable issue of identifying the probability of defects generation occurring when the process is optimized. Indeed, even under optimal working conditions, namely when each process parameter is set at its optimal value, the probability of defects occurrence is never negligible because of the uncertainty affecting the overall manufacturing process. The availability of a mathematical model relating the significant process variables to the output response, i.e., hardness value, enables the propagation of uncertainties related to the manufacturing process and inspection methods, for which the metrological characterization is thus core. Finally, the probability of the occurrence of hardness defect is estimated by exploiting and composing the uncertainty affecting both the obtained mathematical model and the input variables as the probability that the optimized variable falls outside specification boundaries.

3.3.1.2 Multiscale indentation testing for efficient quality inspection of heat-treated AlSi10Mg by Selective Laser Melting[8]

AlSi10Mg is a lightweight Al-alloy with interesting processing properties and enhanced strength thanks to Mg's presence, which, hence, finds application in

[8] Part of this section was also previously published in: Maculotti G, Genta G, Lorusso M, Galetto M (2019) Assessment of Heat Treatment Effect on AlSi10Mg by Selective Laser Melting through Indentation Testing *Key Engineering Materials*, 813:171-177.

several industrial fields. The SLM processing allows overcoming those design constraints set by casting and melt spinning; however, SLM AlSi10Mg components require to be heat-treated, to strengthen the material and to engineer the microstructure. Although AM processes allow manufacturing quasi-free shape geometries and optimize the raw material usage, the part produced still require some post-processing.

Limiting the discussion to the SLM case, typically powder in excess has to be removed; supports, if present, must be sawed; machining may be required to achieve desired roughness, and modifications of the microstructure can be addressed by heat treatments. In fact, SLM process is similar to casting, as locally the material is melted and then solidifies. However, due to the scales at which the local melting and high cooling rate take place, SLM yields to a finer microstructure than the cast or wrought part, greater hardness, and hence higher strength result, which is further enhanced by the alloying elements and the interactions of dislocation for the AlSi10Mg. Additionally, because of the different boundary conditions between the in-skin and the up-skin, different cooling rates generate a thermal gradient that results in residual stresses. Moreover, SLM introduces anisotropy in the material due to the layer-by-layer building strategy, even though it has been demonstrated that it does not introduce significant differences in the material mechanical behavior, at least at macro and micro scales [390].

Therefore, heat treatments are exploited to relieve these issues. Here, heat-treaded components are compared with as-built (AB), i.e., non-heat-treated, components. In general, heat-treated Al-alloys undergo a reduction of tensile properties with respect to AB Al-alloys, i.e., an increase in the elongation at break. However, the aging treatment allows partial recovery of these tensile properties [106]. According to the literature [417], the following are the two most typical heat treatments for AlSi10Mg by SLM:

- Stress Reliving (SR): it consists of heating the component to a temperature below the critical range to relieve the stresses resulting from the additive manufacturing process. SR aims at reducing residual stresses in the component to improve its resistance and eventually avoid fragile failure during operation.
- T6 treatment: it consists of a solution treatment, a water quenching and artificial aging [107,418]. This treatment significantly modifies the microstructure and thus, the mechanical properties of components. It is mostly adopted to recover anisotropies of the material, but it may yield, in the case of AlSi10Mg, to the growth of large and agglomerated Si grains.

However, to qualify the post-processed components and verify the heat-treatment, quality controls are necessary, which, for example, may be based on testing the mechanical properties. This section proposes an ad hoc analysis procedure based on statistical tools applied in combination with indentation

characterization tests to assess the effectiveness of heat treatments on AlSi10Mg by SLM.

Methodology

Traditional Brinell hardness and Instrumented Indentation Test in macro and nano-range are considered to achieve full-scale characterization. IIT is applied both at the lower end of the macro-range to provide consistency and statistically investigate the relationship with the Brinell scale and in the nano-range, enabling local, i.e., grain, and surface properties characterization.

Traditional Brinell hardness [413] is, first of all, exploited to provide a reference to powder supplier specification. By indenting with a spherical indenter at high forces (order of at least tens of newton), it enables bulk, i.e., average, characterization of the material and yields a fast but rough characterization.

IIT is applied both at the nano-range, enabling local, i.e., grain, and surface properties to be characterized and in the lower end of the macro-range. The latter provides consistency and statistically investigates the relationship with Brinell scale. To this aim, according to annex F of ISO 14577-1 [419], as a first step according to Eq.(3.25), indentation hardness H_{IT} can be correlated to Vickers hardness HV by using a scaling function l, that depends on the unit conversion and the ratio between the projected area A_p and the surface area A_S of a Vickers indenter: if IIT is performed with a Vickers indenter l is 94.53. As a second step, the Vickers hardness HV has to be correlated to Brinell hardness HBW through the factor k. To this aim, conversion tables of ISO 18265 [420] may be exploited, providing the value of k = 0.95. However, since AlSi10Mg alloys are not specifically considered in such standard, an empirical conversion formula is derived, as:

$$HBW = k \cdot HV = k \cdot l \cdot H_{IT} \quad (3.26).$$

Experimental setup

In this case study, thirty AlSi10Mg cubes with a side of 20 mm were manufactured by the EOS M290 by SLM process. The SLM machine is one of the most recently introduced in the market by EOS. Hence little characterization has been reported. The powder material is provided and manufactured by EOS to optimize the build and has a composition reported in Table 29, and a nominal hardness of (119±5) HBW 2.5/62.5.

Table 29 Chemical composition of EOS AlSi10Mg for SLM. Al is the remainder.

Element	Si	Fe	Cu	Mn	Mg	Ni	Zn	Pb	Sn	Ti
% relative weight	9.0 -11	≤ 0.55	≤ 0.05	≤ 0.45	0.2-0.45	≤ 0.05	≤ 0.10	≤ 0.05	≤ 0.05	≤ 0.15

Once removed from the base plate and cleaned from residual powder [65], the cubes were then polished to avoid any superficial effect due to the surface

topography and the different processing condition to affect the mechanical characterization results [106].

Out of the thirty cubes, ten were post-processed with an SR treatment by holding a temperature of 300°C for 2 h, ten with a T6 consisting of a solution treatment at 540°C for 5 h, a water quenching and artificial aging at 160°C for 6 h [3,5]; the ten residue cubes are considered in their AB condition.

According to the following discussion, this section investigates the effectiveness of hardness tests in assessing heat treatment effects by tests in the full hardness range. Macro-instrumented indentations are performed by a Bruker UMT TriboLab (located in the FCA-CRF Laboratory – Group Materials, Torino) with a Vickers indenter, whilst nano-indentations are realized by a Hysitron TI 950 (located at Istituto Italiano di Tecnologia, Torino) with a Berkovich indenter.

HBW 2.5/62.5 tests were performed to provide a reference with the material specification sheet from the powder supplier.

To investigate accordance between Brinell and indentation hardness, the scales HBW 1/10 and macro-instrumented indentation test with force-controlled cycles at a maximum force of 100 N, i.e., H_{IT} 100/50/10/40 respectively, were chosen. These scales' choice complies with the material data sheet's force-diameter index of 10 N/mm, which ultimately defines the Brinell scale [413], and the limit test forces achievable with the Brucker indenters and the Brinell scale lower range.

Last, to assess local material properties, nano-instrumented indentation test with force-controlled cycles at a maximum force of 5 mN as H_{IT} 0.005/5/2/5. SLM introduces anisotropy in the manufactured workpieces. Thus, tests were performed on the top (*xy*) surface and one side surface (*xz*) of the cube.

Tests were carried out under the hypothesis that manufactured cubes' mechanical properties are uniform, at least at a macroscopic level, according to the known process repeatability [106,107]. Therefore, Brinell hardness tests, i.e., both HBW 2.5/62.5 and HBW 1/10, were performed on nine out of ten samples per heat treatment, with three replicated measurements. Instrumented indentation test is more refined than Brinell hardness [421]. Therefore, it is exploited to investigate local mechanical properties variability by performing a grid of 7×7 macro-instrumented indentations on one of the nine samples. Process repeatability guarantees the significance of the comparison between the mentioned 3×9 HBW and the macro-instrumented indentations. A devoted sample, i.e., the one left per each treatment, was exploited to perform the mechanical characterization at a small scale using a 11×11 nano-instrumented indentation grid. This choice aimed to test the top surface and avoid residual stress fields locally introduced by indentations at different scales superimpose.

Results discussion

Statistical data analyses were carried out on each data set, i.e., HBW 2.5/62.5, HBW 1/10, macro-IIT and nano-IIT, to test i) their normality, and based on the

heat treatment, ii) the anisotropy effect on mean estimates and iii) on their dispersion.

Firstly, the possible presence of outliers was investigated according to Chauvenet's method [422]. Given the dimensions of data sets, highlighted outliers were excluded from further analyses. Normality tests were performed using χ^2-test at a confidence level of 95% and supported by a graphical investigation through normal probability plot (NPP) [423]. The null hypothesis of normality cannot be rejected for characterization results in the macro range, i.e., HBW 2.5/6.25, HBW 1/10, H_{IT} 100/50/10/40. This is consistent with the scale of investigation of the test, which by design, it is not expected to detect local variations of material properties. Moreover, Figure 77 shows that NPPs have a clustered shape typical of scales with poor resolution, e.g., HBW 2.5/62.5, which, though, it is less evident for more sensitive tests, e.g., macro-IIT and nano-IIT.

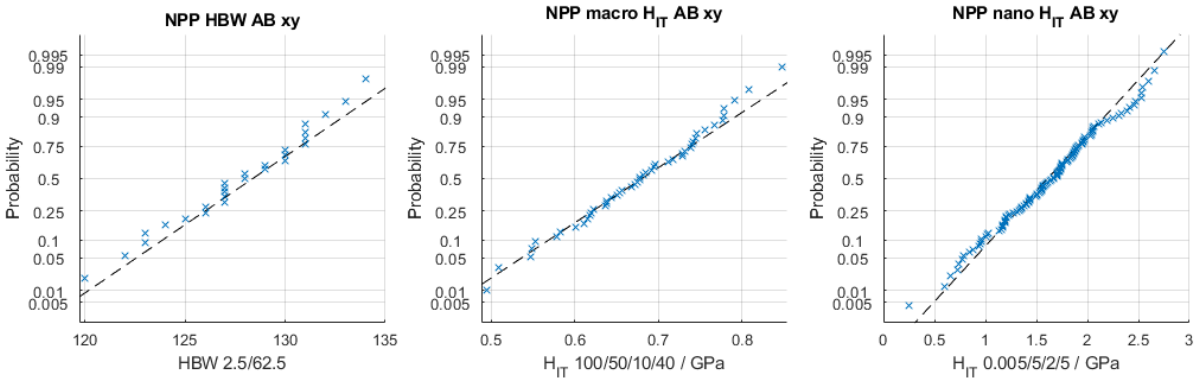

Figure 77 NPP of hardness from macro to nano scale. Normality hypothesis cannot be rejected. Notice the increased resolution at lower scales. AB in the top (*xy*) surface are shown as representative condition.

Investigations of systematic differences between characterization results due to i) heat treatment and ii) anisotropy are carried out by means of 1-way ANOVA and hypothesis t-test on average value at a confidence level of 95%.

Although with different power and capabilities, both statistical tests consistently conclude that, independently from the characterization scale, there are systematic differences in the characterization results amongst different heat treatments within the same direction.

Moreover, when considering the same heat treatment, and the hypothesis of isotropy is addressed, for T6 data, such hypothesis cannot be rejected with a risk of error of 5%. H_{IT} 100/50/10/40 represents an exception to this result as isotropy shall also be rejected for T6. This can be explained considering the greater sensitivity, due to both the shape of the indenter and the testing procedure itself, of the macro-IIT with respect to the Brinell test [421]. This is also confirmed by the hypothesis test on the sample variance performed to investigate homoscedasticity amongst the different conditions. At a confidence level of 95%, the greater sensitivity to local variations of the macro-IIT leads to rejecting homoscedasticity in all cases, whilst HBW 2.5/62.5 and 1/10 cannot reject it for SR and T6. From a microstructural perspective, this result is consistent with the

characteristics of T6 treatment and the resulting microstructure featuring large and agglomerated Si grains [107]. As Figure 78 shows, the 7×7 grid indentations on the T6*xy* were performed on the Al matrix excluding Si: values have a shorter and centered on lower values range than the T6*xz*. The polished surface required to perform IIT hinders an a-priori localization of indentation spot by metallographic microscopes. The collection of more data, also on different samples, could statistically solve the issue, avoiding such systematic effect.

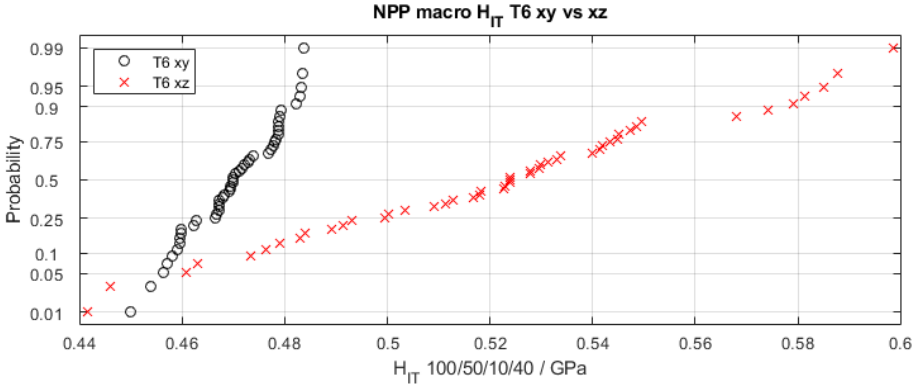

Figure 78 NPP of H_{IT} 100/50/10/40 on T6 on xy (black o) and on xz (red ×) surface. Notice the shorter range centred at lower values for *xy* data highlighting the exclusion from tested region of Si grains, that are harder.

Similarly to the macro-scale case, data sets' nano-scale normality cannot be rejected but for the T6 case. In particular, the T6 microstructure is even more impacting as a significant deviation from normality results. Literature suggests that indentations may have been performed at the interface of two phases, explaining the bimodal shape of the NPP shown in Figure 79 [107]. Systematic differences within the same direction amongst the three treatments are still highlighted by ANOVA and t-test on averages. Differently, anisotropy is no more detected with statistical significance in any cases because of the scale of characterization.

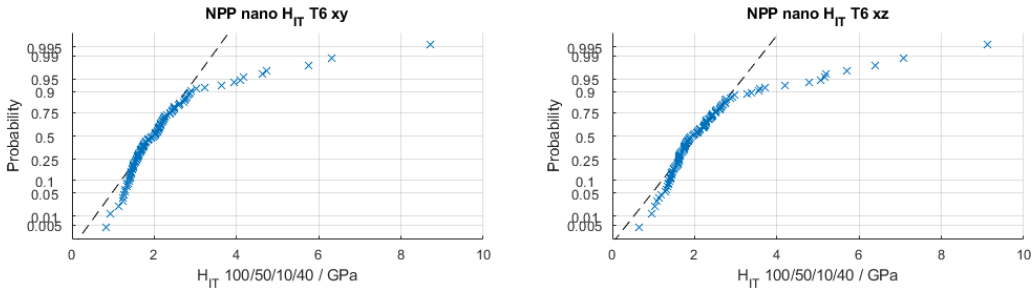

Figure 79 Large and agglomerated second phases of Si, generated by T6, yield bimodal distribution, highlighted by nano-IIT.

As in most common industrial practices, the powder manufacturer specifies in the datasheet HB 2.5/65.2 for the AB. Satisfactory compliance of experimental results with the specification is shown in Figure 80, considering expanded uncertainty from reproducibility of the measurement with a coverage factor of 2.

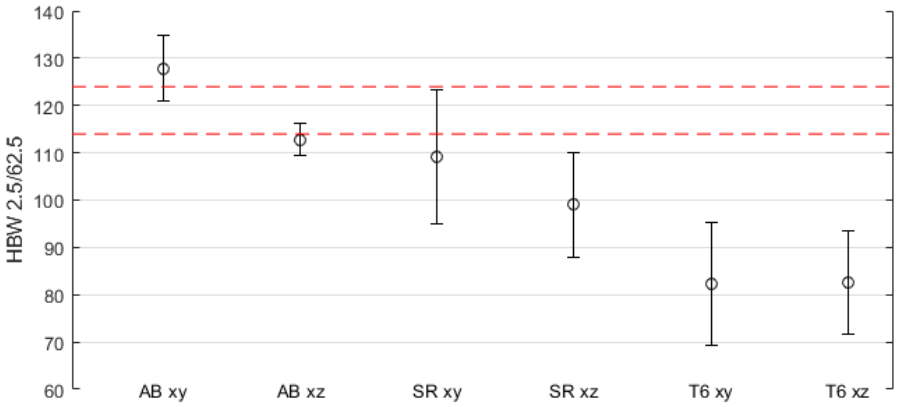

Figure 80 Comparison between AB HBW 2.5/62.5 experimental (error bar) and nominal values (red dashed lines). Notice the decreasing trend of average value due to microstructure change and the recovery of isotropy from AB to T6.

Although hardness scale conversion cannot substitute for an actual measurement, it can still provide relevant information about scale compatibility [420]. Scale conversion is addressed according to the methodology, and results are shown in Figure 81. The regression implemented to estimate the scaling factor $k \cdot l$ of Eq.(3.26) yielded a result of (164±7) HBW/GPa, which entails a k of 1.75, almost twice the tabulated value in [420]. This stresses further the need to assess devoted conversion for specific materials, which is more compelling when AM materials are involved. Scale conversion allows highlighting compatibility and accordance of characterization on different scales, which are relevant for industrial practice. In particular, the recovery of the anisotropy from AB to T6 is shown in Figure 80 and Figure 81 with error bars that, in the latter case, completely overlap. Furthermore, a systematic decreasing trend of the hardness can be highlighted from AB to T6, consistent with the microstructure modification, as the heat treatments promote grain growth to relieve stresses and recover isotropy. IIT greater sensitivity yields larger dispersion, which reduces for T6 due to a more uniform microstructure that is relieved of residual stresses.

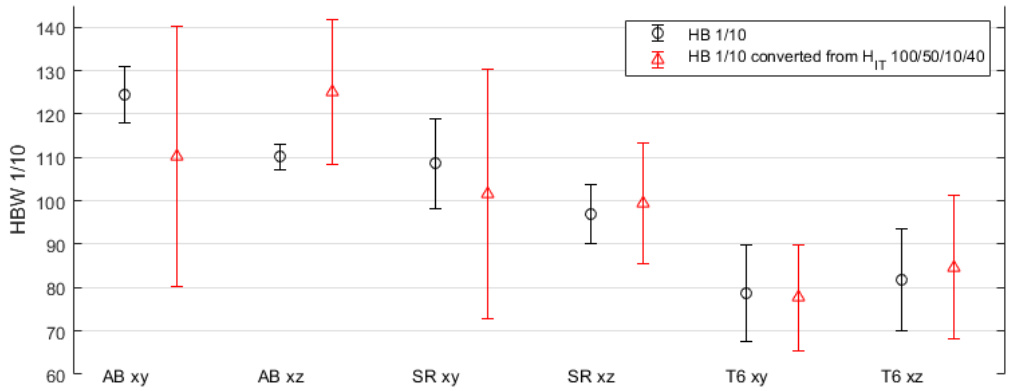

Figure 81 Results of scale conversion. Error bars represent Expanded uncertainty with coverage factor of 2.

Section summary

Entities involved in a supply chain may characterize materials and state specification by a wide set of tools, whose consistency is thus essential to be assessed. The industrial practice relies upon a fast characterization method, as hardness tests, of which several alternatives, with different peculiarities, have been proposed during the past century. This section exploited hardness scale conversion to prove consistency between Brinell hardness scales and IIT. Moreover, a thorough macro- to nano-scale characterization assessed their capability to detect the effects of heat treatments performed on AlSi10Mg by SLM. Indentation testing performs adequately in assessing the effectiveness of heat treatments. IIT, in particular, thanks to its superior refinement, is also capable of providing microstructure-related characterization at all considered scales.

3.3.2 Multi-sensor multi-scale technological surfaces characterization[9]

The need to develop highly engineered materials combined with advanced manufacturing processes is one of the main drivers of technological innovation, with numerous applications in aerospace, automotive, biomedical and other sectors [68,424].

In particular, at the early stages of the product-process development process, a thorough characterization is essential to understand how the material, and hence the final product, is affected by the manufacturing process, and ultimately the mechanical properties it will have in its final form. Currently, academia and industry extensively focus on developing composite materials often reinforced

[9] Part of this section was also previously published in: Maculotti G, Senin N, Oyelola O, Galetto M, Clare A, Leach R (2019) Multi-sensor data fusion for the characterization of laser cladded cermet coatings *Proceedings of the 19th International Conference and Exhibition of EUSPEN*, Bilbao (ES), June

with hard ceramic particles to enhance product performances in terms of tribological properties and durability [234,425–427]. These types of materials assume a multi-phase configuration. This requires a thorough characterization, which usually implies investigating the individual phases, their reciprocal interaction, and their overall layout within the product, observed via cross-sectioning [7]. Multiple heterogeneous measurement technologies can be used, e.g., scanning electron microscopy (SEM), optical areal surface topography measurement, X-ray computed tomography, energy dispersive X-ray spectrometry (EDX), and X-ray diffraction. In parallel, mechanical properties, e.g., hardness, can be investigated by dedicated tests.

An opportunity to improve our knowledge and understanding lies in the capability of integrating multiple sources of experimental information. However, the integration of measurement results presents significant challenges due to the heterogeneity of the information sources and the need to reciprocally localize information contained within the same co-ordinate space to infer correlations.

To achieve this aim, literature resorts to multi-sensor data fusion. As mentioned in the Introduction this is a technique aimed at combining information gathered by means of several sensors to increase the overall informativeness of the acquired data [112]. Sensors, i.e., sources of measured data, can be homogeneous or heterogeneous; they can be combined according to different configurations: competitive, complementary and cooperative [428]. Sensors within a network require to be managed, and their measurements to be fused together. This is the most critical step. Literature addresses this challenge by several complex solutions, ranging from data set registration [111] to Gaussian process regression [429]. In the technological field, multi-sensor data fusion has been largely exploited in dimensional analyses [111]. Cooperative and complementary configurations are often exploited to perform measurement compensation and error correction across measured attribute to achieve a more accurate result [17,430–432].

Conversely, a competitive sensors network allows to reduce measurement uncertainty or achieve across domains, i.e., multi-scale, data fusion [430,433]. Within dimensional applications, multi-sensor data fusion soften consists of augmenting the measurement's informativeness by registering different homogeneous data sets. However, in the current industrial framework, heterogeneous data set, images, point clouds, and volume scans are necessary to describe the analyzed components thoroughly. This requires more advanced solutions to deal with the problem at hand, e.g., Gaussian Process Regression to support data registration [110,199].

The case in which heterogeneous data sets are merged within a complementary configuration is different and more complex. Though, this is typically sought to achieve thorough characterization of technological surfaces for innovative materials and processes, both in industry and academia [7,111,112,434].

Accordingly, in this section, an original multi-sensor data fusion approach is presented, focused on spatial co-localisation of heterogeneous datasets to achieve

thorough characterization of a technological surface and as a fundamental precondition to enable the development of correlation models. Preliminary considerations on uncertainty evaluation are additionally provided to enable uncertainty evaluation of to-be-set correlation models. The method is applied to a case study of industrial interest.

A case study: cermets

A metal matrix composite material obtained from titanium-alloy metal wire and tungsten carbide ceramic powder, i.e., Ti-6Al-4V (WC/W2C) cermet, is selected as the test case. The material is deposited in multiple layers to produce a coating through laser deposition, a beam deposition process [435]. It is a flexible process as the deposition head can be mounted on both CNM and wrist of industrial robots, is traditionally exploited for fixing components' minor damages, and is now adopted for coating deposition [435]. As shown in Figure 82, the deposition head features a laser source and two material feedstock suppliers: one for the primary material of the matrix, typically a metal wire, and the second for the reinforcement, which can either be a powder, mostly for ceramic, or a wire. The material is locally deposited and melted by the laser beam to achieve local consolidation.

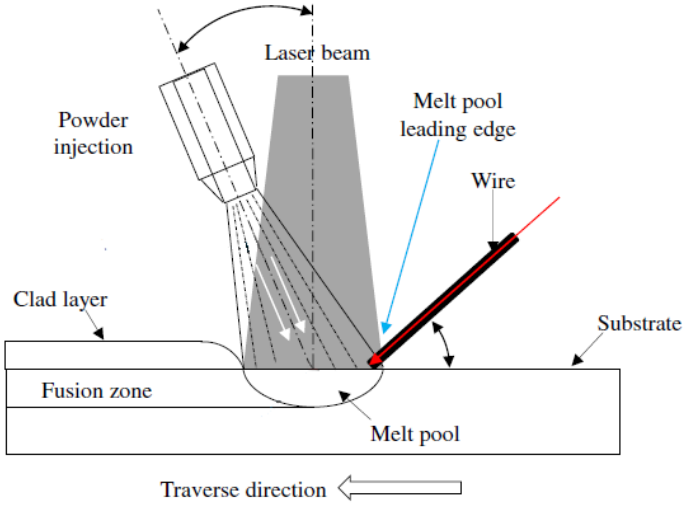

Figure 82 Schematic of laser deposition (adapted from [436]).

In particular, it can deposit composite materials, whom cermets are an example of, based on a metallic matrix and ceramic inclusions. Multi-layer cermets, such as those addressed in this work, are becoming increasingly popular where wear, thermal management, enhanced structural stiffness, and hardness are critical [437–439]. Thus the problem of their characterization is of significant importance. Extended research is currently being performed, to understand the effects on material properties of the several degrees of freedom of laser cladding, including materials, their feedstock, and process parameters [436,440,441]. In this work, the analysis focuses on investigating the interfaces between the metal

matrix and the ceramic particles, the main phases in the deposited cermet. The interfaces are relevant as they feature varying microstructural and mechanical properties due to solid-state diffusion of ceramic material into the metal matrix, yielding to hardness gradients. The geometrical and physical conformation and spatial distribution of the particles, the surface topography, hardness, and hardness gradient as observed in cross-sections of the coating layers are important characterization targets as they affect overall material properties. These targets depend on process parameters and thus are also crucial for process control. Moreover, they influence the choices for further post-processing, e.g., via machining, as inhomogeneous mechanical properties result in high fluctuation of the cutting force and, hence, in reduced tool life [442].

The test case whose analysis is illustrated in this work is a laser deposited Ti-6Al-4V (WC/W2C) cermet component produced by the Advanced Manufacturing Research Group at the University of Nottingham [436].

Sources of measured data

Multiple sources of measured data were considered: SEM and EDX for microstructural imaging and qualification of chemical composition, coherence scanning interferometry (CSI) for optical areal surface topography measurement, and nano-instrumented indentation testing (nano-IIT) to characterize hardness in the nanometre range.

In backscattered electron measurement mode, SEM can be used to distinguish amongst different constituent phases of the material, despite limitations due to poor correlation between phase and grey level in the generated SEM images [443,444]. SEM imaging was performed with an acceleration voltage of 20 keV at different magnifications, i.e., 10 000×, 1 200× and 600×, resulting in a lateral resolution of 46 nm/pixel, 111 nm/pixel and 222 nm/pixel, respectively. Figure 83 shows an example of SEM images at 600× and 1 200×.

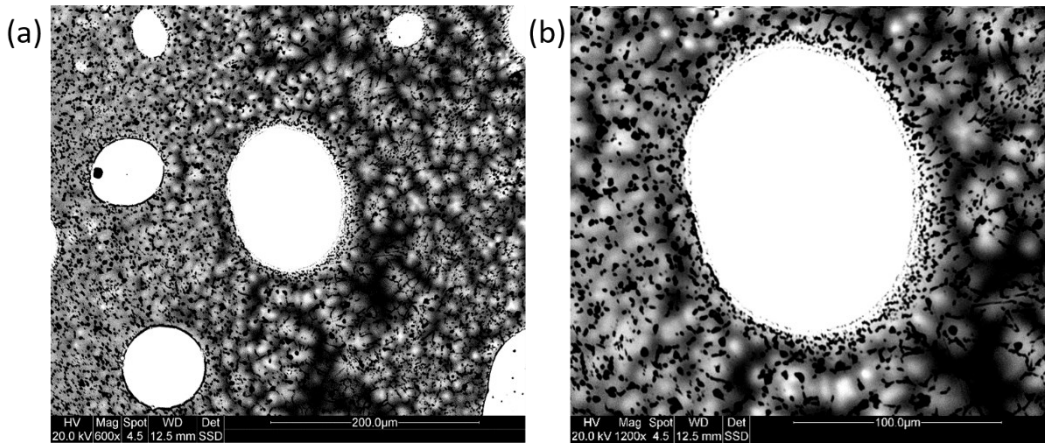

Figure 83 Example SEM images at different magnification showing the cermet cross-section (ceramic particles, i.e., the WC phase, appear bright): (a) 600× and (b) 1 200×.

EDX qualifies the phases' chemical composition by measuring the energy and the number per type of diffracted X-rays. EDX is performed on points selected by the operator on a SEM image, see Figure 84(b). Thus, SEM and EDX datasets feature the same coordinate reference system if generated as part of the same measurement session with the same instrument. In this work, a SEM and EDX Philips FEI XL30 were used at the Nanoscale and Microscale Research Centre, University of Nottingham.

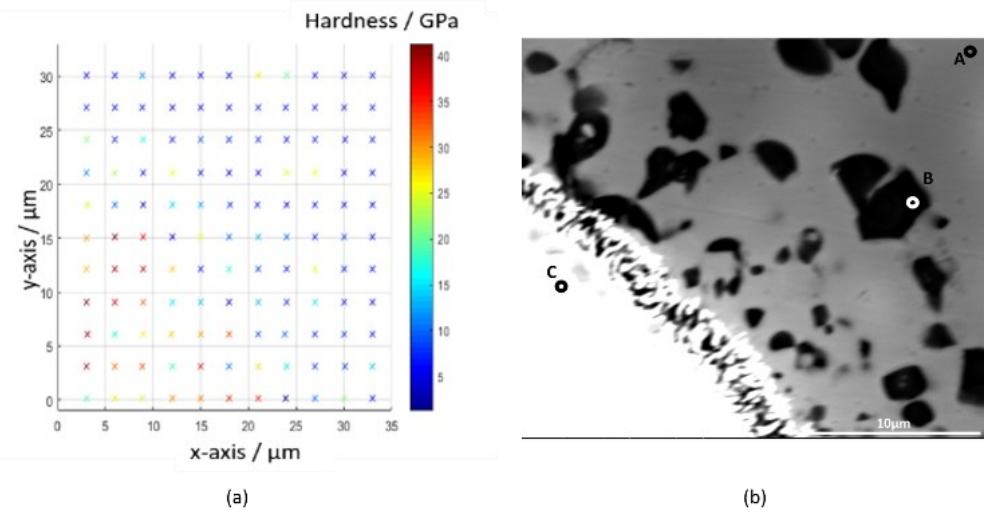

Figure 84 Nano-IIT processed area. (a) nano-hardness map, colour is proportional to measured nano-hardness; (b) SEM at 10 000×: some of the indentation marks are barely visible. A, B, C are examples for the EDX characterization.

A series of nano-IIT tests performed at different positions over a plane allows distinguishing material phases and creating phase maps [336,445–447]. Nano-IIT was performed using a Hysitron TI950 at the Instituto Italiano di Tecnologia of Turin, Italy. A grid of 11×9 indentations at 1 mN maximum cycle test force was performed, with a covered area of (30 × 25) µm, to provide significant testing area and high lateral resolution of nano-hardness values. The horizontal axes transducers of the selected nano-IIT instrument allow localization of the indentations in a co-ordinate space, with a nominal positional accuracy of 1 µm. In Figure 84(a), an indentation map is shown along with a SEM image at 10,000× magnification, where some indentation marks are visible (to cover the whole grid of indentations, multiple images at this magnification are necessary). Visible indentation marks were selected as reference positions for EDX.

Example EDX results are shown in Table 30 for the three inspected points highlighted in Figure 84(b). The white region in the bottom left of the SEM image in Figure 84 (b) represents the WC phase; the grey regions represent the metal matrix, the black regions indicate the second phase of TiC-W precipitates. Spectra of EDX characterization are reported in Figure 85.

Table 30 EDX Results. Chemical composition (wt %) for the three example points shown in Figure 84(b).

Region	C	Al	Ti	V	W
A	27.55	3.67	47.06	2.80	18.92
B	29.01	0.97	64.53	1.12	4.36
C	28.59	-	-	-	71.41

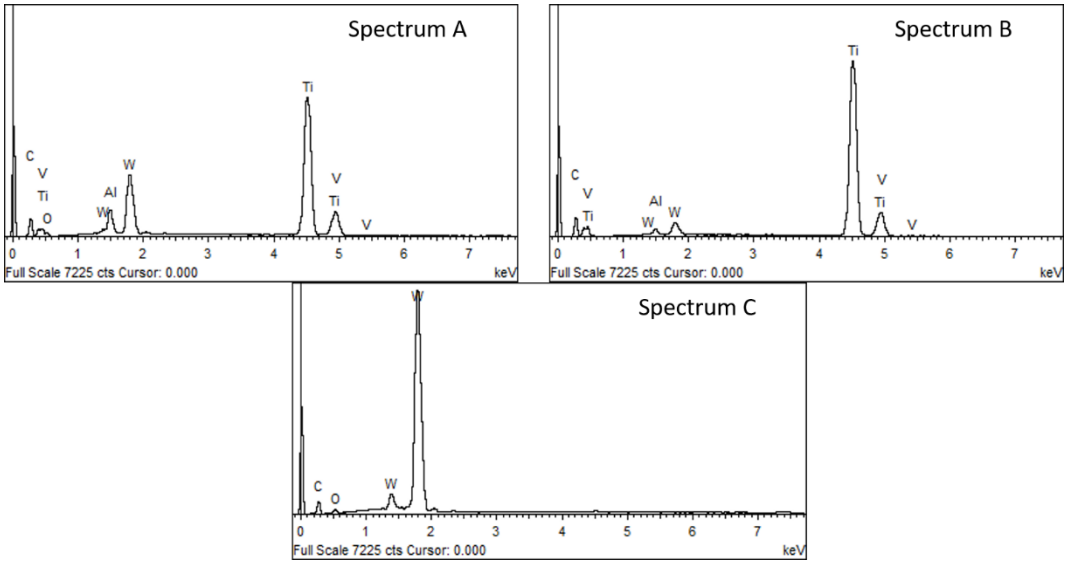

Figure 85 EDX spectra of the three points in Figure 84(b).

Nano-IIT requires the sample cross-section to be ground and polished [448], leading to highly reflective surfaces whose topographies are suitable for capturing via CSI measurement [113]. Surface topography was measured with a Zygo NewView 8300, at the Manufacturing Metrology Team laboratory, University of Nottingham. Because the nano-indentation marks were barely visible given the lateral resolution of the CSI even with the 50× objective, CSI measurement had to be performed without precise referencing to the grid. CSI measurements were performed to cover a wider area of (640 × 1000) μm, to compensate for the former issue. In so doing, larger and visible landmarks could be incorporated, useful for co-localization. A wide area was obtained by measuring 2×3 FOVs, each sized (0.43 × 0.43) μm, using a 20× objective with a lateral resolution, evaluated according to the Sparrow criterion, of 0.63 μm; Figure 86 shows one FOV.

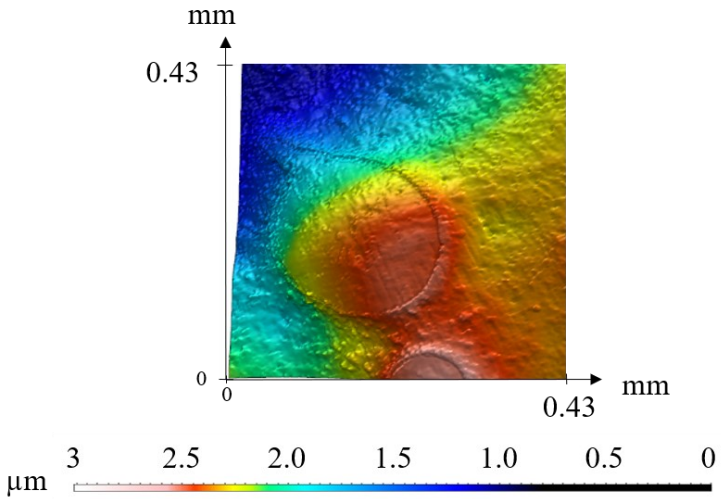

Figure 86 CSI pseudo-color height map (single FOV at 20×) showing a region of the sample cross-section. A large ceramic particle and its interface are visible.

Multi-sensor data fusion

Despite being heterogeneous in content and organization (structure and format), all the discussed datasets feature spatially localized information, although they do not necessarily share the same coordinate systems. The fundamental pre-requisite to search for correlations between the datasets is to solve the co-localization problem (i.e., bringing all the datasets into the same coordinate system). Co-localization may not necessarily imply seeking the maximum overlap of measured data points, as, in principle, heterogeneous datasets will be characterized by different sampling densities and coverage ranges, making it unlikely to have spatially coincident measured points.

Fusion of image-like, homogeneous datasets

Datasets formatted like digital images and obtained from the same instrument and same set-up, but possibly referring to different regions of interest (ROIs), can benefit from co-localization within a common coordinate space, for example, to extend coverage range without sacrificing resolution. The fusion of image data with partially overlapping ROIs (referred to as stitching) can be implemented on optical and non-optical images and height maps. In this work, stitching of SEM images (see example in Figure 87(b)) was implemented with a custom-developed method consisting of alignment of pairwise-matched landmarks algorithmically identified via the SIFT (Scale Invariant Feature Transform) method [449]. Stitching of CSI maps (e.g., see Figure 87 (a)) was implemented instead of using surface metrology software integrated with the CSI instrument.

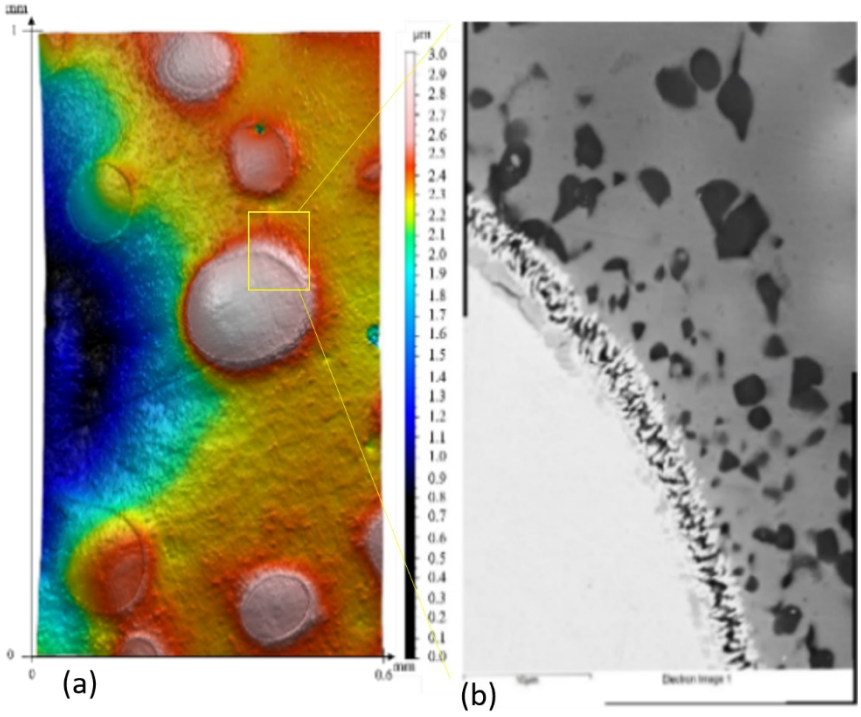

Figure 87 Stitched datasets obtained by (a) CSI at 20× and (b) SEM at 10 000×. An approximate indication of localization of the SEM ROI within the area covered by CSI is provided as a qualitative reference by the yellow box.

Co-localization of heterogeneous datasets

In some simpler cases, heterogeneous datasets may not need co-localization. For the test case, this happened with EDX measurements because the measurement positions were selected on SEM images taken with the same instrument, same set-up, and within the same measurement session; thus, they shared a common co-ordinate system. Usually, though, heterogeneous datasets are obtained from different instruments and in the absence of a common spatial reference frame; thus, co-localization is necessary.

Similarly to stitching, the presence of landmarks shared within overlapping segments of the ROIs is the main facilitator for co-localizing heterogeneous datasets.

However, landmarks are suitable to support co-localization only if represented and recognizable within each dataset, which may not necessarily be the case for measurements that may target different properties and react differently to the measured sample, thus ultimately capturing different aspects of the same landmark, or none at all. When pairwise matching of landmarks is possible and reliable, then heterogeneous datasets can be co-localized by solving the absolute orientation problem [450]: i.e., by finding the transformation matrix that minimizes the root mean squared error (RMSE) between pairwise-matched points.

For the co-localization of the SEM images, CSI height maps and nano-IIT maps, a simpler, two-dimensional version of the absolute orientation problem was adopted, with the optimal transformation constrained to take place in the *x,y*

image plane. In the two-dimensional case, the rotation matrix is driven by one angle α, and the pivot point (x_0, y_0), the translation defined by vector t and a scale vector (s_x, s_y) compensates for potential global magnification errors in the two axes of the SEM or CSI image, thus resulting in Eq.(3.27) which describes the two-dimensional version of the absolute orientation problem:

$$\begin{bmatrix} x' \\ y' \\ 1 \end{bmatrix} = [S] \begin{bmatrix} x \\ y \\ 1 \end{bmatrix} = [s_x \quad s_y \quad 1] \begin{bmatrix} \cos(\alpha) & \sin(\alpha) & -x_0 + t_x \\ -\sin(\alpha) & \cos(\alpha) & -y_0 + t_y \\ 0 & 0 & 1 \end{bmatrix} \begin{bmatrix} x \\ y \\ 1 \end{bmatrix} \qquad (3.27).$$

For the test case, the co-localization of nano-IIT, SEM and CSI datasets was performed in steps.

At the first stage, the nano-IIT dataset was localized in the 10 000× stitched SEM image coordinate system. Pairwise-matched points for alignment were identified from the nano-IIT indentations' coordinates, and the centroids of the visible indentation marks in the SEM image on the other. Because most indentation marks were barely visible in the SEM image, and algorithmic identification [451] would be frequently disturbed by the presence of larger and better-contrasted regions, localization of indentation centroids in SEM was preliminarily performed manually. However, better algorithmic solutions are currently being studied. The transformation matrix to maximize overlapping of pairwise-matched points was computed automatically, considering in a first step all visible indentation marks. A second alignment pass was performed, based again on solving the same absolute orientation problem, to refine further the co-localization. This time it only considered a subset of pairwise matched indentation centroids, selected as the closest to each other after the first alignment step according to a k-nearest neighborhood algorithm [452]. These are the cyan rectangles in Figure 88.

Alignment results were computed, catering also for positional uncertainty in the nano-IIT dataset. Figure 89 shows the co-localization results at two different scales. A colored box is drawn about each nano-IIT indentation centroid to represent location uncertainty originated by the nano-IIT system's positioning error: it can be noted that most of the indentation marks visible in the aligned SEM image fall within the boxes, indicating an acceptable co-localization result.

The second stage of the multi-sensor data fusion co-localization process consisted of positioning the SEM datasets (600×, 1 200× and 10 000×) within the coordinate reference frame of the CSI dataset (20×). It was also based on identifying pairwise-matched landmark points and alignment by solving the absolute orientation problem.

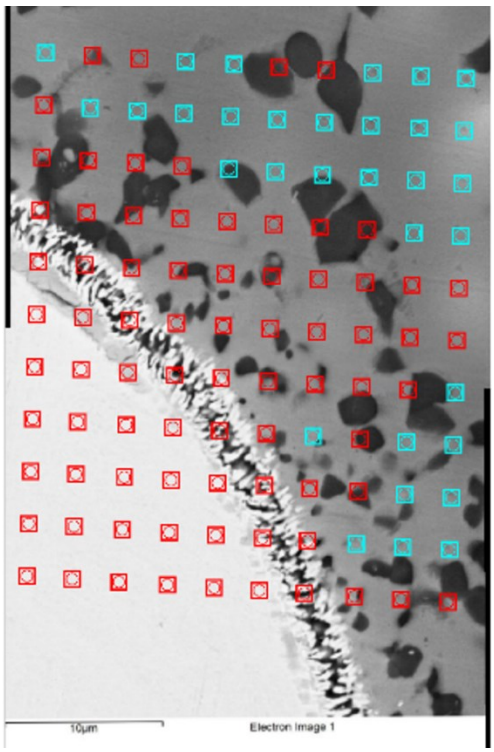

Figure 88 In red, complete grid of indentation, in cyan k-nearest neighborhood set for refined alignment.

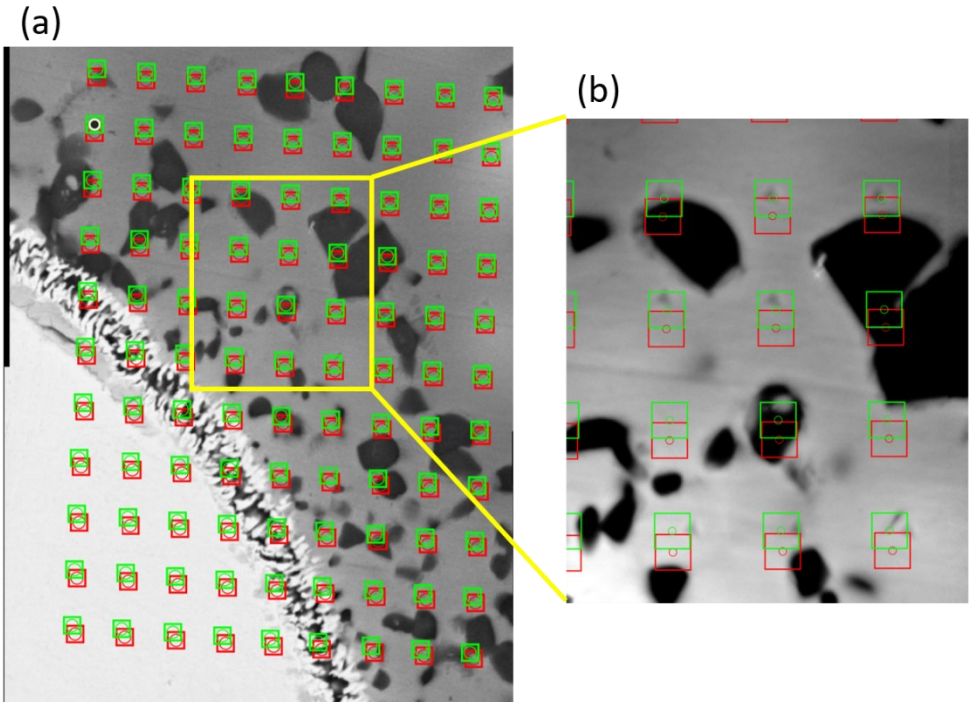

Figure 89 (a) Hardness to SEM registration. Red is coarse alignment; green is fine alignment; boxes represent location uncertainty due to accuracy of nano-IIT platform. (b) Higher detail image of the yellow box, where indentations can be seen.

However, not all the SEM datasets would feature landmarks easily visible within the CSI dataset, because of the sometimes large scale differences (e.g., between 20× CSI and 10 000× SEM).

Therefore, a first co-localization was performed to align the lowest magnification SEM dataset (600×) to the CSI dataset. For this co-localization, the transition edges between phases, i.e., the ceramic particles' boundaries visible in both datasets, were used as alignment landmarks. In fact, SEM distinguishes microstructures whilst CSI macro features, at most; therefore, a method to highlight points to be matched is necessary, and features edge can be exploited to determine robust identification of characteristic points of an image. Here a method is proposed to extract features edge; it consists of i) denoising the surface through a high-pass filter and ii) application of an edge-finding algorithm. Implementation is performed on *MATLAB 2018b,* which requires operation on greyscale images. Even though denoising could be achieved by wavelet deconvolution algorithm [453], due to the fine structures, the application is not effective, and 2D Gaussian smoothing kernel, with a standard deviation of 10 pixels (set by trial and errors) was more robust. Amongst the several edge detection algorithms available in the literature, e.g., Canny, Sobel, Prewitt, Roberts [454], due to its greater robustness to noise and capability of correctly locating complex edges, the Laplacian of Gaussian (LoG) detector, which is based on the detection of intensity change points, i.e., the zero-crossing point of the Laplacian of the image convoluted, for scale detection, to a 2D Gaussian filter [455];

According to Horn's method, once edges have been extracted, couples of matching points have to be found and exploited to evaluate the orientation matrix. The edges were recognized automatically both on SEM images (on grey levels) and CSI maps (on height values) by application of a LoG (Laplacian of Gaussian) operator [454,455]. Adopting the Laplacian filter guarantees independence from orientation, which is critical since intensity change is related to anisotropic optical properties of the operation and reduces the computational cost of convolution.

Then the 1 200× SEM dataset was aligned to the already localized 600× one, and finally, the 10 000× SEM dataset was aligned to the 1 200× one. Both alignments were performed using pairwise-matched landmarks, both again using inter-phase edges as alignment references. The final transformation matrix found for the 10 000× SEM dataset was also applied to the nano-IIT and EDX data to preserve their prior co-localization to the SEM set.

Figure 90 shows some example results of the co-localization process involving CSI and SEM datasets at multiple magnifications.

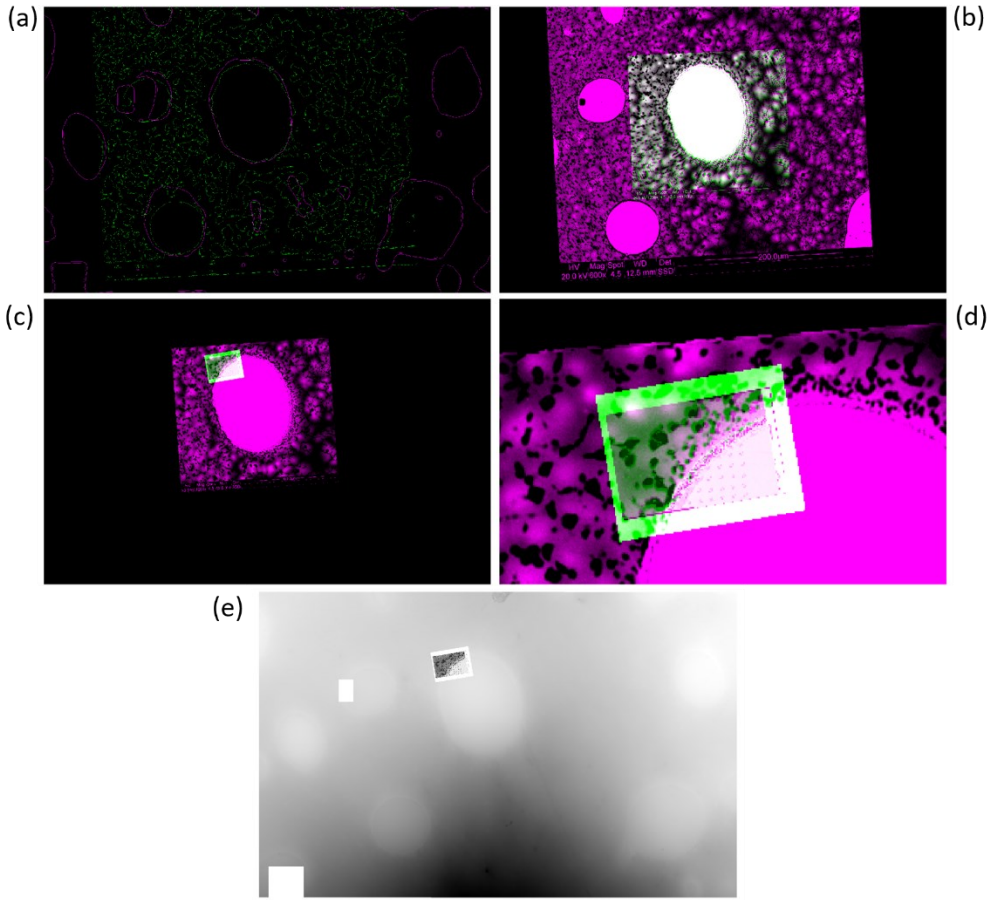

Figure 90 SEM to CSI co-localisation; images in CSI reference frame (90° counter clockwise rotated with respect to previous figures). (a) 600× SEM (green) to CSI (purple), edges are shown for clarity; (b) SEM 1 200× (green) to SEM 600× (purple); (c)) SEM 10 000× (green) to SEM 1 200×; (d) detail to highlight the TiC-W precipitates structures exploited for point pairs selection; (e) 10 000× SEM to CSI height map (rendered in grayscale).

The final co-localization error was estimated as 17.6 µm, combining the individual uncertainties obtained from the respective alignment RMSEs [286]. The individual error contributions are summarised in Table 31. For the test case, Table 31 highlights the SEM dataset's alignment at 600× to the CSI dataset as the most critical step in terms of error contribution. Clearly, a more comprehensive estimation of expanded uncertainty for multi-sensor data fusion has not been achieved yet. Further contributions, here not considered, include stitching and error associated with the individual measurement instruments (e.g., aberration in SEM images [7] positional uncertainty of the nano-IIT).

Table 31 RMSE contributions of each co-localization operation.

	nano-IIT to 10,000x SEM (coarse)	**nano-IIT to 10,000x SEM (fine)**	**SEM 600x to CSI**	**SEM 1200x to CSI**	**SEM 10 000x to CSI**
RMSE / µm	0.48	0.21	17.60	0.43	0.77

Section summary

Multi-sensor data fusion for the wide-spectrum characterization of innovative materials combined with advanced manufacturing processes has been investigated. The analysis has focused on a metal matrix composite deposited in a multi-layered coating using laser deposition. The problem of co-localization of homogeneous and heterogeneous measured datasets has been addressed, and the feasibility of solutions based on the alignment of pairwise-matched landmarks has been analyzed. Automated identification of landmarks has been found to be the most critical aspect of the method. Preliminary considerations on evaluating uncertainty associated with the procedure also indicate that further analyses are needed to cater for a larger number of error sources.

Chapter 4

Conclusions

The modification and characterization of technological surfaces is core in modern industry and within Industry 4.0 to enable the development of manufacturing processes and materials, to provide end customers enhanced functionality, and support sustainable applications. The product and process complexity, to enable effective quality controls, requires information-rich inspection techniques that must also be reliable, robust, accurate, and precise.

Within this framework, this thesis aimed at achieving some advancements to methods available for characterizing technological surfaces, specifically from a geometrical and mechanical perspective. In particular, as discussed in the Introduction and motivated by the relevant literature review, the following research objectives were tackled:

- Effect of augmentation of conventional measurement techniques' informativeness on topography characterization,
- Assessment of measurement uncertainty of wear volume measurement methods based on topographical measurement,
- Reducing measurement uncertainty of instrumented indentation test,
- Improving calibration procedure for nanoindentation testing machines.

Amongst other available point augmentation methods, Kriging methodology was considered, relying on spatial correlation properties typical of manufacturing processes. It proved effective in predicting textured surface patterns even if based on sparse economic measurements since no systematic difference between characterization parameters obtained by the proposed approach, and denser methods could not be highlighted. This may provide an efficient and effective tool to SMEs to cope with surface topographies' characterization requirements by augmenting traditional contact measurement methods' informativeness.

Future works, relying on these results although changing the economic perspective, may exploit this approach to manage, i.e., identify and correct,

measurement disturbances of information-rich and dense optical surface topography measurement methods.

In this work, a performance comparison of different literature methods to estimate wear and damage volumes of surfaces was addressed. The comparison exploited the development of the measurement uncertainty evaluation based on the most recent surface topography measuring instrument characterization standards, which was missing in current literature. Additionally, it proposed a methodology to estimate the uncertainty of surface topography areal field volume parameters. It showed that the current wear volume characterization standards for tribological pin-on-disc tests might require an update to cope with the most recent measurement technologies.

These results may be exploited in the future to support the development of calibration and verification pipelines and the choice of reference blocks for the pin-on-disc test. Similarly, these results may be exploited to develop uncertainty evaluation methods for wear volume measurements in more complex cases, such as: non-localized wear, e.g., fretting, small amounts of wear, e.g., due to hard materials, or wear on complex topographies. In fact, these cases are typically addressed by means of machine vision algorithms. Conversely, the proposed research feature at least one main limitation. It neglected the choice and the selection of the region of interest. This was dispensed with as the considered cases featured a negligible roughness with respect to the wear scar. The simplification that is reasonable for the considered cases is clearly not general. Often practitioners select the region of interest manually. However, ad-hoc automated algorithms are needed to guarantee the repeatability of the results. Future works may aim to develop machine vision methods to cope with this challenge.

Advanced non-conventional mechanical characterization methods of surface topographies were investigated. In particular, this dissertation focused on the instrumented indentation test, which is a non-destructive flexible, and highly informative characterization method.

It was applied to case studies relevant to Industry 4.0, e.g., developing additive manufacturing process, innovative cermet materials, and proving their suitability for quality controls.

Furthermore, to establish traceability and provide end-users of instrumented indentation test with confidence in the obtained results, the main factors influencing measurement uncertainty were addressed.

An alternative methodology for evaluating the sample contact stiffness was outlined; it is based on the direct evaluation of the indentation curve's derivative, thus more adherent to the measurand definition, and yielded promising results in both terms of accuracy and precision.

Moreover, the calibration of main influencing factors, i.e., the frame compliance and the parameters of the indenter area shape function, was investigated, highlighting unreported severe shortcomings in the standardized method, as far as its prescriptiveness and robustness are concerned. Therefore, a

straightforward alternative approach was outlined, which resulted in definitive advantages in accuracy, precision, and computational efforts thanks to a more rigorous mathematical modeling. Last, methodology to assess the calibrated parameters' measurement uncertainty, which is missing in current literature and the standard, was proposed. Due to the complex nature of the calibration pipeline, two simulative methods were proposed: a Monte Carlo Method and a Bootstrap-based method. The latter provides simpler management of the correlated input quantities and reduces the preliminary experimental and statistical efforts required to set up the MCM. These results may promote the development of improved calibration pipelines. Similarly, they may support the investigation of other influence factors, e.g., identifying reference blocks' materials and the functional form of the indenter area function, which may impact the calibration results and ultimately reduce the characterization's measurement uncertainty.

The results obtained addressing the instrumented indentation test's metrological properties are relevant to enable traceability and guarantee high precision of this technique. They were obtained exploiting reference data sets; however, the author acknowledges that an international laboratory comparison may support these claims and test the robustness of the proposed calibration method.

However, the investigation of the influence factors to instrumented indentation test to measurement uncertainty was not thorough. Several aspects were not addressed and may be the object of future investigations: e.g., the area shape function, the calibration material, the thermal drift, and its correction. As far as the calibration of area shape function parameters is concerned, results augmentation might be obtained via the electric contact resistance method, which has been little exploited for this purpose and whose metrological performances are unreported. Last, the obtained results are limited to a specific operation mode of instrumented indentation test, i.e., the standard quasi-static. As discussed, several other alternatives are available, e.g., dynamic indentation, high-speed indentation, which were not considered here and shall be the target of future researches. However, the obtained results may provide useful guidelines for these characterization modes, too.

References

[1] Schmidt M, Merklein M, Bourell D, Dimitrov D, Hausotte T, Wegener K, et al. Laser based additive manufacturing in industry and academia *CIRP Ann* 2017 **66**:561–83.

[2] Mohanty A K, Vivekanandhan S, Pin J M, Misra M Composites from renewable and sustainable resources: Challenges and innovations *Science (80-)* 2018 **362**:536–42.

[3] Choi G M, Jin J, Shin D, Kim Y H, Ko J H, Im H G, et al. Flexible Hard Coating: Glass-Like Wear Resistant, Yet Plastic-Like Compliant, Transparent Protective Coating for Foldable Displays *Adv Mater* 2017 **29**:1–7.

[4] Yin Y, Stecke K E, Li D The evolution of production systems from Industry 2.0 through Industry 4.0 *Int J Prod Res* 2018 **56**:848–61.

[5] Salkin C, Oner M, Ustundag A, Cevikcan E A Conceptual Framework for Industry 4.0, Springer, Cham; 2018, p. 3–23.

[6] Jose R, Ramakrishna S Materials 4.0: Materials big data enabled materials discovery *Appl Mater Today* 2018 **10**:127–32.

[7] Bruzzone A A G, Costa H L, Lonardo P M, Lucca D A Advances in engineered surfaces for functional performance *CIRP Ann - Manuf Technol* 2008 **57**:750–69.

[8] Leach R Characterization of Areal Surface Texture2013.

[9] Griffiths B J Manufacturing Surface Technology: Surface Integrity and Functional Performance2001.

[10] Schlesinger G Research on surface finish *J Inst Prod Eng* 1942 **21**:1.

[11] Whitehouse D J Typology of Manufactured Surfaces *Ann CIRP* 1971 **19**:417–31.

[12] Chetwynd D G, McKee F A, Rakels J H Machined Surfaces: Final Texture and Underlying Structure 1982 **83**:233–40.

[13] Eppinger S D, Huber C D, Pham V H A methodology for manufacturing process signature analysis *J Manuf Syst* 1995 **14**:20–34.

[14] Peters J, Vanherck P, Sastrodinoto M ASSESSMENT OF SURFACE TYPOLOGY ANALYSIS TECHNIQUES. *CIRP Ann - Manuf Technol* 1979 **28**:539–54.

[15] Goeke S, Biermann D, Stickel D, Stemmer P, Fischer A, Geenen K, et al. Enhancing the surface integrity of tribologically stressed contacting surfaces by an adjusted surface topography *Procedia CIRP* 2014 **13**:214–8.

[16] Costa A B, Timm A D, Boutin F F, Elias S V F, Guimaraes I A, Fiad do Amaral P L, et al. Influence of RAM EDM Parameters on 3D Surface Roughness of the Quenched and Tempered Vc-131 Tool Steel. 22nd Int. Congr. Mech. Eng., Ribeirao Preto, SP, Brazil: 2013, p. 1–6.

[17] Bordin A, Bruschi S, Ghiotti A The effect of cutting speed and feed rate on the surface integrity in dry turning of CoCrMo alloy *Procedia CIRP* 2014 **13**:219–24.

[18] Goindi G S, Sarkar P Dry machining: A step towards sustainable machining – Challenges and future directions *J Clean Prod* 2017 **165**:1557–71.
[19] Gavalda Diaz O, Garcia Luna G, Liao Z, Axinte D The new challenges of machining Ceramic Matrix Composites (CMCs): Review of surface integrity *Int J Mach Tools Manuf* 2019 **139**:24–36.
[20] Tamás P, Illés B, Dobos P Waste reduction possibilities for manufacturing systems in the industry 4.0 *20th Innov Manuf Eng Energy Conf* 2016:012074.
[21] Chen X, Zhao J, Dong Y, Li A, Wang D Research on the machined surface integrity under combination of various inclination angles in multi-axis ball end milling *Proc Inst Mech Eng Part B J Eng Manuf* 2014 **228**:31–50.
[22] Cheng M N, Cheung C F, Lee W B, To S A Study of Factors Affecting Surface Quality in Ultra-Precision Raster Milling *Key Eng Mater* 2007 **339**:400–6.
[23] Boujelbene M, Moisan A, Tounsi N, Brenier B Productivity enhancement in dies and molds manufacturing by the use of C1 continuous tool path *Int J Mach Tools Manuf* 2004 **44**:101–7.
[24] Martínez-Mateo I, Carrión-Vilches F J, Sanes J, Bermúdez M D Surface damage of mold steel and its influence on surface roughness of injection molded plastic parts 2011 **271**:2512–6.
[25] Rytka C, Kristiansen P M, Neyer A Iso- and variothermal injection compression moulding of polymer micro- and nanostructures for optical and medical applications *J Micromechanics Microengineering* 2015 **25**:65008.
[26] Kuo H C, Jeng M C The influence of injection molding and injection compression molding on ultra-high molecular weight polyethylene polymer microfabrication *Int Polym Process* 2011 **26**:508–16.
[27] Chen T, Wang D, Gao F, Liu X Experimental study on milling CFRP with staggered PCD cutter *Appl Sci* 2017 **7**.
[28] Zhang P, Liu Z Modeling and prediction for 3D surface topography in finish turning with conventional and wiper inserts *Meas J Int Meas Confed* 2016 **94**:37–45.
[29] Bergstrom J, Thuvander F, Devos P, Boher C Wear of die materials in full scale plastic injection moulding of glass fibre reinforced polycarbonate 2001 **250**:1511–21.
[30] Loaldi D, Quagliotti D, Calaon M, Parenti P, Annoni M, Tosello G Manufacturing signatures of injection molding and injection compression molding for micro-structured polymer fresnel lens production 2018 **9**.
[31] Polini W, Moroni G Manufacturing Signature for Tolerance Analysis *J Comput Inf Sci Eng* 2015 **15**:1–5.
[32] Colosimo B M, Pacella M On the use of principal component analysis to identify systematic patterns in roundness profiles *Qual Reliab Eng Int* 2007 **23**:707–25.
[33] Pacella M, Colosimo B M Different formulations of principal component analysis for 3D profiles and surfaces modeling *Procedia CIRP* 2013 **12**:474–9.
[34] Murphy K P Machine Learning: A Probabilistic PerspectiveCambridge, MA: The MIT Press; 2012.
[35] Bengio Y, Goodfellow I, Courville A Deep learningCambridge, MA: MIT Press; 2016.

[36] Pacella M, Semeraro Q Understanding ART-based neural algorithms as statistical tools for manufacturing process quality control *Eng Appl Artif Intell* 2005 **18**:645–62.
[37] Pacella M, Semeraro Q Using recurrent neural networks to detect changes in autocorrelated processes for quality monitoring *Comput Ind Eng* 2007 **52**:502–20.
[38] Pacella M, Semeraro Q Monitoring roundness profiles based on an unsupervised neural network algorithm *Comput Ind Eng* 2011 **60**:677–89.
[39] Henke R P, Summerhays K D, Baldwin J M, Cassou R M, Brown C W Methods for evaluation of systematic geometric deviations in machined parts and their relationships to process variables *Precis Eng* 1999 **23**:273–92.
[40] Qi Q, Li T, Scott P J, Jiang X A correlational study of areal surface texture parameters on some typical machined surfaces *Procedia CIRP* 2015 **27**:149–54.
[41] Colosimo B M, Pacella M Analyzing the effect of process parameters on the shape of 3D profiles *J Qual Technol* 2011 **43**:169–95.
[42] Pacella M, Colosimo B M Multilinear principal component analysis for statistical modeling of cylindrical surfaces: a case study *Qual Technol Quant Manag* 2018 **15**:507–25.
[43] Yan H, Paynabar K, Pacella M Structured Point Cloud Data Analysis Via Regularized Tensor Regression for Process Modeling and Optimization 2019 **61**:385–95.
[44] Silvestrini R T, Silvestrini A C An Investigation of the Relationship between the Gaussian Process Model Parameters and Surface Area in Three Dimensions *Qual Reliab Eng Int* 2016 **32**:391–402.
[45] Colosimo B M, Cicorella P, Pacella M, Blaco M From profile to surface monitoring: SPC for cylindrical surfaces via Gaussian processes *J Qual Technol* 2014 **46**:95–113.
[46] Pacella M, Grieco A, Blaco M Machine vision based quality control of free-form profiles in automatic cutting processes *Comput Ind Eng* 2017 **109**:221–32.
[47] Grieco A, Pacella M, Blaco M Image Based Quality Control of Free-form Profiles in Automatic Cutting Processes *Procedia CIRP* 2017 **62**:405–10.
[48] Senin N, Ziliotti M, Groppetti R Three-dimensional surface topography segmentation through clustering 2007 **262**:395–410.
[49] Whitehouse D J Surfaces — A Link between Manufacture and Function *Proc Inst Mech Eng* 1978 **192**:179–88.
[50] Evans C J, Bryan J B `Structured', `textured' or `engineered' surfaces *CIRP Ann - Manuf Technol* 1999 **48**:541–56.
[51] Bewilogua K, Bräuer G, Dietz A, Gäbler J, Goch G, Karpuschewski B, et al. Surface technology for automotive engineering *CIRP Ann - Manuf Technol* 2009 **58**:608–27.
[52] Leach R K, Boyd R, Burke T, Danzebrink H U, Dirscherl K, Dziomba T, et al. The European nanometrology landscape *Nanotechnology* 2011 **22**.
[53] Davoudinejad A, Cai Y, Pedersen D B, Luo X, Tosello G Fabrication of micro-structured surfaces by additive manufacturing, with simulation of dynamic contact angle *Mater Des* 2019 **176**:107839.
[54] El Zaatari S, Marei M, Li W, Usman Z Cobot programming for collaborative industrial tasks: An overview *Rob Auton Syst* 2019 **116**:162–80.

[55] Aggarwal J, Kotlicki A, Mossman M, Whitehead L Liquid transport based on electrostatic deformation of fluid interfaces *J Appl Phys* 2006 **99**.
[56] Buguin A, Talini L, Silberzan P Ratchet-like topological structures for the control of microdrops *Appl Phys A Mater Sci Process* 2002 **75**:207–12.
[57] Bataille C, Deltombe R, Jourani A, Bigerelle M Joint properties of a tool machining process to guarantee fluid-proof abilities *Surf Topogr Metrol Prop* 2017 **5**:aa8073.
[58] Regi F, Doest M, Loaldi D, Li D, Frisvad J R, Tosello G, et al. Functionality characterization of injection moulded micro-structured surfaces *Precis Eng* 2019 **60**:594–601.
[59] Campbell J C Cylinder bore surface roughness in internal combustion engines: Its appreciation and control 1972 **19**:163–8.
[60] Pawlus P A study on the functional properties of honed cylinders surface during running-in 1994 **176**:247–54.
[61] Grabon W, Pawlus P, Wos S, Koszela W, Wieczorowski M Effects of honed cylinder liner surface texture on tribological properties of piston ring-liner assembly in short time tests *Tribol Int* 2017 **113**:137–48.
[62] Ryk G, Etsion I Testing piston rings with partial laser surface texturing for friction reduction 2006 **261**:792–6.
[63] Etsion I, Halperin G, Becker E The effect of various surface treatments on piston pin scuffing resistance 2006 **261**:785–91.
[64] Etsion I, Sher E Improving fuel efficiency with laser surface textured piston rings *Tribol Int* 2009 **42**:542–7.
[65] Gibson I, Rosen D W, Stucker B Additive manufacturing technologies. 2010 *Google Sch* n.d.
[66] Calignano F, Manfredi D, Ambrosio E P, Iuliano L, Fino P Influence of process parameters on surface roughness of aluminum parts produced by DMLS *Int J Adv Manuf Technol* 2013 **67**:2743–51.
[67] Renjith S C, Park K, Kremer G E O A Design Framework for Additive Manufacturing: Integration of Additive Manufacturing Capabilities in the Early Design Process *Int J Precis Eng Manuf* 2020 **21**:329–45.
[68] Levy G N, Schindel R, Kruth J P Rapid manufacturing and rapid tooling with layer manufacturing (LM) technologies, state of the art and future perspectives *CIRP Ann - Manuf Technol* 2003 **52**:589–609.
[69] Baumers M, Dickens P, Tuck C, Hague R The cost of additive manufacturing: Machine productivity, economies of scale and technology-push *Technol Forecast Soc Change* 2016 **102**:193–201.
[70] Rüßmann M, Lorenz M, Gerbert P, M W, Justus J, Engel P, et al. Future of Productivity and Growth in Manufacturing *Bost Consult Gr* 2015 **9**:54–89.
[71] Patterson A E, Messimer S L, Farrington P A Overhanging features and the SLM/DMLS residual stresses problem: Review and future research need 2017 **5**:15.
[72] Yao X, Moon S K, Lee B Y, Bi G Effects of Heat Treatment on Microstructures and Tensile Properties of IN718/TiC Nanocomposite Fabricated by Selective Laser Melting *Int J Precis Eng Manuf* 2017 **18**.
[73] Simchi A, Petzoldt F, Pohl H On the development of direct metal laser sintering for rapid tooling *J Mater Process Technol* 2003 **141**:319–28.
[74] Simchi A Direct laser sintering of metal powders: Mechanism, kinetics and microstructural features *Mater Sci Eng A* 2006 **428**:148–58.
[75] Manfredi D, Calignano F, Krishnan M, Canali R, Ambrosio E P, Atzeni E From powders to dense metal parts: Characterization of a commercial

alsimg alloy processed through direct metal laser sintering *Materials (Basel)* 2013 **6**:856–69.
[76] C Yan L H A H Microstructure and mechanical properties of aluminium alloy cellular lattice structures manufactured by direct metal laser sintering *Mater Sci Eng A* 2015 **628**:238–46.
[77] OO Salman F B T N Impact of the scanning strategy on the mechanical behavior of 316L steel synthesized by selective laser melting *J Manuf Process* 2019 **45**:255–61.
[78] J Deckers K S J V J-P K Isostatic pressing assisted indirect selective laser sintering of alumina components *Rapid Prototyp J* 2012 **18**:409–19.
[79] K Shahzad J D J-P K J V Additive manufacturing of alumina parts by indirect selective laser sintering and post processing *J Mater Process Technol* 2013 **213**:1484–94.
[80] K Shahzad J D S B Preparation and indirect selective laser sintering of alumina/PA microspheres *Ceram Int* 2012 **38**:1241–7.
[81] M Dewidar K D A comparison between direct and indirect laser sintering of metals *J Mater Sci Technol* 2008 **24**:227–32.
[82] A Boschetto L B Manufacturability of non-assembly joints fabricated in AlSi10Mg by selective laser melting *J Manuf Process* 2019 **37**:425–37.
[83] Grasso M, Colosimo B M Process defects and in situ monitoring methods in metal powder bed fusion: a review *Meas Sci Technol* 2017 **28**:44005.
[84] Sharratt B M, Sharrat B M Non-Destructive Techniques and Technologies for Qualification of Additive Manufactured Parts and Processes *Dep Natl Def Canada* 2015 **55**:95–100.
[85] Mousa A A Experimental investigations of curling phenomenon in selective laser sintering process *Rapid Prototyp J* 2016 **22**:405–15.
[86] Yasa E, Deckers J, Craeghs T, Badrossamay M, Kruth J-P Investigation on occurrence of elevated edges in selective laser melting. Int. Solid Free. Fabr. Symp., Austin, TX: 2009, p. 180–92.
[87] Kleszczynski S, zur Jacobsmühlen J, Sehrt J, Witt G Error Detection in Laser Beam Melting Systems by High Resolution Imaging *23rd Annu Int Solid Free Fabr Symp - An Addit Manuf Conf* 2012.
[88] Thompson A, Senin N, Leach R Towards an additive surface atlas *ASPE/Euspen Conf Dimens Accuracy Surf Finish Addit Manuf* 2016:27–30.
[89] Tolochko N K, Mozzharov S E, Yadroitsev I A, Laoui T, Froyen L, Titov V I, et al. Balling processes during selective laser treatment of powders *Rapid Prototyp J* 2004 **10**:78–87.
[90] Gong H, Gu H, Zeng K, Dilip J J S, Pal D, Stucker B, et al. Melt Pool Characterization for Selective Laser Melting of Ti-6Al-4V Pre-alloyed Powder *Solid Free Form Fabr Proc* 2014:256–67.
[91] Simonelli M, Tuck C, Aboulkhair N T, Maskery I, Ashcroft I, Wildman R D, et al. A Study on the Laser Spatter and the Oxidation Reactions During Selective Laser Melting of 316L Stainless Steel, Al-Si10-Mg, and Ti-6Al-4V *Metall Mater Trans A Phys Metall Mater Sci* 2015 **46**:3842–51.
[92] Kempen K, Thijs L, Van Humbeeck J, Kruth J-P Mechanical properties of AlSi10Mg produced by selective laser melting *Phys Procedia* 2012 **39**:439–46.
[93] M. S, Levy G Quality Management and Estimation of Quality Costs for Additive Manufacturing with SLS. vol. 9, 2012.
[94] Thijs L, Kempen K, Kruth J P, Van Humbeeck J Fine-structured aluminium products with controllable texture by selective laser melting of pre-alloyed

AlSi10Mg powder *Acta Mater* 2013 **61**:1809–19.
[95] M Krishnan E A R C On the effect of process parameters on properties of AlSi10Mg parts produced by DMLS *Rapid Prototyp J* 2014 **20**:449–58.
[96] C Yan L H A H Evaluation of light-weight AlSi10Mg periodic cellular lattice structures fabricated via direct metal laser sintering *J Mater Process Technol* 2014 **214**:856–64.
[97] M Ghasri-Khouzani H P R A Comparing microstructure and hardness of direct metal laser sintered AlSi10Mg alloy between different planes *J Manuf Process* 2019 **37**:274–80.
[98] Adam G A O, Zimmer D Design for Additive Manufacturing-Element transitions and aggregated structures *CIRP J Manuf Sci Technol* 2014 **7**:20–8.
[99] Cain V, Thijs L, Van Humbeeck J, Van Hooreweder B, Knutsen R Crack propagation and fracture toughness of Ti6Al4V alloy produced by selective laser melting *Addit Manuf* 2015 **5**:68–76.
[100] Bo S, Shujuan D, Qi L, Hanlin L, Coddet C Vacuum heat treatment of iron parts produced by selective laser melting: Microstructure, residual stress and tensile behavior *Mater Des* 2014 **54**:727–33.
[101] Read N, Wang W, Essa K, Attallah M M Selective laser melting of AlSi10Mg alloy: Process optimisation and mechanical properties development *Mater Des* 2015 **65**:417–24.
[102] Salmi A, Atzeni E, Iuliano L, Galati M Experimental Analysis of Residual Stresses on AlSi10Mg Parts Produced by Means of Selective Laser Melting (SLM) *Procedia CIRP* 2017 **62**:458–63.
[103] Childs T H G, Hauser G, Badrossamay M Selective laser sintering (melting) of stainless and tool steel powders: Experiments and modelling *Proc Inst Mech Eng Part B J Eng Manuf* 2005 **219**:339–57.
[104] Gibson I, Rosen D W, Stucker B Additive manufacturing technologiesNew York: Springer; 2010.
[105] Calignano F, Manfredi D, Ambrosio E P, Iuliano L, Fino P Influence of process parameters on surface roughness of aluminum parts produced by DMLS *Int J Adv Manuf Technol* 2013 **67**:2743–51.
[106] Manfredi D, Calignano F, Krishnan M, Ambrosio E P, Biamino S, Ugues D, et al. Additive Manufacturing of Al Alloys and Aluminium Matric Composites (AMCs). In: Monteiro W A, editor. Light Met. Alloy. Appl., vol. 1, London, UK: IntechOpen; 2014, p. 64.
[107] Trevisan F, Calignano F, Lorusso M, Pakkanen J, Aversa A, Ambrosio E P, et al. On the selective laser melting (SLM) of the AlSi10Mg alloy: Process, microstructure, and mechanical properties *Materials (Basel)* 2017 **10**.
[108] Lonardo P M, Lucca D A, De Chiffre L Emerging trends in surface metrology *CIRP Ann - Manuf Technol* 2002 **51**:701–23.
[109] De Chiffre L, Kunzmann H, Peggs G N, Lucca D A Surfaces in precision engineering, microengineering and nanotechnology *CIRP Ann - Manuf Technol* 2003 **52**:561–77.
[110] Senin N, Colosimo B M, Pacella M Point set augmentation through fitting for enhanced ICP registration of point clouds in multisensor coordinate metrology *Robot Comput Integr Manuf* 2013 **29**:39–52.
[111] Weckenmann A, Jiang X, Sommer K D, Neuschaefer-Rube U, Seewig J, Shaw L, et al. Multisensor data fusion in dimensional metrology *CIRP Ann - Manuf Technol* 2009 **58**:701–21.
[112] Liggins M, Hall D, Llinas J Handbook of Multisensor Data Fusion Theory

and PracticeBoca Ranton, FL (USA): CRC press; 2009.
[113] Leach R K Optical Measurement of Surface TopographyBerlin: Springer; 2011.
[114] Senin N, Leach R Information-rich surface metrology *Procedia CIRP* 2018 **75**:19–26.
[115] Leach R Metrology for Additive Manufacturing *Meas Control (United Kingdom)* 2016 **49**:132–5.
[116] Executive Agency for Small and Medium-size Enterprises (EASME) Annual report on European SMEs 2018/2019 : research & development and innovation by SMEs.European Commission, Brussel; 2019.
[117] Lucca D A, Herrmann K, Klopfstein M J Nanoindentation: Measuring methods and applications *CIRP Ann - Manuf Technol* 2010 **59**:803–19.
[118] ISO 4287-1:1998 Geometrical product specifications (GPS) -Surface texture: Profile method — Terms, definitions and surface texture parameters n.d.
[119] Blunt L, Jiang X Advanced Techniques for Assessment Surface TopographyLondon: Kogan Page Science; 2003.
[120] Stout K, Blunt L, Dong W, Mainsah E, Luo N, Mathia T, et al. Development of Methods for the Characterization of Roughness in Three DimensionsBrussels: Commision of the European Communities; 1993.
[121] ISO 14638:2015 Geometrical product specifications (GPS) — Matrix model n.d.
[122] Cariolaro G Unified signal theorySpringer, Berlin; 2011.
[123] ISO 25178-2:2012 Geometrical product specifications (GPS) — Surface texture : Areal Part 2 : Terms , definitions and surface n.d.
[124] Waterworth A Quantitative characterization of surface finishes on stainless steel sheet using 3D surface topography analysis. University of Huddersfield, 2006.
[125] ISO 25178-6:2010 Geometrical product specifications (GPS) — Surface texture : Areal Part 6 : Classification of methods for measuring surface texture n.d.
[126] Townsend A, Pagani L, Scott P, Blunt L Areal surface texture data extraction from X-ray computed tomography reconstructions of metal additively manufactured parts *Precis Eng* 2017 **48**:254–64.
[127] Thompson A, Senin N, Maskery I, Körner L, Lawes S, Leach R Internal surface measurement of metal powder bed fusion parts *Addit Manuf* 2018 **20**:126–33.
[128] Townsend A, Senin N, Blunt L, Leach R K, Taylor J S Surface texture metrology for metal additive manufacturing: a review *Precis Eng* 2016 **46**:34–47.
[129] Leach R K, Giusca C L, Haitjema H, Evans C, Jiang X Calibration and verification of areal surface texture measuring instruments *CIRP Ann - Manuf Technol* 2015 **64**:797–813.
[130] ISO 3274:1998 Geometric Product Specifications (GPS) — Surface texture : Profile method — Nominal characteristics of contact (stylus) instruments — n.d.
[131] ISO 25178-601:2010 Geometrical Product Specification - Surface texture: Areal - Part 601: Nominal characteristics of contact (stylus) instruments n.d.
[132] Leach R K The measurement of surface texture using stylus instruments. *Meas Good Pract Guid No 37* 2001:100.

[133] de Groot P Phase Shifting Interferometry. In: Leach R K, editor. Opt. Meas. Surf. Topogr., Berlin: Springer-Verlag; 2011, p. 167–86.
[134] de Groot P Coherence Scanning Interferometry. In: Leach R K, editor. Opt. Meas. Surf. Topogr., Berlin: Springer-Verlag; 2011, p. 187–208.
[135] ISO 25178-603:2013 Geometrical product specifications (GPS) — Surface texture : Areal Part 603 : Nominal characteristics of non-contact (phase-shifting interferometric microscopy) instruments n.d.
[136] ISO 25178-604: 2013 Geometrical product specifications (GPS) — Surface texture : Areal Part 604 : Nominal characteristics of non-contact (coherence scanning interferometry) instruments n.d.
[137] Leach R K, Brown L, Jiang X, Blunt R, Conroy M, Mauger D Measurement Good Practice Guide No. 108 Guide to the Measurement of Smooth Surface Topography using Coherence Scanning InterferometryTeddington: National Physics Laboratory; 2008.
[138] Petzing J, Coupland J, Leach R K Good Practice Guide No . 116 The Measurement of Rough Surface Topography using Coherence Scanning InterferometryTeddington: National Physics Laboratory; 2010.
[139] Artigas R Imaging Confocal Microscopy. In: Leach R K, editor. Opt. Meas. Surf. Topogr., Berlin: Springer-Verlag; 2011, p. 236–86.
[140] ISO 25178-607:2019 Geometrical product specifications (GPS) — Surface texture : Areal Part 607 : Nominal characteristics of non-contact (confocal microscopy) instruments n.d.
[141] Helmli F Focus Variation Instruments. In: Leach R K, editor. Opt. Meas. Surf. Topogr., Berlin: Springer-Verlag; 2011, p. 131–66.
[142] ISO 25178-606:2015 Geometrical product specifications (GPS) — Surface texture : Areal Part 606 : Nominal characteristics of non-contact (focus variation) instruments n.d.
[143] Miura K, Nose A Point Autofocus Instruments. In: Leach R K, editor. Opt. Meas. Surf. Topogr., Berlin: Springer-Verlag; 2011, p. 105–29.
[144] Miura K, Tsukamoto T, Nose A, Takeda R, Ueda S Accuracy verification of gear measurement with a point autofocus probe. In: Euspen, editor. Euspen's 18th Int. Conf. Exhib., Venice: Euspen; 2018, p. 121–2.
[145] Miura K, Nose A, Suzuki H, Okada M Cutting Tool Edge and Textured Surface Measurements with a Point Autofocus Probe *Int J Autom Technol* 2017 **11**:761–5.
[146] Joint Committee For Guides In Metrology - BIPM Vocabulaire international de métrologie *Int Vocab Metrol* 2012 **3**:104.
[147] Giusca C L, Leach R K, Forbes A B A virtual machine-based uncertainty evaluation for a traceable areal surface texture measuring instrument *Meas J Int Meas Confed* 2011 **44**:988–93.
[148] Novikov D A, Kononogov S A, Zolotarevskii S Y, Vishnyakov G N, Gusev A S, Levin G G, et al. Analysis of uncertainties caused by procedural and instrumental interferometry errors in the texture and shape parameters of a surface *Meas Tech* 2013 **56**:1006–10.
[149] Wan D-S, Schmitz T L, Novak E Uncertainty contributors for optical profiler with internal displacement measuring interferometer. Proc. ASPE, 2005.
[150] Harris P M, Leach R K, Giusca C L Uncertainty evaluation for the calculation of a surface texture parameter in the profile case *NPL Report, MS* 2010 **8**.
[151] Haitjema H Uncertainty in measurement of surface topography *Surf Topogr*

Metrol Prop 2015 **3**:35004.
[152] ISO 25178-600:2019 Geometrical product specification (GPS) - Surface texture: Areal Part 600: Metrological characteristics for areal-topography measuring methods n.d.
[153] ISO 25178-70:2014 Geometrical product specification (GPS) — Surface texture : Areal Part 70 : Material measures n.d.
[154] Giusca C L, Leach R K, Helery F Calibration of the scales of areal surface topography measuring instruments: Part 2. Amplification, linearity and squareness *Meas Sci Technol* 2012 **23**.
[155] Maculotti G, Feng X, Su R, Galetto M, Leach R Residual flatness and scale calibration for a point autofocus surface topography measuring instrument *Meas Sci Technol* 2019 **30**.
[156] Giusca C L, Leach R K, Helary F, Gutauskas T, Nimishakavi L Calibration of the scales of areal surface topography measuring instruments: part 1. Measurement noise and residual flatness *Meas Sci Technol* 2012 **23**:065005.
[157] Evans C J PVr—a robust amplitude parameter for optical surface specification *Opt Eng* 2009 **48**:043605.
[158] de Groot P The meaning and measure of vertical resolution in optical surface topography measurement *Appl Sci* 2017 **7**:1–6.
[159] Leach R, Haitjema H Bandwidth characteristics and comparisons of surface texture measuring instruments *Meas Sci Technol* 2010 **21**.
[160] de Groot P J Progress in the specification of optical instruments for the measurement of surface form and texture *Proc SPIE 911023* 2014 **9110**:1–12.
[161] Leach R, Chetwynd D, Blunt L, Haycocks J, Harris P, Jackson K, et al. Recent advances in traceable nanoscale dimension and force metrology in the UK *Meas Sci Technol* 2006 **17**:467–76.
[162] Leach R K Why do we rarely see uncertainty statements with surface form and texture measurement? Euspen's 20th Int. Conf. Exhib., Genève: Euspen; 2020.
[163] Venditti K, Evans C, Falaggis K, Blum A, Chaudhuri R, Goodsell J, et al. Design for metrology for freeform optics manufacturing *Procedia CIRP* 2019 **84**:169–72.
[164] Isa M A, Sims-Waterhouse D, Piano S, Leach R Volumetric error modelling of a stereo vision system for error correction in photogrammetric three-dimensional coordinate metrology *Precis Eng* 2020 **64**:188–99.
[165] Sims-Waterhouse D, Isa M, Piano S, Leach R Uncertainty model for a traceable stereo-photogrammetry system *Precis Eng* 2020 **63**:1–9.
[166] Su R, Thomas M, Liu M, Drs J, Bellouard Y, Pruss C, et al. Lens aberration compensation in interference microscopy *Opt Lasers Eng* 2020 **128**.
[167] Thomas M, Su R, Nikolaev N, Coupland J, Leach R Modeling of interference microscopy beyond the linear regime *Opt Eng* 2020 **59**:1.
[168] Giusca C L, Claverley J D, Sun W, Leach R K, Helmli F, Chavigner M P J Practical estimation of measurement noise and flatness deviation on focus variation microscopes *CIRP Ann - Manuf Technol* 2014 **63**:545–8.
[169] Alburayt A, Syam W P, Leach R Lateral scale calibration for focus variation microscopy *Meas Sci Technol* 2018 **29**.
[170] Maculotti G, Feng X, Galetto M, Leach R Measurement noise evaluation, noise bandwidth specification and temperature effects in 3D point autofocusing microscopy *Eur Soc Precis Eng Nanotechnology, Conf Proc* -

18th Int Conf Exhib EUSPEN 2018 2018:2–3.
[171] Weckenmann A, Tan O, Hoffmann J, Sun Z Practice-oriented evaluation of lateral resolution for micro- and nanometre measurement techniques *Meas Sci Technol* 2009 **20**.
[172] Giusca C L, Leach R K Calibration of the scales of areal surface topography measuring instruments: part 3. Resolution *Meas Sci Technol* 2013 **24**:105010.
[173] Thompson A, Maskery I, Leach R K X-ray computed tomography for additive manufacturing: A review *Meas Sci Technol* 2016 **27**.
[174] Thompson A, Senin N, Giusca C, Leach R Topography of selectively laser melted surfaces: A comparison of different measurement methods *CIRP Ann - Manuf Technol* 2017 **66**:543–6.
[175] Senin N, Thompson A, Leach R K Characterization of the topography of metal additive surface features with different measurement technologies *Meas Sci Technol* 2017 **28**:095003.
[176] Leach R K Characterization of Areal Surface TextureSpringer, Berlin; 2013.
[177] Leach R K, Giusca C L, Haitjema H, Evans C, Jiang X Calibration and verification of areal surface texture measuring instruments *CIRP Ann - Manuf Technol* 2015 **64**:797–813.
[178] Takamasu K Present problems in Coordinate Metrology for nano and micro scale measurements *J Metrol Soc India* 2011 **26**:3–14.
[179] Gunasekaran A, Subramanian N, Ngai W T E Quality management in the 21st century enterprises: Research pathway towards Industry 4.0 *Int J Prod Econ* 2019.
[180] Savio E, De Chiffre L, Schmitt R Metrology of freeform shaped parts *CIRP Ann - Manuf Technol* 2007 **56**:810–35.
[181] Leach R K Metrology for Additive Manufacturing *Meas Control* 2016 **49**:132–5.
[182] Townsend A, Senin N, Blunt L, Leach R K, Taylor J S Surface texture metrology for additive manufacturing: a review *Precis Eng* 2016 **46**:34–47.
[183] Medeossi F, Carmignato S, Lucchetta G, Savio E Effect of void pixels on the quantification of surface topography parameters *Proc 16th Int Conf Eur Soc Precis Eng Nanotechnology, EUSPEN 2016* 2016:2–3.
[184] Pawlus P, Reizer R, Wieczorowski M Problem of non-measured points in surface texture measurements *Metrol Meas Syst* 2017 **24**:525–36.
[185] Colosimo B M Modeling and monitoring methods for spatial and image data *Qual Eng* 2018 **30**:94–111.
[186] Cleveland W S Robust locally weighted regression and smoothing scatterplots *J Am Stat Assoc* 1979 **74**:829–36.
[187] Cressie N A C Statistics for spatial dataJohn Wiley & Sons Inc.; 1993.
[188] Colosimo B M Modeling and monitoring methods for spatial and image data *Qual Eng* 2018 **30**:94–111.
[189] Pedone P, Vicario G, Romano D Kriging-based sequential inspection plans for coordinate measuring machines *Appl Stoch Model Bus Ind* 2009 **25**:133–49.
[190] Vicario G, Ruffa S, Panciani G D, Ricci F, Barbato G Form tolerance verification using the Kriging method *Stat Appl* 2011 **22**:323–40.
[191] Pistone G, Vicario G Kriging prediction from a circular grid: application to wafer diffusion *Appl Stoch Model Bus Ind* 2013 **29**:350–61.
[192] Ruffa, S., Panciani, G.D., Ricci, F., Vicario, G. Assessing measurement

uncertainty in CMM measurements: comparison of different approaches *Int J Metrol Qual Eng* 2013 **4**:163–8.
[193] Ascione R, Moroni G, Petrò S, Romano D Adaptive inspection in coordinate metrology based on kriging models *Precis Eng* 2013 **37**:44–60.
[194] Kolios A, Salonitis K Surrogate modelling for reliability assessment of cutting tools *Proc 11th Int Conf Manuf Res* 2013:405–10.
[195] Song S, Wang A, Huang Q, Tsung F Shape deviation modeling for fused deposition modeling processes *IEEE Int Conf Autom Sci Eng* 2014:758–63.
[196] Wang A, Song S, Huang Q, Tsung F In-plane shape-deviation modeling and compensation for fused deposition modeling processes *IEEE Trans Autom Sci Eng* 2017 **14**:968–76.
[197] Colosimo B M, Mammarella F, Petrò S Quality control of manufactured surfaces. In: Lenz H-J, Wilrich P-T, Schmid W, editors. Front. Mech. Eng., Berlin: Physica-Verlag; n.d.
[198] Del Castillo E, Colosimo B M, Tajbakhsh S D Geodesic gaussian processes for the parametric reconstruction of a free-form surface 2015 **57**:87–99.
[199] Colosimo B M, Pacella M, Senin N Multisensor data fusion via Gaussian process models for dimensional and geometric verification *Precis Eng* 2015 **40**:199–213.
[200] Wang A, Wang K, Tsung F Statistical surface monitoring by spatial-structure modeling *J Qual Technol* 2014 **46**:359–76.
[201] Wells L J, Dastoorian R, Camelio J A A novel NURBS surface approach to statistically monitor manufacturing processes with point cloud data *J Intell Manuf* 2020.
[202] Dastoorian R, Wells L, Tian W A hybrid approach for heterogeneous high-density data for surface topology classification: A case study *ASME 2019 14th Int Manuf Sci Eng Conf MSEC 2019* 2019 **1**:1–8.
[203] Senin N, Moretti M, Leach R K Shape descriptors and statistical classification on areal topography data for tile inspection in tessellated surfaces *Meas J Int Meas Confed* 2017 **95**:82–92.
[204] Xie K, Camelio J A, Izqierdo L E Part-by-part dimensional error compensation in compliant sheet metal assembly processes *J Manuf Syst* 2012 **31**:152–61.
[205] Yue X, Shi J Surrogate model-based optimal feed-forward control for dimensional-variation reduction in composite parts' assembly processes *J Qual Technol* 2018 **50**:279–89.
[206] Pistone G, Vicario G A note on semivariogram. In: T. Di Battista E. Moreno W R, editor. Top. Methodol. Appl. Stat. Inference, Springer; 2016, p. 181–90.
[207] Pistone G, Vicario G How to Model the Covariance Structure in a Spatial Framework: Variogram or Correlation Function? In: Markrides A, A K, Skiadas C H, editors. Data Anal. Appl. 4 Financ. Data Anal. Methods, London, UK: iSTE WILEY; 2020.
[208] Vicario G, Craparotta G, Pistone G Meta-models in Computer Experiments: Kriging versus Artificial Neural Networks *Qual Reliab Eng Int* 2016 **32**:2055–65.
[209] Vicario G, Giraudo M T, Calì V Kriging modelization in predicting metal sheet elongation *Qual Reliab Eng Int* 2018 **34**:1390–9.
[210] Ruffa S, Vicario G, Pistone G Analysis of the Covariance Structure in Manufactured Parts *Commun Stat - Theory Methods* 2015 **44**:4540–51.
[211] Vicario G, Pistone G Simulated variogram-based error inspection of

manufactured parts *Stat Pap* 2018 **59**:1411–23.
[212] Santner T J, Williams B J, Notz W I The design and analysis of computer experimentsSpringer-Verlag; 2003.
[213] Matheron G Traité de géostatistique appliquéEditions Technip; 1962.
[214] Pistone G Empirical {V}ariograms2020.
[215] Sacks J, Welch W J, Mitchell T J, Wynn H P Design and analysis of computer experiments (with discussion) *Stat Sci* 1989 **4**:409–35.
[216] Sacks J, Welch W J, Mitchell T J, Wynn H P Design and analysis of computer experiments *Stat Sci* 1989 **4**:409–35.
[217] Gunasekaran A, Subramanian N, Ngai W T E Quality management in the 21st century enterprises: Research pathway towards Industry 4.0 *Int J Prod Econ* 2019 **207**:125–9.
[218] Schmidt M, Merklein M, Bourell D, Dimitrov D, Hausotte T, Wegener K, et al. Laser based additive manufacturing in industry and academia *CIRP Ann - Manuf Technol* 2017 **66**:561–83.
[219] Barbato G, Germak A, Genta G Misurare per decidere3rd ed.Bologna: Societa` Editrice Esculapio; 2014.
[220] Straffelini G Friction and Wear Methodologies for Design and ControlSpringer; 2015.
[221] Zum Gahr K-H Microstructure and wear of materialsvol. 10Elsevier; 1987.
[222] Whitenton E P, Blau P J A comparison of methods for determining wear volumes and surface parameters of spherically tipped sliders 1988 **124**:291–309.
[223] Bhushan B Modern tribology handbookCRC press; 2000.
[224] Blau P J Friction science and technology: from concepts to applicationsBoca Ranton, FL (USA): CRC press; 2008.
[225] Stachowiak G W, Batchelor A W, Stachowiak G B Experimental methods in tribologyAmsterdam: Elsevier; 2004.
[226] Joseph J, Haghdadi N, Shamlaye K, Hodgson P, Barnett M, Fabijanic D The sliding wear behaviour of CoCrFeMnNi and AlxCoCrFeNi high entropy alloys at elevated temperatures 2019 **428**–**429**:32–44.
[227] Sharma S, Patel B, Patel R Friction and wear characteristics of robust carbon-carbon composites developed solely from petroleum pitch without reimpregnation 2020 **8**:945–56.
[228] An J, Sun W, Niu X D Dry Sliding Wear Behavior and a Proposed Criterion for Mild to Severe Wear Transition of Mg–3Al–0.4Si–0.1Zn Alloy *Tribol Lett* 2017 **65**.
[229] Madhukar P, Selvaraj N, Rao C S P, Veeresh Kumar G B Fabrication and characterization two step stir casting with ultrasonic assisted novel AA7150-hBN nanocomposites *J Alloys Compd* 2020 **815**:152464.
[230] Baran Ö, Keleş A, Çiçek H, Totik Y, Efeoğlu İ The mechanical and tribological properties of Ti [Nb, V] N films on the Al-2024 alloy *Surf Coatings Technol* 2017 **332**:312–8.
[231] Sundaraselvan S, Senthilkumar N, Tamizharasan T, Naveen Sait A Surface modification of AZ61 Magnesium Alloy with Nano TiO2/Al2O3 using Laser Cladding Technique *Mater Today Proc* 2020 **21**:717–21.
[232] Falqueto L E, Butkus D J, De Mello J D B, Bozzi A C, Scandian C Sliding wear of cobalt-based alloys used in rolling seamless tubes 2017 **376**–**377**:1739–46.
[233] Aliyu I K, Mohammed A S, Al-Qutub A Tribological performance of ultra high molecular weight polyethylene nanocomposites reinforced with

graphene nanoplatelets *Polym Compos* 2019 **40**:E1301–11.
[234] Hernandez M A, Bakoglidis K D, Withers P J, Xiao P Role of SiC and Si3N4 reinforcing particles in the tribological performance of graphite-based composites 2020 **456**–**457**:203399.
[235] Yildiz B, Balkanci A, Ovali I, Ünlü C G Investigation of tribological behaviours of graphene-coated journal bearing *Tribol - Mater Surfaces Interfaces* 2018 **12**:177–85.
[236] Mura A, Wang H, Adamo F, Kong J Graphene coatings to enhance tribological performance of steel *Mech Adv Mater Struct* 2019:1–8.
[237] Mura A, Canavese G, Goti E, Rivolo P, Wang H, Ji X, et al. Effect of different types of graphene coatings on friction and wear performance of aluminum alloy *Mech Adv Mater Struct* 2020:1–9.
[238] Ambadekar P K, Choudhari C S Measurement of Tungsten Carbide Tool Wear by Tribological Investigations *J Bio- Tribo-Corrosion* 2020 **6**:44.
[239] Zhang J, Zhang J, Xiao G, Chen Z, Yi M, Zhang Y, et al. Orentational effect of graphene on the friction and wear behavior of Si3N4/TiC based composite ceramic tool materials *Ceram Int* 2020 **46**:3550–7.
[240] Zappelino B F, de Almeida E A dos S, Krelling A P, da Costa C E, Fontana L C, Milan J C G Tribological behavior of duplex-coating on Vanadis 10 cold work tool steel 2020 **442**–**443**:203133.
[241] Kovacı H Comparison of the microstructural, mechanical and wear properties of plasma oxidized Cp-Ti prepared by laser powder bed fusion additive manufacturing and forging processes *Surf Coatings Technol* 2019 **374**:987–96.
[242] Lerebours A, Demangel C, Dembiski L, Bouvier S, Rassineux A, Egles C Effect of the Residual Porosity of CoCrMo Bearing Parts Produced by Additive Manufacturing on Wear of Polyethylene 2020 **23**:100138–49.
[243] Schiltz J, Rosenberger A, Render T, Gatrell B A, Qu H, Steiner C, et al. Wear of structural oxide ceramics produced through additive manufacturing *Procedia Manuf* 2019 **34**:780–8.
[244] Zhang M, Chen C, Qin L, Yan K, Cheng G, Jing H, et al. Laser additive manufacturing of M2 high-speed steel *Mater Sci Technol (United Kingdom)* 2018 **34**:69–78.
[245] Norani M N M, Abdollah M F Bin, Abdullah M I H C, Amiruddin H, Ramli F R, Tamaldin N 3D printing parameters of acrylonitrile butadiene styrene polymer for friction and wear analysis using response surface methodology *Proc Inst Mech Eng Part J J Eng Tribol* 2020:1350650120925601.
[246] Olesik P, Godzierz M, Kozioł M Preliminary characterization of novel LDPE-based wear-resistant composite suitable for FDM 3D printing *Materials (Basel)* 2019 **12**.
[247] Bochkareva S A, Grishaeva N Y, Buslovich D G, Kornienko L A, Lyukshin B A, Panin S V, et al. Development of a Wear-Resistant Extrudable Composite Material Based on an Ultrahigh-Molecular Polyethylene with Predetermined Properties *Mech Compos Mater* 2020 **56**:15–26.
[248] Salguero J, Vazquez-Martinez J M, Del Sol I, Batista M Application of Pin-On-Disc techniques for the study of tribological interferences in the dry machining of A92024-T3 (Al-Cu) alloys *Materials (Basel)* 2018 **11**:1–11.
[249] Grützmacher P G, Rosenkranz A, Rammacher S, Gachot C, Mücklich F The influence of centrifugal forces on friction and wear in rotational sliding

Tribol Int 2017 **116**:256–63.
[250] Bai L, Meng Y, Khan Z A, Zhang V The Synergetic Effects of Surface Texturing and MoDDP Additive Applied to Ball-on-Disk Friction Subject to Both Flooded and Starved Lubrication Conditions *Tribol Lett* 2017 **65**:163.
[251] Müller M, Ostermeyer G-P Measurements of partially lubricated contacts on different scales 2017 **17**:629–30.
[252] Singh H, Bhowmick H Lubrication characteristics and wear mechanism mapping for hybrid aluminium metal matrix composite sliding under surfactant functionalized MWCNT-oil *Tribol Int* 2020 **145**:106152.
[253] Mousavi S B, Heris S Z, Estellé P Experimental comparison between ZnO and MoS2 nanoparticles as additives on performance of diesel oil-based nano lubricant *Sci Rep* 2020 **10**:1–17.
[254] Wang X, Zhang Y, Yin Z, Su Y, Zhang Y, Cao J Experimental research on tribological properties of liquid phase exfoliated graphene as an additive in SAE 10W-30 lubricating oil *Tribol Int* 2019 **135**:29–37.
[255] Singh Y, Sharma A, Singh N K, Noor M M Effect of SiC nanoparticles concentration on novel feedstock Moringa Oleifera chemically treated with neopentylglycol and their trobological behavior 2020 **280**:118630.
[256] Chaurasia S K, Sehgal A K, Singh N K Improved Lubrication Mechanism of Chemically Modified Mahua (Madhuca indica) Oil with Addition of Copper Oxide Nanoparticles *J Bio- Tribo-Corrosion* 2020 **6**:94.
[257] ASTM G99-17 Standard Test Method for Wear Testing with a Pin-on-Disk Apparatus n.d.
[258] Bolelli G, Cannillo V, Lusvarghi L, Manfredini T Wear behaviour of thermally sprayed ceramic oxide coatings 2006 **261**:1298–315.
[259] Miyoshi K, Ishibashi K, Suzuki M Surface characterization techniques in wear of materials *ASTM Spec Tech Publ* 2008 **1501 STP**:126–33.
[260] Bolelli G, Rauch J, Cannillo V, Killinger A, Lusvarghi L, Gadow R Microstructural and tribological investigation of high-velocity suspension flame sprayed (HVSFS) Al 2O 3 coatings *J Therm Spray Technol* 2009 **18**:35–49.
[261] Hu B, Peng L, Yang Y, Ding W Effect of solidification conditions on microstructure, mechanical and wear properties of Mg-5Al-3Ca-0.12Sr magnesium alloy *Mater Des* 2010 **31**:3901–7.
[262] Lahiri D, Benaduce A P, Rouzaud F, Solomon J, Keshri A K, Kos L, et al. Wear behavior and in vitro cytotoxicity of wear debris generated from hydroxyapatite-carbon nanotube composite coating *J Biomed Mater Res - Part A* 2011 **96 A**:1–12.
[263] Bao M, Zhang C, Lahiri D, Agarwal A The tribological behavior of plasma-sprayed Al-Si composite coatings reinforced with nanodiamond 2012 **64**:702–8.
[264] Lahiri D, Gill P K, Scudino S, Zhang C, Singh V, Karthikeyan J, et al. Cold sprayed aluminum based glassy coating: Synthesis, wear and corrosion properties *Surf Coatings Technol* 2013 **232**:33–40.
[265] Chung I, Lee S, Kwon J do Fretting wear volume calculation on cylindrical surface: Inaccuracy due to misalignment of measured object with respect to 3D profiler 2013 **297**:1074–80.
[266] Sharma S, Sangal S, Mondal K On the optical microscopic method for the determination of ball-on-flat surface linearly reciprocating sliding wear volume 2013 **300**:82–9.

[267] Dong R, Zhu W, Zhao C, Zhang Y, Ren F Microstructure, Mechanical Properties, and Sliding Wear Behavior of Spark Plasma Sintered Ti-Cu Alloys *Metall Mater Trans A Phys Metall Mater Sci* 2018 **49**:6147–60.
[268] Türedi E On the precise measurement capability of the direct microscopic measurement method for wear volume characterization *MATEC Web Conf* 2018 **188**.
[269] DIN 50320:1979 Wear - Terms - System analysis of wear processes - Classification of the field of wear n.d.
[270] ASTM G40-17 Standard Terminology Relating to Wear and Erosion n.d.
[271] Peterson M B, Winer W O, editors OCED Glossary. Wear Control Handb., New York: American Society for Testing and Materials; 1980.
[272] Wood F W Summary on the Role and Analysis of Wear in Failures *J Test Eval* 1994 **22**:470–3.
[273] Bayer R G Mechanical Wear Fundamental and TestingNew York, NY, USA: Marcel Dekker Inc.; 2004.
[274] Aksulu M, Palabiyik M Uncertainty of Wear Rate and Coefficient of Friction for a Polymer Wear Experiment in a pad-on-disc Tribotester. Proc. 9th Bienn. ASME Conf. Eng. Syst. Des. Anal., 2008, p. 1–6.
[275] D'Amato R, Calvo R, Ruggiero A, Gómez E Measurement capabilities for ball bearing wear assessment *Procedia Manuf* 2017 **13**:647–54.
[276] ISO 18535-2:2016 Diamond-like carbon films - Determination of friction and wear characteristics of Diamond-like carbon films by ball-on-disc method n.d.
[277] Colbert R S, Krick B A, Dunn A C, Vail J R, Argibay N, Sawyer W G Uncertainty in pin-on-disk wear volume measurements using surface scanning techniques *Tribol Lett* 2011 **42**:129–31.
[278] Burris D L, Sawyer W G Measurement uncertainties in wear rates *Tribol Lett* 2009 **36**:81–7.
[279] Takimoto R Y, de Sales Guerra Tsuzuki M, Ueda E K, Sato A K, de Castro Martins T, Cousseau T, et al. Rough Surface Wear Analysis Using Image Processing Techniques 2016 **49**:7–12.
[280] Carmignato S, Spinelli M, Affatato S, Savio E Uncertainty evaluation of volumetric wear assessment from coordinate measurements of ceramic hip joint prostheses 2011 **270**:584–90.
[281] Valigi M C, Logozzo S, Affatato S New challenges in tribology: Wear assessment using 3D optical scanners *Materials (Basel)* 2017 **10**:1–13.
[282] Green N C, Bowen J, Hukins D W L, Shepherd D E T Assessment of non-contacting optical methods to measure wear and surface roughness in ceramic total disc replacements *Proc Inst Mech Eng Part H J Eng Med* 2015 **229**:245–54.
[283] Niemczewska-Wójcik M, Mańkowska-Snopczyńska A, Piekoszewski W The investigation of wear tracks with the use of noncontact measurement methods *Arch Civ Mech Eng* 2013 **13**:158–67.
[284] Fleming G J P, Reilly E, Dowling A H, Addison O Data acquisition variability using profilometry to produce accurate mean total volumetric wear and mean maximum wear depth measurements for the OHSU oral wear simulator *Dent Mater* 2016 **32**:e176–84.
[285] Baryshev S V., Erck R A, Moore J F, Zinovev A V., Tripa C E, Veryovkin I V. Characterization of surface modifications by white light interferometry: applications in ion sputtering, laser ablation, and tribology experiments. *J Vis Exp* 2013 **m**:1–16.

[286] JCGM100: Evaluation of measurement data — Guide to the expression of uncertainty in measurement (GUM) 2008:Sèvres, France.
[287] Fang F Z, Zhang X D, Weckenmann A, Zhang G X, Evans C Manufacturing and measurement of freeform optics *CIRP Ann* 2013 **62**:823–46.
[288] Gross K A, Saber-Samandari S, Heemann K S Evaluation of commercial implants with nanoindentation defines future development needs for hydroxyapatite coatings *J Biomed Mater Res - Part B Appl Biomater* 2010 **93**:1–8.
[289] Vayron R, Barthel E, Mathieu V, Soffer E, Anagnostou F, Haiat G Nanoindentation Measurements of Biomechanical Properties in Mature and Newly Formed Bone Tissue Surrounding an Implant *J Biomech Eng* 2012 **134**:021007.
[290] Saber-Samandari S, Alamara K, Saber-Samandari S Calcium phosphate coatings: Morphology, micro-structure and mechanical properties *Ceram Int* 2014 **40**:563–72.
[291] ASTM E1875-20 Standard Test Method for Dynamic Young's Modulus, Shear Modulus, and Poisson's Ratio by Sonic Resonance n.d.
[292] Spinner S, Reichard T W, Tefft W E A Comparison of Experimental and Theoretical Relations Between Young's Modulus and the Flexural and Longitudinal Resonance Frequencies of Uniform Bars *J Res Natl Bur Stand Sect A, Phys Chem* 1960 **64A**:147–55.
[293] Afrin N, Ngan A H W Creep of micron-sized Ni3Al columns *Scr Mater* 2006 **54**:7–12.
[294] Steinmann P A, Tardy Y, Hintermann H E Adhesion testing by the scratch test method: The influence of intrinsic and extrinsic parameters on the critical load *Thin Solid Films* 1987 **154**:333–49.
[295] Laugier M The development of the scratch test technique for the determination of the adhesion of coatings *Thin Solid Films* 1981 **76**:289–94.
[296] Akono A T, Randall N X, Ulm F J Experimental determination of the fracture toughness via microscratch tests: Application to polymers, ceramics, and metals *J Mater Res* 2012 **27**:485–93.
[297] Li W, Sharples S D, Smith R J, Clark M, Somekh M G Determination of crystallographic orientation of large grain metals with surface acoustic waves *J Acoust Soc Am* 2012 **132**:738–45.
[298] Smith R J, Li W, Coulson J, Clark M, Somekh M G, Sharples S D Spatially resolved acoustic spectroscopy for rapid imaging of material microstructure and grain orientation *Meas Sci Technol* 2014 **25**:55902.
[299] Dryburgh P, Pieris D, Martina F, Patel R, Sharples S, Li W, et al. Spatially resolved acoustic spectroscopy for integrity assessment in wire–arc additive manufacturing *Addit Manuf* 2019 **28**:236–51.
[300] Small L Hardenss, theory and practiceNovi, MI: Service Diamond Tool Co; 1960.
[301] Wilde H R, Wehrstedt A Introduction of Martens Hardness HM. An internationally accepted designation for `Hardness under test force' *Mater Test* 2000 **42**:468–70.
[302] Alekhin V P, Berlin G S, Shorshorov M C Instruments for Micromechanical Tests of Solid Materials *Instruments Exp Tech - URSS* 1971 **14**:1265.
[303] Doerner M F, Nix W D A method for interpreting the data from depth-

sensing indentation instruments 1986.
[304] Oliver W C, Pharr G M An improved technique for determining hardness and elastic modulus using load and displacement sensing indentation experiments *J Mater Reseach* 1992 **7**:1564–83.
[305] Roa J J, Sudharshan Phani P, Oliver W C, Llanes L Mapping of mechanical properties at microstructural length scale in WC-Co cemented carbides: Assessment of hardness and elastic modulus by means of high speed massive nanoindentation and statistical analysis *Int J Refract Met Hard Mater* 2018 **75**:211–7.
[306] Engqvist H, Wiklund U Mapping of mechanical properties of WC–Co using nanoindentation *Tribol Lett* 2000 **8**:147–52.
[307] Nix W D, Gao H WILLIAM D. NIX*$ and HUAJIAN GAO? *Science (80-)* 1998 **46**.
[308] Kim J Y, Kang S K, Lee J J, Jang J il, Lee Y H, Kwon D Influence of surface-roughness on indentation size effect *Acta Mater* 2007 **55**:3555–62.
[309] Hou X, Jennett N M, Parlinska-Wojtan M Exploiting interactions between structure size and indentation size effects to determine the characteristic dimension of nano-structured materials by indentation *J Phys D Appl Phys* 2013 **46**.
[310] Puchi-Cabrera E S, Staia M H, Iost A Modeling the composite hardness of multilayer coated systems *Thin Solid Films* 2015 **578**:53–62.
[311] Renzelli M, Mughal M Z, Sebastiani M, Bemporad E Design, fabrication and characterization of multilayer Cr-CrN thin coatings with tailored residual stress profiles *Mater Des* 2016 **112**:162–71.
[312] Sebastiani M, Bemporad E, Carassiti F, Schwarzer N Residual stress measurement at the micrometer scale: focused ion beam (FIB) milling and nanoindentation testing *Philos Mag* 2011 **91**:1121–36.
[313] Sebastiani M, Bemporad E, Melone G, Rizzi L, Korsunsky A M A new methodology for in-situ residual stress measurement in MEMS structures *AIP Conf Proc* 2010 **1300**:120–6.
[314] Sebastiani M, Johanns K E, Herbert E G, Pharr G M Measurement of fracture toughness by nanoindentation methods: Recent advances and future challenges *Curr Opin Solid State Mater Sci* 2015 **19**:324–33.
[315] Herbert E G, Pharr G M, Oliver W C, Lucas B N, Hay J L On the measurement of stress – strain curves by spherical indentation 2001 **399**:331–5.
[316] Bradby J E, Williams J S, Swain M V In situ electrical characterization of phase transformations in Si during indentation *Phys Rev B* 2003 **67**:85205.
[317] Herbert E G, Oliver W C, Pharr G M Nanoindentation and the dynamic characterization of viscoelastic solids *J Phys D Appl Phys* 2008 **41**:74021.
[318] Rossi E, Sebastiani M, Gigliotti R, D'Amato M An Innovative Procedure for the In-situ Characterization of Elastomeric Bearings by Using Nanoindentation Test *Int J Archit Herit* 2020:1–13.
[319] ISO 14577-1:2014 Metallic materials — Instrumented indentation test for hardness and material parameters - Part 1: Test method n.d.
[320] ISO 14577-2:2015 Metallic materials-Instrumented indentation test for hardness and materials parameters-Part 2: Verification and calibration of testing machines n.d.
[321] ISO 14577-3:2014 Metallic materials - Instrumented indentation test for hardness and materials parameters - Part 3: Calibration of reference blocks n.d.

[322] ISO 14577-4:2015 Metallic materials - Instrumented indentation test for hardness and materials parameters - Part 4: Test method for metallic and non-metallic coatings n.d.
[323] Jennett N M INDICOAT Final Report - Determination of Hardness and Modulus of Thin Films and Coatings by Nanoindentation. NPL Report MATC(A)Teddington, UK: 2001.
[324] PD ISO/TR 29381:2008 Metallic materials — Measurement of mechanical properties by instrumented indentation test — Indentation tensile properties n.d.
[325] Cagliero R, Barbato G, Maizza G, Genta G Measurement of elastic modulus by instrumented indentation in the macro-range: Uncertainty evaluation *Int J Mech Sci* 2015 **101**–**102**:161–9.
[326] Herrmann K, Jennet N M, Wegener W, Meneve J, Hasche K, Seeman R Progress in determination of the area function of indenters used for nanoindentation *Thin Solid Films* 2000 **377**–**378**:394–400.
[327] Oliver W C, Pharr G M Measurement of hardness and elastic modulus by instrumented indentation: Advances in understanding and refinements to methodology *J Mater Res* 2004 **19**:3–20.
[328] Jiang W G, Su J J, Feng X Q Effect of surface roughness on nanoindentation test of thin films *Eng Fract Mech* 2008 **75**:4965–72.
[329] Xia Y, Bigerelle M, Marteau J, Mazeran P E, Bouvier S, Iost A Effect of surface roughness in the determination of the mechanical properties of material using nanoindentation test *Scanning* 2014 **36**:134–49.
[330] Maslenikov I, Useinov A, Birykov A, Reshetov V Reducing the influence of the surface roughness on the hardness measurement using instrumented indentation test *IOP Conf Ser Mater Sci Eng* 2017 **256**.
[331] Chen L, Ahadi A, Zhou J, Ståhl J E Modeling effect of surface roughness on nanoindentation tests *Procedia CIRP* 2013 **8**:334–9.
[332] Cheng Y T, Cheng C M Effects of 'sinking in' and 'piling up' on estimating the contact area under load in indentation *Philos Mag Lett* 1998 **78**:115–20.
[333] Giannakopoulos A E, Suresh S Determination of elasto-plastic properties by instrumented sharp indentation *Scr Mater* 1999 **40**:1191–8.
[334] Moharrami N, Bull S J A comparison of nanoindentation pile-up in bulk materials and thin films *Thin Solid Films* 2014 **572**:189–99.
[335] Fleck N A, Muller G M, Ashby M F, Hutchinson J W Strain gradient plasticity: Theory and experiment *Acta Metall Mater* 1994 **42**:475–87.
[336] Barbato G, Genta G, Cagliero R, Galetto M, Klopfstein M J, Lucca D A, et al. Uncertainty evaluation of indentation modulus in the nano-range : Contact stiffness contribution *CIRP Ann - Manuf Technol* 2017 **66**:495–8.
[337] Ullner C Critical points in ISO 14577 part 2 and 3 considering the uncertainty in measurement 2004:1–5.
[338] Sneddon I N The relation between load and penetration in the axisymmetric boussinesq problem for a punch of arbitrary profile *Int J Eng Sci* 1965 **3**:47–57.
[339] Loubet J L, Georges J M, Marchesini O, Meille G Vickers Indentation Curves of Magnesium Oxide (MgO) *J Tribol* 1984 **106**:43–8.
[340] Chudoba T, Richter F Investigation of creep behaviour under load during indentation experiments and its influence on hardness and modulus results *Surf Coatings Technol* 2001 **148**:191–8.
[341] Barbato G, Brondino G, Galetto M, Vicario G "Zero-point" in the

evaluation of martens hardness uncertainty *11th IMEKO TC5 Conf Hardness Meas 2002 - Jt Int Conf Force, Mass, Torque, Hardness Civ Eng Metrol Age Glob* 2002:72–7.
[342] Cagliero R Macro instrumented indentation test for structural materials : experimental and numerical methods 2016.
[343] Tabor D The hardness of metalsLondon, UK: Oxford University Press; 1951.
[344] Taljat B, Zacharia T, Pharr G M, Science C, Division M, Ridge O, et al. PILE-UP BEHAVIOR OF SPHERICAL INDENTATIONS IN ENGINEERING MATERIALS B. TALJAT*, T. ZACHARIA*, and G. M. PHARR** *Computer Science and Mathematics Division, Oak Ridge National Laboratory, Oak Ridge, TN 37831 1998 **522**:33–8.
[345] Ahn J H, Kwon D Derivation of plastic stress-strain relationship from ball indentations: Examination of strain definition and pileup effect *J Mater Res* 2001 **16**:3170–8.
[346] Kim S H, Lee B W, Choi Y, Kwon D Quantitative determination of contact depth during spherical indentation of metallic materials - A FEM study *Mater Sci Eng A* 2006 **415**:59–65.
[347] Kim J Y, Lee K W, Lee J S, Kwon D Determination of tensile properties by instrumented indentation technique: Representative stress and strain approach *Surf Coatings Technol* 2006 **201**:4278–83.
[348] Kim K H, Kim Y C, Jeon E chae, Kwon D Evaluation of indentation tensile properties of Ti alloys by considering plastic constraint effect *Mater Sci Eng A* 2011 **528**:5259–63.
[349] Fu K, Chang L, Zheng B, Tang Y, Wang H On the determination of representative stress-strain relation of metallic materials using instrumented indentation *Mater Des* 2015 **65**:989–94.
[350] Li Y, Stevens P, Sun M, Zhang C, Wang W Improvement of predicting mechanical properties from spherical indentation test *Int J Mech Sci* 2016 **117**:182–96.
[351] Dao M, Chollacoop N, Van Vliet K J, Venkatesh T A, Suresh S Computational modeling of the forward and reverse problems in instrumented sharp indentation *Acta Mater* 2001 **49**:3899–918.
[352] Bucaille J L, Stauss S, Felder E, Michler J Determination of plastic properties of metals by instrumented indentation using different sharp indenters *Acta Mater* 2003 **51**:1663–78.
[353] Herrmann K, Lucca D A, Klopfstein M J, Menelao F CIRP sponsored international comparison on nanoindentation 2010 **47**.
[354] Shuman D J, Costa A L M, Andrade M S Calculating the elastic modulus from nanoindentation and microindentation reload curves *Mater Charact* 2007 **58**:380–9.
[355] Yang G H, Zhao B, Gao Y, Pan F Investigation of nanoindentation on Co/Mo multilayers by the continuous stiffness measurement technique *Surf Coatings Technol* 2005 **191**:127–33.
[356] Pharr G M, Strader J H, Oliver W C Critical issues in making small-depth mechanical property measurements by nanoindentation with continuous stiffness measurement *J Mater Res* 2009 **24**:653–66.
[357] Constantinides G, Ravi Chandran K S, Ulm F J, Van Vliet K J Grid indentation analysis of composite microstructure and mechanics: Principles and validation *Mater Sci Eng A* 2006 **430**:189–202.
[358] Randall N X, Vandamme M, Ulm F J Nanoindentation analysis as a two-

dimensional tool for mapping the mechanical properties of complex surfaces *J Mater Res* 2009 **24**:679–90.
[359] Sebastiani M, Moscatelli R, Ridi F, Baglioni P, Carassiti F High-resolution high-speed nanoindentation mapping of cement pastes: Unravelling the effect of microstructure on the mechanical properties of hydrated phases *Mater Des* 2016 **97**:372–80.
[360] Hintsala E D, Hangen U, Stauffer D D High-Throughput Nanoindentation for Statistical and Spatial Property Determination 2018 **70**:494–503.
[361] Vignesh B, Oliver W C, Kumar G S, Phani P S Critical assessment of high speed nanoindentation mapping technique and data deconvolution on thermal barrier coatings *Mater Des* 2019 **181**:108084.
[362] Mughal M Z, Moscatelli R, Sebastiani M Load displacement and high speed nanoindentation data set at different state of charge (SoC) for spinel LixMn2O4 cathodes *Data Br* 2016 **8**:203–6.
[363] Ruffell S, Bradby J E, Williams J S, Warren O L An in situ electrical measurement technique via a conducting diamond tip for nanoindentation in silicon *J Mater Res* 2007 **22**:578–86.
[364] Ruffell S, Bradby J E, Fujisawa N, Williams J S Identification of nanoindentation-induced phase changes in silicon by in situ electrical characterization *J Appl Phys* 2007 **101**:1–7.
[365] Nguyen H H, Wei P J, Lin J F Electric contact resistance for monitoring nanoindentation-induced delamination *Adv Nat Sci Nanosci Nanotechnol* 2011 **2**:15007.
[366] Mann A B, Heerden D van, Pethica J B, Bowes P, Weihs T P Contact resistance and phase transformations during nanoindentation of silicon *Philos Mag A* 2002 **82**:1921–9.
[367] Juliano T, Domnich V, Gogotsi Y Examining pressure-induced phase transformations in silicon by spherical indentation and Raman spectroscopy: A statistical study *J Mater Res* 2004 **19**:3099–108.
[368] Fang L, Muhlstein C L, Collins J G, Romasco A L, Friedman L H Continuous electrical in situ contact area measurement during instrumented indentation *J Mater Res* 2008 **23**:2480–5.
[369] Fang L, Muhlstein C L, Romasco A L, Collins J G, Friedman L H Augmented instrumented indentation using nonlinear electrical contact current-voltage curves *J Mater Res* 2009 **24**:1820–32.
[370] Comby-Dassonneville S, Volpi F, Parry G, Pellerin D, Verdier M Resistive-nanoindentation: contact area monitoring by real-time electrical contact resistance measurement *MRS Commun* 2019 **9**:1008–14.
[371] Bell T J, Thwaite E G Report on a CIRP sponsored international intercomparison of ultra micro hardness and elasticity measurement *Ann CIRP* 1998 **42**:733–44.
[372] Ames W F Numerical methods for partial differential equationsLondon: ACADEMIC PRESS LIMITED; 1992.
[373] Fornberg B Generation of finite difference formulas on arbitrarily spaced grids *Math Comput* 1988 **51**:699–699.
[374] ASTM E2546-15 Standard Practice for Instrumented Indentation Testing n.d.
[375] Galetto M, Maculotti G, Genta G, Barbato G, Levi R Instrumented Indentation Test in the Nano-range: Performances Comparison of Testing Machines Calibration Methods *Nanomanufacturing Metrol* 2019.
[376] Meneve J L, Smith J F, Jennett N M, Saunders S R J Surface mechanical

property testing by depth sensing indentation *Appl Surf Sci* 1996 **100**–**101**:64–8.
[377] Maculotti G, Genta G, Lorusso M, Pavese M, Ugues D, Galetto M Instrumented Indentation Test: Contact Stiffness Evaluation in the Nano-range *Nanomanufacturing Metrol* 2018 **2**:16–25.
[378] Joint Committee for Guides in Metrology JCGM 101:2008 Evaluation of measurement data -- Supplement 1 to the "Guide to the expression of uncertainty in measurement" -- Propagation of distributions using a Monte Carlo method 2008 **JCGM 101:2**:90.
[379] ISO 14253-2:2011 Geometrical Product Specification (GPS)- Inspection by measurement of workpieces and measuring equipment- Part 2: Guide to the estimation of uncertainty in GPS measurement, in calibration of measuring equipment and in product verification n.d.
[380] Montgomery D, Runger G, Hubele N Engineering statisticsNew York: John Wiley & Sons Inc.; 2010.
[381] Brown M B, Forsythe A B Robust tests for the equality of variances *J Am Stat Assoc* 1974 **69**:364–7.
[382] Bartlett M S, A P R S L Properties of sufficiency and statistical tests *Proc R Soc London Ser A - Math Phys Sci* 1937 **160**:268–82.
[383] Feltz C J, Miller G E An asymptotic test for the equality of coefficients of variation from k populations *Stat Med* 1996 **15**:647–58.
[384] Boggs P T, Byrd R H, Schnabel R B A Stable and Efficient Algorithm for Nonlinear Orthogonal Distance Regression *SIAM J Sci Stat Comput* 1987 **8**:1052–78.
[385] Galetto M, Maculotti G, Genta G, Barbato G, Levi R Instrumented Indentation Test in the Nano-range: Performances Comparison of Testing Machines Calibration Methods *Nanomanufacturing Metrol* 2019 **2**:91–9.
[386] Maculotti G, Genta G, Galetto M Criticalities of iterative calibration procedures for indentation testing machines in the nano-range. Proc. 20th Int. Conf. Exhib. EUSPEN, Genève: Euspen; 2020, p. 2–5.
[387] Efron B Bootstrap methods: another look at the jackkife *Ann Stat* 1979 **7**:1–26.
[388] Manfredi D, Calignano F, Krishnan M, Canali R, Ambrosio E P, Atzeni E From powders to dense metal parts: Characterization of a commercial AlSiMg alloy processed through direct metal laser sintering *Materials (Basel)* 2013 **6**:856–69.
[389] Schmidt M, Merklein M, Bourell D, Dimitrov D, Hausotte T, Wegener K, et al. Laser based additive manufacturing in industry and academia *CIRP Ann* 2017 **66**:561–83.
[390] Ghasri-Khouzani M, Peng H, Attardo R, Ostiguy P, Neidig J, Billo R, et al. Comparing microstructure and hardness of direct metal laser sintered AlSi10Mg alloy between different planes *J Manuf Process* 2019 **37**:274–80.
[391] Vilaro T, Abed S, Knapp W Direct manufacturing of technical parts using selective laser melting: example of automotive application. Proc. 12th Eur. Forum Rapid Prototyp., Paris: 2008.
[392] Wong M, Tsopanos S, Sutcliffe C J, Owen I Selective laser melting of heat transfer devices *Rapid Prototyp J* 2007 **13**:291–7.
[393] Yan C, Hao L, Hussein A, Young P, Huang J, Zhu W Microstructure and mechanical properties of aluminium alloy cellular lattice structures manufactured by direct metal laser sintering *Mater Sci Eng A* 2015

628:238–46.
[394] Salman O O, Brenne F, Niendorf T, Eckert J, Prashanth K G, He T, et al. Impact of the scanning strategy on the mechanical behavior of 316L steel synthesized by selective laser melting *J Manuf Process* 2019 **45**:255–61.
[395] Deckers J, Shahzad K, Vleugels J, Kruth J-P Isostatic pressing assisted indirect selective laser sintering of alumina components *Rapid Prototyp J* 2012 **18**:409–19.
[396] Shahzad K, Deckers J, Kruth J-P, Vleugels J Additive manufacturing of alumina parts by indirect selective laser sintering and post processing *J Mater Process Technol* 2013 **213**:1484–94.
[397] Shahzad K, Deckers J, Boury S, Neirinck B, Kruth J-P, Vleugels J Preparation and indirect selective laser sintering of alumina/PA microspheres *Ceram Int* 2012 **38**:1241–7.
[398] Dewidar M, Dalgarno K W A comparison between direct and indirect laser sintering of metals *J Mater Sci Technol* 2008 **24**:227–32.
[399] Boschetto A, Bottini L Manufacturability of non-assembly joints fabricated in AlSi10Mg by selective laser melting *J Manuf Process* 2019 **37**:425–37.
[400] Miranda G, Faria S, Bartolomeu F, Pinto E, Alves N, Peixinho N, et al. A study on the production of thin-walled Ti6Al4V parts by selective laser melting *J Manuf Process* 2019 **39**:346–55.
[401] Ning J, Mirkoohi E, Dong Y, Sievers D E, Garmestani H, Liang S Y Analytical modeling of 3D temperature distribution in selective laser melting of Ti-6Al-4V considering part boundary conditions *J Manuf Process* 2019 **44**:319–26.
[402] Gusarov A V., Yadroitsev I, Bertrand P, Smurov I Heat transfer modelling and stability analysis of selective laser melting *Appl Surf Sci* 2007 **254**:975–9.
[403] Gusarov A V., Yadroitsev I, Bertrand P, Smurov I Model of Radiation and Heat Transfer in Laser-Powder Interaction Zone at Selective Laser Melting *J Heat Transfer* 2009 **131**:072101.
[404] Masoomi M, Gao X, Thompson S M, Shamsaei N, Bian L, Elwany A Modeliing, simulation and experimental validation of heat transfer during selective laser melting. Proc. ASME 2015 Int. Mech. Eng. Congr. Expo. IMECE2015, Houston, Texas: 2015.
[405] Krishnan M, Atzeni E, Canali R, Calignano F, Manfredi D, Ambrosio E P, et al. On the effect of process parameters on properties of AlSi10Mg parts produced by DMLS *Rapid Prototyp J* 2014 **20**:449–58.
[406] Tian Y, Tomus D, Rometsch P, Wu X Influences of processing parameters on surface roughness of Hastelloy X produced by selective laser melting *Addit Manuf* 2017 **13**:103–12.
[407] Li Y, Gu D Parametric analysis of thermal behavior during selective laser melting additive manufacturing of aluminum alloy powder *Mater Des* 2014 **63**:856–67.
[408] Song B, Zhao X, Li S, Han C, Wei Q, Wen S, et al. Differences in microstructure and properties between selective laser melting and traditional manufacturing for fabrication of metal parts: A review *Front Mech Eng* 2015 **10**:111–25.
[409] Lam L P, Zhang D Q, Liu Z H, Chua C K Phase analysis and microstructure characterization of AlSi10Mg parts produced by Selective Laser Melting *Virtual Phys Prototyp* 2015 **10**:207–15.
[410] Li X P, O'Donnell K M, Sercombe T B Selective laser melting of Al-12Si

alloy: Enhanced densification via powder drying *Addit Manuf* 2016 **10**:10–4.
[411] Mason R L, Gunst R F, Hess J L Statistical design and analysis of experiments: with applications to engineering and science, 2nd EditionNew York: John Wiley & Sons; 2003.
[412] Montgomery D C, Runger G C, Hubele N F Engineering Statistics5th ed.Hoboken (NJ): Wiley; 2010.
[413] ISO 6506-1:2014 Metallic materials — Brinell hardness Test Part 1 : Test methodGenève: International Organization for Standardization; 2014.
[414] Devore J L Probability and Statistics for Engineering and the SciencesBoston, USA: Cengage learning; 2011.
[415] Kempen K, Thijs L, Van Humbeeck J, Kruth J-P Processing AlSi10Mg by selective laser melting: parameter optimisation and material characterization *Mater Sci Technol* 2015 **31**:917–23.
[416] Galetto M, Genta G, Maculotti G, Verna E Defect Probability Estimation for Hardness-Optimised Parts by Selective Laser Melting *Int J Precis Eng Manuf* 2020 **21**:1739–53.
[417] Trevisan F, Calignano F, Lorusso M, Pakkanen J, Aversa A, Ambrosio E P, et al. On the selective laser melting (SLM) of the AlSi10Mg alloy: Process, microstructure, and mechanical properties *Materials (Basel)* 2017 **10**.
[418] Mertens A, Dedry O, Reuter D, Rigo O, Lecomte-Beckers J Thermal treatments of AlSi10Mg processed by laser beam melting. Proc. 26th Int. Solid Free. Fabr. Symp., Austin, TX: 2015, p. 1007–16.
[419] ISO 14577-1:2015 Metallic materials — Instrumented indentation test for hardness and materials parametes - Part 1: Test method n.d.
[420] ISO 18265:2013 Metallic materials - Conversion of hardness values n.d.
[421] Herrmann K Hardness testing Principles and ApplicationsMaterials Park, Ohio: ASM International; 2011.
[422] Barbato G, Barini E M, Genta G, Levi R Features and performance of some outlier detection methods *J Appl Stat* 2011 **38**:2133–49.
[423] Montgomery D Statistical quality control 2012.
[424] M Schmidt M M D B Laser based additive manufacturing in industry and academia *CIRP Ann* 2017 **66**:561–83.
[425] Oyelola O, Crawforth P, M'Saoubi R, Clare A T Machining of functionally graded Ti6Al4V/ WC produced by directed energy deposition *Addit Manuf* 2018 **24**:20–9.
[426] Settineri L, Faga M G, Gautier G, Perucca M Evaluation of wear resistance of AlSiTiN and AlSiCrN nanocomposite coatings for cutting tools *CIRP Ann - Manuf Technol* 2008 **57**:575–8.
[427] Çelik Y H, Demir M E, Kilickap E, Kalkanli A Investigation of wear behavior of aged and non-aged SiC-reinforced AlSi7Mg2 metal matrix composites in dry sliding conditions *J Brazilian Soc Mech Sci Eng* 2020 **42**:1–9.
[428] Durrant-Whyte H F Sensor Models and Multisensor Integration *Int J Rob Res* 1988 **7**:97–113.
[429] Gu D, Hu H Spatial gaussian process regression with mobile sensor networks *IEEE Trans Neural Networks Learn Syst* 2012 **23**:1279–90.
[430] Birch K P, Downs M J An updated Edlén equation for the refractive index of air 1993 **30**:155–62.
[431] Rodger J A Advances in multisensor information fusion: A Markov–Kalman viscosity fuzzy statistical predictor for analysis of oxygen flow,

diffusion, speed, temperature, and time metrics in CPAP *Expert Syst* 2018 **35**:1–21.
[432] Ghiotti A, Simonetto E, Bruschi S, Savio E Enhancing the accuracy of in-process springback measurements of complex tube bending processes using cost-effective embedded sensorsvol. in press2020.
[433] Marinello F, Bariani P, Pasquini A, De Chiffre L, Bossard M, Picotto G B Increase of maximum detectable slope with optical profilers, through controlled tilting and image processing *Meas Sci Technol* 2007 **18**:384–9.
[434] E Savio L C S C J M Economic benefits of metrology in manufacturing *CIRP Ann* 2016 **65**:495–8.
[435] Gibson I, Rosen D W, Stucker B Additive Manufacturing Technologiesvol. 42016.
[436] Farayibi P K, Abioye T E, Clare A T A parametric study on laser cladding of Ti-6Al-4V wire and WC/W2C powder *Int J Adv Manuf Technol* 2016 **87**:3349–58.
[437] Gassmann R C Laser cladding with (WC + W2C)/Co-Cr-C and (WC + W2C)/Ni-B-Si composites for enhanced abrasive wear resistance *Mater Sci Technol* 1996 **12**:691–6.
[438] Sun R L, Yang D Z, Guo L X, Dong S L Laser cladding of Ti-6Al-4V alloy with TiC and TiC+NiCrBSi powders *Surf Coatings Technol* 2001 **135**:307–12.
[439] Mohanty R M, Roy M Thermal sprayed WC-Co coatings for tribological application. Mater. Surf. Eng. Res. Dev., Sawston, Cambridge, UK: Woodhead Publishing Limited; 2012, p. 121–62.
[440] Kathuria Y P Nd-YAG laser cladding of Cr3C2 and TiC cerments *Surf Coatings Technol* 2001 **140**:195–9.
[441] Abioye T E, Farayibi P K, Clare A T A comparative study of Inconel 625 laser cladding by wire and powder feedstock *Mater Manuf Process* 2017 **32**:1653–9.
[442] Oyelola O, Crawforth P, M'Saoubi R, Clare A T On the machinability of directed energy deposited Ti6Al4V *Addit Manuf* 2018 **19**:39–50.
[443] Goodhew P J, Humphreys J, Beanland R Electron Microscopy and Analysis3rd ed.London: Taylor & Francis; 2001.
[444] Gu Y Automated scanning electron microscope based mineral liberation analysis *J Miner Mater Charact Eng* 2003 **2**:33–41.
[445] Genta G, Maculotti G, Barbato G, Levi R, Galetto M Effect of contact stiffness and machine calibration in nano-indentation testing *Procedia CIRP* 2018 **78**:208–12.
[446] Chen L, Iyengar S, Zhou J, Turba K, Ståhl J E Characterization of Microstructure and Mechanical Properties of High Chromium Cast Irons Using SEM and Nanoindentation *J Mater Eng Perform* 2015 **24**:98–105.
[447] Haušild P, Materna A, Kocmanová L, Matějíček J Determination of the individual phase properties from the measured grid indentation data *J Mater Res* 2016 **31**:3538–48.
[448] ISO ISO 14577-1 Metallic materials-Instrumented indentation test for hardness and materials parameters - Part 1: Test method 2014 **2014**.
[449] Lowe D G Distinctive Image Features from Scale-Invariant Keypoints *Int J Comput Vis* 2004 **2**:91–110.
[450] Horn B K P Closed-form solution of absolute orientation using unit quaternions *J Opt Soc Am A* 1987 **4**:629.
[451] Alcantarilla P F, Bartoli A, Andrew J D KAZE Features *ECCVV 2012,*

Part VI 2012 **LNCS 7577**:214–27.
[452] Fukunaga K, Narendra P M A branch and bound algorithm for computing k-nearest neighbors *IEEE Trans Comput* 1975 **C**–**24**:750–3.
[453] Mallat S G A theory for Multiresolution Signal Decomposition: The Wavelet Representation *IEEE Trans Pattern Anal Mach Intell* 1989 **2**:674–93.
[454] Sharifi M, Fathy M, Mahmoudi M T A Classified and Comparative Study of Edge Detection Algorithms. Proceedings. Int. Conf. Inf. Technol. Coding Comput., Las Vegas, NV: IEEE; 2002.
[455] Marr D, Hildreth E Theory of edge detection *Proc R Soc London Ser B, Contain Pap a Biol Character R Soc (Great Britain)* 1980 **207**:187–217.

Appendix A

This appendix reports tables the with relative accuracy between the different method to estimate volumes related to total damage, wear and galling in disc after a pin-on-disc tribological test, investigated in Section 2.4.

The key for reading the tables is in the following Table A 1.

Table A 1 Key to Annex A table headings.

A	B	C	D	E	F	G	H	I…P	Q…V
ISO $\boldsymbol{R_{nom}}$ 4 CSI 20×	ISO $\bar{R}$ 4 CSI 20x	Prof, alt 4 CSI 20x	ISO R_{nom} 8 CSI 20×	ISO $\bar{R}$ 8 CSI 20x	Prof, alt 8 CSI 20x	aut. CSI 20x	VP CSI 20x	As A…H, with CSI 5.5 x	As A…F with CS

Table report also the results on the hypothesis t-test on the difference of sample average built as follows, considering two different average volume estimation by two different methods, i.e., $\overline{V_{M1}}$ and $\overline{V_{M2}}$, each related to a standard uncertainty $u(\overline{V_{M1}})$ and $u(\overline{V_{M2}})$:

$$H_0: \overline{V_{M1}} - \overline{V_{M2}} = 0$$
$$H_1: \overline{V_{M1}} - \overline{V_{M2}} \neq 0$$

At a confidence level p of 95%, the null hypothesis H_0 is rejected if

$$\overline{V_{M1}} - \overline{V_{M2}} \notin \left[t_{0.025,30}s\ ;\ t_{0.975,30}s\right]$$
$$s = u(\overline{V_{M1}} - \overline{V_{M2}}) = \sqrt{u^2(\overline{V_{M1}}) + u^2(\overline{V_{M2}})}$$

Table A 2 Relative Accuracy Total Damage volume PTFE.

	A	B	C	D	E	F	G	H	I	J	K	L	M	N	O	P	Q	R	S	T	U	V
A	0.00																					
B	-0.15%	0.00%																				
C	-0.15%	0.00%	0.00%																			
D	1.12%	1.27%	1.27%	0.00%																		
E	0.98%	1.12%	1.13%	-0.15%	0.00%																	
F	1.40%	1.54%	1.54%	0.27%	0.42%	0.00%																
G	1.18%	1.33%	1.33%	0.06%	0.21%	-0.21%	0.00%															
H	2.05%	2.19%	2.19%	0.93%	1.08%	0.66%	0.87%	0.00%														
I	-1.34%	-1.20%	-1.19%	-2.50%	-2.35%	-2.78%	-2.56%	-3.46%	0.00%													
J	-1.01%	-0.87%	-0.86%	-2.16%	-2.01%	-2.44%	-2.22%	-3.12%	0.33%	0.00%												
K	-1.01%	-0.86%	-0.86%	-2.16%	-2.01%	-2.44%	-2.22%	-3.12%	0.33%	0.00%	0.00%											
L	-0.34%	-0.19%	-0.19%	-1.48%	-1.33%	-1.76%	-1.54%	-2.44%	0.99%	0.67%	0.67%	0.00%										
M	-0.01%	0.13%	0.14%	-1.15%	-1.00%	-1.43%	-1.21%	-2.10%	1.31%	0.99%	0.99%	0.33%	0.00%									
N	0.15%	0.30%	0.30%	-0.99%	-0.84%	-1.26%	-1.05%	-1.94%	1.47%	1.15%	1.15%	0.49%	0.16%	0.00%								
O	1.30%	1.44%	1.44%	0.18%	0.32%	-0.10%	0.12%	-0.76%	2.61%	2.29%	2.29%	1.63%	1.31%	1.15%	0.00%							
P	2.43%	2.57%	2.58%	1.32%	1.47%	1.05%	1.26%	0.39%	3.73%	3.41%	3.41%	2.76%	2.44%	2.29%	1.15%	0.00%						
Q	0.62%	0.77%	0.77%	-0.51%	-0.36%	-0.78%	-0.57%	-1.45%	1.94%	1.62%	1.62%	0.96%	0.63%	0.47%	-0.69%	-1.86%	0.00%					
R	-1.06%	-0.91%	-0.91%	-2.21%	-2.06%	-2.49%	-2.27%	-3.17%	0.28%	-0.04%	-0.05%	-0.72%	-1.05%	-1.21%	-2.39%	-3.58%	-1.69%	0.00%				
S	-1.05%	-0.90%	-0.90%	-2.20%	-2.05%	-2.48%	-2.26%	-3.16%	0.29%	-0.04%	-0.04%	-0.71%	-1.04%	-1.20%	-2.38%	-3.57%	-1.68%	0.01%	0.00%			
T	-0.49%	-0.34%	-0.34%	-1.63%	-1.49%	-1.91%	-1.70%	-2.59%	0.84%	0.52%	0.52%	-0.15%	-0.48%	-0.64%	-1.81%	-3.00%	-1.12%	0.56%	0.55%	0.00%		
U	-2.19%	-2.04%	-2.04%	-3.35%	-3.20%	-3.64%	-3.41%	-4.32%	-0.83%	-1.17%	-1.17%	-1.84%	-2.18%	-2.34%	-3.54%	-4.74%	-2.83%	-1.12%	-1.13%	-1.69%	0.00%	
V	-1.93%	-1.78%	-1.78%	-3.09%	-2.94%	-3.37%	-3.15%	-4.06%	-0.58%	-0.91%	-0.91%	-1.59%	-1.92%	-2.09%	-3.27%	-4.47%	-2.57%	-0.87%	-0.87%	-1.43%	0.25%	0.00%

Table A 3 Relative Accuracy Wear volume PTFE.

	A	B	C	D	E	F	G	H	I	J	K	L	M	N	O	P	Q	R	S	T	U	V
A	0.00%																					
B	-0.15%	0.00%																				
C	-0.15%	0.00%	0.00%																			
D	1.84%	1.98%	1.98%	0.00%																		
E	1.69%	1.84%	1.84%	-0.15%	0.00%																	
F	2.10%	2.25%	2.25%	0.27%	0.42%	0.00%																
G	4.73%	4.87%	4.87%	2.94%	3.09%	2.68%	0.00%															
H	5.63%	5.77%	5.77%	3.87%	4.01%	3.60%	0.95%	0.00%														
I	-0.57%	-0.42%	-0.42%	-2.45%	-2.30%	-2.73%	-5.56%	-6.57%	0.00%													
J	-0.24%	-0.09%	-0.09%	-2.11%	-1.96%	-2.39%	-5.21%	-6.22%	0.33%	0.00%												
K	-0.24%	-0.09%	-0.09%	-2.11%	-1.96%	-2.39%	-5.21%	-6.22%	0.33%	0.00%	0.00%											
L	1.28%	1.42%	1.42%	-0.57%	-0.43%	-0.85%	-3.62%	-4.62%	1.83%	1.51%	1.51%	0.00%										
M	1.60%	1.74%	1.74%	-0.24%	-0.10%	-0.52%	-3.29%	-4.28%	2.15%	1.83%	1.83%	0.33%	0.00%									
N	1.75%	1.89%	1.90%	-0.09%	0.06%	-0.36%	-3.12%	-4.11%	2.30%	1.98%	1.98%	0.48%	0.16%	0.00%								
O	5.05%	5.19%	5.19%	3.27%	3.41%	3.01%	0.34%	-0.62%	5.58%	5.27%	5.27%	3.82%	3.51%	3.36%	0.00%							
P	6.31%	6.44%	6.44%	4.55%	4.69%	4.29%	1.66%	0.72%	6.83%	6.53%	6.53%	5.10%	4.79%	4.64%	1.33%	0.00%						
Q	2.63%	2.77%	2.77%	0.80%	0.95%	0.53%	-2.21%	-3.18%	3.17%	2.86%	2.86%	1.37%	1.05%	0.89%	-2.55%	-3.93%	0.00%					
R	0.98%	1.13%	1.13%	-0.87%	-0.72%	-1.15%	-3.93%	-4.93%	1.54%	1.22%	1.21%	-0.30%	-0.63%	-0.78%	-4.28%	-5.69%	-1.69%	0.00%				
S	0.99%	1.13%	1.13%	-0.86%	-0.72%	-1.14%	-3.92%	-4.92%	1.55%	1.22%	1.22%	-0.29%	-0.62%	-0.78%	-4.28%	-5.68%	-1.68%	0.01%	0.00%			
T	1.54%	1.68%	1.68%	-0.31%	-0.16%	-0.58%	-3.35%	-4.34%	2.09%	1.77%	1.77%	0.26%	-0.06%	-0.22%	-3.70%	-5.09%	-1.12%	0.56%	0.55%	0.00%		
U	-0.13%	0.02%	0.02%	-2.00%	-1.85%	-2.28%	-5.10%	-6.10%	0.43%	0.11%	0.11%	-1.42%	-1.75%	-1.91%	-5.45%	-6.87%	-2.83%	-1.12%	-1.13%	-1.69%	0.00%	
V	0.12%	0.27%	0.27%	-1.74%	-1.60%	-2.02%	-4.83%	-5.84%	0.69%	0.36%	0.36%	-1.17%	-1.50%	-1.66%	-5.19%	-6.60%	-2.57%	-0.86%	-0.87%	-1.43%	0.25%	0.00%

Table A 4 Relative Accuracy Galling volume PTFE.

	A	B	C	D	E	F	G	H	I	J	K	L	M	N	O	P	Q	R	S	T	U	V
A	0.00%																					
B	-0.15%	0.00%																				
C	-0.17%	-0.02%	0.00%																			
D	-22.45%	-22.27%	-22.24%	0.00%																		
E	-22.63%	-22.45%	-22.42%	-0.15%	0.00%																	
F	-22.06%	-21.88%	-21.86%	0.31%	0.46%	0.00%																
G	-116.12%	-115.80%	-115.76%	-76.50%	-76.24%	-77.06%	0.00%															
H	-116.65%	-116.33%	-116.29%	-76.93%	-76.67%	-77.49%	-0.24%	0.00%														
I	-27.08%	-26.90%	-26.87%	-3.79%	-3.64%	-4.12%	41.20%	41.34%	0.00%													
J	-26.67%	-26.48%	-26.46%	-3.45%	-3.30%	-3.78%	41.39%	41.53%	0.33%	0.00%												
K	-26.68%	-26.50%	-26.47%	-3.46%	-3.31%	-3.79%	41.38%	41.52%	0.31%	-0.01%	0.00%											
L	-53.79%	-53.56%	-53.53%	-25.59%	-25.41%	-25.99%	28.84%	29.02%	-21.01%	-21.41%	-21.39%	0.00%										
M	-53.28%	-53.06%	-53.03%	-25.18%	-25.00%	-25.58%	29.07%	29.25%	-20.62%	-21.01%	-21.00%	0.33%	0.00%									
N	-52.84%	-52.61%	-52.58%	-24.82%	-24.64%	-25.21%	29.28%	29.45%	-20.26%	-20.66%	-20.64%	0.62%	0.29%	0.00%								
O	-122.81%	-122.48%	-122.44%	-81.96%	-81.70%	-82.54%	-3.10%	-2.84%	-75.32%	-75.90%	-75.88%	-44.88%	-45.36%	-45.78%	0.00%							
P	-125.83%	-125.50%	-125.45%	-84.43%	-84.16%	-85.01%	-4.49%	-4.24%	-77.70%	-78.28%	-78.26%	-46.84%	-47.33%	-47.76%	-1.35%	0.00%						
Q	-65.73%	-65.49%	-65.46%	-35.35%	-35.15%	-35.78%	23.31%	23.50%	-30.41%	-30.84%	-30.82%	-7.77%	-8.12%	-8.44%	25.62%	26.61%	0.00%					
R	-68.53%	-68.29%	-68.25%	-37.64%	-37.44%	-38.07%	22.02%	22.21%	-32.62%	-33.05%	-33.03%	-9.59%	-9.95%	-10.27%	24.36%	25.37%	-1.69%	0.00%				
S	-68.58%	-68.33%	-68.30%	-37.67%	-37.47%	-38.11%	22.00%	22.19%	-32.65%	-33.08%	-33.07%	-9.62%	-9.98%	-10.30%	24.34%	25.35%	-1.72%	-0.03%	0.00%			
T	-67.58%	-67.34%	-67.30%	-36.86%	-36.66%	-37.29%	22.46%	22.65%	-31.87%	-32.30%	-32.28%	-8.97%	-9.33%	-9.65%	24.79%	25.79%	-1.12%	0.56%	0.59%	0.00%		
U	-70.42%	-70.17%	-70.13%	-39.17%	-38.97%	-39.61%	21.15%	21.34%	-34.10%	-34.53%	-34.52%	-10.81%	-11.18%	-11.50%	23.52%	24.54%	-2.83%	-1.12%	-1.09%	-1.69%	0.00%	
V	-70.01%	-69.77%	-69.73%	-38.85%	-38.64%	-39.29%	21.33%	21.53%	-33.78%	-34.22%	-34.20%	-10.55%	-10.91%	-11.24%	23.70%	24.71%	-2.58%	-0.88%	-0.85%	-1.45%	0.24%	0.00%

Table A 5 t-test on sample averages of Total Damage volume on PTFE. 1 rejects null hypothesis that the two averages are statistically the same.

	A	B	C	D	E	F	G	H	I	J	K	L	M	N	O	P	Q	R	S	T	U	V
A																						
B																						
C																						
D																						
E																						
F																						
G																						
H																						
I																						
J																						
K																						
L																						
M																						
N																						
O																						
P								1														
Q																						
R																						
S																						
T																						
U																						
V																						

Table A 6 t-test on sample averages of Wear volume on PTFE. 1 rejects null hypothesis that the two averages are statistically the same.

	A	B	C	D	E	F	G	H	I	J	K	L	M	N	O	P	Q	R	S	T	U	V
A																						
B																						
C																						
D																						
E																						
F																						
G																						
H																						
I																						
J																						
K																						
L																						
M																						
N																						
O																						
P								1														
Q																						
R																						
S																						
T																						
U																						
V																						

Table A 7 t-test on sample averages of Galling volume on PTFE. 1 rejects null hypothesis that the two averages are statistically the same.

	A	B	C	D	E	F	G	H	I	J	K	L	M	N	O	P	Q	R	S	T	U	V
A																						
B																						
C																						
D																						
E																						
F																						
G	1	1	1	1	1	1																
H	1	1	1	1	1	1																
I							1	1														
J							1	1														
K							1	1														
L							1	1														
M							1	1														
N							1	1														
O	1	1	1	1	1	1	1	1	1	1	1	1	1	1								
P	1	1	1	1	1	1	1	1	1	1	1	1	1	1								
Q																						
R																						
S																						
T	1	1	1												1	1						
U	1	1	1												1	1						
V	1	1	1												1	1						

Table A 8 Relative Accuracy Total Damage volume Aluminium.

	A	B	C	D	E	F	G	H	I	J	K	L	M	N	O	P	Q	R	S	T	U	V
A	0.00%																					
B	0.87%	0.00%																				
C	0.90%	0.04%	0.00%																			
D	-40.25%	-41.47%	-41.53%	0.00%																		
E	-39.03%	-40.25%	-40.30%	0.87%	0.00%																	
F	-38.63%	-39.84%	-39.89%	1.15%	0.29%	0.00%																
G	-55.91%	-57.27%	-57.33%	-11.16%	-12.14%	-12.46%	0.00%															
H	-55.65%	-57.01%	-57.07%	-10.98%	-11.95%	-12.27%	0.17%	0.00%														
I	-1.60%	-2.49%	-2.53%	27.56%	26.92%	26.71%	34.83%	34.72%	0.00%													
J	-0.47%	-1.35%	-1.39%	28.36%	27.74%	27.53%	35.56%	35.45%	1.11%	0.00%												
K	-0.51%	-1.39%	-1.43%	28.33%	27.70%	27.49%	35.53%	35.42%	1.07%	-0.04%	0.00%											
L	-41.53%	-42.76%	-42.82%	-0.91%	-1.79%	-2.09%	9.22%	9.07%	-39.30%	-40.86%	-40.80%	0.00%										
M	-39.96%	-41.18%	-41.23%	0.21%	-0.66%	-0.96%	10.23%	10.08%	-37.75%	-39.30%	-39.24%	1.11%	0.00%									
N	-39.68%	-40.90%	-40.96%	0.40%	-0.47%	-0.76%	10.41%	10.26%	-37.48%	-39.03%	-38.97%	1.30%	0.19%	0.00%								
O	-55.83%	-57.20%	-57.26%	-11.11%	-12.08%	-12.41%	0.05%	-0.12%	-53.38%	-55.10%	-55.04%	-10.11%	-11.35%	-11.56%	0.00%							
P	-56.78%	-58.15%	-58.21%	-11.79%	-12.77%	-13.09%	-0.56%	-0.73%	-54.31%	-56.05%	-55.98%	-10.78%	-12.02%	-12.24%	-0.61%	0.00%						
Q	-48.16%	-49.45%	-49.51%	-5.64%	-6.56%	-6.87%	4.97%	4.81%	-45.83%	-47.46%	-47.40%	-4.69%	-5.86%	-6.07%	4.93%	5.50%	0.00%					
R	-52.13%	-53.46%	-53.51%	-8.47%	-9.42%	-9.74%	2.42%	2.26%	-49.73%	-51.41%	-51.35%	-7.49%	-8.70%	-8.91%	2.38%	2.97%	-2.68%	0.00%				
S	-52.16%	-53.49%	-53.55%	-8.50%	-9.44%	-9.76%	2.40%	2.24%	-49.77%	-51.45%	-51.39%	-7.52%	-8.72%	-8.94%	2.36%	2.95%	-2.70%	-0.02%	0.00%			
T	-54.82%	-56.17%	-56.23%	-10.39%	-11.36%	-11.68%	0.70%	0.53%	-52.38%	-54.10%	-54.03%	-9.39%	-10.62%	-10.84%	0.65%	1.25%	-4.50%	-1.77%	-1.75%	0.00%		
U	-58.97%	-60.36%	-60.42%	-13.35%	-14.34%	-14.67%	-1.96%	-2.13%	-56.46%	-58.22%	-58.15%	-12.32%	-13.59%	-13.81%	-2.01%	-1.39%	-7.30%	-4.50%	-4.47%	-2.68%	0.00%	
V	-56.64%	-58.01%	-58.07%	-11.69%	-12.66%	-12.99%	-0.47%	-0.64%	-54.17%	-55.90%	-55.84%	-10.68%	-11.92%	-12.14%	-0.52%	0.09%	-5.72%	-2.97%	-2.94%	-1.17%	1.47%	0.00%

Table A 9 Relative Accuracy Wear volume Aluminium.

	A	B	C	D	E	F	G	H	I	J	K	L	M	N	O	P	Q	R	S	T	U	V
A	0.00%																					
B	0.87%	0.00%																				
C	0.91%	0.05%	0.00%																			
D	-54.64%	-55.99%	-56.07%	0.00%																		
E	-53.30%	-54.64%	-54.71%	0.87%	0.00%																	
F	-52.82%	-54.16%	-54.23%	1.17%	0.31%	0.00%																
G	-73.05%	-74.56%	-74.64%	-11.90%	-12.88%	-13.23%	0.00%															
H	-72.71%	-74.22%	-74.30%	-11.68%	-12.66%	-13.01%	0.20%	0.00%														
I	-2.48%	-3.38%	-3.43%	33.73%	33.15%	32.94%	40.78%	40.66%	0.00%													
J	-1.34%	-2.23%	-2.28%	34.46%	33.89%	33.69%	41.43%	41.32%	1.11%	0.00%												
K	-1.39%	-2.28%	-2.33%	34.43%	33.86%	33.65%	41.41%	41.29%	1.06%	-0.05%	0.00%											
L	-59.81%	-61.21%	-61.29%	-3.35%	-4.25%	-4.57%	7.65%	7.47%	-55.94%	-57.69%	-57.62%	0.00%										
M	-58.04%	-59.42%	-59.50%	-2.20%	-3.09%	-3.41%	8.67%	8.49%	-54.21%	-55.94%	-55.86%	1.11%	0.00%									
N	-57.71%	-59.09%	-59.16%	-1.99%	-2.88%	-3.20%	8.86%	8.68%	-53.89%	-55.62%	-55.54%	1.32%	0.21%	0.00%								
O	-74.04%	-75.56%	-75.64%	-12.54%	-13.53%	-13.88%	-0.57%	-0.77%	-69.82%	-71.73%	-71.64%	-8.90%	-10.12%	-10.35%	0.00%							
P	-74.28%	-75.80%	-75.89%	-12.70%	-13.68%	-14.04%	-0.71%	-0.91%	-70.06%	-71.97%	-71.88%	-9.05%	-10.28%	-10.50%	-0.14%	0.00%						
Q	-59.73%	-61.13%	-61.20%	-3.29%	-4.19%	-4.52%	7.70%	7.51%	-55.86%	-57.61%	-57.53%	0.05%	-1.07%	-1.28%	8.22%	8.35%	0.00%					
R	-64.01%	-65.44%	-65.52%	-6.06%	-6.98%	-7.32%	5.22%	5.04%	-60.03%	-61.83%	-61.75%	-2.62%	-3.78%	-3.99%	5.76%	5.89%	-2.68%	0.00%				
S	-64.14%	-65.57%	-65.65%	-6.14%	-7.07%	-7.40%	5.15%	4.96%	-60.16%	-61.96%	-61.88%	-2.71%	-3.86%	-4.08%	5.69%	5.82%	-2.76%	-0.08%	0.00%			
T	-61.94%	-63.35%	-63.43%	-4.72%	-5.64%	-5.96%	6.42%	6.23%	-58.01%	-59.79%	-59.71%	-1.33%	-2.47%	-2.68%	6.95%	7.08%	-1.38%	1.26%	1.34%	0.00%		
U	-66.28%	-67.73%	-67.81%	-7.52%	-8.46%	-8.80%	3.91%	3.72%	-62.25%	-64.07%	-63.99%	-4.04%	-5.21%	-5.43%	4.46%	4.59%	-4.10%	-1.38%	-1.30%	-2.68%	0.00%	
V	-63.99%	-65.42%	-65.50%	-6.04%	-6.97%	-7.30%	5.24%	5.05%	-60.01%	-61.81%	-61.73%	-2.61%	-3.76%	-3.98%	5.77%	5.91%	-2.66%	0.01%	0.09%	-1.26%	1.38%	0.00%

Table A 10 Relative Accuracy Galling volume Aluminium.

	A	B	C	D	E	F	G	H	I	J	K	L	M	N	O	P	Q	R	S	T	U	V
A	0.00%																					
B	0.87%	0.00%																				
C	0.87%	0.00%	0.00%																			
D	12.95%	12.19%	12.19%	0.00%																		
E	13.71%	12.95%	12.95%	0.87%	0.00%																	
F	13.84%	13.09%	13.09%	1.02%	0.16%	0.00%																
G	7.45%	6.65%	6.64%	-6.32%	-7.24%	-7.42%	0.00%															
H	7.43%	6.62%	6.61%	-6.35%	-7.28%	-7.45%	-0.03%	0.00%														
I	1.66%	0.81%	0.80%	-12.97%	-13.95%	-14.14%	-6.26%	-6.22%	0.00%													
J	2.76%	1.91%	1.91%	-11.71%	-12.69%	-12.87%	-5.08%	-5.04%	1.11%	0.00%												
K	2.74%	1.89%	1.89%	-11.73%	-12.71%	-12.89%	-5.09%	-5.06%	1.09%	-0.02%	0.00%											
L	26.07%	25.43%	25.42%	15.07%	14.33%	14.19%	20.12%	20.14%	24.82%	23.98%	23.99%	0.00%										
M	26.89%	26.25%	26.25%	16.02%	15.28%	15.15%	21.00%	21.03%	25.66%	24.82%	24.83%	1.11%	0.00%									
N	26.96%	26.32%	26.32%	16.09%	15.36%	15.22%	21.08%	21.10%	25.72%	24.89%	24.90%	1.20%	0.09%	0.00%								
O	11.45%	10.68%	10.68%	-1.72%	-2.61%	-2.78%	4.32%	4.35%	9.95%	8.94%	8.96%	-19.77%	-21.12%	-21.23%	0.00%							
P	7.90%	7.09%	7.09%	-5.81%	-6.73%	-6.90%	0.48%	0.51%	6.34%	5.29%	5.30%	-24.58%	-25.98%	-26.10%	-4.02%	0.00%						
Q	-5.39%	-6.31%	-6.31%	-21.07%	-22.12%	-22.32%	-13.88%	-13.84%	-7.17%	-8.37%	-8.35%	-42.55%	-44.15%	-44.29%	-19.02%	-14.42%	0.00%					
R	-8.21%	-9.15%	-9.16%	-24.31%	-25.40%	-25.60%	-16.93%	-16.89%	-10.04%	-11.28%	-11.26%	-46.37%	-48.01%	-48.15%	-22.20%	-17.49%	-2.68%	0.00%				
S	-7.89%	-8.84%	-8.84%	-23.95%	-25.03%	-25.23%	-16.58%	-16.55%	-9.72%	-10.95%	-10.93%	-45.94%	-47.58%	-47.72%	-21.85%	-17.14%	-2.38%	0.29%	0.00%			
T	-28.51%	-29.63%	-29.64%	-47.63%	-48.92%	-49.16%	-38.86%	-38.82%	-30.69%	-32.15%	-32.13%	-73.83%	-75.78%	-75.95%	-45.13%	-39.53%	-21.94%	-18.76%	-19.11%	0.00%		
U	-31.95%	-33.11%	-33.11%	-51.59%	-52.91%	-53.15%	-42.58%	-42.54%	-34.19%	-35.69%	-35.67%	-78.49%	-80.49%	-80.66%	-49.02%	-43.27%	-25.21%	-21.94%	-22.30%	-2.68%	0.00%	
V	-29.48%	-30.61%	-30.62%	-48.75%	-50.05%	-50.29%	-39.91%	-39.87%	-31.67%	-33.15%	-33.13%	-75.15%	-77.11%	-77.28%	-46.23%	-40.58%	-22.86%	-19.66%	-20.01%	-0.76%	1.87%	0.00%

Table A 11 t-test on sample averages of Total Damage volume on Aluminium. 1 rejects null hypothesis that the two averages are statistically the same.

	A	B	C	D	E	F	G	H	I	J	K	L	M	N	O	P	Q	R	S	T	U	V
A																						
B																						
C																						
D																						
E																						
F																						
G	1	1	1																			
H	1	1	1																			
I							1	1														
J							1	1														
K							1	1														
L																						
M																						
N																						
O	1	1	1						1	1	1											
P	1	1	1					1	1	1	1											
Q																						
R																						
S																						
T																						
U																						
V																						

Table A 12 t-test on sample averages of Wear volume on Aluminium. 1 rejects null hypothesis that the two averages are statistically the same.

	A	B	C	D	E	F	G	H	I	J	K	L	M	N	O	P	Q	R	S	T	U	V
A																						
B																						
C																						
D																						
E																						
F																						
G	1	1	1																			
H	1	1	1																			
I							1	1														
J							1	1														
K							1	1														
L																						
M																						
N																						
O	1	1	1						1	1	1											
P	1	1	1					1	1	1	1											
Q																						
R																						
S																						
T																						
U																						
V																						

Table A 13 t-test on sample averages of Galling volume on Aluminium. 1 rejects null hypothesis that the two averages are statistically the same.

	A	B	C	D	E	F	G	H	I	J	K	L	M	N	O	P	Q	R	S	T	U	V
A																						
B																						
C																						
D																						
E																						
F																						
G																						
H																						
I																						
J																						
K																						
L																						
M																						
N																						
O							1	1														
P								1							1							
Q																						
R																						
S																						
T												1	1	1								
U												1	1	1								
V												1	1	1								

Appendix B

Publications in Journals

1. Maculotti G, Pistone G, Vicario G 2021 Inference on errors in industrial parts: Kriging and variogram versus geometrical product specifications standard *Applied Stochastic Models in Business and Industry* in press
2. Galetto M, Genta G, Maculotti G, Verna E 2020 Defect probability estimation for hardness-optimised parts by Selective Laser Melting *International Journal of Precision Engineering and Manufacturing* **21**: 1739-1753
3. Galetto M, Genta G, Maculotti M 2020 Single-step calibration method for nano indentation testing machines *CIRP Annals – Manufacturing Technology* **69**(1) 429-432
4. Maculotti G, Feng X, Su R, Galetto M, Leach R 2019 Residual flatness and scale calibration for a point autofocus surface topography measuring instrument *Measurement Science and Technology* **30** 065008
5. Maculotti G, Genta G, Lorusso M, Galetto M 2019 Assessment of heat treatment effect on AlSi10Mg by Selective Laser Melting through indentation testing *Key Engineering Materials* **813** 171-177
6. Galetto M, Maculotti G, Genta G, Barbato G, Levi R 2019 Instrumented Indentation Test in the Nano-Range: Performances Comparison of Testing Machines Calibration Methods *Nanomanufacturing and Metrology* **2**(2) 91-99
7. Maculotti G, Genta G, Lorusso M, Pavese M, Ugues D, Galetto M 2019 Instrumented Indentation Test: Contact Stiffness Evaluation in the Nano-range *Nanomanufacturing and Metrology* **2**(1) 16-25
8. Maculotti G, Feng X, Galetto M, Leach R 2018 Noise evaluation of a point autofocus surface topography measuring instrument *Measurement Science and Technology* **29** 065008

Publications in Conferences

1. Maculotti G, Genta G, Galetto M 2020 Criticalities of iterative calibration procedures for indentation testing machines in the nano-range *20th International conference of the European society for* precision *engineering and nanotechnology* CERN, Geneva 8-12 June
2. Maculotti G, Genta G, Galetto M 2019 Comparison of calibration methods for nano-indentation testing machines *XIV Convegno dell'Associazione Italiana Tecnologie Manifatturiere* Padova 9-11 September
3. Maculotti G, Genta G, Galetto M 2019 Monte Carlo estimation of calibration uncertainty for Instrumented Indentation testing machines *Mathematical and Statistical Method for Metrology* Turin 30-31 May

4. Maculotti G, Senin N, Oyelola O, Galetto M, Clare A T, Leach R 2019 Multi-sensor data fusion for the characterization of laser cladded cermet coatings *19th International conference of the European society for* precision *engineering and nanotechnology* Bilbao 3-7 June
5. Genta G, Maculotti G, Barbato G, Levi R, Galetto M 2018 Effect of contact stiffness and machine calibration in nano-indentation testing *Proceeding CIRP* **78** 208-212
6. Maculotti G, Genta G, Lorusso M, Pavese M, Ugues D, Galetto M 2018 Instrumented indentation test: Contact stiffness evaluation in the nano-range *Proceedings 6th International conference on nanoManufacturing* London 4-6 July
7. Maculotti G, Feng X, Galetto M, Leach R 2018 Measurement noise evaluation, noise bandwidth specification and temperature effects in 3D point autofocusing microscopy *Proceedings of 18th International conference of the European society for precision engineering and nanotechnology* Venice 4-8 June
8. Feng X, Quagliotti D, Maculotti G, Syam W P, Tosello G, Hansen H N, Galetto M, Leach R 2017 Measurement noise of a point autofocus surface topography instrument *Proceedings of 21st International Conference on Metrology and Properties of Engineering Surfaces* Göteborg 26-29 June